AAAS

Science

SPECIAL ISSUE

MANDALAY QUAKE

30 OCTOBER 2025

Can AI predict the workings of a complete cell?
p. 436

Chimpanzees can weigh the evidence
pp. 444 & 521

Neuronal rewiring wins Eppendorf & *Science* Prize
p. 482

Your bridge to successful innovation.

NEB's Customized Solutions Team is here to help, and serves as a bridge to the support and resources you need to ensure your success.

Creating the right partnership is essential when pioneering a new life science product. Every aspect of development – technical expertise, reagent optimization, manufacturing scale, turnaround time, reagent quality, and comprehensive logistical support – is vital for achieving your objectives. And in the regulated markets landscape, these challenges magnify, demanding an even more specialized approach.

Your Bridge to Successful Innovation

- Leverage NEB's 50 years of experience in enzymology and reagent manufacturing
- As an extension of your team, we prioritize a deep understanding of your objectives, work with you on an optimal solution, and help to anticipate your future needs
- Benefit from our ISO 9001- and 13485-certified processes and commitment to quality, as well as our GMP-grade* production facility, and specialized lyophilization facility for the highest quality production standards
- Access unparalleled support from our dedicated account managers, program managers, technical scientists and production teams
- We work closely with you on inventory management and global distribution through our network of NEB-owned subsidiaries, to ensure successful commercialization

NEB's Customized Solutions Team will help you access novel products, meet quality specifications, speed time to market, and streamline your supply chain, allowing you to focus more on what matters most — innovation.

Ready to start the discussion? Learn more at **www.neb.com/customizedsolutions**.

NEW ENGLAND
Biolabs®

** "GMP-grade" is a branding term NEB uses to describe products manufactured or finished at NEB's Rowley facility. The Rowley facility was designed to manufacture products under more rigorous infrastructure and process controls to achieve more stringent product specifications and customer requirements. Products manufactured at NEB's Rowley facility are manufactured in compliance with ISO 9001 and ISO 13485 quality management system standards. However, at this time, NEB does not manufacture or sell products known as Active Pharmaceutical Ingredients (APIs), nor does NEB manufacture its products in compliance with all of the Current Good Manufacturing Practice regulations.*

CONTENTS

30 OCTOBER 2025
VOLUME 390
ISSUE 6772

A March 2025 earthquake caused severe damage at its epicenter in Mandalay, Myanmar, including to pagodas and other religious sites.

ON THE COVER

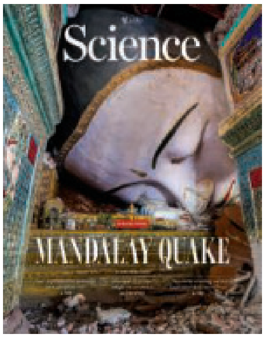

A Buddha statue lies face down in rubble in this photo taken a week after the 28 March earthquake in Mandalay, Myanmar. The earthquake caused fatalities across a broad swath of the country and beyond. This issue features papers exploring the risk and reasons behind the anomalously fast, sustained rupture. See the special section beginning on page 454. Photo: Reuters

SPECIAL ISSUE

2025 Mandalay earthquake

INTRODUCTION

PERSPECTIVE

RESEARCH ARTICLES

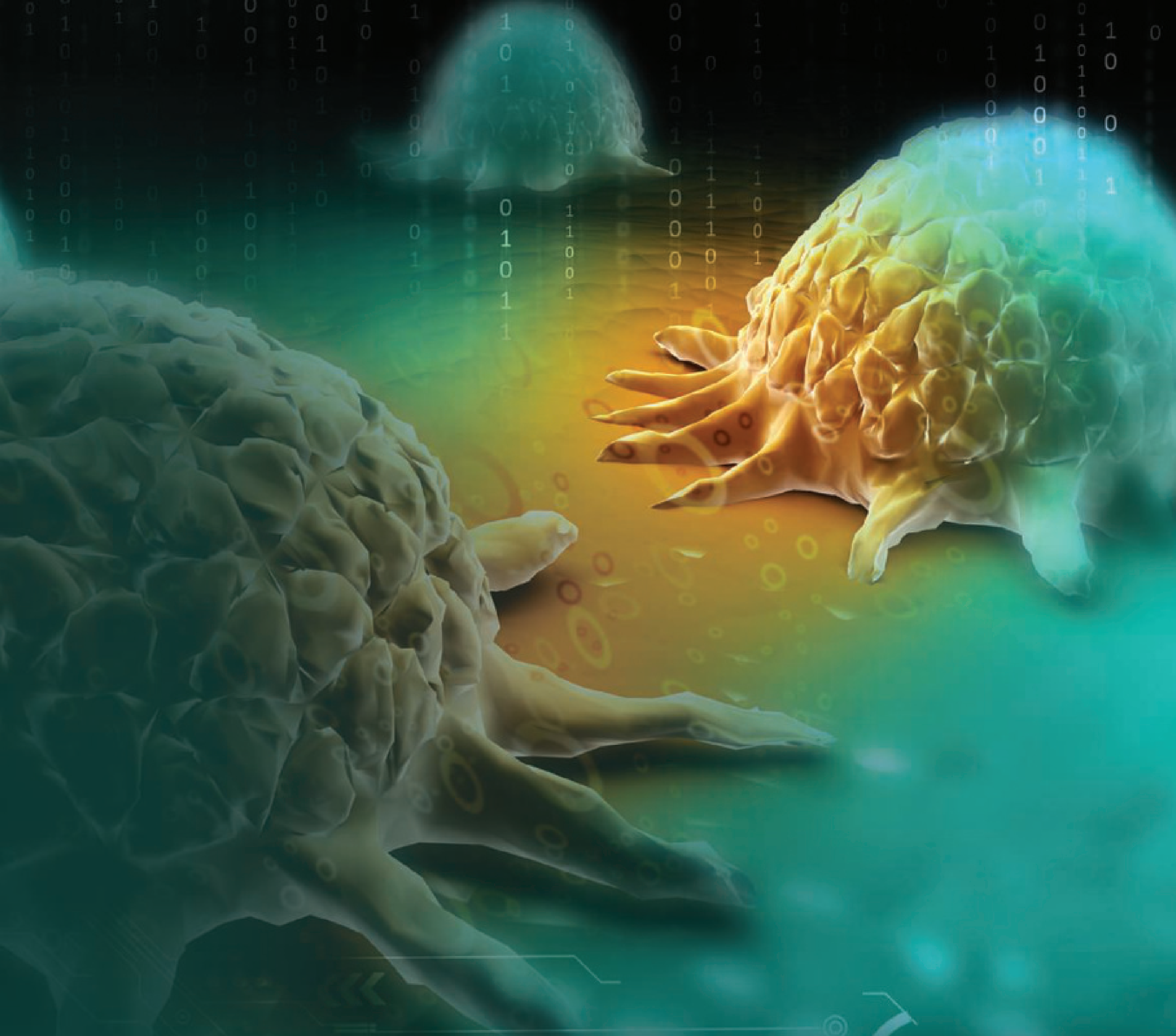

EDITORIAL

NEWS

FEATURES

COMMENTARY

PERSPECTIVES

POLICY FORUM

BOOKS ET AL.

LETTERS

PRIZE ESSAY

REVIEWS

REVIEW SUMMARY

RESEARCH

HIGHLIGHTS

RESEARCH SUMMARIES

RESEARCH ARTICLES

WORKING LIFE

***Science* serves as a forum for discussion of important issues related to the advancement of science by publishing material on which a consensus has been reached as well as including the presentation of minority or conflicting points of view. Accordingly, all articles published in *Science*—including editorials, news, commentary, and book reviews—are signed and reflect the individual views of the authors and not official points of view adopted by AAAS or the institutions with which the authors are affiliated.** *Science* (ISSN 0036-8075) is published weekly on Thursday, except last week in December, by the American Association for the Advancement of Science, 1200 New York Avenue, NW, Washington, DC 20005. Periodicals mail postage (publication No. 484460) paid at Washington, DC, and additional mailing offices. Copyright © 2025 by the American Association for the Advancement of Science. The title *Science* is a registered trademark of the AAAS. Domestic individual membership, including subscription (12 months): $165 ($74 allocated to subscription). Domestic institutional subscription (51 issues): $2865; Foreign postage extra: Air assist delivery: $135. First class, airmail, student, and emeritus rates on request. Canadian rates with GST available upon request, GST #125488122. Publications Mail Agreement Number 1069624. **Printed in the U.S.A. Change of address:** Allow 4 weeks, giving old and new addresses and 8-digit account number. **Postmaster:** Send change of address to AAAS, P.O. Box 96178, Washington, DC 20090–6178. **Single-copy sales:** $15 each plus shipping and handling available from backissues.science.org; bulk rate on request. **Authorization to reproduce** material for internal or personal use under circumstances not falling within the fair use provisions of the Copyright Act can be obtained through the Copyright Clearance Center (CCC), www.copyright.com. The identification code for *Science* is 0036-8075. *Science* is indexed in the *Reader's Guide to Periodical Literature* and in several specialized indexes.

A high-mobility quadruped robotic dog, developed at KFUPM.

Nurturing entrepreneurship to drive economic success

Saudi Arabia's King Fahd University of Petroleum and Minerals (KFUPM) aims to create new economic sectors by attracting top talent and nurturing their entrepreneurial spirit.

KFUPM is in the midst of a complete transformation. "Not a single stone has been left unturned," says Muhammad M. Al-Saggaf, president of the university.

An alum of KFUPM and experienced industry leader, Al-Saggaf understands both where the university has been and where it needs to go. About a decade ago, as Saudi Arabia launched its economic development plan, Vision 2030, the government recognized that KFUPM would need to be an independent institution in order to reach its full potential. In 2020, Al-Saggaf was appointed as KFUPM president and began leading the university's transformation following its newfound independence. Since then, he has implemented sweeping changes to give KFUPM the flexibility and agility needed to strengthen both the local and global economies.

Diversity is a key component of the changes. That means diversity in thought, with more than 100 new interdisciplinary academic programs and more than 20 new interdisciplinary research centers. It also means embracing a rich cultural diversity with students coming from more than 75 countries. And although KFUPM was historically a male-only university for 60 years, the university also recognized the importance of gender diversity by opening the university's doors to women for the first time in 2021. At KFUPM, women now make up a remarkable 50% of undergraduate engineering students, well above the averages at many top institutions worldwide.

Science Custom Publishing sat down with Al-Saggaf to learn more about the evolution of KFUPM to a leading university that is transforming the research landscape and training the next generation of entrepreneurs to innovate in service of humanity.

KFUPM by the numbers

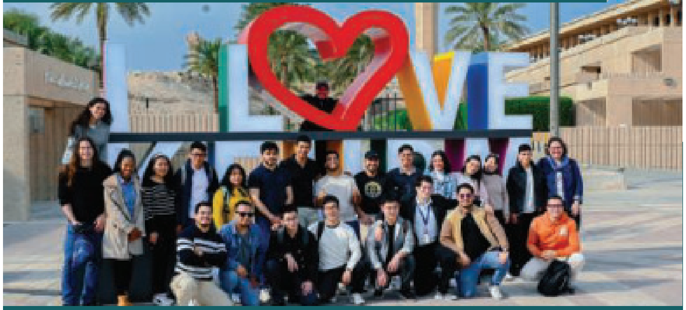

- ~100 new academic programs
- More than 20 new interdisciplinary research centers
- Students represent 75+ countries
- Ranks 67th globally overall
- Ranks 5th globally in # of patents
- 39% pursue graduate degrees
- Employability rate is 93%

PHOTO: PHOTOS PROVIDED BY KFUPM

Muhammad Al-Saggaf, President of KFUPM.

When you became president, you began a deliberate transformation of the university. What is KFUPM's current mandate?

We have a very definite mandate to help expand the economy of Saudi Arabia and, by implication, the global economy. But how do you expand the economy of a country that relies substantially on one sector, which is oil and gas? The answer is, you can only expand the economy by spawning new sectors, creating and nourishing them. To do this, you need two things: investment and talent, and one cannot make up for the other.

Our niche at KFUPM is developing economy-creating talent, the people who are going to create the future sectors, and subsequently the future jobs, and therefore contribute to the expansion of the economy. We tell our students when they join KFUPM, "You are not here to learn to get a job; you are here to learn to create a job." We know that this is achievable, as our students are some of the smartest students worldwide. The requirements to get into KFUPM are higher than those of medical schools, and we attract the top 0.8% of the talent in the region. With this, we have a stronghold on attracting the talent that are suitable to be economy-creating talent, to create the sectors of tomorrow.

How has research changed during the transformation?

We overhauled research 100% at KFUPM. The objective of research is not to produce publications and glory for the researcher or the institution, but rather to help humanity, to impact society at large, to improve the human condition. Therefore, we need to research things that are relevant to the challenges facing humanity, like access to water and food, as well as affordable and clean energy.

In addition, we say this is a research university that does teaching, not the other way around. Every faculty member at KFUPM must engage in research, and we do this through more than 20 new interdisciplinary research centers created over the past 5 years. The crux of each of these research centers is interdisciplinary activities. We believe that knowledge is created at the intersection of disciplines, that it is the nexus of disciplines that gives rise to innovation. If you limit yourself to a certain discipline, you plateau very quickly and run out of ideas.

How does KFUPM's research tie into industry's needs and real-world global challenges?

Research cannot be done in a vacuum—you need to have a constant pollination of industry and academic thinking. The short answer is that we emphasize strong links with industry, and we strive to be a "tech-leaping" institution. That means that we should foresee challenges facing humanity and start developing and articulating solutions for them right now, before industry comes knocking. Hence, all of our 100 new programs are interdisciplinary, and all of them are future-facing. Our programs include topics such as AI and machine learning, cybersecurity and blockchain, visual computing, and quantum computing.

How do you nurture and encourage entrepreneurship among faculty and students?

Entrepreneurship is the natural catalyst that turns research into actual products. We are recognizing 2025 as the year of entrepreneurship at KFUPM, and we reorganized the entrepreneurship function at KFUPM from the ground up. For example, we tied the creation of new ventures to performance evaluations of our faculty. We have developed what we call our 0-0-0 policy to unlock full startup ownership rights for faculty and students, whether Saudi or international. Simply put, we require zero equity, zero royalty, and zero other tangential fees from our faculty and students, in order to support their success. It is now practically free for faculty and students to pursue their dream of establishing new startups with no strings attached—absolutely none.

Other highlights include a postdoc fellowship for entrepreneurs, where postdocs spend 50% of their time developing startups, and a new fellowship for undergraduate student founders. In addition, we are building a large prototyping center and scale-up facilities. We are launching the KFUPM Venture Craft Challenge, a worldwide global prize for startup ideas that have the potential to make a real impact on society.

AI is a key element of the educational program at KFUPM. Could you explain how AI is incorporated into the curriculum and why?

We have to foresee the future before industry develops that future, and AI is one concrete example of this. When we started the transformation 5 years ago, AI was not a hot technology, but we knew that AI is to this generation what mathematics was to our generation. You could not be an engineer, a scientist, or a financier if you didn't study mathematics. So, we came up with something that we called AI + X. You first learn AI at KFUPM, and then you learn X, X being your major. That is a requirement for all students, and it has added significant value to them in the marketplace because employers value this knowledge.

As the university continues to evolve, what are your aspirations for KFUPM and its place within the international academic and research landscape?

We want to transform KFUPM from a good regional university to a top international university whose impact is felt. I think becoming a top international university has, to some degree, been achieved, but I want the second part of that statement to be true. Our aspiration is that somebody will say, "Humanity is getting better access to clean water because of this technology that was invented at KFUPM." This is my personal aspiration and why I came to KFUPM—to make an impact on humanity. It will be a long journey, but we are in it till the end.

Sponsored by

KFUPM

PHOTO: PHOTOS PROVIDED BY KFUPM

Science AAAS

EDITOR-IN-CHIEF **Holden Thorp**, hthorp@aaas.org
EXECUTIVE EDITOR Valda Vinson
EDITORS, RESEARCH Sacha Vignieri, Jake S. Yeston **EDITOR, COMMENTARY** Lisa D. Chong
DEPUTY EXECUTIVE EDITOR Lauren Kmec

DEPUTY EDITORS Stella M. Hurtley (UK), Phillip D. Szuromi **SENIOR EDITORS** Caroline Ash (UK), Michael A. Funk, Angela Hessler, Di Jiang, Priscilla N. Kelly, Marc S. Lavine (Canada), Sarah Lempriere (UK), Mattia Maroso, Yevgeniya Nusinovich, Ian S. Osborne (UK), Joana Osório (UK), L. Bryan Ray, H. Jesse Smith, Keith T. Smith (UK), Jelena Stajic, Peter Stern (UK), Yury V. Suleymanov, Valerie B. Thompson, Brad Wible **ASSOCIATE EDITORS** Jack Huang, Sumin Jin, Bianca Lopez, Sarah Ross (UK), Madeleine Seale (UK), Corinne Simonti, Ekeoma Uzogara **SENIOR LETTERS EDITOR** Jennifer Sills **NEWSLETTER EDITOR** Christie Wilcox **RESEARCH & DATA ANALYST** Jessica L. Slater **LEAD CONTENT PRODUCTION EDITORS** Chris Filiatreau, Harry Jach **SR. CONTENT PRODUCTION EDITOR** Amelia Beyna **CONTENT PRODUCTION EDITORS** Anne Abraham, Robert French, Julia Haber-Katris, Nida Masiulis, Abigail Shashikanth, Suzanne M. White **SENIOR PROGRAM ASSOCIATE** Maryrose Madrid **EDITORIAL MANAGER** Joi S. Granger **EDITORIAL ASSOCIATES** Aneera Dobbins, Lisa Johnson, Jerry Richardson, Anita Wynn **SENIOR EDITORIAL COORDINATORS** Alexander Kief, Ronmel Navas, Isabel Schnaidt, Alice Whaley (UK), Brian White **EDITORIAL COORDINATORS** Samuel Bates, Clair Goodhead (UK), Kat Kirkman, Daniel Young **ADMINISTRATIVE COORDINATOR** Karalee P. Rogers **ASI DIRECTOR, OPERATIONS** Janet Clements (UK) **ASI OFFICE MANAGER** Carly Hayward (UK) **ASI SR. OFFICE ADMINISTRATORS** Simon Brignell (UK), Jessica Waldock (UK) **COMMUNICATIONS DIRECTOR** Meagan Phelan **DEPUTY DIRECTOR** Matthew Wright **SENIOR WRITERS** Walter Beckwith, Joseph Cariz, Abigail Eisenstadt **WRITER** Mahathi Ramaswamy **SENIOR COMMUNICATIONS ASSOCIATES** Zachary Graber, Sarah Woods **COMMUNICATIONS ASSOCIATES** Kiara Brooks, Haley Riley, Mackenzie Williams

NEWS EDITOR Tim Appenzeller

NEWS MANAGING EDITOR John Travis **INTERNATIONAL EDITOR** David Malakoff **DEPUTY NEWS EDITORS** Rachel Bernstein, Martin Enserink, David Grimm, Eric Hand, Michael Price, Kelly Servick, Matt Warren (Europe) **SENIOR CORRESPONDENTS** Daniel Clery (UK), Jon Cohen, Jeffrey Mervis **ASSOCIATE EDITORS** Michael Greshko, Katie Langin **NEWS REPORTERS** Jeffrey Brainard, Adrian Cho, Phie Jacobs, Jocelyn Kaiser, Robert F. Service, Jennie Erin Smith, Erik Stokstad, Paul Voosen **CONSULTING EDITOR** Elizabeth Culotta **CONTRIBUTING CORRESPONDENTS** Vaishnavi Chandrashekhar, Dan Charles, Warren Cornwall, Andrew Curry (Berlin), Ann Gibbons, Kai Kupferschmidt (Berlin), Andrew Lawler, Mitch Leslie, Virginia Morell, Dennis Normile (Tokyo), Catherine Offord, Cathleen O'Grady, Elisabeth Pain (Careers), Charles Piller, Zack Savitsky, Richard Stone (Senior Asia Correspondent), Gretchen Vogel (Berlin), Lizzie Wade (Mexico City) **INTERNS** Celina Zhao **COPY EDITORS** Julia Cole (Senior Copy Editor), Hannah Knighton, Cyra Master (Copy Chief) **ADMINISTRATIVE SUPPORT** Meagan Weiland

CREATIVE DIRECTOR Beth Rakouskas

DESIGN MANAGING EDITOR Chrystal Smith **GRAPHICS MANAGING EDITOR** Chris Bickel **PHOTOGRAPHY MANAGING EDITOR** Emily Petersen **MULTIMEDIA MANAGING PRODUCER** Kevin McLean **DIGITAL DIRECTOR** Kara Estelle-Powers **DESIGN EDITOR** Marcy Atarod **DESIGNER** Noelle Jessup **SENIOR SCIENTIFIC ILLUSTRATOR** Noelle Burgess **SCIENTIFIC ILLUSTRATORS** Austin Fisher, Kellie Holoski, Ashley Mastin **SENIOR GRAPHICS EDITOR** Monica Hersher **GRAPHICS EDITOR** Veronica Penney **SENIOR PHOTO EDITOR** Charles Borst **PHOTO EDITOR** Elizabeth Billman **SENIOR PODCAST PRODUCER** Sarah Crespi **SENIOR VIDEO PRODUCER** Meagan Cantwell **SOCIAL MEDIA STRATEGIST** Jessica Hubbard **SOCIAL MEDIA PRODUCER** Sabrina Jenkins **WEB DESIGNER** Jennie Pajerowski

CHIEF EXECUTIVE OFFICER AND EXECUTIVE PUBLISHER
Sudip Parikh
PUBLISHER, SCIENCE FAMILY OF JOURNALS Bill Moran

DIRECTOR, BUSINESS OPERATIONS & ANALYSIS Eric Knott **MANAGER, BUSINESS OPERATIONS** Jessica Tierney **SENIOR MANAGER, BUSINESS ANALYSIS** Cory Lipman **BUSINESS ANALYSTS** Kurt Ennis, Maggie Clark, Isacco Fusi **BUSINESS OPERATIONS ADMINISTRATOR** Taylor Fisher **DIGITAL SPECIALIST** Marissa Zuckerman **SENIOR PRODUCTION MANAGER** Jason Hillman **SENIOR MANAGER, PUBLISHING AND CONTENT SYSTEMS** Marcus Spiegler **CONTENT OPERATIONS MANAGER** Rebecca Doshi **PUBLISHING PLATFORM MANAGER** Jessica Loayza **PUBLISHING SYSTEMS SPECIALIST, PROJECT COORDINATOR** Jacob Hedrick **SENIOR PRODUCTION SPECIALIST** Kristin Wowk **PRODUCTION SPECIALISTS** Kelsey Cartelli, Audrey Diggs **SPECIAL PROJECTS ASSOCIATE** Shantel Agnew

MARKETING DIRECTOR Sharice Collins **ASSOCIATE DIRECTOR, MARKETING** Justin Sawyers **GLOBAL MARKETING MANAGER** Allison Pritchard **ASSOCIATE DIRECTOR, MARKETING SYSTEMS & STRATEGY** Aimee Aponte **SENIOR MARKETING MANAGER** Shawana Arnold **MARKETING MANAGER** Ashley Evans **MARKETING ASSOCIATES** Hugues Beaulieu, Ashley Hylton, Lorena Chirinos Rodriguez, Jenna Voris **MARKETING ASSISTANT** Courtney Ford **SENIOR DESIGNER** Kim Huynh

DIRECTOR AND SENIOR EDITOR, CUSTOM PUBLISHING Erika Gebel Berg **ADVERTISING PRODUCTION OPERATIONS MANAGER** Deborah Tompkins **DESIGNER, CUSTOM PUBLISHING** Jeremy Huntsinger **SENIOR TRAFFIC ASSOCIATE** Christine Hall

DIRECTOR, PRODUCT MANAGEMENT Kris Bishop **PRODUCT DEVELOPMENT MANAGER** Scott Chernoff **ASSOCIATE DIRECTOR, PUBLISHING INTELLIGENCE** Rasmus Andersen **SR. PRODUCT ASSOCIATE** Robert Koepke **PRODUCT ASSOCIATES** Caroline Breul, Anne Mason

ASSOCIATE DIRECTOR, INSTITUTIONAL LICENSING MARKETING Kess Knight **ASSOCIATE DIRECTOR, INSTITUTIONAL LICENSING SALES** Ryan Rexroth **INSTITUTIONAL LICENSING MANAGER** Nazim Mohammedi, Claudia Paulsen-Young **SENIOR MANAGER, INSTITUTIONAL LICENSING OPERATIONS** Judy Lillibridge **MANAGER, RENEWAL & RETENTION** Lana Guz **SYSTEMS & OPERATIONS ANALYST** Ben Teincuff **FULFILLMENT ANALYST** Aminta Reyes

ASSOCIATE DIRECTOR, INTERNATIONAL Roger Goncalves **ASSOCIATE DIRECTOR, US ADVERTISING** Stephanie O'Connor **US MID WEST, MID ATLANTIC AND SOUTH EAST SALES MANAGER** Chris Hoag **DIRECTOR, OUTREACH AND STRATEGIC PARTNERSHIPS, ASIA** Shoupeng Liu **SALES REP, ROW** Sarah Lelarge **SALES ADMIN ASSISTANT, ROW** Victoria Glasbey **DIRECTOR OF GLOBAL COLLABORATION AND ACADEMIC PUBLISHING RELATIONS, ASIA** Xiaoying Chu **ASSOCIATE DIRECTOR, INTERNATIONAL COLLABORATION** Grace Yao **SALES MANAGER** Danny Zhao **MARKETING MANAGER** Kilo Lan **ASCA CORPORATION, JAPAN** Rie Rambelli (Tokyo), Miyuki Tani (Osaka)

DIRECTOR, COPYRIGHT, LICENSING AND SPECIAL PROJECTS Emilie David **RIGHTS AND PERMISSIONS ASSOCIATE** Elizabeth Sandler **LICENSING ASSOCIATE** Virginia Warren **RIGHTS AND LICENSING COORDINATOR** Dana James **CONTRACT SUPPORT SPECIALIST** Michael Wheeler

---

EDITORIAL
science_editors@aaas.org

NEWS
science_news@aaas.org

INFORMATION FOR AUTHORS
science.org/authors/science-information-authors

REPRINTS AND PERMISSIONS
science.org/help/reprints-and-permissions

MULTIMEDIA CONTACTS
SciencePodcast@aaas.org
ScienceVideo@aaas.org

MEDIA CONTACTS
scipak@aaas.org

PRODUCT ADVERTISING & CUSTOM PUBLISHING
advertising.science.org
science_advertising@aaas.org

CLASSIFIED ADVERTISING
advertising.science.org/science-careers
advertise@sciencecareers.org

JOB POSTING CUSTOMER SERVICE
employers.sciencecareers.org
support@sciencecareers.org

MEMBERSHIP AND INDIVIDUAL SUBSCRIPTIONS
science.org/subscriptions

MEMBER BENEFITS
aaas.org/membership/benefits

INSTITUTIONAL SALES AND SITE LICENSES
science.org/librarian

Saving science by the sea

Susan Fitzpatrick and **Jane Maienschein**

As funding for science tightens across the United States, attention has turned to pressures faced by universities and biomedical research institutions. An often overlooked part of the nation's science ecosystem, however, are the small, independent marine laboratories that are also bearing the brunt of funding cuts and other constraints imposed by the Trump administration. These institutions have long nurtured generations of scientists—from high school students to Nobel laureates—and precipitated discoveries that have advanced modern science. Yet they now face an uncertain future, and losing them would eliminate not only a powerful convergence of research and education but also a wellspring of scientific advancement.

Marine laboratories occupy a rare niche. They are mostly independent but often loosely affiliated with universities by sharing faculty, space, or other resources. They host students and scientists from weeks to months, mixing disciplines and experience levels that break down traditional academic silos across the spectrum of life sciences, from molecular to microbial to ecological. The knowledge that many of the participants will be there for only a short period creates a sense of urgency for thinking beyond the typical and asking questions that challenge assumptions and lead to exploring problems in new ways. People come to work intensively in this atmosphere and in nonheirarchical teams, sharing ideas over meals and debating hard questions long into the night. They work together, live together, and share the excitement of discovery together.

These laboratories are… an important scientific culture.

The Marine Biological Laboratory in Woods Hole, Massachusetts, founded in 1888, established the precedent. Forged by a Boston consortium committed to educating both men and women, it became the model for bringing together diverse perspectives. It also opened the research community to new environments and organisms as model systems for studying a wide scope of problems, from the details of embryonic development to the scope of biodiversity in different habitats. As physician and writer Lewis Thomas put it, this "national laboratory" for biology serves as a paradigm for collaborative integrated investigation and learning. It was here in 1954 that graduate students Matthew Meselson and Franklin Stahl met and began a collaboration that led to their elegant experiment showing how DNA replicates.

There are more than 100 marine research institutions in the United States that hold memberships in the National Association of Marine Laboratories (NAML) (plus others that are not members). This includes university-affiliated and independent laboratories, many as nonprofit entities. Some are well known for their emphasis on oceans (The Scripps Institution of Oceanography and Bermuda Institute of Ocean Sciences among them) or on integrating research with education (Cold Spring Harbor Laboratory and MDI Biological Laboratory, for example). Each has its own focus, but all promote a tight-knit community driven by curiosity, an immersive experience in the natural environment of their science, and a spirit of openness to trying new things and being willing to fail.

Collectively, these marine laboratories have trained hundreds of thousands of students and researchers, many of whom have gone on to careers in academia, government, industry, and other sectors. Yet, the laboratories' independence, which has been a strength, may now be a vulnerability with funding mechanisms that favor large research institutions. These modest laboratories cannot adjust as readily to new constraints on funding and on more risk-taking research. For example, some are reporting the need to fire staff, curtail student internships, cut back on course offerings, and take other actions that affect both research and training of the next generation of scientists. NAML was established in 1989 in response to funding cuts in 1984 for marine research administered by the National Oceanic and Atmospheric Administration. Marine laboratory directors and scientists joined together to forge a forum to address common challenges across the marine science enterprise. Recent NAML meetings, including earlier this month, continue to address the future of federal science partners and relevant funding and policy issues to strengthen the marine science community against vulnerabilities and maximize opportunities for the field.

Marine laboratories encourage exploratory and creative thinking. They are a reminder that progress is often the result of serendipity—through conversations in dining halls, working side by side in a shared laboratory space, or a chance meeting during a coffee break. These laboratories are not just generators of data but incubators of an important scientific culture. Against the current backdrop of anxiety about the future of science, the scientific community and public need these places now more than ever. □

Susan Fitzpatrick is president emerita of the James S. McDonnell Foundation, St. Louis, MO, USA, and a trustee of the Marine Biological Laboratory, Woods Hole, MA, USA. susan@jsmf.org **Jane Maienschein** is university professor in the School of Life Sciences at Arizona State University, Tempe, AZ, USA, and a fellow of the Marine Biological Laboratory, Woods Hole, MA, USA. maienschein@asu.edu

10.1126/science.aed1909

ASTRONOMY

Argentine telescope caught in U.S.-China crossfire

Superpower tensions have abruptly derailed a nearly finished radio telescope **MARÍA DE LOS ÁNGELES ORFILA**

A decade in the making, the China-Argentina Radio Telescope in the foothills of the Andes is nearly complete.

Later this year, astronomers in Argentina expected to begin testing the largest radio dish in Latin America: a 40-meter-diameter instrument designed to detect electromagnetic whispers from the distant cosmos. The Argentine and Chinese governments launched the project a decade ago as a symbol of scientific cooperation between the two nations. But now the China-Argentina Radio Telescope (CART), which is nearly finished, is stuck in limbo—a victim of growing tensions between the United States and China.

"We're 90% complete. Very close. That's why what's happening is so difficult, because we don't want it to become scrap metal," says María Verónica Benavente, a senior official at the National University of San Juan (UNSJ), which is leading the project.

Researchers trace CART's difficulties to efforts by Argentina's libertarian president, Javier Milei, to forge close ties with U.S. President Donald Trump, whose administration has made curbing China's global influence a priority. The first signs of trouble came in June, when Argentina's science agency missed a deadline for renewing a scientific cooperation agreement with China. Then, in September, customs officials in Buenos Aires held up a shipment of key dish parts made in China, which has contributed some $15 million in equipment and engineering to the project. Last month brought another setback when U.S. Secretary of the Treasury Scott Bessent said the Trump administration would provide up to $20 billion to shore up Argentina's beleaguered economy—but only if Milei's government suspended strategic ties with China, including efforts to build "observational facilities."

That policy was aimed "directly" at CART, believes Benavente, who is the former science secretary for San Juan, the mountainous western province where the observatory is located.

PHOTO: RICARDO CÉSAR PODESTÁ

"There is direct interference from the White House here."

The Chinese embassy in Argentina condemned Bessent's comments, saying they represented a "Cold War mentality." In a second statement, it warned that "Latin America and the Caribbean are no one's backyard."

The latest setback came on 17 October, when Milei's government issued a requirement that the Ministry of Defense approve "any installation of radars, observatories, or aerospace systems." That rule is especially vexing because "CART is 100% scientific," says Ricardo Podestá, director of the Félix Aguilar Astronomical Observatory, where the radio telescope is being built. "If this were a military project, everyone would notice."

Others note that the requirement seems redundant because CART already received Defense Ministry approval in 2016 under a previous president who is politically aligned with Milei. "I don't know what else this government wants," says Jorge Castro, a science dean at UNSJ. "I hope they're simply unaware of this objective fact."

The Milei administration's policies are "simply an over-the-top move to show themselves obsequiously aligned with the Trump administration, to the detriment of the entire astronomical community in Argentina," Roberto Salvarezza, head of the Buenos Aires Scientific Research Commission, told the media outlet *Página/12*.

The delays have left astronomers frustrated. "If the equipment is released, we could have the antenna ready this year or early next year," Podestá says, opening the way to a wide range of research, including studies of celestial objects such as pulsars and quasars, as well as collaborations with the more than 100 other radio telescopes around the world. "San Juan has some of the clearest skies in the world," Podestá notes. "You can see the galactic nucleus high in the sky."

To ensure that such observing opportunities don't go to waste, the government should issue an "immediate guarantee of [CART's] continuity," UNSJ's science faculty said in a statement. "The development of science has no borders," it added, "and a cosmopolitan vision must prevail." ☐

María de los Ángeles Orfila is a journalist in Uruguay.

SOCIAL MEDIA RESEARCH

Europe faults Big Tech platforms for lack of research access

Scientists welcome preliminary finding that Meta and TikTok are in breach of the Digital Services Act

KAI KUPFERSCHMIDT

When Philipp Lorenz-Spreen set out in 2024 to study how politicians across Europe communicate online and how much divisive language they use, he knew he had the law on his side. The European Union's Digital Services Act (DSA), which had come into force in February of that year, guaranteed researchers like Lorenz-Spreen, a computational social scientist at the Dresden University of Technology, access to data from social media platforms X, TikTok, Facebook, and Instagram. All he had to do was ask.

But the reality was frustrating. X kept asking follow-up questions and eventually denied his request without giving a reason. TikTok provided access, but Lorenz-Spreen decided not to rely on the company because other researchers had found big gaps in the data it shared. Meta, the parent company of Facebook and Instagram, offered an online dashboard that came with serious limitations; for example, it captured data only on accounts with more than 25,000 followers, more than some European politicians have. Lorenz-Spreen's conclusion: The DSA wasn't working the way it should.

> "The public is entitled to know what platforms and their algorithms are doing to the information landscape."
>
> **Stephen Lewandowsky**
> University of Bristol

Now, the European Commission has made clear it agrees. On 24 October, it announced that after an investigation it had "preliminarily found both TikTok and Meta in breach of their obligation to grant researchers adequate access to public data" under the DSA. (The same announcement also faulted Meta for its content moderation procedures.)

The Commission did not reveal details about its investigation nor say what prompted it. But the move, which follows a similar preliminary finding against X in July 2024, is a welcome sign the Commission is serious about enforcing the DSA, says Stephen Lewandowsky, a psychologist at the University of Bristol. "Access to data by researchers is a crucial element of ensuring transparency and democratic accountability," Lewandowsky says. "The public is entitled to know what platforms and their algorithms are doing to the information landscape."

The Commission can impose a billion-dollar fine on each company if it ultimately decides they are not complying with the DSA, but first the companies will have a chance to defend themselves. Rebekah Tromble, a political scientist at Northeastern University, says they might do so vigorously. "In recent months, many of these companies have been more aggressively pushing back" against the DSA's provisions, she says. In an email, a Meta spokesperson told *Science* the company was "confident" it had already taken the necessary steps to comply with the DSA. A spokesperson for TikTok wrote that the company is reviewing the Commission's findings and argued the DSA's data sharing requirements were in tension with EU privacy regulations.

Data from Big Tech is vital for researchers who want to study, say, how election lies spread on Facebook, or whether the algorithm determining what you see on TikTok leads to polarization. The DSA, enacted in 2022, guaranteed access for researchers—anywhere in the world—who are studying "systemic risks" for the EU, such as negative effects on elections or public health. At the time, only a few companies were relatively generous with such information. X, then still named Twitter, was seen as very transparent and as a result was "disproportionately studied," says Daphne Keller, an internet law expert at Stanford University. Other companies cooperated with small groups of scientists on research projects.

But "it is clear to me that those days are over," Tromble says. The rise of artificial intelligence has made things worse by making companies more protective of their data, to keep them from being used to train large language models, says Przemyslaw Grabowicz, a researcher at University College Dublin.

LK Seiling of the Weizenbaum Institute, founded in Germany in 2017 to study the "networked society," and his colleagues have surveyed researchers about their experiences using the DSA. They found the platforms use several techniques to delay or deny requests for data. X, for example, has a very simple online application form that never seems to lead to quick acceptance. "If I'm lucky I'm rejected after 43 days, but if I'm not, then I end up in what I call the circle of hell," a loop of more and more questions that may or may not result in data, Seiling says. Even if they grant access, companies often make insufficient data available.

So far, researchers have only been able to request "publicly available" information under the DSA—for instance, what specific users post or repost, or whom they follow. For a host of logistical and legal reasons, researchers often prefer the companies to provide such data, but they can also collect data themselves with the help of computer programs that "scrape" web pages and collect vast amounts of data. Some companies' terms of service ban scraping, but the DSA allows it, Keller says. (Many researchers are already using this technique but prefer not to talk about it.)

On 29 October, however, the DSA entered a new, likely even more contentious phase, in which researchers can also request data that aren't public, for example what content is shown to individual people. The platforms are expected to protect such information even more zealously, but for researchers, it's an opportunity to better understand how they really work, Lorenz-Spreen says.

Take, for example, the well-documented finding that outrage-inducing content gets more likes. "The question always remains whether that is because that's people's psychology, and they just like this content more, or whether it is somehow being pushed by the platforms," Lorenz-Spreen says. "That kind of data is what we really need if we want to make serious progress in our field."

The investigation that led to a preliminary finding against X last year is still continuing, a Commission spokesperson says. "This is the first case we opened under the DSA, and we are building the case to make sure it is solid."

Researchers and governments elsewhere will be watching Europe's battles closely. U.S. President Donald Trump's administration has attacked misinformation research as a gateway to censorship, and a Republican-led committee in the U.S. House of Representatives called the DSA "the EU's comprehensive digital censorship law," silencing conservative voices and infringing on "American free speech." U.S. Secretary of State Marco Rubio has reportedly ordered U.S. diplomats to lobby against the DSA.

That makes last week's finding even more important, Grabowicz says: "It signals that the Commission is willing to resist the pressure from right-wing U.S. policymakers." □

BY THE NUMBERS

40%

Proportion of more than 240 papers on animal models of hemorrhagic stroke found to have problematic or duplicated images in a new analysis. (*PLOS Biology*)

BIOMEDICINE

New antivenom is a 'potential game changer' for snakebites

Synthetic cocktail of llama and alpaca "nanobodies" protected mice **CHRISTIE WILCOX**

Venomous snakebites kill upward of 100,000 people every year and maim many times more, a toll that has led the World Health Organization to call snakebite a neglected tropical disease. Current antivenoms have done all they can do to stem it. But a cocktail of lab-synthesized "nanobodies" inspired by alpacas and llamas could change the picture. They should be safer to administer, cheaper to produce, and more effective than the best available antivenoms, according to a report this week in *Nature*.

This new kind of antivenom has proved protective only in mice so far. But "the science is solid," says Robert Rono, a doctor and epidemiologist with the Kenyan Ministry of Health in Baringo County, where snakebite is a pernicious public health issue. "It's a potential game changer if all goes well."

Current antivenoms can save lives and limbs if administered quickly and properly, but people in need rarely get them. "In our part of the world, a bite from a black mamba or cobra is almost akin to a death sentence," Rono says. "It's a very unfair disease that really hits the poorest of the poor," adds Andreas Laustsen-Kiel, a toxinologist and bioengineer at the Technical University of Denmark whose lab produced the new antivenom.

Infrastructure is one problem: Most bites occur in rural areas, where clinics are small. Even if a person reaches a larger, regional facility, there's no guarantee the doctors there will have enough antivenom available or the confidence in the drugs to use them.

Current products are also a barrier. They are made by injecting animals, usually horses or sheep, with snake venoms and harvesting the antibodies. The care and upkeep of these animals is expensive, which drives up the price. And because the mixtures are a mishmash of antibodies, some effective and others not, a lot of antivenom is often required to treat a bite. A regional center might have just one or two vials—and a single bitten person could need up to 10, Rono says.

Furthermore, the foreign antibodies sometimes set off a strong immune reaction, known

An innovative antivenom protected mice from lethal doses of venom from 17 of 18 African snakes—all except the eastern green mamba (*Dendroaspis angusticeps*).

PHOTO: WOLFGANG WÜSTER

as anaphylactic shock, that is also life-threatening. Many medical professionals in Africa are hesitant to administer the drugs, having had bad experiences with them.

To make their alternative, Laustsen-Kiel and colleagues injected mixtures of venoms from 18 African snakes into llamas and alpacas. Their antibodies are smaller than those of horses and humans and have only one protein chain, instead of two, on each arm of the Y-shaped molecule. Each arm, dubbed a nanobody, can be separated from its base while remaining able to bind a target molecule, such as a toxin. The isolated arms lack the animal-specific sections that set off allergic reactions.

The team took the DNA sequences for the llama and alpaca nanobodies and added them to *Escherichia coli* bacterial cells to mass produce them in vitro. Then they screened for the ones that most effectively inactivated the toxins of the 18 snakes, including 13 species of cobras, four species of mamba, and one rinkhal.

They ultimately identified eight nanobodies that, injected together with lethal doses of the venoms of the 18 snakes, protected mice from all but one, the eastern green mamba (*Dendroaspis angusticeps*). “You can take surprisingly few nanobodies … and actually get extremely broad coverage,” Laustsen-Kiel says. When the mice were injected first with the venom and received the cocktail 5 minutes later, it protected them from eight of 11 snake species tested. Laustsen-Kiel says the group now plans to investigate adding more effective nanobodies for the toxins of the three remaining snakes.

For all species but the black mamba, the nanobody mix outperformed the currently available antivenom, Inoserp PAN-AFRICA. In addition to saving more mice, the cocktail prevented more tissue damage than PAN-AFRICA, notes Kartik Sunagar, an evolutionary biologist and toxinologist with the Indian Institute of Science, Bangalore. Laustsen-Kiel suggests the smaller nanobodies may make their way deeper into tissues to reach the wound site more effectively.

Rono believes that if medical professionals don’t fear an allergic reaction, they will be more comfortable administering the nanobodies outside of large hospital settings, even in the fields or forests where people are bitten. “If the technology does what it says in the paper on the ground … this should be a very popular product,” he says.

It might also be cheaper. Laustsen-Kiel predicts that synthesizing the nanobodies in the lab will be cheaper than procuring antibodies from live animals. And if it does end up being more effective per vial than current antivenoms, that should lower cost, too, Rono says.

Between tweaking the mixture and additional testing, Laustsen-Kiel estimates the team is about 3 years away from being ready for human testing. That will be the real hurdle, Sunagar says. “These formulations will need to successfully navigate human clinical trials.” □

IN OTHER NEWS

ALZHEIMER’S FRAUD CASE DROPPED

A much-anticipated scientific fraud case against a neuroscientist for his preclinical work on a potential drug for Alzheimer’s disease evaporated last week after the jury had been chosen, when the U.S. Department of Justice (DOJ) abruptly dropped the charges. Former City University of New York (CUNY) researcher Hoau-Yan Wang had been indicted in 2023 for “defrauding the National Institutes of Health of approximately $16 million” in grants related to early studies on a candidate Alzheimer’s drug called simufilam. Its developer, biotech Cassava Sciences, abandoned the drug after it failed in a large, phase 3 trial. Federal prosecutors did not reply to questions about why they dropped the charges. Wang’s defense attorneys had filed a request to dismiss the case, in part because they said DOJ failed to disclose a 30 May letter from CUNY concluding that Wang had not engaged in proven scientific misconduct, although it also noted that an investigative panel had found signs of improper image manipulation in scores of his studies. Wang’s lawyers confirmed he has retired from CUNY. —John Travis

Palmer Station is the base of operations for many U.S. scientists studying the changing Antarctic ecosystem.

PHOTO: NATASJA VAN GESTEL/TEXAS TECH UNIVERSITY

POLAR SCIENCE

How NSF floats Antarctic research with no icebreaker

Ending *Palmer* lease is one of many belt-tightening moves amid budget uncertainty

JEFFREY MERVIS

In 2022, the National Science Foundation (NSF) gave University of Alabama geoscientist Tom Tobin a grant to drill rock cores at a remote site off the Antarctic peninsula. NSF told Tobin, who works on mass extinctions, that he'd have to wait 4 years for a vessel to take him there.

This summer, however, NSF canceled the lease on his long-awaited ride, the *RV Nathaniel B. Palmer*, the only U.S. research icebreaker dedicated to working in the treacherous waters of the Southern Ocean. NSF has since rebooked him on another ship, but it's one that normally operates in the Arctic and lacks the *Palmer*'s capacity to crunch through thick sea ice.

Tobin's odyssey reflects the precarious state of the U.S. Antarctic Program (USAP), which NSF manages. Losing the *Palmer*, which NSF said it could no longer afford, comes only a year after NSF ended its lease for the *ARSV Laurence Gould*, which did double duty as a supply ship to NSF's Palmer Station as well as hosting research cruises. The belt-tightening in its $559 million Office of Polar Programs, which supports science and logistics in both the Arctic and Antarctic, has already led to downsizing and cancellations of long-running programs. Many more would be imperiled under President Donald Trump's plan to slash NSF's overall $9 billion budget to $4 billion in 2026.

Antarctic scientists say abandoning the *Palmer*, a mainstay of Antarctic research since 1992, is a big step in the wrong direction. "Access is the biggest barrier to doing Antarctic science, and losing the *Palmer* will mean less access," says Oscar Schofield, a biological oceanographer at Rutgers University who leads a long-running NSF-funded ecological monitoring project on the Antarctic Peninsula that was also scheduled to sail on the *Palmer* this winter. Instead, the *Palmer* completed its last cruise for NSF this month and reverted to its owner, Offshore Service Vessels.

NSF, which is currently closed because of the government shutdown, said in a 9 September posting it "plans to continue supporting the entire portfolio of marine cruise projects planned for the 2025-2026 field season … using the U.S. Academic Research Fleet, supported by University-National Oceanographic Laboratory System (UNOLS) operators."

The agency's decision to turn to UNOLS's 17-vessel fleet came as a surprise to Doug Russell, executive secretary for UNOLS. "I had no inkling of this," he says. Russell says NSF officials told him they needed to use UNOLS vessels because "we have important science programs to be covered down in Antarctica."

So far, NSF has kept its word by finding alternative rides for scientists who expected to be aboard the *Palmer*. And polar scientists seem willing to cut NSF some slack. "I think [canceling the *Palmer* lease] was shortsighted," says Julia Wellner, a marine geologist at the University of Houston who helped draft a 28 July petition signed by more than 200 scientists asking NSF to rethink its decision. "But NSF is caught between a rock and a hard place, and they're doing their best to keep the program going."

Even so, those new arrangements are only a short-term solution. Unlike the *Palmer*, which was based in Punta Arenas, Chile, the replacement ships have home ports thousands of kilometers away, forcing long voyages at daily operating rates of $75,000 or higher. And the ships are not available for other cruises during those weeks at sea.

In addition, the two ships that have so far taken on work scheduled for the *Palmer*—the *RV Sikuliaq* and the *RV Roger Revelle*—are in many ways less well suited for Antarctic cruises. The *Sikuliaq* has fewer berths for scientists, a shorter cruise range, and a less robust ice-breaking capacity than the larger *Palmer*. And although the *Revelle* is similar in size to the *Palmer*, it has never operated as far south as Antarctica and will have to maneuver around any ice hazards. Researchers aboard both ships might be forced to revise or abandon some expedition objectives if they encounter heavy ice.

Given such constraints, is the ship shuffling "really cheaper than maintaining an Antarctic research presence?" wonders Margaret Mars Brisbin, a biological oceanographer at the University of South Florida who, like Tobin, had her cruise switched to the *Sikuliaq*. "Sharing ships is going to really diminish the capacity of the U.S. polar program in general and make us less competitive with the rest of the world," she adds.

The upheaval has taken a toll, she and others say. NSF initially told Mars Brisbin that her upcoming cruise to measure how changing ice melt patterns affect phytoplankton growth and carbon emissions from the ocean was canceled and that she might even have to resubmit her proposal. When she got the good news that she and her colleagues would be using the *Sikuliaq*, she also learned they would depart much earlier than planned. They had to race to meet a 2-week deadline for a long list of logistical, medical, and paperwork requirements that usually take months to complete.

"Our cruise was going to be a month later than [Schofield's] and we were going to use some of their equipment," Mars Brisbin says. "But now they are happening at the same time, so we've had to hunt for replacements."

Schofield also had to scramble. "At first NSF put us on the *Sikuliaq*," Schofield says. "But it would have meant fewer people and a shorter cruise than the 8 weeks from dock to dock. It was also later in the season, which would have skewed the time series we've been collecting. So NSF decided to go with the *Revelle*, which is a much better fit for us."

Although Wellner applauds NSF for finding other ships for her colleagues, she worries their science could suffer because of the rushed preparations. "We think about every little thing on a ship, like what type of winch will be deploying our gear over the side," she says.

In addition to ships, many Antarctic scientists rely on remote sensing and satellite data from an NSF-funded Polar Geospatial Center at the University of Minnesota to pinpoint and collect data on their research locations. But this year the center, which provides such information free to any USAP-funded researcher, felt the ripple effects of NSF's looming budget crisis.

In May, after its application for a 5-year renewal had been stalled for more than a year, the center suspended accepting new requests for data. Shortly after, it laid off three of its 11 staffers. In August, the center received funding for another 5 years, but at roughly two-thirds of its previous operating level.

Ironically, some Arctic scientists wonder whether NSF's efforts to keep Antarctic science afloat are coming at their expense. Audrey Taylor, executive director of the Arctic Research Consortium of the United States (ARCUS), says assigning double duty to the *Sikuliaq* suggests Antarctica will get more than its share of whatever NSF allocates for polar science. ARCUS, whose $9 million NSF grant to build scientific networks and strengthen ties with Indigenous communities expires in early 2026, was preparing to compete for a new NSF-funded Arctic communications hub. But earlier this year, NSF decided not to fund the hub. Without any prospect of NSF support, ARCUS folded its tent on 30 September.

For his part, Tobin is content to have a way to get to his research site on Seymour Island, which offers an easily accessible fossil record of climate shifts following the impact of the meteor that wiped out the dinosaurs 65 million years ago. Although he's made four previous trips to Antarctica aboard the *Palmer* and the *Gould*, Tobin also carries out summer digs in Wyoming and Montana. "I could never spend all of my time doing polar research," he says, "because you never know when you'll be able to go down there." □

The National Science Foundation has ended the lease of its sole icebreaker, the *RV Nathaniel B. Palmer*.

PHOTO: NATASJA VAN GESTEL/TEXAS TECH UNIVERSITY

IN OTHER NEWS

PARATYPHOID VACCINE SHOWS ITS METTLE

A candidate vaccine against paratyphoid fever, a bacterial illness estimated to kill more than 20,000 people each year worldwide, has shown promise in a human "challenge" study, in which healthy volunteers are deliberately exposed to an infectious agent under tightly controlled circumstances. *Salmonella Paratyphi A*, which causes most cases of the illness, spreads via contaminated water or food, primarily in places that lack clean drinking water and sanitation. It can cause high fever, headache, abdominal pain, and diarrhea. In a trial at the University of Oxford, 70 volunteers were given either two doses of the vaccine—consisting of live but attenuated versions of the bacterium—or a placebo. Four weeks later, subjects in both groups swallowed a small amount of liquid containing bacteria from a wild *S. Paratyphi* strain isolated from a patient in Nepal in 2006. Compared with the placebo group, the vaccine reduced infection risk by 73%, researchers report this week in *The New England Journal of Medicine*. (Subjects in both groups who fell sick were cured with an antibiotic.) If licensed, the vaccine would likely be used in combination with existing oral vaccines for *Salmonella typhi*, which causes the more common—and more lethal—disease typhoid fever.
—Martin Enserink

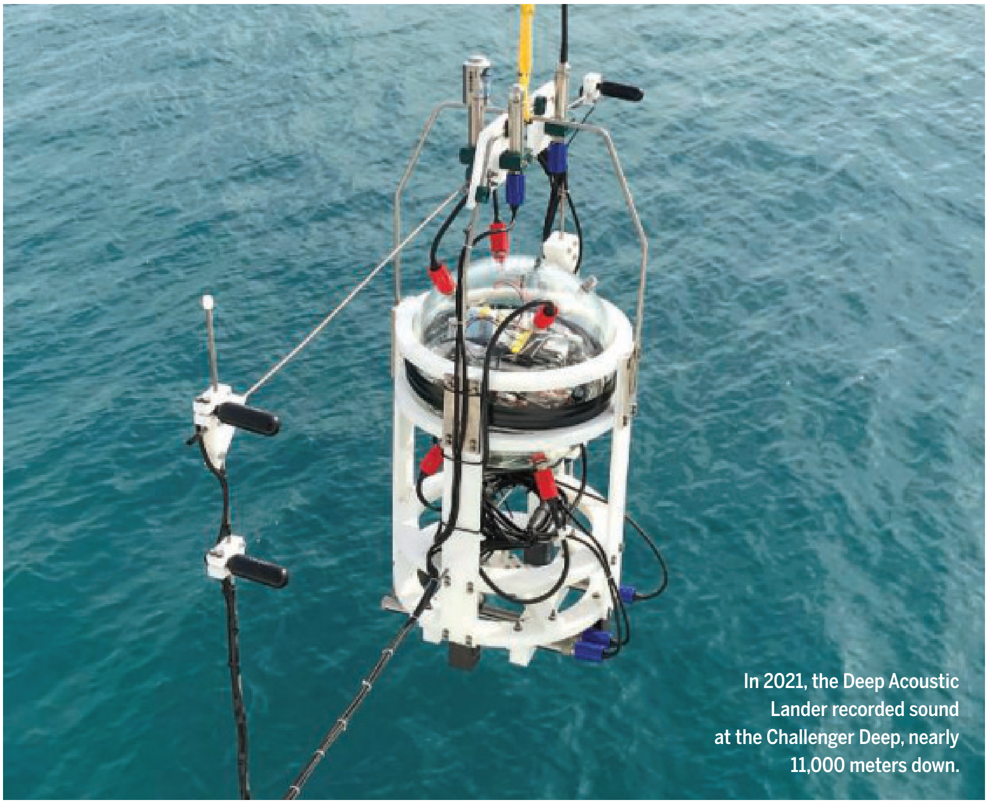

In 2021, the Deep Acoustic Lander recorded sound at the Challenger Deep, nearly 11,000 meters down.

PHOTO: DAVID BARCLAY

OCEANOGRAPHY

Dangerous ocean acidification tracked using ambient noise

Acoustic technique could make it easier to monitor threat to marine life stemming from rising carbon emissions

PAUL VOOSEN

The ocean is a noisy place. Ship propellers and whale songs reverberate at the lowest pitches, while at higher tones dolphins click and shrimp snap their claws. Between these frequencies are the sounds of the churning sea itself, generated as waves, wind, and rain roil its surface. Researchers have now used this ambient noise to probe the rising acidity of the ocean. The acoustic technique, published this month in the *Journal of Geophysical Research: Oceans*, could make it easier to measure this key parameter of ocean health across vast distances rather than relying on point measurements.

"This is a really cool idea," says Andone Lavery, an acoustical oceanographer at Oregon State University. "And they've shown that it is possible."

The carbon emissions that are warming the globe also acidify seawater. The ocean naturally absorbs about one-third of annual carbon dioxide emissions; as this gas dissolves and reacts, it creates bicarbonate and hydrogen ions. The hydrogen lowers the pH of seawater, increasing ocean acidity, which can harm sea life and slow future carbon uptake. Ship-based measurements in shallow parts of the ocean have found that, since 1985, pH has already dropped from 8.11 to 8.04.

The waters of the ocean are layered, however, and measurements at one depth may not apply to others. Adding pH sensors to the thousands of robotic Argo floats that patrol the seas, diving as deep as 2000 meters, is one way to get a broader picture of acidity. But David Barclay, an acoustical oceanographer at Dalhousie University, and his co-authors found a way to measure average pH across even greater depth ranges, by taking advantage of the intrinsic physics of sound.

The work originated in 2009, when Barclay led a cruise to the Philippine Sea, funded by the U.S. Navy, to test a new acoustic listening device, called Deep Sound. Barclay's team dropped the instrument—two hydrophones and their associated electronics encased in reinforced glass spheres—down 5000 meters. And then they listened.

One immediate surprise was that the abyss wasn't as quiet as they expected. They found that when surface winds whipped up to more than 10 knots or so, the sounds of breaking waves reached all the way to Deep Sound, at frequencies of about 1 to 10 kilohertz (kHz). Barclay knew that two compounds in the ocean, borate and magnesium sulfate, can dampen sounds at 1 kHz and 10 kHz, respectively, because of the particular way the molecules absorb a bit of the sound wave's energy.

Crucially, rising acidity decreases the abundance of borate, and its attenuating effect, while leaving magnesium sulfate unscathed. By comparing the two frequencies, the researchers thought they could get at the integrated pH of the entire water column, much as the echoes of earthquakes rippling through the ocean can be used to measure overall ocean heat.

It took 15 years to be sure: five more ship deployments and several upgrades of the instrument that ultimately allowed it to survive at depths of more than 10,000 meters in the Challenger Deep, in the Mariana Trench near the island of Guam. It also took a lot of painstaking mathematical analysis, says Ernst Uzhansky, an acoustic physicist now at the Naval Postgraduate School. "I can't tell you how happy I was," says Uzhansky, who was skeptical the team would find the signal. "Now it really opens up an opportunity to do large-scale pH monitoring."

Not everyone is convinced. Liqing Jiang, a chemical oceanographer at the University of Maryland, notes that the team did not compare its measurement with known observations. "This is a serious flaw," he says. The technique is not as accurate as measurements from the new biogeochemical (BGC) Argo probes, some 500 of which will finish being deployed by the United States by late next year. "The data shown in the paper is not the kind of quality we need yet," says Ken Johnson, a chemical oceanographer at the Monterey Bay Aquarium Research Institute and a leader of BGC-Argo. But it certainly seems possible to get there, he adds. "With a little signal processing, who knows?"

At a minimum, the new method could serve as a backup for BGC-Argo, whose future is in doubt. Several years ago, Honeywell stopped making the pH sensor used by the floats, only to reverse its decision when former President Joe Biden's administration intervened. And although the National Science Foundation funded the first large-scale BGC-Argo deployment, neither the U.S. nor other countries have committed the money needed to keep the program going past next year. At some point, this acoustic method "might be what we've got," Johnson says.

The next step for proving out the technique will be leaving one of these instruments on the sea floor for months at a time, Barclay says. A lower cost version of the instrument might also prove useful for monitoring geoengineering experiments that aim to draw down atmospheric carbon by increasing the alkalinity of coastal waters. It's also possible that the fiber optic cables increasingly being used to sense acoustic signals on the ocean floor could pick up these pH-sensitive frequencies, Lavery says. "If you could set something up for continuous measurements, then it would become pretty useful." □

Tim Andrews (left) recovered well after receiving a pig kidney earlier this year.

PHOTO: KATE FLOCK/MASSACHUSETTS GENERAL HOSPITAL

Pig kidney transplant falters

A pig kidney that had been functioning in a New Hampshire man for nearly 9 months has failed, a few days short of setting a record for the longest any organ from another species has worked in a human. In January, surgeons at Massachusetts General Hospital (MGH) gave Tim Andrews a kidney from a pig that had 69 genes altered to make its organs more suitable for use in people. But that editing—and the powerful immunosuppressive drugs Andrews took—apparently weren't enough to stop his body from rejecting the organ. On 23 October, surgeons removed the kidney, which Andrews called "Wilma" because that was the name of his pig donor. Andrews, who is 67, was able to go back on dialysis, but is not eligible for another pig kidney because of the toll the experimental transplant has taken on his health. The xenotransplant record he had been about to pass belonged to Edyth Parker, who in 1964 received a chimpanzee kidney at Charity Hospital in New Orleans and died 1 day before the 9-month anniversary of the transplant. MGH says it is continuing with the experimental transplant of more gene-edited pig kidneys. —Jon Cohen

ARTIFICIAL INTELLIGENCE

At a novel meeting, AI wrote and reviewed the papers

Organizers aim to tune algorithms to reduce peer-review burdens and accelerate science

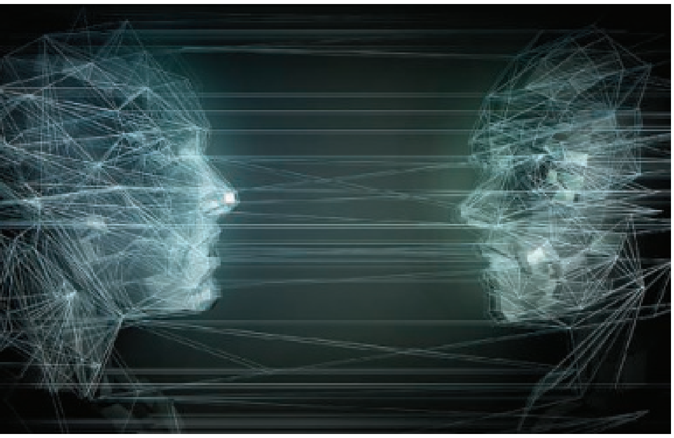

ILLUSTRATION: MINA DE LA O/GETTY IMAGES

JEFFREY BRAINARD

Major scientific journals and conferences ban crediting an artificial intelligence (AI) program, such as ChatGPT, as an author or reviewer of a study. Computers can't be held accountable, the thinking goes. But last week, a norm-breaking meeting turned that taboo on its head: All 48 papers presented, covering topics ranging from designer proteins to mental health, were required to list an AI as the lead author and be scrutinized by AIs acting as reviewers.

The virtual meeting, Agents4-Science, was billed as the first to explore a theme that only a year ago might have seemed like science fiction: Can AIs take the lead in developing useful hypotheses, designing and running computations to test them, and writing a paper summarizing the results? And can large language models, the type of AI that powers ChatGPT, then effectively vet the work?

"There's still some stigma about using AI, and people are incentivized to hide or to minimize it," a lead conference organizer, AI researcher James Zou of Stanford University, tells *Science*. The conference aimed "to have this study in the open so that we can start to collect real data, to start to answer these important questions." Ultimately, the organizers hope a fuller embrace of AI could accelerate science—and ease the burden on peer reviewers facing a ballooning number of manuscripts submitted to journals and conferences.

But some researchers reject the conference's very premise. "No human should mistake this for scholarship," said Raffaele Ciriello of the University of Sydney, who studies digital innovation, in a statement released by the Science Media Centre before the meeting. "Science is not a factory that converts data into conclusions. It is a collective human enterprise grounded in interpretation, judgment, and critique. Treating research as a mechanistic pipeline … presumes that the process of inquiry is irrelevant so long as the outputs appear statistically valid."

Most of the 315 manuscripts submitted to the conference, which attracted 1800 registrants, were reviewed and scored on a six-point scale by three popular large language models—GPT-5, Gemini 2.5 Pro, and Claude Sonnet 4. The results were averaged for each paper and humans were asked to review 80 papers that passed a threshold score. Organizers accepted 48 covering multiple disciplines, based on both the AI and human reviews.

One accepted paper that organizers highlighted was submitted by Sergey Ovchinnikov, a biologist at the Massachusetts Institute of Technology. His team asked advanced versions of ChatGPT to generate amino acid sequences that code for biologically active proteins with a structure called a four-helix bundle. Scientists typically use specialized software to design proteins. But to Ovchinnikov's surprise, ChatGPT produced sequences without further refinement of his team's query. He and his human colleagues tested two of the sequences in the lab, confirming that a protein derived from one had a four-helix bundle. Still, Ovchinnikov found ChatGPT's performance wasn't flawless. Most of the sequences did not garner "high confidence" on a score predicting whether they would form the desired protein structure.

Data presented at the conference also probed how researchers collaborate with AIs. The organizers asked human authors to report how much work AI contributed in several key areas, including generating hypotheses, analyzing data, and writing the paper. AI did more than half of the hypothesis-generation labor in just 57% of submissions and 52% of accepted papers. But in about 90% of papers, AI played a big role in writing the manuscripts, perhaps because that task is less computationally challenging.

Some human authors who presented at the meeting said their AI partners enabled them to complete in just a few days tasks that usually take much longer, and eased interdisciplinary collaborations with scholars outside their fields. But they also pointed to AI's drawbacks, including a tendency to misinterpret complex methods, write code that humans needed to debug, and fabricate irrelevant or nonexistent references in papers.

Scientists should remain skeptical about applying AI for tasks that require deep, conceptual reasoning and scientific judgment, according to Stanford computational astrophysicist Risa Wechsler, who reviewed some of the submitted papers.

"I'm genuinely excited about the use of AI for research, but I think that this conference usefully also demonstrates a lot of limitations," she said during a panel discussion at the meeting. "I am not at all convinced that AI agents right now have the capability to design robust scientific questions that are actually pushing forward the forefront of the field." One paper she reviewed "may have been technically correct but was neither interesting nor important," she said. "One of the most important things we teach human scientists is how to have good scientific taste. And I don't know how we will teach AI that."

The conference organizers plan to analyze and compare the AI- and human-written reviews. But the remarks garnered by Ovchinnikov's protein-design paper hinted that people and machines may often diverge. An AI reviewer called it "profound." But a human deemed it "an interesting proof-of-concept study with some lingering questions." ☐

eppendorf
& Science
PRIZE FOR
NEURO
BIOLOGY

Congratulations
to Cheng Lyu, Ph.D.
Stanford University
Department of Biology
Stanford, USA

Meet the Winner 2025

Eppendorf & Science Prize for Neurobiology
Congratulations to Cheng Lyu, Ph.D., Postdoctoral Fellow at Stanford University, School of Medicine, Stanford, USA, on winning the 2025 Eppendorf & Science Prize. Dr. Lyu's winning essay describes the molecular mechanisms how olfactory receptor neurons choose one synaptic partner out of all potential candidates. The olfactory neural circuit of the fruit fly builds its three-dimensional structure by breaking the developmental task into a series of one-dimensional steps. By manipulating this process, Dr. Lyu was able to rewire the neural circuit and altered the animal's courtship behavior. These findings link genetic variation, through circuit assembly, to animal behavior, paving the way to explore how developmental changes influence brain function.

Two finalists are also recognized. Sara Mederos, Ph.D., Wellcome Early Career Fellow at the Sainsbury Wellcome Centre, University College London, for her work revealing how the brain learns to adapt fear responses and suppress them when there is no reason for fear, and Dr. Constanze Depp, Postdoctoral Research Fellow at the Boston Children's Hospital, Harvard Medical School, Broad Institute of MIT and Harvard, for her work examining the role of myelin and oligodendrocytes in Alzheimer's disease.
The annual US$25,000 Eppendorf & Science Prize for Neurobiology honors early career scientists for their outstanding contributions to neurobiological research. The winner and two finalists will be recognized at a Prize Ceremony on November 16, 2025, at the Hard Rock Hotel in San Diego, USA.
If you are interested in joining the Prize Ceremony go to **event.eppendorf.com/prizeceremony-2025** or scan the QR code.

You could be next to win this Prize
If you are 35 years of age or younger and currently performing neurobiological research, you could be next to win this Prize. Deadline for entries is June 15, 2026.

eppendorf Science AAAS

Learn more at: eppendorf.com/prize

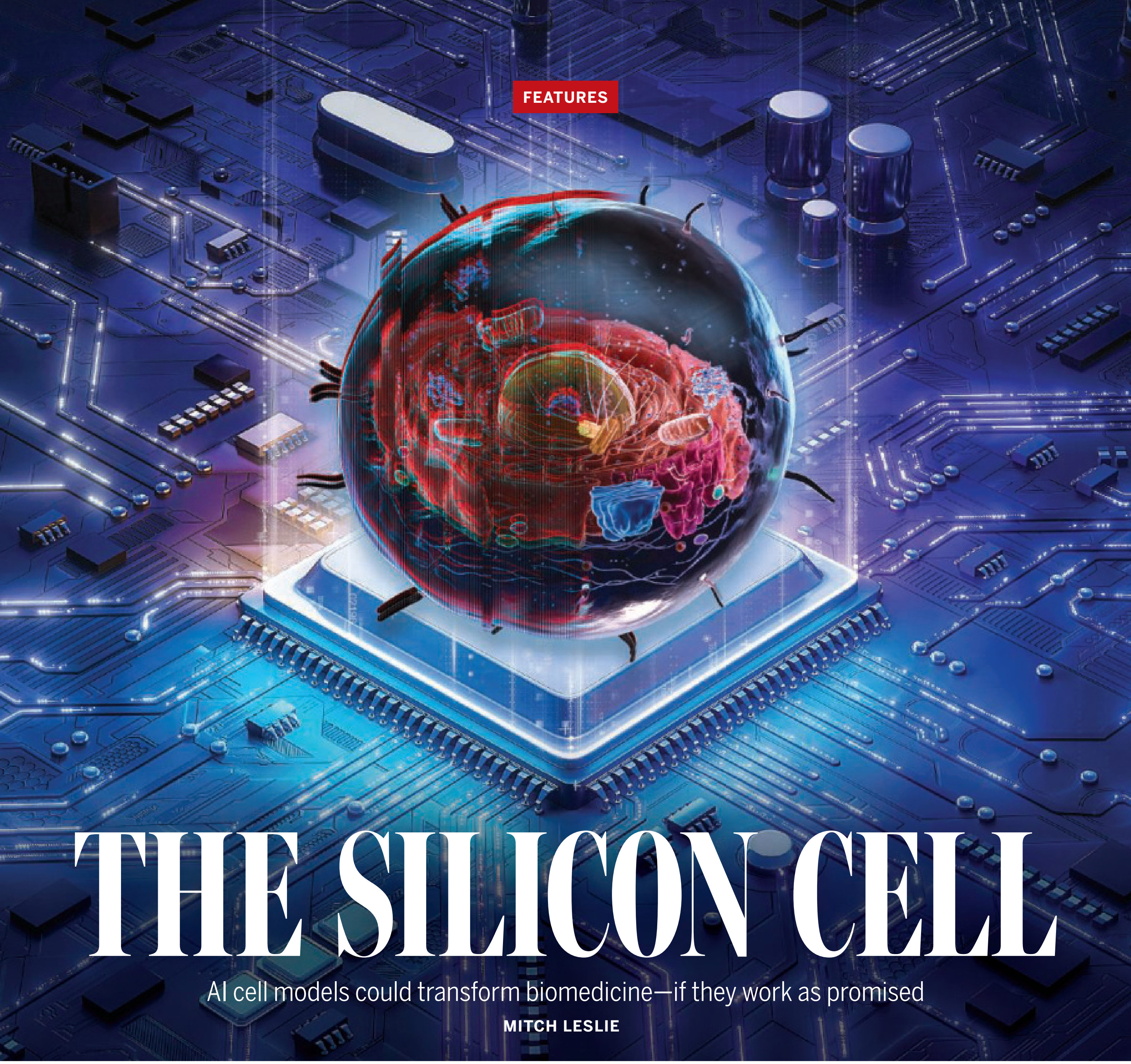

FEATURES

THE SILICON CELL

AI cell models could transform biomedicine—if they work as promised

MITCH LESLIE

A human cell swarms with trillions of molecules, including some 42 million proteins and a plethora of carbohydrates, lipids, and nucleic acids. Crowded with organelles and other structures, the cell boasts an intricate organization that makes baroque architecture seem plain. Its cytoplasm is a frenzied chemical lab, with molecules continuously reacting, rearranging, and reshaping. In the nucleus, thousands of genes are constantly switching on and off to turn the seeming chaos into concerted actions that help the cell survive and reproduce.

This complexity is more than the human mind can yet fully understand or predict. But many researchers think artificial intelligence (AI), with its prodigious ability to assimilate and process information, might be up to the task. More than 2 decades ago researchers started to build systems of equations meant to simulate some of the cell's workings. Now, they have progressed to AI-driven replicas that, like the large language models taking business and popular culture by storm, ingest vast amounts of data to learn on their own. ChatGPT's attention-grabbing debut nearly 3 years ago inspired the virtual cell builders. "People want this kind of moment for biology," says Kasia Kedzierska, an AI research scientist at the Allen Institute.

IMAGE: 3DARTISTS/SHUTTERSTOCK, ILEXX/ISTOCK. ADAPTED BY N. JESSUP/*SCIENCE*

How soon it is coming depends on whom you ask. Virtual cells that emulate their living counterparts would be a boon for many areas of research. In pharma labs, scientists could use them to quickly evaluate large numbers of potential drugs without the expense and difficulty of experiments. They might serve as test beds for engineering cells to perform novel functions. Virtual cells customized to match a patient's molecular profile could help doctors choose tailored medications. Researchers might even weave cell models into virtual tissues and organs to tackle questions such as how a tumor's environment affects its growth.

Such models could also help researchers make sense of the vast amount of diverse information pouring into molecular databases, says Theofanis Karaletsos, head of AI for science at the Chan Zuckerberg Initiative (CZI). An AI-powered cell mimic, Karaletsos says, "creates an integrated map of knowledge."

Like ChatGPT and its ilk, AI cell models have spawned big promises and hefty expectations. "Whenever a new model appears, it's always the best," says computational biologist Hani Goodarzi of the Arc Institute, who develops such models himself. In June he and more than 20 other researchers launched the Virtual Cell Challenge, a new contest that will put the models to the test annually. Much like a structural biology competition that started in 1994 and helped researchers largely solve the problem of how proteins fold, the Virtual Cell Challenge is meant to spur improvement in a very complex task. For its debut, it is asking AI aficionados to predict the effects of silencing certain genes in human embryonic stem cells.

So far, more than 1000 teams—with names like Cellamander, Zebulon Chow, SmartCell, and Mean Predictors—have entered and are vying for prizes donated by sponsors including Nvidia, the giant tech company that makes the graphics processing units (GPUs) at the heart of many AIs. On 6 December, contest organizers will reveal the final standings, with the top team taking home $100,000 in cash and GPU time. "We want to learn what works and what doesn't work," Goodarzi says.

Even if the models perform well on the test, some scientists expect a long road before they can deliver compelling new science or help biologists. "Despite the hype, [the models] are underperforming," says Alex Lu of Microsoft Research, who studies how AI can identify patterns in biology data. Some seem to have no more predictive power than simpler simulations. The profusion of models is itself a bad sign, says computational biologist Qin Ma of Ohio State University. "One model should be powerful enough that we wouldn't need to see so many of them."

The creators of the models say success is only a matter of time. "We haven't solved the problem yet, but [the approach] is very promising," says Bo Wang, head of biomedical AI for Xaira Therapeutics, a company that hopes to harness the technology for drug discovery.

INSPIRED BY ADVANCES in computing capabilities, researchers began trying to create virtual cells about 25 years ago. They first used computational methods that rely on large sets of equations to recapitulate metabolism, protein synthesis, DNA duplication, and other cell processes.

In 2012, Jonathan Karr, now a computational systems biologist at the Mount Sinai School of Medicine, and colleagues in Markus Covert's lab at Stanford University unveiled the first whole-cell model, a silicon version of *Mycoplasma genitalium*. They chose the microbe because it had the smallest genome of any bacterium known at the time: just over 500 genes, compared with more than 4000 in the familiar *Escherichia coli*. To replicate the organism's metabolism, the model calculated the concentrations of more than 700 metabolites as they churn through 1100 chemical reactions. With representations of a chromosome and protein-synthesizing organelles known as ribosomes, the ersatz cell reflected some of the internal structure of its real-life counterpart.

In 2022, cell biologist and biological physicist Zan Luthey-Schulten of the University of Illinois Urbana-Champaign and colleagues unveiled a model that had slightly fewer genes but was more sophisticated. It was based on a minimal bacterial cell, a microbe pared down in the lab to carry a mere 493 genes. But the researchers increased the realism of the model by making it 3D, using data collected by imaging real cells with cryogenic electron tomography. This level of detail came at a computational cost—simulating just 20 minutes of a cell's life required 8 to 10 hours of processing time with high-level GPUs.

Scientists have also developed similar whole-cell models of other bacteria, including *E. coli*. When the

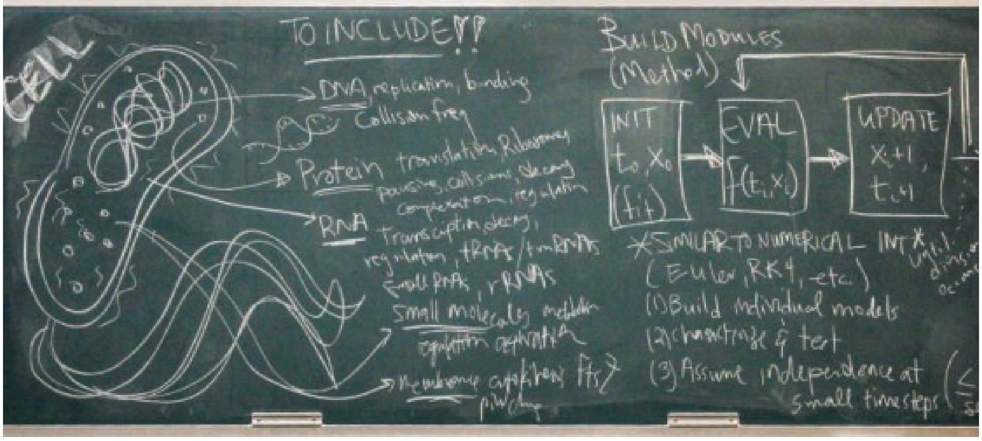

This chalkboard from 2012 depicts elements that went into the first published computional model of a whole cell, from Markus Covert's lab.

IMAGE: ERIK JACOBSEN/THREESTORY

researchers set these models into motion, they can simulate, second by second, a cell's existence as it metabolizes, grows, and divides. The ability to predict short-term cell dynamics, such as changes in concentrations of specific molecules, "is where these models really shine," Karr says. And Luthey-Schulten says researchers will one day be able to create computational models of human cells. "Do I think it will eventually be done? Yes."

Still, Wang says, these non-AI models can only follow biological rules set down by their developers, and it's unclear how closely the mathematical equations that underlie their behavior recapitulate reality. In addition, the models can't handle many of the questions that researchers most want to answer, says computational biologist Fabian Theis of the Technical University of Munich. "It's safe to say they have completely failed" at making certain kinds of predictions, such as forecasting the effects of silencing genes, he says.

THE VIRTUAL CELL CHALLENGE reflects hopes that the newer AI-driven models will be more successful. In place of inviolable equations, they learn cells' operating principles on their own, from huge amounts of experimentally derived cell biology data. "We don't teach it any biology," biophysicist Steve Quake of Stanford University says of the AI model TranscriptFormer, which he and CZI colleagues developed.

The models can exploit a torrent of new data, particularly single-cell measurements of gene activity. CZI's CELLxGENE collection, for example, houses gene activity data from more than 35 million human and mouse cells. Model builders also "get to take advantage of a tidal wave of technical development," Karr says.

Like the popular general-use AIs, such as GPT-5, Claude, and Gemini, most AI cell efforts released so far are so-called foundation models, meaning they can in principle probe a wide range of cell processes without further training. So far, AI cell foundation models capture only a sliver of biology and perform a limited set of tasks, such as classifying cells and predicting how they will respond to changes in gene activity. But researchers hope to ultimately combine them into something more comprehensive. "One model that rules them all is the vision," Theis says.

One early cell foundation model was Geneformer, which computational biologist Christina Theodoris of the University of California, San Francisco and her team described in *Nature* in May 2023. The group hoped to improve on a previous, less capable AI model that scrutinized a network of interacting genes and predicted the effects of modifying it. In a 2021 *Science* paper, Theodoris and colleagues reported they had used the model to identify a molecule that may combat a type of heart disease marked by excessive calcium buildup in the organ's valves. Other scientists have been investigating the molecule as a potential therapy. But that success was hard won: The researchers had to deduce the gene network themselves from experimental data and provide it to the model. With Geneformer, "I wanted to see if we could make a foundation model that had a basic knowledge of gene networks," Theodoris says.

She and her colleagues trained Geneformer with measurements of gene activity from nearly 30 million human cells. They found it could infer gene interactions and predict the effects of tampering with specific genes. The model then went through another round of training with gene activity data from heart cells of people who were healthy or who suffered from cardiomyopathy, in which the heart muscle weakens. It then picked out several genes whose inactivation should shift weakened heart cells toward normal operation.

The Geneformer team next went a step beyond most AI research groups and experimentally tested these predictions, using the gene editor CRISPR to disable two of those genes in lab-grown heart muscle cells with mutations that induce cardiomyopathy. Shutting down either of the genes boosted the cells' contraction strength, the researchers found, suggesting drugs that suppress the genes' function could be helpful in people. The results show Geneformer "could point to new directions and accelerate drug discovery," Theodoris says.

Still, Geneformer, like many AI cell models, was trained only on human data, although a few others also incorporate mouse results. TranscriptFormer, which Quake, Karaletsos, and colleagues described in a bioRxiv preprint earlier this year, stands out for its evolutionary breadth. The researchers produced three versions of the model, the most comprehensive of which schooled itself on gene activity data for 112 million cells from 12 species, including humans, mice, nematodes, sponges, and a malaria parasite.

That diverse education may have sharpened its abilities. TranscriptFormer topped scGPT, an AI model Wang and colleagues released in 2024, and Geneformer at classifying rare types of human cells, the researchers reported. The team also found it could classify cells from species that were not in its training set, discriminate lung cells infected by SARS-CoV-2 from healthy cells, and predict the cellular impacts of drugs. These feats are notable, Karaletsos says, because the model received no additional training—it was capable of what researchers call zero-shot learning. TranscriptFormer's performance, he says, “shows how people could use tools like this to discover fundamental biology.”

Researchers could also integrate cell foundation models into virtual helpers known as AI scientists, which can comb the research literature, devise hypotheses, conduct simulated experiments based on actual data, and write up the results. When computational biologist Marinka Zitnik of Harvard University and colleagues released a set of more than 600 tools earlier this year to help researchers develop AI scientists, TranscriptFormer was among them. Because of the way the model is designed, she says, “results come faster and with higher fidelity.”

SO, WHAT’S HOLDING BACK virtual cells? For one thing, most current AI models rely on a single type of data: measurements of gene activity. Researchers are just beginning to include other types of information, such as cell images, that could lead to more powerful and useful models, Ma says. And even though the amount of cell data has exploded in recent years, there’s still not enough to fuel the models. “The data limitation is a massive barrier to cell models,” Karr says. “There’s a limited set of questions we can pursue.”

Karr notes that despite the debut of collections like CELLxGENE, many results don’t end up in central storehouses where other scientists can easily access them. What the field needs, he says, is a repository like the Protein Data Bank (PDB), which was instrumental in the achievements of AlphaFold, the protein-folding predictor that is probably the most successful AI model in science. (Two of its developers shared a Nobel Prize in Chemistry in 2024.) The PDB houses almost every experimentally determined protein structure in a standard format, in part because most funders and journals required researchers to add any new structure they produced to the database. There’s no such requirement for cell data, which are also far more diverse than protein structures, Karr says. “You can’t characterize a cell with one technology.”

To improve current models, researchers also need a good way to assess how well they work—but scientists are still trying to decide how to do that. After models complete their initial training, developers often educate them further to improve certain abilities before putting them to the test. That practice mirrors what happens with widely available foundation models, such as GPT-5, which undergo extensive fine-tuning before the public can use them. But some researchers argue that tests should measure a model’s zero-shot performance. “If they are inferring a fundamental understanding of biology, it should be true before we fine-tune,” Theis says.

> “One model that rules them all is the vision.
>
> **Fabian Theis**
> Technical University of Munich

IMAGE: 3DARTISTS/SHUTTERSTOCK

A number of studies that gauged the zero-shot performance of recent AI cell models found them wanting. For example, Lu, Kedzierska, and colleagues pitted scGPT and Geneformer against a more primitive AI model and two non-AI methods. To their surprise, the simpler methods outclassed the two foundation models in tasks such as classifying cells, the researchers revealed earlier this year in *Genome Biology*.

Theodoris counters that the tasks had to be relatively easy so the simpler methods could accomplish them. As a result, the tests did not plumb Geneformer’s capabilities.

Even with fine-tuning, some AI cell models still fall short, as postdoc Constantin Ahlmann-Eltze of University College London and colleagues reported in *Nature Methods* in August. The challenge they set was to predict how certain genes would respond to alterations in the activity of other genes. They found that a basic mathematical formula provided more accurate results than five cell foundation models and two other AI models. “I was very surprised. Based on the publications, they all looked very good,” Ahlmann-Eltze says.

Studies like these test a limited number of models and apply varying criteria. But the field is developing a better sense of what the models should do and how to measure their performance, Kedzierska says. She points to new benchmarking tools that CZI posted earlier this year, which allow researchers to gauge different models’ abilities on standard criteria.

The Virtual Cell Challenge that Goodarzi and colleagues have launched has a similar goal. To produce the raw data for the challenge, researchers at the Arc Institute used CRISPR to shut down 300 genes, one at a time, in human embryonic stem cells and then monitored the effects on other genes. Entrants train their models on data for 150 of the genes—and on any other comparable cell data they can find. In the preliminary round, contestants try to predict the effects of silencing a second set of 50 genes. The results go on the contest leaderboard and give the entrants an opportunity to refine their models. The final results will depend on how well the models do on data for a third group of 100 genes. The task is difficult enough that “we don’t expect it will be a slam dunk,” Goodarzi says.

A few other contests have tried to assess AI models’ ability to predict how cells respond to changes, Theis notes. “But it is very good and exciting to see more of these at scale. We need bigger evaluations.”

When the contest’s results are released in December, they will provide more information to help researchers boost the performance of cell foundation models. And even scientists who have critiqued current virtual cells say they are optimistic about the future of the AI approach. “I wouldn’t give up on these models,” Kedzierska says. “Where they fail gives us a lot of information.” In the end, “I think we will get really good models.”

Karaletsos agrees. TranscriptFormer is the “dumbest model we will ever build.” □

PHOTO: SWETLANA MESHCHERYAGINA0

GENOMICS

How common cuckoos adapt to multiple hosts

Genomic data reveal the complexity of egg mimicry evolution in cuckoos

Michael D. Sorenson[1] and **Claire N. Spottiswoode**[2,3]

Like other obligate brood parasites, common cuckoos (*Cuculus canorus*) reproduce by depositing eggs in "host" nests, thereby exploiting the parental care of another species. After hatching, the cuckoo chick eliminates its competition by ejecting host eggs (and/or chicks) from the nest. Given these extreme costs, hosts evolved the ability to recognize and reject foreign eggs, and cuckoos evolved eggs that mimic the appearance of host eggs to better escape detection (*1*). This coevolutionary arms race is complicated, however, by the cuckoo's exploitation of multiple host species, which presents a puzzle: How does a single cuckoo species evolve eggs that mimic those of many different hosts? On page 527 of this issue, Merondun *et al.* (*2*) report genomic data that reveal a complex geographic mosaic of cuckoo-host coevolution, in which maternally inherited genes, autosomal (biparental) genes, and population structure all contribute to the evolution of a diversity of cuckoo egg phenotypes.

Nearly a century ago, Reginald Punnett (*3*) suggested that maternal inheritance of egg traits through the female-limited W chromosome (female birds have Z and W sex chromosomes, whereas males are ZZ) would allow different female lineages or matrilines to specialize on different host species and evolve distinct, mimetic egg phenotypes, even if males and females mated randomly within a single interbreeding population. Molecular genetic data provide support for this long-standing hypothesis in three different brood parasites. The African cuckoo finch (*Anomalospiza imberbis*) most closely adheres to Punnett's hypothesis, with clear evidence of multiple, host-specific matrilines with different mimetic egg phenotypes (*4*). In the greater honeyguide (*Indicator indicator*), another African species, two highly divergent matrilines are associated with tree- and ground-nesting hosts, respectively, but it is not clear that maternal inheritance explains additional phenotypic variation within each of these major lineages (*5*). Similarly, an earlier study showed that common cuckoo females in Europe and Asia that lay immaculate blue eggs belong to the same ancient matriline (*6*) but left unexplained the genetic basis of the many other egg phenotypes in this species (see the photo).

When avian brood parasites experience diversifying selection associated with their exploitation of multiple hosts, matrilineal diversification and the evolution of new species (speciation) are alternative outcomes that allow for host-specific adaptation (*7*). In both scenarios, the young female brood parasites are assumed to imprint behaviorally on characteristics of their host species (e.g., preferred habitat and/or songs) (*8*, *9*), such that daughters generally parasitize the same species as their mothers. However, speciation requires a mechanism for assortative mating (i.e., mating between male and female parasites reared by the same host species)—which could be enabled by temporal, ecological, and/or geographic segregation of hosts—or host imprinting in both male and female parasites (*8*, *10*). A second critical distinction is that maternal inheritance is effective only for female-limited phenotypes such as egg coloration, whereas speciation allows for host-specific diversification in traits shared by both sexes (e.g., mimetic appearance and behaviors of parasitic chicks) (*11*, *12*). Accordingly, the available data suggest that matrilineal diversification is associated with selection for egg mimicry (*4*–*6*), whereas speciation is associated with chick mimicry (*11*, *13*).

Merondun *et al.* analyzed whole-genome sequencing data for an impressive sampling of cuckoos from across Eurasia to provide improved resolution of matrilineal history and population structure, along with

The common cuckoo (*Cuculus canorus*) has evolved egg features (top row) to mimic eggs of different host species (bottom row).

the power to identify autosomal loci associated with egg phenotypes. Their analysis confirms prior results that support maternal inheritance of immaculate blue eggs while also identifying a more recent, independent origin of blue-green background color in a matriline mimicking the brambling (*Fringilla montifringilla*), which has blue eggs that are variably patterned with brown markings. Importantly, Merondun *et al.* show that autosomal genes and geography also contribute to variation in egg phenotypes in both the common cuckoo and the closely related oriental cuckoo (*Cuculus optatus*). This suggests that spatial segregation of hosts, at least in portions of each parasite's range, may be sufficient to allow local adaptation based on genes with biparental inheritance. At the same time, and despite the common cuckoo's vast geographic range and array of host species, maternal inheritance of some egg phenotypes may impede speciation by reducing the potential advantages of assortative mating. Overall, the results suggest a geographic mosaic of host-specific adaptation across Eurasia based on multiple mechanisms, rather than a simple model of purely matrilineal diversification. More extensive geographic sampling for other brood parasites will likely reveal similarly complex mosaics (*11*).

For species in which natural selection has favored maternal inheritance as a "solution" for evolving mimicry of multiple hosts, the lack of recombination (i.e., the exchange of genetic material between paired chromosomes during meiosis) in maternally inherited genome components may limit future evolutionary potential, including coevolutionary responses to hosts. In common cuckoos, for example, an adaptive, female-limited plumage polymorphism is also maternally inherited (*14*), but having originated in one matriline, there is no opportunity to recombine this trait with a maternally inherited egg phenotype from another existing matriline. Similarly, maternal inheritance in cuckoo finches, in which different matrilines lay eggs with blue and red background color, respectively, may explain their apparent failure to evolve olive-colored eggs (which require expression of both blue and red pigments), a frequent phenotype in one of their primary host species (*4*).

The lack of recombination also makes it harder to identify the specific genes that underlie differences in egg phenotype. Although Punnett highlighted the female-limited W chromosome, changes in mitochondrial DNA (mtDNA) could also be involved in maternally inherited phenotypes. The W chromosome (except for its pseudoautosomal region) and mtDNA are both nonrecombining and effectively linked by their shared matrilineal history. Thus, the mutations that distinguish divergent matrilines are all correlated with each other, making a standard genome-wide association study ineffective for pinpointing which mutational differences are functionally important. Nonetheless, the suggestion that mitochondria are involved in egg coloration through the heme pathway is an intriguing possibility. Protoporphyrin IX, which is typically responsible for red and brown colors in avian eggshells, is the immediate precursor to heme, which is a component of respiratory complexes II, III, and IV and helps regulate mitochondrial activity, whereas biliverdin, typically responsible for blue or green eggshells, is an intermediate product in heme degradation. Interestingly, one of the autosomal genes that Merondun *et al.* identified as potentially contributing to egg phenotypes, perhaps through interaction with maternally inherited genes, is biliverdin reductase A (*BLVRA*), which converts biliverdin to bilirubin. A presently unknown *BLVRA* allele or nearby regulatory change altering its expression might increase the concentration of biliverdin during eggshell formation. Note that mitochondrial involvement in egg coloration may or may not depend on mutations in mitochondrial genes, as many nuclear genes, including some W-linked genes, are involved in mitochondrial function.

Broad geographic sampling and genomic data allowed Merondun *et al.* to reveal the complexity of host-parasite coevolution in the most famous and well-studied brood parasite. Notably, their results suggest potential interaction between maternally inherited and autosomal genes and, more generally, show that maternal inheritance alone does not account for the diversity of cuckoo egg phenotypes. Learning more about the molecular basis of maternally inherited traits in birds will continue to be challenging. Comparing gene expression in the shell gland, where the eggshell forms and its pigments are deposited, could be informative for egg phenotypes but is infeasible for most wild birds. Comparative genomic analyses that include more brood parasites, their hosts, and other nonparasitic species may do more to expand understanding of host-specific adaptation. Achieving this will require fieldwork on more of the world's ~100 brood parasites, including many species in Africa and Asia that have never been studied intensively in the field. □

REFERENCES AND NOTES

1. N. B. Davies, *Cuckoos, Cowbirds and Other Cheats* (T & A. D. Poyser, 2000).
2. J. Merondun *et al.*, *Science* **390**, 527 (2025).
3. R. C. Punnett, *Nature* **132**, 892 (1933).
4. C. N. Spottiswoode *et al.*, *Proc. Natl. Acad. Sci. U.S.A.* **119**, e2121752119 (2022).
5. C. N. Spottiswoode, K. F. Stryjewski, S. Quader, J. F. R. Colebrook-Robjent, M. D. Sorenson, *Proc. Natl. Acad. Sci. U.S.A.* **108**, 17738 (2011).
6. F. Fossøy *et al.*, *Nat. Commun.* **7**, 10272 (2016).
7. G. Dillenseger, *J. Avian Biol.* **2024**, e03252 (2024).
8. R. B. Payne, L. L. Payne, J. L. Woods, M. D. Sorenson, *Anim. Behav.* **59**, 69 (2000).
9. C. Yang, W. Liang, A. P. Møller, *Behav. Ecol. Sociobiol.* **72**, 126 (2018).
10. R. B. Payne, L. L. Payne, J. L. Woods, *Anim. Behav.* **55**, 1537 (1998).
11. N. E. Langmore *et al.*, *Science* **384**, 1030 (2024).
12. G. A. Jamie *et al.*, *Evolution* **74**, 2526 (2020).
13. M. D. Sorenson, K. M. Sefc, R. B. Payne, *Nature* **424**, 928 (2003).
14. J. Merondun *et al.*, *Sci. Adv.* **10**, eadl5255 (2024).

ACKNOWLEDGMENTS

The authors thank C. N. Balakrishnan for comments.

10.1126/science.aec1973

---

[1]Department of Biology, Boston University, Boston, MA, USA. [2]FitzPatrick Institute of African Ornithology, Department of Biological Sciences, University of Cape Town, Cape Town, South Africa. [3]Department of Zoology, University of Cambridge, Cambridge, UK. Email: msoren@bu.ed

EPIDEMIOLOGY

Broad benefits of the COVID-19 pandemic response

Nonpharmaceutical interventions protected the US population from other infectious diseases

David N. Durrheim

The COVID-19 pandemic exacted an enormous toll in lives and livelihoods, and post-COVID syndrome now afflicts millions of individuals worldwide (*1*). While awaiting the development and rollout of effective vaccines, many countries used a combination of nonpharmaceutical interventions (NPIs), such as restrictions on mass gatherings, school and workplace closures, stay-at-home orders, contact tracing and testing, and requirements for face coverings, to control the spread of the disease and minimize COVID-related deaths. Weighing the costs and benefits of these interventions on physical, mental, and economic health is essential to understand their impact. On page 510 of this issue, Brett and Rohani (*2*) report the effects of NPIs on other common legally notifiable infectious diseases in the US during the COVID-19 pandemic.

Many countries and states underestimated the COVID-19 pandemic threat at a point when aggressive domestic suppression of disease transmission using NPIs, and rapid closure of international borders, could have minimized deaths and allowed a return to near-normal functioning of their economies. A review of Organisation for Economic Co-operation and Development (OECD) country responses to the COVID-19 pandemic demonstrates that countries that responded early with robust NPIs to suppress severe acute respiratory syndrome coronavirus 2 (SARS-CoV-2) viral transmission, including Australia, Japan, New Zealand, Norway, Singapore, South Korea, and Taiwan, best balanced death prevention and economic metrics (*3*). However, NPIs had a negative impact on the education and development of young children, and the well-being and mental health of families, particularly in the lowest socioeconomic strata. Concerns have been raised that NPIs implemented during the COVID-19 pandemic could also have disrupted the seasonal and longer-term exposure patterns of other infectious diseases. These disruptions could have led to increased susceptibility of populations to these diseases, resulting in disease resurgence after relaxation of NPIs (*4*).

Brett and Rohani focused on the effects of NPIs on the incidence (rate of disease occurrence in a specified population in a defined period) and trends of other infectious diseases in the US from 2014 to 2024. All diseases included were notifiable by law and were defined as “not rare” (exceeding 1000 notified cases in the US from 2014 to 2022), with no full years of missing data. Animal rabies was the only nonhuman disease included. Compared with other countries, the US has good universal access to diagnostic services and robust disease notification systems, which enabled reliable disease trend analysis. The variable intensity and duration of NPIs across different US states supported thorough comparison of disease trends across the span of the pandemic.

The behavior of the diseases in this analysis statistically coalesced into three distinct clusters that corresponded to their predominant transmission mechanism: environmentally transmitted and zoonotic infections (which spread from animals to humans), sexually transmitted infections, and airborne or aerosol-transmitted infections. Analysis of environmentally transmitted and zoonotic infections, which were not expected to be affected by NPIs, confirmed that surveillance systems for notifiable diseases continued to function adequately during the pandemic. The analysis of sexually transmitted infections demonstrated that NPIs during the pandemic had only a small and nonlasting effect on these infections. Animal rabies and hepatitis A were outliers in the analysis, as their incidence decreased after the pandemic. This trend is explained by a postpandemic wildlife rabies vaccination campaign and a large multistate outbreak of hepatitis A during the 3 years preceding the pandemic.

NPIs resulted in a sharp reduction in the incidence of airborne and aerosol-transmitted infections. Once NPIs were relaxed, their incidence remained lower than that predicted by mathematical modeling in most US states, despite some rebounds. This observation bolsters the “collateral benefit” case for NPIs during pandemic responses. However, the observations and conclusions of the study are US specific, and it would be important to validate them in other countries. As the analysis is based on disease notification data that require well-developed laboratory and diagnostic capacity, this validation would unfortunately be mostly restricted to other high-income settings. Countries across the full spectrum of NPI implementation during the COVID-19 pandemic, including minimal mitigation (e.g., Sweden), partial implementation (e.g., United Kingdom), and elimination (e.g., New Zealand), should be included.

Brett and Rohani did not include measles in their analysis because this disease was rare in the US, where endemic measles was declared as eliminated 25 years ago (*5*). However, measles has resurged in the US and large outbreaks of measles have also been reported in many other countries, particularly in 2024 to 2025. This resurgence suggests that NPIs during the pandemic may have concealed an accumulation of unvaccinated susceptible children before and during the pandemic, which then became apparent once these measures were relaxed. These observations also highlight the fragility of individual countries’ measles elimination efforts and the need to set a global eradication goal for this disease (*6*).

COVID-19 vaccines were developed in record time, taking just 326 days from the release of the virus’s genetic sequence to market authorization of a safe, effective vaccine. The Coalition for Epidemic Preparedness Innovations, an international organization that funds vaccine development, plans to abbreviate vaccine development against the next pandemic threat to 100 days (*7*). Setting NPIs at a maximum level could be the best approach to smother transmission of the infectious agent while buying time for vaccine rollout. Frameworks for deciding whether a public-health disease elimination approach is warranted have been developed (*8*).

Comprehensive analysis of the full array of positive and negative effects of pandemic control measures enables the identification of the most effective, efficient, and proportionate measures and their optimal timing, targeting, and intensity. This knowledge enables evidence-based guidance for the inevitable next pandemic. □

REFERENCES AND NOTES

1. E. Pazukhina *et al.*, *BMJ Glob. Health* **9**, e015245 (2024).
2. T. S. Brett, P. Rohani, *Science* **390**, 510 (2025).
3. H. Masuhara, K. Hosoya, *J. Policy Model.* 10.1016/j.jpolmod.2025.05.008 (2025).
4. R. E. Baker *et al.*, *Proc. Natl. Acad. Sci. U.S.A.* **117**, 30547 (2020).
5. A. D. Mathis *et al.*, *MMWR Morb. Mortal. Wkly. Rep.* **74**, 232 (2025).
6. D. N. Durrheim *et al.*, *Nature* **641**, 1101 (2025).
7. Coalition for Epidemic Preparedness Innovations, “Delivering pandemic vaccines in 100 days: What will it take?” (2022); CEPI-100-Days-Report-Digital-Version_29-11-22.pdf.
8. M. G. Baker, D. Durrheim, L. Y. Hsu, N. Wilson, *Lancet* **401**, 265 (2023).

10.1126/science.aeb5722

University of Newcastle, Newcastle, NSW, Australia. Email: david.durrheim@newcastle.edu.au

Two diverging paths for clean fuel

Fischer-Tropsch synthesis can produce liquid fuels from nonpetroleum sources

Mark Saeys[1,2]

Discovered a hundred years ago, the Fischer-Tropsch synthesis (*1*) has recently been considered as a possible route to produce liquid fuels and chemical building blocks without the use of fossil sources. This chemical reaction converts syngas—a mixture of carbon monoxide and hydrogen—to commercially important chemicals, such as light olefins (*2*) and long-chain hydrocarbons, through a surface polymerization reaction on cobalt or iron catalysts (*3*). However, hydrogen can form water as a by-product, and carbon monoxide can lead to carbon dioxide production. Indeed, the Fischer-Tropsch synthesis produces more unwanted derivatives than hydrocarbons. On pages 516 and 494 of this issue, Cai *et al.* (*4*) and Gao *et al.* (*5*), respectively, report strategies to maximize the incorporation of hydrogen and carbon atoms into hydrocarbon compounds, offering sustainable routes to liquid fuel production with improved efficiency.

Generating sustainable liquid fuels

The Fischer-Tropsch synthesis converts the syngas mixture into liquid hydrocarbons. Introducing a trace amount of bromomethane gas can reduce the amount of carbon dioxide by-product. Alternatively, an iron oxide coating can decrease the formation of water, which improves hydrogen efficiency.

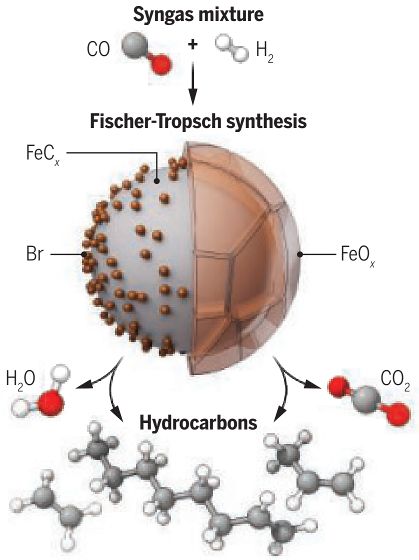

CO, carbon monoxide; CO_2, carbon dioxide; FeC_x, iron carbide; FeO_x, iron oxide; H_2, hydrogen gas; H_2O, water; *x*, number of atoms.

In the Fischer-Tropsch synthesis, the removed oxygen from carbon monoxide can lead to two different by-products (see the figure). It first forms water by combining with two hydrogen atoms (*3*, *6*). However, the water molecule can further react with carbon monoxide to produce hydrogen through a water-gas shift reaction that generates carbon dioxide. This reversible side reaction can regenerate hydrogen if coupled to an active catalyst. This even allows hydrocarbon production without hydrogen input (*7*, *8*). Conversely, the reverse water-gas shift reaction permits the Fischer-Tropsch synthesis without carbon monoxide input by using hydrogen and carbon dioxide as the reactants (*9*). Controlling these reactions determines the incorporation of hydrogen and carbon into valuable hydrocarbons.

Catalyst choice is important in determining the activity of the Fischer-Tropsch and the water-gas shift reactions. Cobalt catalysts limit the water-gas shift side reaction and carbon dioxide production (*10*). By contrast, iron catalysts have higher activity toward the water-gas shift reaction than cobalt, which makes them more favorable for converting hydrogen-poor syngas mixtures (with a hydrogen-to–carbon monoxide ratio below 2) to hydrocarbons. However, iron catalysts also reduce the incorporation of carbon atoms into hydrocarbon compounds, instead generating more carbon dioxide. Although the reaction mechanism of cobalt catalysts is relatively well understood (*3*), the iron-based Fischer-Tropsch synthesis remains unclear. Catalytically active sites that are responsible for the water-gas shift reaction are still debated (*11*).

Cai *et al.* showed that feeding trace amounts (<20 parts per million) of bromomethane gas with a syngas mixture reduces water-gas shift activity of iron-carbide catalysts and maximizes carbon incorporation in the hydrocarbon compounds. Bromine atoms covered about 30% of the catalyst surface and reduced the rate of carbon dioxide formation by nearly two orders of magnitude, decreasing carbon dioxide selectivity more than 30-fold. As a result, oxygen atoms were primarily removed as water molecules. Bromomethane also improved selectivity toward the production of olefins, which are important building blocks for the chemical industry. The method of Cai *et al.* improves the carbon atom economy (fraction of carbon from carbon monoxide incorporated in hydrocarbon products) of the Fischer-Tropsch synthesis.

Gao *et al.* coated an iron carbide particle with a thin layer of iron oxide to create a core-shell catalyst. The iron oxide shell maximized the extent of the water-gas shift, which regenerated hydrogen by using the water by-product of the Fischer-Tropsch reaction. This reduced the need for hydrogen in a syngas feedstock, promoting a better hydrogen atom economy (fraction of hydrogen incorporated in the hydrocarbon products). The authors could direct 80% of hydrogen in syngas to olefins. In the method of Gao *et al.*, oxygen atoms from carbon monoxide were mostly removed as carbon dioxide.

Renewable hydrogen production is costly and energy intensive. Driven by the desire to use a range of different carbon sources, such as natural gas, coal, biomass, waste plastic, and carbon dioxide, the Fischer-Tropsch synthesis is experiencing a surge of interest and investment globally. For example, China has commissioned iron-based coal-to-liquid plants to handle a capacity of megatons per year. The electro-sustainable aviation fuel mandates of Europe have driven research in the carbon dioxide–based Fischer-Tropsch synthesis to produce synthetic jet fuel (*12*). The studies of Cai *et al.* and Gao *et al.* demonstrate the rich tunability of iron carbide as a catalyst for the Fischer-Tropsch synthesis. □

REFERENCES AND NOTES

1. F. Fischer, H. Tropsch, German Patent DRP 484337 (1926).
2. H. M. Torres Galvis *et al.*, *Science* **335**, 835 (2012).
3. K. T. Rommens, M. Saeys, *Chem. Rev.* **123**, 5798 (2023).
4. Y. Cai *et al.*, *Science* **390**, 516 (2025).
5. C. Gao *et al.*, *Science* **390**, eaea0774 (2025).
6. P. Wang *et al.*, *Nature* **635**, 102 (2024).
7. H. Kölbel, F. Engelhardt, *Erdöl Kohle* **2**, 52 (1949).
8. Y. Xu *et al.*, *Nat. Commun.* **10**, 1389 (2019).
9. B. Yao *et al.*, *Nat. Commun.* **11**, 6395 (2020).
10. B. C. A. de Jong *et al.*, *ACS Catal.* **15**, 10946 (2025).
11. N. S. Featherstone, E. van Steen, *Catal. Today* **452**, 115240 (2025).
12. CARE-o-SENE, Research for a green future: CARE-O-SENE – Catalyst Research for Sustainable Kerosene; https://care-o-sene.com/en/.

ACKNOWLEDGMENTS

The author acknowledges support from the Research Foundation – Flanders (S005226N).

10.1126/science.aec1997

GRAPHIC: N. BURGESS/*SCIENCE*

---

[1] Laboratory for Chemical Technology, Ghent University, Ghent, Belgium. [2] Centre for Advanced Process Technology for Urban REsource recovery (CAPTURE), Zwijnaarde, Belgium. Email: mark.saeys@ugent.be

Chimpanzees living at the Ngamba Island Chimpanzee Sanctuary in Uganda were rescued from the illegal bushmeat trade.

PSYCHOLOGICAL SCIENCE

Chimpanzees are natural scientists

Humans and chimpanzees share the potential to rationally revise their beliefs

Brian Hare[1,2,3]

The ability of humans to identify relevant information as evidence and update their beliefs in the face of contradictory evidence is foundational to all scientific inquiry (*1*). The extent to which nonhuman animals are capable of similar forms of reasoning has long been under debate. In his book *The Descent of Man*, Charles Darwin proposed that the greatest challenge for evolutionary theory is human intelligence (*2*). He predicted that psychological elements would be found in nonhumans, particularly in nonhuman apes, that bridge the gap between human and nonhuman cognition (*3*). On page 521 of this

PHOTO: INNOCENT AMPEIRE

issue, Schleihauf *et al.* (*4*) report that chimpanzees can update their beliefs on the basis of the quantity and quality of new evidence, providing more support for Darwin's radical idea.

An early experimental advance in studying self-knowledge in nonhuman apes was made by hiding a food treat in one of many hollow tubes and observing when the animals peeked inside it. Although they rarely peeked if they had watched the baiting, they frequently visually inspected the tubes when they had not observed it (*5*). Moreover, nonhuman apes were more likely to check the tubes when the stakes were higher (with more desirable food hidden) or when a delay that increased their likelihood of forgetting was introduced before they searched (*6*). These experiments also demonstrated that peeking does not come from practice. When faced with uncertainty, the majority of juvenile and adult chimpanzees spontaneously sought information in this way on their first exposure to the experimental setup (*7*, *8*). Great apes (human and nonhuman) have also shown some capacity to revise a choice when confronted with contradictory evidence. In a different set of experiments, chimpanzees made an initial selection between two boxes containing food of varying desirability. A magnifying glass was then introduced, altering the appearance of the food. When the new evidence was inconsistent with prior information, chimpanzees often peeked into the boxes from another angle before making a final decision, which suggests that they might have revised their beliefs when confronted with conflicting evidence (*9*).

...chimpanzees consistently made rational choices two or three times more often than nonrational ones in all scenarios.

Despite this progress, it has remained unclear whether chimpanzees possess the capacity to rationally evaluate the strength of new evidence in relation to their existing beliefs and revise those beliefs only when appropriate, as humans do. This capacity for reflective responsiveness to reasons is likely to be the only definition of rationality that the strictest opponents of animal rationality will admit (*1*). Schleihauf *et al.* adopted a previously developed experimental setup in which subjects are given a chance to revisit an initial choice after being presented with additional evidence (*9*). Across five experiments, 15 to 23 chimpanzees living at the Ngamba Island Chimpanzee Sanctuary in Uganda were tested on their ability to revise decisions when presented with varying strengths of evidence regarding the location of hidden food rewards.

Schleihauf *et al.* gave subjects eight opportunities to locate food hidden in two identical containers. Chimpanzees could select one of the containers but not both. For each trial, they received two sequential clues: one providing strong, conclusive evidence, and the other offering weak, inconclusive evidence. In half of the trials, the strong clue was presented first, followed by the weak; in the other half, the order was reversed. Chimpanzees consistently based their choices on the strong form of evidence, regardless of the order or modality (visual, when food could be seen inside the container, or auditory, when the container made a noise indicative of food when shaken) in which they received the information. Notably, when weak evidence was encountered first, subjects frequently revised their choice after being exposed to the stronger evidence, which is consistent with rational revision of beliefs.

To determine whether chimpanzees were simply discarding weaker evidence in favor of stronger evidence, three containers were used: One container provided auditory evidence, another provided visual evidence, and the third provided no evidence. Critically, the container with the strongest visual evidence of food was removed after presentation. If subjects had simply discarded weaker evidence once encountering stronger evidence, then their choices of a container should have been random. Instead, chimpanzees chose the container with weaker auditory evidence, suggesting that they integrated the relative strength of all evidence rather than overwriting weaker clues.

The study also revealed that chimpanzees are sensitive not only to the type but also to the quantity of evidence available to support their choices. Subjects were first exposed to weak evidence (a sound resembling food being dropped) and then stronger evidence (a treat visible in another container). As expected, subjects initially chose the container with the visible treat. However, when provided with additional auditory evidence suggesting that two treats might be hidden together, they revised their decision and switched away from the container where they had seen only one treat. This change occurred more often than in a control condition in which subjects only received auditory evidence that reaffirmed that the food they initially heard was still present in the container.

What about the effect of misleading evidence? Subjects were shown food in a container through a transparent cover only to discover that what they had initially seen was not a treat but a picture of a treat painted on the cover. Chimpanzees switched away from the misleading evidence more often than in a control condition in which the transparent cover was unmarked.

In the experiments by Schleihauf *et al.*, chimpanzees consistently made rational choices two or three times more often than nonrational ones in all scenarios. These findings demonstrate that nonhuman apes have a spontaneous ability to weigh evidence of varying strengths, revise prior choices, and adapt when evidence is revealed to be unreliable.

Science fiction author Arthur C. Clarke allegedly stated that "either we are alone in the Universe or we are not. Both are equally terrifying." The finding that other great apes are capable of self-reflection means that humans are not alone as rational beings. How tragic it would be if, just as humans discover this shared rationality, they bring about the loneliness that Clarke may have found so terrifying. Humanity should not ignore, so soon after primatologist Jane Goodall's passing, that the chimpanzees in Schleihauf *et al.*'s study were rescued by her and others from the illegal bushmeat trade that threatens their species' survival (*10*). Meanwhile, it is a profound gift to know that when a chimpanzee stares into a person's eyes, they too could be reflecting on their beliefs about humans. □

REFERENCES AND NOTES

1. G. Melis, S. Monsó, *Philos. Q.* **74**, 844 (2024).
2. C. Darwin, *The Descent of Man*, vol. 1 (J. Murray, 1871).
3. B. Hare, "The Darwinian road to morality" in *A Most Interesting Problem*, J. Desilva, Ed. (Princeton Univ. Press, 2021).
4. H. Schleihauf *et al.*, *Science* **390**, 521 (2025).
5. J. Call, M. Carpenter, *Anim. Cogn.* **3**, 207 (2001).
6. J. Call, *Anim. Cogn.* **13**, 689 (2010).
7. A. G. Rosati, B. Hare, *Biol. Lett.* **7**, 15 (2011).
8. A. G. Rosati, E. Felsche, M. F. Cole, R. Atencia, J. Rukundo, *Cognition* **251**, 105898 (2024).
9. C. O'Madagain *et al.*, *Proc. Biol. Sci.* **289**, 20212686 (2022).
10. S. R. Ross, J. G. Leinwand, *Biol. Lett.* **16**, 20200033 (2020).

ACKNOWLEDGMENTS

The author acknowledges support from the Templeton World Charity Foundation (funder DOI 501100011730), grant TWCF-2022-30062.

10.1126/science.aeb7565

---

[1]Department of Evolutionary Anthropology, Duke University, Durham, NC, USA. [2]Department of Psychology & Neuroscience, Duke University, Durham, NC, USA. [3]Center for Cognitive Neuroscience, Duke University, Durham, NC, USA. Email: apeminds@gmail.com

POLICY FORUM

INNOVATION

How collaboration with China can revitalize US automotive innovation

Strategic collaboration, not protectionist barriers, should be pursued

John Paul Helveston

The United States stands at a crossroads in its approach to China's rapidly advancing plug-in electric vehicle (PEV) industry, one that will shape not only domestic economic competition but also global climate goals, the future of automotive innovation, and the principles that will govern international trade in an era of rapid technological transformation. Although current protectionist US policies may temporarily benefit the Big Three US automakers, they can also stifle competitive pressure that drives innovation. The European Union offers an example of how a more collaborative approach can lead to important local investments that accelerate PEV development. Rather than retreating behind protectionist barriers, US policy-makers and industry leaders should pursue strategic collaboration that leverages China's manufacturing scale and cost advantages while preserving US strengths in advanced research.

Ford chief executive officer Jim Farley recently provided stark evidence of the competitive gap with China after personally evaluating a Xiaomi SU7—a Chinese battery electric vehicle (BEV) priced at around $30,000 with a driving range of more than 450 miles [the PEV category includes both BEVs and plug-in hybrid vehicles (PHEVs)] (*1*). The verdict was unambiguous: Chinese manufacturers are now producing superior electric vehicles at considerably lower price points than those of US manufacturers. Market data unequivocally support this conclusion. Whereas Chinese manufacturers offer numerous options under $40,000 with competitive driving ranges of 300 to 450 miles, US offerings remain concentrated in premium segments with considerably higher pricing for comparable ranges (see the figure). Chinese BEV makers are also pushing the frontier of achievable charging speeds and driving ranges on a single charge. Both BYD and CATL (Contemporary Amperex Technology Co., Limited) have produced batteries capable of charging at rates as high as 1 MW, translating to 250 to 325 miles of range in just 5 min. (*2*). The highest-range BEV in China, the Zeekr 001, delivers 645 miles at $56,426, whereas the sole US BEV that exceeds 500 miles—the Lucid Air—costs $169,000 for 517 miles (*3*). In 2024, China had 52 BEV models with ranges greater than 400 miles; the United States had four, all priced above $75,000 (*3*).

With high driving ranges, rapid charging speeds, and low prices, BEVs are quickly becoming the dominant vehicle technology in China, with PEV sales reaching 12.86 million in 2024 (46.7% of new vehicle sales) (see fig. S1) compared with just 1.56 million (9.8%) in the United States (*3*). China has also emerged as a net vehicle exporter, exporting 1.28 million PEVs in 2024—nearly as much as domestic US PEV sales (*3*).

The US auto industry faces a concerning future, with implications that could reverberate throughout the US economy. Protectionist policies may not only stifle domestic innovation, they also cannot prevent losses abroad where Chinese PEV manufacturers are rapidly gaining ground. The trajectory of General Motors (GM) illustrates this challenge: Once a leading manufacturer in China, the company finished 2024 ranked 16th in sales, going from highly profitable (25% margins) to losing money on every sale (–20.5% margins) and acknowledging that its Chinese operations are worth $5 billion less than previously estimated (*4*). The United States risks becoming an "island of tailpipes," isolated from global automotive innovation and dependent on domestic sport utility vehicle and truck sales while forfeiting historical global profits derived from international markets. The employment impacts could be substantial; the auto industry supports an estimated 10.1 million US jobs (about 5% of private-sector employment) and generates $730 billion in annual paychecks (*5*).

Summary of public charge points in China and the United States as of January 2025

	Total public chargers		Charges per 100 EVs	
	United States	China	United States	China
All charge points	200,000	3,580,000	3.1	10.4
Fast (dc) charge points	50,000	1,600,000	0.8	4.7
Slow (level 2) charge points	150,000	1,980,000	2.3	5.8

DATA: GLOBAL EV OUTLOOK 2025: ELECTRIC VEHICLE CHARGING", INTERNATIONAL ENERGY AGENCY (*4*)

The path to revitalizing the American auto industry requires strategic engagement with the forces reshaping the global automotive landscape through carefully structured agreements that address security concerns, protect worker interests, and ensure reciprocity in market access. The success of such engagement depends on the willingness of China to collaborate on more balanced terms than in previous decades and the willingness of the United States to allow innovative Chinese firms market access while managing risks instead of imposing wholesale restrictions.

HOW CHINA GOT AHEAD

China's current leadership in PEVs is the result of a long history of factors, not the least of which is a 20-year policy strategy that included forced technology transfer requirements for foreign automakers, preferential treatment for domestic battery suppliers, and an estimated $230 billion in subsidies between 2009 and 2023 (*6*). Local-level policies were also critical; in many Chinese cities, obtaining a license plate for an internal combustion engine vehicle (ICEV) involves lengthy wait times and high costs, whereas PEV plates are often free and immediately available. PEV drivers also enjoy access to many parts of cities where ICEVs face restrictions. Last, Chinese firms have made substantial investments into production innovations and supply chain development (*7*), scaling up critical material processing and battery manufacturing (*8*) while pioneering automation techniques that have reduced vehicle-development time to 18 months—nearly half that of typical incumbents.

Despite pioneering electric vehicle development with GM's EV1 in 1996 and Tesla's innovations in the 2000s, the United States has struggled to develop a competitive PEV industry to counter Chinese market dominance. Policy inconsistency made it difficult for automakers to justify large investments into building a comprehensive PEV supply chain (*9*). Consumer preferences are also important, with research showing that US consumers are on average less willing than their Chinese counterparts to adopt a PEV (*10*). Electricity rates are also considerably lower relative to gasoline prices in China compared with those in the United States, making the operational cost advantages of PEVs more pronounced in China. The United States also has fewer local-level policy tools to promote PEV adoption beyond preferential parking or access to restricted lanes on highways. Last, the United States has struggled to keep pace with China's charging infrastructure construction. The $5 billion National Electric Vehicle Infrastructure program exemplifies this struggle, with only 19 stations built over 2 years because of coordination challenges between installers, utilities, and other stakeholders (*11*). By the end of 2024, the United States had installed just 200,000 public charging points compared with China's 3.58 million (*2*), translating to more than three times as many chargers per EV in China than in the United States (see the table).

The United States risks becoming an "island of tailpipes"...

COMPETITIVENESS THROUGH COOPERATION

The disparities in PEV market offerings between China and the United States reflect not merely differences in policy priorities but a fundamental divergence in innovation and manufacturing capabilities that raises an urgent question: How can the United States gain access to affordable, high-performance PEVs? The answer may lie not in protectionism but rather in strategic collaboration with Chinese manufacturers.

Strategic collaboration can facilitate the transfer of leading battery and PEV technology from China without necessarily creating over-dependency. One path is to pursue technology licensing agreements with Chinese firms that have developed cost-effective battery and vehicle technologies. The discussions between Ford and CATL, for example, on licensing battery technology represent a promising model that would give Ford access to high-performance battery technology while maintaining local manufacturing in the United States. Likewise, the United States could leverage access to its large domestic market as a negotiating tool to secure more favorable terms for US companies operating in China while facilitating Chinese investment in the United States. A strategic integration with Chinese manufacturing expertise through foreign direct investment (FDI) by leading Chinese firms could improve the cost competitiveness of US-made vehicles. Investments by Gotion Battery in Illinois and Michigan demonstrate how Chinese firms can bring capital and expertise to the United States while creating local jobs for US auto workers. Strategic coordination of these investments, rather than blanket restrictions, would better serve long-term US interests.

Furthermore, the United States maintains substantial advantages in fundamental research, software development, and advanced materials, whereas China excels in manufacturing scale, commercialization, and cost reduction (*8*). Fostering formal and informal innovation networks that connect these complementary strengths could accelerate progress in next-generation technologies such as solid-state batteries and autonomous systems more effectively than either nation could achieve independently. For example, the United States and China could establish a dedicated advanced transportation technology dialogue focused on technical standards, regulatory harmonization, and targeted joint research initiatives, potentially leveraging the recently renewed US–China Science and Technology Agreement. This government-to-government engagement would create a supportive framework for private-sector collaboration while addressing legitimate concerns about intellectual property protection and market access.

Equally important is to revise existing policy to facilitate these opportunities. Current Foreign Entity of Concern (FEOC) restrictions—which ban Chinese, Russian, Iranian, and North Korean companies from US EV supply chains and federal incentives—should be refined to allow case-by-case security reviews for manufacturers seeking to establish US facilities. Restoring and expanding the Inflation Reduction Act (IRA) incentives—particularly the $7500 consumer tax credits for EV purchases that have been restricted by FEOC rules—would help to establish a domestic market for more affordable PEVs while preserving the IRA's effectiveness in stimulating domestic investments. The IRA spurred $277 billion in announced private investments for battery and PEV manufacturing facilities across the United States, supporting an estimated 350,000 manufacturing jobs (*12*). Likewise, when evaluating Chinese investments, the Committee on Foreign Investment in the United States review process should distinguish between strategic and nonstra-

Prices versus driving ranges for BEVs available in the United States and China

Chinese manufacturers offer many model year 2024 battery electric vehicles (BEVs) at more affordable prices with higher driving ranges on a single charge. US offerings remain concentrated in premium segments with higher pricing for comparable range performance. Data include BEV specifications collected from autocango.com for China and carsheet.io for the United States (*3*).

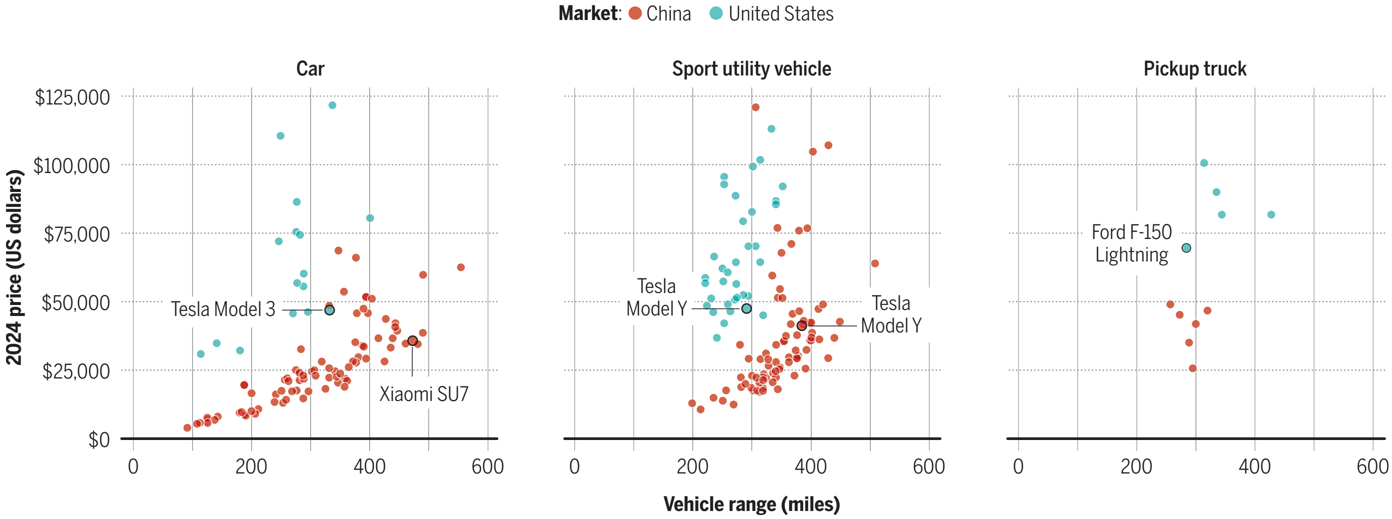

GRAPHIC: V. PENNEY/*SCIENCE*; (DATA): AUTOCANGO/AUTOCANGO.COM; CARSHEET/CARSHEET.IO

tegic technologies, such as advanced semiconductors or defense systems versus commercial EV manufacturing. Rather than relying solely on tariffs—which provide temporary market protection but no access to cutting-edge technologies—the United States could implement a calibrated approach combining modest protective tariffs sufficient to encourage foreign investment with streamlined approval processes for companies willing to manufacture domestically and share technological expertise with US partners.

LESSONS FROM SUCCESSFUL COLLABORATIONS

Historical precedent supports a more balanced approach that embraces FDI from Chinese firms to revitalize local manufacturing while creating jobs. When Japanese automakers such as Toyota established US production facilities in southern US states beginning in the 1980s, initial concerns about job displacement gave way to recognition of substantial benefits. US automakers learned from the Toyota Production System, adopting lean manufacturing principles that improved their own capabilities and efficiencies. These investments brought not just jobs but knowledge transfer that strengthened the entire US automotive ecosystem. A similar dynamic could occur with Chinese EV investments, in which US firms could gain exposure to cutting-edge manufacturing techniques and supply chain innovations developed in China.

Tesla's entry into China is another example that demonstrates how engagement can yield mutual benefits rather than zero-sum outcomes. When Tesla established its Shanghai Gigafactory in 2019, local suppliers upgraded their capabilities to meet Tesla's quality requirements, all while reducing manufacturing costs. The Shanghai facility became Tesla's most efficient factory, producing vehicles at substantially lower costs than that of its US operations and improving the company's global competitiveness by applying that manufacturing knowledge to newer facilities. The competitive pressure brought by Tesla benefited both sides: Tesla achieved profitability, and Chinese manufacturers benefitted from better-quality suppliers, sparking an innovation cycle that drove down costs industrywide. The first Tesla BEVs rolled off the Shanghai facility lines in December 2019, and PEV prices in China fell below ICEV prices on average for the first time just 2 years later, leading China's government to phase out consumer purchase subsidies for PEVs (*2*).

Crucially, Tesla's experience shows that security concerns can be managed through targeted solutions rather than blanket restrictions. China was concerned that Tesla's vehicles—equipped with cameras and sensors for navigation—could potentially collect sensitive visual data near government buildings, military installations, or high-technology zones. To address these concerns, Tesla agreed to specific requirements: storing all vehicle data collected in China within Chinese data centers (preventing potential US government access), restricting vehicle operations in designated sensitive areas, and using only Chinese government–approved mapping and navigation systems. Only after implementing these cybersecurity measures did the Chinese government grant Tesla permission to activate its Full Self-Driving technology. By contrast, the United States has used cybersecurity concerns to justify broad restrictions specifically targeting Chinese companies, including legislation that categorically blocks Chinese EV manufacturers from the US market (*13*). Although security risks are real, blanket exclusions are counterproductive. A more effective approach would develop transparent security standards and compliance verification that all connected vehicles must meet, regardless of origin (*14*).

In Europe, we can see promising examples of such cooperation. By opening to investments from Chinese firms, incumbent automakers are gaining access to the latest battery technologies, improving their competitiveness in the European market. CATL is building a $7.6-billion battery plant in Debrecen, Hungary, expected to produce 100 GWh of batteries annually for European automakers, including Mercedes-Benz, BMW, and Volkswagen. Similarly, BYD is constructing its first European electric vehicle manufacturing facility in Hungary to produce both BEVs and PHEVs specifically for the European market.

THE STAKES ARE GLOBAL

An isolationist approach in the United States undermines both climate and innovation objectives. Light-duty vehicles generate 16% of US carbon emissions (*2*), making the rapid deployment of affordable PEVs essential for meeting climate targets. Furthermore, isolating one of the world's largest automotive markets from leading PEV technology could have profound negative consequences for global innovation. Solid-state batteries, advanced materials, and more efficient motors could all develop more rapidly through collaborative networks than through parallel, isolated efforts. Research on wind and solar industries demonstrates that cross-border partnerships accelerated innovation while allowing each country to maintain distinctive industrial specializations when appropriate collaborative frameworks were established (*15*).

At the center of the PEV revolution lies a nexus of advanced computing, data security, and critical minerals that requires engagement to develop sustainable solutions. By developing a policy strategy that fosters FDI while protecting core interests, the United States can accelerate its electric transition and maintain a globally competitive automotive industry. The alternative—excluding Chinese technology and expertise—risks leaving US automakers uncompetitive while delaying the urgent global transition to sustainable transportation. □

REFERENCES AND NOTES

1. E. Halper, *The Washington Post* 25 April 2025.
2. International Energy Agency, "Global EV outlook 2025" (International Energy Agency, 2025); https://www.iea.org/reports/global-ev-outlook-2025/.
3. J. P. Helveston, jhelvy/us-china-pev-policy-2025: Main release. Zenodo (2025); https://zenodo.org/records/16878932.
4. K. Bradsher, *The New York Times* 19 December 2024.
5. Alliance for Automotive Innovation, "State of the US automotive industry" (Industry Report, Alliance for Automotive Innovation, 2025).
6. S. Kennedy, "The Chinese EV dilemma: Subsidized yet striking" (Center for Strategic and International Studies, 2024); https://www.csis.org/blogs/trustee-china-hand/chinese-ev-dilemma-subsidized-yet-striking.
7. J. P. Helveston, Y. Wang, V. J. Karplus, E. R. H. Fuchs, *Res. Policy* **48**, 206 (2019).
8. J. Helveston, J. Nahm, *Science* **366**, 794 (2019).
9. J. D. Graham, K. B. Belton, S. Xia, *Issues Sci. Technol.* **37**, 72 (2021).
10. J. P. Helveston *et al*. Transport. Res. A Pol., *Pract.* **73**, 96 (2015).
11. D. Ferris, *E&E News* 8 October 2024.
12. J. Turner, The Big Green Machine: Tracking the North American Clean Energy Supply Chain (2025); https://www.the-big-green-machine.com.
13. C. D. Miller, End Chinese Dominance of Electric Vehicles in America Act of 2024, H.R.7980 — 118th Congress (2023-2024); https://www.congress.gov/bill/118th-congress/house-bill/7980.
14. M. R. Davidson, V. J. Karplus, J. I. Lewis, J. Nahm, A. Wang, *Science* **377**, 1266 (2022).
15. J. Nahm, *Collaborative Advantage: Forging Green Industries in the New Global Economy* (Oxford Univ. Press, 2021).

ACKNOWLEDGMENTS

The author thanks the Fudan-UC Center on Contemporary China at the University of California, San Diego's School of Global Policy and Strategy for continuing to support a meaningful dialogue between the United States and China, and specifically the workshops on climate and United States–China relations organized by M. Davidson and L. Guang; this paper was greatly informed by conversations at these workshops. The author also thanks E. Wilson, J. Busby, and P. Triolo for their comments and suggestions. Anthropic's Claude 4.0 Sonnet AI model was used for editorial assistance purposes only during the preparation of this manuscript. All AI-generated content was reviewed, edited, and verified for factual accuracy and citation validity by the author. The author takes full responsibility for the final manuscript.

SUPPLEMENTARY MATERIALS

science.org/doi/10.1126/science.adz0541

10.1126/science.adz0541

Department of Engineering Management and Systems Engineering, George Washington University, Washington, DC, USA. Email: jph@gwu.edu

BOOKS ET AL.

PUBLIC HEALTH

More than a miracle

Pandemic preparedness is as essential as ever, argues a journalist

Caitlin Rivers

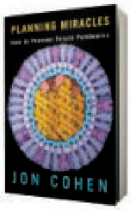

Jon Cohen
Knopf, 2025.
448 pp.

PLANNING MIRACLES | *Planning Miracles*, by Jon Cohen—a veteran journalist at *Science*—introduces readers to the world of pandemic preparedness at a chaotic time for the field. The United States is weathering an erosion of public health institutions, with far-reaching rollbacks diminishing funding, legal authorities, and trust. The book reminds readers of the distance humans have traveled to secure good health and illustrates the dangers that may befall us should our commitment to those protections wane. It is both a celebration of scientific achievement and a warning about the costs of complacency.

The book's title comes from one of history's most welcome achievements: the development of the Salk polio vaccine in 1955. March of Dimes founder Basil O'Connor described the vaccine's development as a planned miracle. "None of us dared to believe 17 years ago that this would happen in less than a century," O'Connor wrote that year in the introduction to the foundation's annual report. "And yet when it happened, it took everyone's breath away."

Cohen contrasts these miracles—which is to say, the deliverances of scientific breakthroughs and the scientists who accomplish them—with the tolls exacted by failure. "The opposite of a miracle is a disaster," he writes, "and few disasters exact a higher price than a pandemic."

The book's narrative is built around a theme captured in Benjamin Franklin's famous aphorism "an ounce of prevention is worth a pound of cure," coined after witnessing the abysmal response mounted by a ragtag volunteer firefighting effort to a destructive fire in Philadelphia. Throughout, Cohen successfully argues that investing in pandemic preparedness is as pragmatic and essential as investing in professional firefighting. The book weaves together historical accounts of the characters and breakthroughs that built our current armamentarium with firsthand interviews with contemporary scientists.

"Outbreaks are inevitable," Cohen writes. "If we want to prevent them from becoming epidemics…we must improve our understanding of what sparks them and evolve our responses, too." To that end, the book covers an enormous breadth, managing to survey a myriad of pandemic-prone pathogens, including influenza, the coronaviruses, and filoviruses, and exploring the scientific tools to combat each, in turn. Readers join Cohen as he tours a startup in Boulder, Colorado, developing the next generation of respirators; they tag along as he probes the enormously complicated and, at times, political nature of international clinical trial planning; and they follow him into mountains and rainforests where new viruses are found.

The most timely chapters examine viral threats that continue to knock at humanity's door. Influenza, particularly the avian influenza A(H5N1) that infected millions of birds before expanding into dairy cows, is one such hazard. Cohen traces the long history of influenza preparedness efforts, noting that H5N1 has threatened "ruination" since its emergence in 1996. This history will be of particular interest to readers seeking to go behind the headlines. His treatment of mpox follows a similar arc, showing how the virus transitioned from a rare zoonotic disease to a global outbreak in 2022 that continues even today. Together, these chapters illustrate Cohen's key insight: that the viruses we know about, and have tools to address, still pose serious threats when surveillance, countermeasures, and response capacities are neglected.

The book does not shy away from technical details. Cohen's treatment of the science behind pandemic preparedness is extensive and sophisticated, which may be a challenge for some readers. He delves into structural virology, immunology, genomics, and more, with technical passages sometimes extending for several pages. However, he balances these sections with human stories of the researchers doing the work, which should help sustain momentum for nonexpert readers.

Cohen also departs somewhat from the book's main themes on countermeasures to argue strongly in favor of a natural origin of severe acute respiratory syndrome coronavirus 2. He includes a defense of Peter Daszak—leader of the nonprofit organization EcoHealth Alliance, whose work on coronoviruses with a virology laboratory in Wuhan, China, has been heavily scrutinized as a potential origin of the COVID-19 pandemic. Not all readers will find Daszak to be a sympathetic character. Still, the inclusion of more contentious topics furthers the book's effort to portray science as a purposeful endeavor populated by real, complex people.

Planning Miracles will appeal to readers interested in public health, pandemic preparedness, and the history of medicine—particularly those hungry for scientific detail. The book's central argument about the importance of investing in pandemic preparedness resonates, especially now, as the devastation from the COVID-19 pandemic fades into memory and is replaced by corrosive skepticism and indifference. In reminding us that miracles must be planned, Cohen delivers an essential message for our tumultuous times. ☐

10.1126/science.aeb9832

The reviewer is director of the Center for Outbreak Response Innovation, a senior scholar at the Center for Health Security, and an associate professor at Johns Hopkins Bloomberg School of Public Health, Johns Hopkins University, Baltimore, MD, USA. She is also the author of *Crisis Averted: The Hidden Science of Fighting Outbreaks* (Viking, 2024). Email: crivers6@jhu.edu

PODCAST

A composite image shows a star's death in the constellation Taurus.

SCIENCE OF DEATH

Rounding out our 2025 series on the science of death, this week on the *Science* podcast, astrophysicist Katie Mack, author of **The End of Everything (Astrophysically Speaking)**, succinctly summarizes the ways our Universe may eventually end, placing our existential concerns about the end of life as we know it into cosmological perspective.

https://scim.ag/TheEndOfEverything

10.1126/science.aec7043

IMAGE: NASA/JPL-CALTECH/ESA/CXC/UNIV. OF ARIZ./UNIV. OF SZEGED

PHYSICS

Extraterrestrials illustrated

A physicist and a cartoonist join forces with an accessible guide to thinking about life in the cosmos

Matt von Hippel

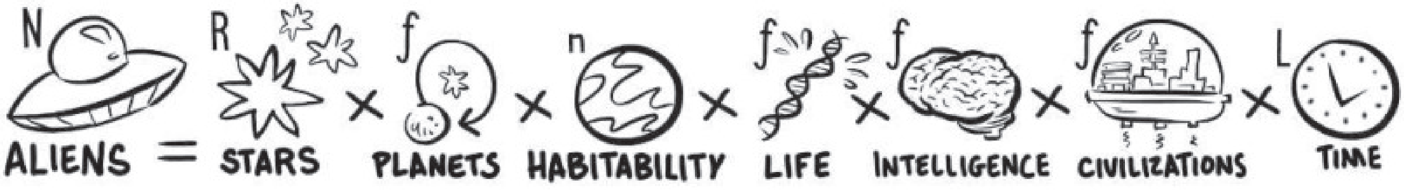

The Drake equation estimates the number of alien civilizations whose messages we should be able to receive.

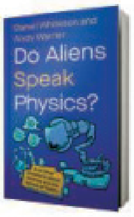

Do Aliens Speak Physics?
Daniel Whiteson and Andy Warner
Norton, 2025. 272 pp.

Since Randall Munroe's *What If?* published in 2014, illustrated pop science books have earned a niche on bookstore shelves. And their subject matter has gradually grown in ambition, as cartoonists and scientists work together to present increasingly well-researched takes on fascinating and obscure topics, with Kelly and Zach Weinersmith's 2023 book, *A City on Mars*, a standout recent example (*1*).

Do Aliens Speak Physics? brings together two veterans of the form: Daniel Whiteson, a physicist who has written two previous books with cartoonist Jorge Cham, and Andy Warner, a cartoonist who has previously covered weighty topics, such as Lebanon's Cedar Revolution (*2*). Like the Weinersmiths, Whiteson and Warner are trying something ambitious and well researched, attempting to convey a topic much deeper than the book's whimsical illustrations of goo-dripping aliens would suggest. To spoil my conclusion: They don't quite get there, but the questions they ask may justify reading the book, regardless.

The questions posed by Whiteson and Warner stem from their book's deceptively simple title: Do aliens speak physics? Historically, many physicists assumed so. When Frank Drake and Carl Sagan composed missives meant for aliens, such as the Pioneer plaque (*3*) and the Arecibo message (*4*), they began with references to physics and chemistry, invoking ideas such as hyperfine transitions in hydrogen and the chemical composition of DNA. The belief, it would seem, was that these concepts were universals—things anyone in the Universe would recognize. *Do Aliens Speak Physics?* asks whether that assumption is warranted.

Suppose we find an alien civilization. Could we talk physics with them at all? That's not really a physics question or a question about aliens. Instead, it's a question for almost every other corner of the sciences and humanities. It's a question about evolutionary biology—about whether very different types of intelligence could arise in the cosmos that would be impossible for humans to communicate with. It's a question about history—about whether humanity could have had technology without science, or science without math, or math with a radically different focus. And it's a question about philosophy—about how sure we are that the laws of the Universe are not just the laws of our own heads.

Whiteson is a physicist, not an evolutionary biologist, historian, or philosopher. Aware of this, he clearly tried to do his homework. The book has an extensive bibliography, and in between illustrations of extraterrestrials that would look at home in Calvin and Hobbes are cartoons of a comprehensive cross section of intellectuals, from Daniel Dennett to Steven Weinberg. This is a book with multiple quotes from Noam Chomsky. (He appears in a wizard robe, profusely thanked for his amazing willingness to answer the authors' emails.)

"Do aliens speak physics?" is thus an extremely ambitious question. And unsurprisingly, the book does not really answer it.

In its attempt, the book considers an extended Drake equation. Building off of Frank Drake's attempt to estimate the number of alien civilizations whose messages we should be able to receive, Whiteson and Warner add terms to calculate how many of those civilizations would be able to talk physics with us, with factors for how likely they are to do something we recognize as science, to be able to communicate their science with us, to be interested in questions we consider scientifically relevant, and to have answers that we can meaningfully learn from. For each factor, the authors spend a couple of chapters trying to break down what sorts of things might contribute to it.

In a scholarly book, a reader would expect to find a probability for each factor, likely with very large error bars. No such estimate appears in this book. That is because *Do Aliens Speak Physics?*, despite pulling in more scholarship on this question than any source I have seen, is still ultimately a pop science book—one that mentions a wide variety of fascinating ideas across disciplines but that, in the name of accessibility, cannot actually delve deeply into any of them.

The best use of *Do Aliens Speak Physics?*, in my mind, is to start a conversation. It is a book you can give to your grandfather to chat about over a long lunch or to your niece to spur a conversation on a summer evening spent on the back porch staring at the stars. Unlike other pop science books, it offers a conversation where neither the reader nor the author is an expert. Instead of a lecture, it is an honest exploration of some of the deepest questions behind science.

I would still love a book that actually answers the question "do aliens speak physics?"—even with the biggest error bars in the cosmos. But lacking that, it is fun to read a book that just asks the question. □

REFERENCES AND NOTES

1. K. Weinersmith, Z. Weinersmith, *A City on Mars: Can We Settle Space, Should We Settle Space, and Have We Really Thought This Through?* (Penguin, 2023).
2. A. Warner, *Spring Rain: A Graphic Memoir of Love, Madness, and Revolutions* (St. Martin's Griffin, 2020).
3. Wikipedia, "Pioneer plaque"; https://en.wikipedia.org/wiki/Pioneer_plaque.
4. Wikipedia, "Arecibo message"; https://en.wikipedia.org/wiki/Arecibo_message.

10.1126/science.aeb1978

The reviewer is a freelance journalist based in Copenhagen, Denmark.
Email: mattvonhippelsciencewriting@proton.me

ILLUSTRATION: ANDY WARNER

Edited by
Jennifer Sills

In 2023, a strong cold front triggered a super dust event in Haiyuan County, Ningxia Province, China.

PHOTO: NINGXIA NEWS NETWORK

Asian dust threatens air pollution control efforts

In April, a dust storm originating in Mongolia swept more than 3000 km southward over the course of a week, covering eastern China (*1*). Asian dust storms have increased in both intensity and frequency (*2, 3*), and their pathways have shifted to the east and south (*2, 4*). Dust increasingly reaches densely populated regions in eastern China, threatening air quality in major cities (*5*). Over the past decade, China has made substantial progress in reducing urban air pollution (*6*), but large natural particle sources, such as mineral dust, continue to offset air quality improvements (*5*). China should streamline dust and air quality efforts and work with other countries in the region to prevent and manage dust storms.

The China Meteorological Administration monitors dust storms, whereas environmental regulators concentrate on anthropogenic pollution. This regulatory gap leads to an underappreciation of the effects of natural dust, which can decrease air quality and harm human health (*7*). During long-range transport, dust particles undergo complex gas-phase and multiphase chemical reactions, accumulating harmful inorganic and organic pollutants on their surfaces (*8*). As dust storms travel, the particle size of the dust decreases, enhancing toxicity (*9*) and exacerbating health risks in downstream regions, such as Beijing, Shanghai, and Hong Kong.

To maintain its air quality gains, China must prioritize the prevention and management of Asian dust storms. Regional cooperation with upwind source countries, such as Mongolia, is critical. Joint efforts should focus on mitigating the development of dust storms by limiting unsustainable mining and agriculture in vulnerable desert regions and promoting ecological restoration and reforestation (*10*). In addition, China should expand monitoring frameworks, which currently focus on particulate matter smaller than 2.5 μm in diameter (PM2.5) and ozone (O_3) (11), to include routine natural dust storm surveillance and emergency response mechanisms. Policies must account for transboundary dust storms that travel thousands of kilometers and affect air quality in cities far from their source. Public awareness campaigns should emphasize the health risks posed by dust storms and promote protective measures during dust events.

Globally, mineral dust affects the respiratory health of an estimated 330 million people, influences surface O_3 levels, and disrupts ecosystem functions (*5, 12*). Effectively addressing the challenges of Asian dust storms will reinforce China's progress in air pollution control and contribute to global public health, climate adaptation, and sustainable development.

Guochen Wang, Shoujuan Shu, Weijun Li

State Key Laboratory of Ocean Sensing and Department of Atmospheric Sciences, School of Earth Sciences, Zhejiang University, Hangzhou, China. Email: liweijun@zju.edu.cn

REFERENCES AND NOTES

1. World Meteorological Organization, "Severe SDS Sweep Across Much of China" (RSMC-ASDF BEIJING, 14 April 2025); http://www.asdf-bj.net/publish/cms/view/f74171ef822042e7aa38298178ed6666.html.
2. Y. Ma *et al.*, *Global Planet. Change* **242**, 104578 (2024).
3. Z. Yin, Y. Wan, Y. Zhang, H. Wang, *Natl. Sci. Rev.* **9**, nwab165 (2022).
4. Y.-X. Li *et al.*, *Natl. Sci. Rev.* **12**, nwaf274 (2025).
5. Z. Wang, X. Huang, N. Wang, J. Xu, A. Ding, *J. Geophys. Res. Atmos.* **125**, e2020JD033601 (2020).
6. G. Geng *et al.*, *Nat. Geosci.* **17**, 987 (2024).
7. C. Zhang *et al.*, *Nat. Commun.* **14**, 6867 (2023).
8. W. Li *et al.*, *Natl. Sci. Rev.* **12**, nwaf221 (2025).
9. X. Zhang *et al.*, *Atmosphere* **7**, 158 (2016).
10. C. Zucca, R. Fleiner, E. Bonaiuti, U. Kang, *Catena* **219**, 106575 (2022).
11. Q. Xiao *et al.*, *Environ. Sci. Technol.* **56**, 6922 (2022).
12. J. M. Prospero *et al.*, *Global Biogeochem. Cycles* **34**, e2020GB006536 (2020).

10.1126/science.aeb2629

Restore strict protection for wolves in Europe

After centuries of persecution that drove wolf (*Canis lupus*) populations to the brink of extinction in most European countries (*1*), conservation measures and changes in land use have allowed the species to start slowly recovering (*2*). However, on 5 June, the Council of Europe approved the decision of the European Commission (EC) to downgrade the legal status of wolves in the Habitats Directive from Strictly Protected to Protected (*3*). Wolves classified as Strictly Protected could only be removed by derogation and on an individual basis, whereas wolves with Protected status could be removed as a result of culling plans, which puts population recovery in jeopardy (*4*). Given the gaps in knowledge about wolf populations and continued threats to the species in Europe, wolves should remain Strictly Protected.

With the monitoring currently in place, reliably estimating the number of wolves in Europe is not possible. The available demographic data are heterogeneous, approximate, largely qualitative, and unverifiable (*5*). Wolves have not yet reached a favorable conservation status in most European countries (*4*). Up to half of European wolf populations do not meet the effective population size criterion required for long-term genetic and demographic sustainability (*6*).

Wolf populations across Europe are primarily threatened by overhunting (including illegal killing), conflicts driven by livestock depredation, and political pressures from interest groups such as hunters and farmers to reduce population numbers through lethal removal (*4*). New threats are emerging as eastern and southern European countries erect border fences. This growing network of physical barriers, covering thousands of kilometers, has fragmented habitats and disrupted the genetic connectivity of wildlife species, including wolves (*7*).

The proposal to downgrade the wolf's status was based on a non–peer-reviewed technical report commissioned by the EC (*8*) and concerns about wolves' socioeconomic impact (*3*). However, the economic impact of wolf depredation is marginal and can be substantially mitigated by effective prevention programs (*5*), whereas lethal removal has been ineffective (*9*).

LIFE IN SCIENCE

The Coronation Chair of Denmark was crafted from narwhal tusks in the 17th century.

A legendary request for narwhal DNA

The Coronation Chair of Denmark, displayed at Rosenborg Castle, a museum in central Copenhagen, is a national treasure that was used in the coronation of Danish kings from 1671 to 1840 (*1*). The throne is pearly white with gold accents, a regal piece befitting its noble history. In 2007, as a PhD student, I called the curator of the museum to request access to the chair. I wanted to drill holes in it.

King Frederik III commissioned the throne in about 1660. According to legend, the chair was made of unicorn horns—rare mythical objects that had healing powers. In fact, the king had sent an expedition to Greenland to collect the spiraled tusks of male narwhals.

I hoped to collect samples from the 350-year-old tusks to investigate why narwhals have lower genetic diversity compared with other marine mammals of the polar north, but I feared that my request would be met with horror. To my astonishment, the curator found the project fascinating and said that my timing was perfect: The throne had been disassembled to undergo restoration.

We arranged for me to visit with my equipment—a dental drill, plastic gloves, and sample tubes. The throne's parts were laid out in a former royal horse stable. Centuries after being cut, the narwhal tusks' distinctive structure had continued to twist into a spiral, so the pieces that formed the backrest and front were soaking in a solution to straighten them. I drilled tiny holes in the large tusk segments that form the throne's pillars. Later, the chair was reassembled, and the holes are now invisible to viewers.

Unlike narwhals in the 17th century, today's narwhal populations face substantial changes to their arctic habitat driven by anthropogenic climate change. The data that I collected could provide information that improves management and conservation policies. I hope that my unusual request will ultimately help safeguard this legendary species.

Eva Garde

Greenland Institute of Natural Resources, Copenhagen, Denmark. Email: evga@ghsdk.dk

REFERENCES AND NOTES

1. J. Hein, Ivories and Narwhal Tusks at Rosenborg Castle: Catalogue of Carved and Turned Ivories and Narwhal Tusks in the Royal Danish Collection 1600–1875, vol. 2 (Museum Tusculanum Press, 2018).

10.1126/science.ady6674

CALL FOR SUBMISSIONS

Life in Science is an occasional feature highlighting some of the humorous or unusual day-to-day realities that face our readers. Can you top this? Submit your story to www.submit2science.org.

PHOTO: LARS ØIVIND KNUTSEN

To remain consistent with the European Nature Restoration Law, which places ecosystem health above economic and stakeholder interests (*10*), Europe should restore strict protection for wolves and implement reliable population monitoring and policies that recognize their ecological role. Priorities should include cross-species ecosystem recovery, ecological corridors, and livestock depredation mitigation. The EC should integrate science-based information on wolf behavioral ecology into nature conservation programs, considering ecosystem health and resilience as well as human well-being, and should also combat illegal killing and other threats to biodiversity. A full wolf recovery would restore the ability of this top predator to regulate and maintain the health of prey populations and promote reforestation, landscape heterogeneity, and biodiversity, all of which are achieved by both natural and assisted recolonization of wolves in Europe and elsewhere (*11*, *12*).

Ettore Randi[1], Hugh Jansman[2], Josip Kusak[3,4,5], Michela Pacifici[6], Gianluca Piovesan[7], Urmas Saarma[8], Krzysztof Schmidt[9], Geraldine Werhahn[10]

[1]Department of Chemistry and Bioscience, Aalborg University, Aalborg, Denmark. [2]Wageningen Environmental Research, Wageningen, Netherlands. [3]Department of Veterinary Biology, University of Zagreb, Zagreb, Croatia. [4]College of Sciences, Koç University, Istanbul, Turkey. [5]School of Biological Sciences, University of Utah, Salt Lake City, UT, USA. [6]Sapienza University of Rome, Rome, Italy. [7]Department of Ecological and Biological Sciences, University of Tuscia, Viterbo, Italy. [8]Institute of Ecology and Earth Sciences, University of Tartu, Tartu, Estonia. [9]Mammal Research Institute, Polish Academy of Sciences, Białowieża, Poland. [10]Himalayan Wolves Project, IUCN/SSC Canid Specialist Group, Wildlife Conservation Research Unit, University of Oxford, Oxford, UK. Email: ettorerandi17@gmail.com

REFERENCES AND NOTES

1. P. Kaczensky *et al.*, "Large carnivore distribution maps and population updates 2017–2022/23. Report to the European Commission under contract no. 09.0201/2023/907799/SER/ENV.D.3" (IUCN/SSC Large Carnivore Initiative for Europe and Istituto di Ecologia Applicata, 2024).
2. L. Boitani *et al.*, "Assessment of the conservation status of the Wolf (*Canis lupus*) in Europe" (Council of Europe Publishing, 2022).
3. Council of the EU, "Habitats directive: Council gives final approval to the new protection status of wolves," press release (5 June 2025); https://www.consilium.europa.eu/en/press/press-releases/2025/06/05/habitats-directive-council-gives-final-approval-to-the-new-protection-status-of-wolves/.
4. M. Kutal, M. Duľa, M. Haring, J. V. López-Bao, *Conserv. Lett.* **18**, e13125 (2025).
5. C. Di Bernardi *et al.*, *PLOS Sustain. Transform.* **4**, e0000158 (2025).
6. J. Mergeay *et al.*, *Evol. Appl.* **17**, e70021 (2024).
7. K. Nowak *et al.*, *Science* **389**, 358 (2025).
8. J. C. Blanco, K. Sundseth, "The situation of the wolf (*Canis lupus*) in the European Union—An in-depth analysis" (N2K Group for DG Environment, European Commission, 2023).
9. R. J. Lennox, A. J. Gallagher, E. G. Ritchie, S. J. Cooke, *Biol. Conserv.* **224**, 277 (2018).
10. E. Chiti, *Eur. L. Open* **3**, 190 (2024).
11. M. Rodríguez Recio, C. Wikenros, B. Zimmermann, H. Sand, *Biology* **11**, 317 (2022).
12. W. J. Ripple *et al.*, *Glob. Ecol. Conserv.* **58**, e03428 (2025).

10.1126/science.aeb0660

SPECIAL ISSUE

2025 MANDALAY EARTHQUAKE

ANGELA HESSLER and **SUMIN JIN**

The moment magnitude 7.7 to 7.8 earthquake that struck just outside Mandalay, Myanmar, on 28 March hit the region with strikingly widespread force. Thousands lost their lives, and strong shaking and damage were experienced as far away as Bangkok, Thailand. The research presented in this Special Issue helps to explain the properties and mechanisms behind the rupture and what these mean for earthquake forecasting along the Sagaing and similar faults. Goldberg *et al.* report on the earthquake's anomalously long, fast rupture, which outpaced typical shear-wave velocity and exacerbated ground shaking and damage over much of its ~500-km run. The Mandalay event was also the first time a rupture was captured by a closed-circuit television camera, which was located just meters away. High-resolution video analysis by Latour *et al.* tracked the motion of objects on either side of the fault and found an asymmetric progression of slip over 1.4 s, which provided direct evidence for how pulsed slip added up to produce the full 2-min-long rupture. The sustained, fast rupture may have been enabled by certain properties of the Sagaing fault. Xu *et al.* combined seismic and satellite data to link the rapid transition to supershear rupture to the contrasting rock properties on either side of the fault, and Wei *et al.* found that this transition occurred at a change in fault dip and thickness by integrating multiscale observations to reconstruct the event's displacement field. Together, these studies point to the rupture dynamics and fault properties that drive seismic hazard along this, and other, major strike-slip faults.

10.1126/science.aec3871

Teams from China carry out a search-and-rescue operation in Mandalay, Myanmar, on 1 April after the devastating earthquake.

PHOTO: CAI YANG XINHUA/EYEVINE/REDUX

High-speed fault rupture greatly expanded the damage area in Myanmar.

PHOTO: JIANG CHAO/XINHUA/GETTY IMAGES

2025 MANDALAY EARTHQUAKE

PERSPECTIVE

Mandalay earthquake pushes rupture limits

Fast rupture of Earth's crust breaks a long fault, expanding the damaged area

Kyle E. Bradley[1,2] and **Judith A. Hubbard**[1,2]

On 28 March 2025, a magnitude 7.7 earthquake struck the Sagaing Fault—a fracture in Earth's crust that runs the north-to-south length of Myanmar. The earthquake killed more than 4000 people and damaged a wide region, including the capital (Naypyidaw) and the country's second-largest city (Mandalay). Although a strong earthquake had long been anticipated for this dangerous fault, the rupture that caused the earthquake ran for more than 460 km, which is far longer than expected. On pages 458, 463, 468, and 476 of this issue, Goldberg *et al.* (*1*), Latour *et al.* (*2*), Wei *et al.* (*3*), and Xu *et al.* (*4*), respectively, report the detailed growth of the fault rupture over the course of 2 min. The studies provide a compelling account of the important role of high-speed fault rupture in greatly increasing the area of damage.

Earthquakes are generated by a sudden fault slip: an opposing movement of rock along a fracture in Earth's crust. Strong earthquakes caused by large fault ruptures expose hundreds of millions of people around the globe to intense ground shaking hazard. These earthquakes also provide rare opportunities to study the physical processes that govern natural fault ruptures. Understanding how these ruptures spread along a fault and grow to great size is particularly relevant for the largest earthquakes that cause the greatest harm.

Over the past half century, interest has grown in a type of fault rupture that breaks an apparent speed limit for rupture growth (*5*–*7*). These so-called "supershear" ruptures were once considered to be quite rare. Seismological methods that track rupture growth over time have shown that they are more common than previously thought (*8*, *9*). However, many questions about the physical processes underlying supershear ruptures, and their implications for seismic hazard, remain unanswered.

The Sagaing Fault is an earthquake "superhighway": a long, straight fault that can host especially fast and dangerous ruptures (*10*). Sections of a fault that have accumulated tectonic strain from constant plate motion but have not released it during recent large earthquakes are called seismic gaps and pose a special hazard. The Ava seismic gap—a 230-km section of the fault between Mandalay and Naypyidaw that had not experienced a major earthquake since 1839—has been particularly worrisome (*11*). Nevertheless, scenarios for supershear rupture during a large earthquake along the Sagaing Fault had been largely speculative.

Goldberg *et al.*, Wei *et al.*, and Xu *et al.* derived broadly similar models of the evolving fault rupture during the 2025 Mandalay earthquake by combining measurements of seismic waves with satellite measurements of ground movement near the fault. The earthquake nucleated 10 km below Earth's surface and then advanced toward the north and the south along the Sagaing Fault as two separate ruptures. The northbound rupture lasted for only half a minute, growing at a subshear speed (~3 km/s) and causing large fault offsets of up to 6 m. The seismic waves caused by this rupture heavily damaged the Sagaing and Mandalay regions. By contrast, the southbound rupture propagated for almost 2 min, passing Naypyidaw at a supershear speed (~5 km/s) and overrunning the southern end of the Ava seismic gap by 100 km. Sustained supershear rupture was confirmed by the presence of surface wave Mach cones, which are generated when a rupture outpaces its own shear waves. This is analagous to the sonic boom caused by jets flying faster than the speed of sound in air. Wei *et al.* and Xu *et al.* further observed supershear rupture in the spatiotemporal evolution of high-frequency seismic radiation. A seismic recording made near the fault at Naypyidaw also indicated a passing supershear rupture. The total rupture length exceeded 460 km, which is almost twice the length expected of a typical magnitude 7.7 earthquake. These features of the Myanmar earthquake echo the destructive 1906 San Francisco earthquake (magnitude 7.9), which is also thought to have exhibited rupture in two directions, an extremely long rupture length, and a sustained supershear propagation (*12*).

The southbound rupture was fortuitously captured by a security camera located near the fault, providing a high-resolution record of surface slip during an earthquake. Latour *et al.* tracked the surface motions across the fault over time to measure the instantaneous slip rate (the speed at which two fault blocks move past each other) and slip acceleration (the rate of change in slip). At the camera location, the fault slipped for only 1.4 s at a maximum velocity of 3.5 m/s. These measurements show that only a very small area of the large fault was slipping at a given moment. This supports the idea that pulse-like rupture may be common for large crustal earthquakes (*13*).

The studies of Goldberg *et al.*, Latour *et al.*, Wei *et al.*, and Xu *et al.* collectively showed that a sustained supershear rupture can break a much longer section of a fault than predicted by magnitude-length scaling laws. These are observed relationships between the magnitude of an earthquake and the length of a fault rupture and are widely used in seismic hazard modeling. Goldberg *et al.* argued that this excess rupture length doubled the human population exposed to very strong ground shaking compared with a more typical magnitude 7.7 earthquake. The unusual rupture length also implied a shorter-than-expected recurrence time of a successive earthquake on the same fault, suggesting that these events may be more common than previously appreciated. Thus, understanding how and why a sustained supershear rupture occurs is important for preparing for future events.

Numerous physical mechanisms have been proposed to explain the initiation or inhibition of supershear ruptures. These include the material properties of the faulted rocks, complex stresses arising from the fault zone structure, and dynamic pressurization of fluids that fill the pores of rocks inside the fault zone (*14*). Field observations have largely failed to discriminate between these mechanisms and other effects during natural earthquakes. Precisely determining the location and timing of supershear initiation can help reduce this uncertainty but has proved to be difficult.

The inferred initiation location of the Sagaing Fault supershear rupture varied notably across the four studies. Xu *et al.* inferred an almost immediate transition to sustained supershear rupture, implicating the stress conditions near the location where the earthquake began (called the hypocenter). Goldberg *et al.* also suggested an early switch to supershear rupture, followed by a brief subshear interval, and then a second shift to sustained supershear. This series of transitions requires two separate initiation events, each with its own causes. Wei *et al.* determined that the fault rupture initiated at a point located almost 50 km farther south of the hypocenter that was used in Xu *et al.* and Goldberg *et al.* On the basis of this updated hypocenter, Wei *et al.* proposed a single transition to a supershear rupture later in time, suggesting a more important role for the conditions along a larger area of the fault. Latour *et al.* interpret subshear rupture at the camera location, supporting the late transition proposed by Wei *et al.* These disagreements are caused by a lack of near-fault observations, which are critical for pinpointing the hypocenter and tracking rupture behavior (*15*).

In Myanmar, a decade of political liberalization (2011 to 2021) allowed for rapid growth in local efforts to monitor seismic hazards and engineer buildings to withstand earthquakes. Observational networks were also greatly expanded through international collaborations, providing valuable data for earthquake research and providing a training ground for young scientists. After the return of military rule and the onset of civil war in 2021, most of this capacity has disappeared. Field observations, global positioning system (GPS) data, and near-field seismic recordings are thus largely absent for the 2025 Myanmar earthquake. History shows that the period of recovery and assessment after a large earthquake can spur coordinated efforts to reduce the risk of future disasters. This is when new investments in science, engineering, and policy can begin to improve resiliency over the long term. In Myanmar, this period is passing with little governmental action. Although the failed monitoring networks were a missed opportunity for science in 2025, a failed response could represent a far worse missed opportunity for Myanmar for decades to come. □

REFERENCES AND NOTES

1. D. E. Goldberg *et al.*, *Science* **390**, 458 (2025).
2. S. Latour *et al.*, *Science* **390**, 463 (2025).
3. S. Wei *et al.*, *Science* **390**, 468 (2025).
4. L. Xu *et al.*, *Science* **390**, 476 (2025).
5. R. Burridge, *Geophys. J. Int.* **35**, 439 (1973).
6. A. J. Rosakis, O. Samudrala, D. Coker, *Science* **284**, 1337 (1999).
7. R. J. Archuleta, *J. Geophys. Res.* **89**, 4559 (1984).
8. H. Bao *et al.*, *Nat. Geosci.* **15**, 942 (2022).
9. J. Atterholt, J. J. McGuire, A. J. Barbour, C. Stewart, M. P. Moschetti, *Science* **389**, 1361 (2025).
10. D. P. Robinson, S. Das, M. P. Searle, *Tectonophysics* **493**, 236 (2010).
11. Y. Wang, K. Sieh, S. T. Tun, K. Y. Lai, T. J. Myint, *J. Geophys. Res. Solid Earth* **119**, 3767 (2014).
12. S. G. Song, G. C. Beroza, P. Segall, *BSSA* **98**, 823 (2008).
13. V. Lambert, N. Lapusta, S. Perry, *Nature* **591**, 252 (2021).
14. P. Pampillón, D. Santillán, J. C. Mosquera, L. Cueto-Felgueroso, *Sci. Rep.* **13**, 398 (2023).
15. A. J. Rosakis, M. Abdelmeguid, A. Elbanna, *Nat. Geosci.* **18**, 534 (2025).

10.1126/science.aec0791

---

[1]Earthquake Insights, Ithaca, NY, USA. [2]Cornell University Department of Engineering, Ithaca, NY, USA. Email: geokyle@gmail.com

2025 MANDALAY EARTHQUAKE

RESEARCH ARTICLE

Ultralong, supershear rupture of the 2025 M_w 7.7 Mandalay earthquake reveals unaccounted risk

Dara E. Goldberg[1]*, William L. Yeck[1], Catherine E. Hanagan[2], James Atterholt[1], Haiyang Kehoe[1], Nadine G. Reitman[1], William D. Barnhart[3], David R. Shelly[1], Alexandra E. Hatem[1], David Wald[1], Paul S. Earle[1]

The 28 March 2025 moment magnitude (M_w) 7.7 earthquake in Mandalay, Burma (Myanmar), ruptured 475 kilometers of the Sagaing Fault, which was more than twice the length predicted by magnitude scaling relationships. Kinematic slip models and observation of a Rayleigh Mach wave that passed through parts of Thailand confirmed that rupture occurred at supershear velocities of greater than 5 kilometers per second. The anomalous length exposed a vast population to violent near-fault shaking. The Mandalay earthquake is a modern analog for the M_w 7.9 1906 San Francisco earthquake, another atypically long and fast rupture. Probabilistic seismic hazard analyses use scaling relations that do not account for such long ruptures at moderate magnitudes. This limitation, in conjunction with a likely increased population and infrastructure exposure for atypically long ruptures, contributes to a potential mischaracterization of seismic risk.

On 28 March 2025 at approximately 12:51 local time (6:21 UTC), a moment magnitude (M_w) 7.7 earthquake struck with an epicenter near Mandalay, Burma (Myanmar), the country's second largest city (Fig. 1). According to the US Geological Survey (USGS) community science reporting tool "Did You Feel It?" (DYFI) (*1*), the earthquake was felt in many neighboring countries and reached modified Mercalli intensity (MMI) X (extreme shaking) in near-fault regions. The USGS Prompt Assessment of Global Earthquakes for Response (PAGER) loss product (*2*) indicates that economic loss (estimated ~$53 billion) is likely to exceed the annual gross domestic product of Burma (Myanmar) and that fatalities likely exceeded 10,000, with 18.6 million people experiencing MMI VII (very strong) and stronger shaking (*3*). The earthquake was quickly attributed to the nearby Sagaing Fault, a documented fault capable of hosting large, damaging earthquakes [for example, (*4*, *5*)]. Established magnitude-rupture length scaling relations (*6*–*8*) indicate that the mean fault length of a M_w 7.7 strike-slip earthquake is less than 200 km. Empirical relations are central to earthquake hazard models (*9*) and are used to help estimate shaking intensities. Early DYFI reports of stronger-than-expected shaking and damage south toward Yangon and as far as Bangkok (more than 1000 km from the epicenter) suggested that the fault rupture extended farther than expected according to conventional magnitude-rupture length scaling relations. In the days after the 28 March 2025 earthquake, satellite imagery confirmed that the earthquake rupture extended ~475 km (Fig. 1). This anomalously long rupture inspires a reassessment of the physics of large strike-slip earthquakes and a reevaluation of the magnitude-rupture length scaling relationships used in seismic hazard models.

The Sagaing Fault

Burma (Myanmar) lies in a tectonically complex and seismically active region, straddling the India and Eurasia plates (Fig. 1). As the India plate moves northeastward, strain is partitioned with a right-lateral strike-slip component of faulting that is accommodated by the north-south-striking Sagaing Fault (Fig. 1). The Sagaing Fault is roughly 1400 km long and extends northward from the northern Andaman Sea to the Eastern Himalayan Syntaxis (*5*, *10*). The southern Sagaing Fault, the causative fault of the 28 March earthquake, accommodates about 24 mm/year of dextral motion (*4*). The seismogenic depth of the Sagaing Fault is inferred to be variable, generally between 10 and 20 km in depth (*4*, *11*). The Sagaing Fault has hosted many destructive earthquakes, including six magnitude (M) 7 or greater events since 1900. Additionally, a large-magnitude (~M 7.9) earthquake occurred in 1839 in approximately the same location as the 2025 event (Fig. 1) (*5*).

The central to southern Sagaing Fault is commonly subdivided into five along-strike segments (from north to south, the Sagaing, Meiktila, Nay Pyi Taw, Pyu, and Bago segments) (Fig. 1) (*5*). In 2021, interseismic geodetic velocity fields indicated that the northern two segments had accumulated enough slip to host M_w 7.3 and 7.4 earthquakes, respectively, whereas the southernmost segment (Bago) had accumulated the equivalent slip of a M_w 7.3 earthquake (*4*). No comparable interseismic observations were available at the time in the south-central Nay Pyi Taw and Pyu segments. The 2025 Mandalay earthquake spanned from the Sagaing to the Pyu segment and appears to have ruptured through, and beyond, a previously identified ~220-km-long seismic gap between Mandalay and Naw Pyi Daw that had not ruptured in more than a century (*5*).

Evidence for supershear rupture

Pixel tracking of Sentinel-2 optical imagery [supplementary materials (SM), materials and methods] illuminated ~475 km of continuous rupture along the Sagaing Fault from ~22.5°N to ~18.3°N (Fig. 2C), and USGS W-phase moment tensor analysis indicates an ~80-s source duration (37.5 s half duration) (*3*). This duration requires that the roughly 400 km of rupture south of the hypocenter occurred at speeds of ~5 km/s on average, exceeding the local shear-wave velocity. Robinson *et al.* (*12*) identified the Sagaing Fault as an earthquake "superhighway," one of about a dozen faults with long zones largely free from bends and stepovers that might slow or arrest rupture and could therefore allow for rupture speeds exceeding the upper-crustal shear wave speed (~3.5 km/s)—that is, supershear rupture [for example, (*13*, *14*)]. We investigated the details of the rupture process with kinematic rupture modeling of available teleseismic, regional accelerometer observations and the Sentinel-2 pixel tracking results (Fig. 2C).

The finite-fault modeling procedure (*15*) allows for variable rupture velocity and rise time (local rupture duration) throughout the fault, up to 6.5 km/s (SM, materials and methods). From our finite-fault model (Fig. 2), we calculated the approximate rupture velocity v_{rupt} as the distance to the hypocenter (d_{source}) divided by the sum of allowable onset time at each subfault (t_{onset}) and half the rise time (t_{rise}) (Fig. 3D)

$$v_{\mathrm{rupt}} = \frac{d_{\mathrm{source}}}{t_{\mathrm{onset}} + {}^{t_{\mathrm{rise}}}/_{2}} \tag{1}$$

The denominator of Eq. 1 is the time to peak moment release on the subfault, which we believe to be a more robust measurement than onset time alone because our modeling does not require slip to occur at the earliest allowable onset time. Therefore, our calculated rupture velocity is a minimum estimate of the true velocity of the rupture front. Furthermore, because we calculated average rupture velocity from the hypocenter, or location of rupture onset, instantaneous velocities would necessarily reach even greater values. Rupture propagated to the north

---

[1]US Geological Survey, Geologic Hazards Science Center, Golden, CO, USA. [2]US Geological Survey, Earthquake Science Center, Moffett Field, CA, USA. [3]US Geological Survey, Earthquake Hazards Program, Golden, CO, USA. ***Corresponding author. Email: degoldberg@usgs.gov**

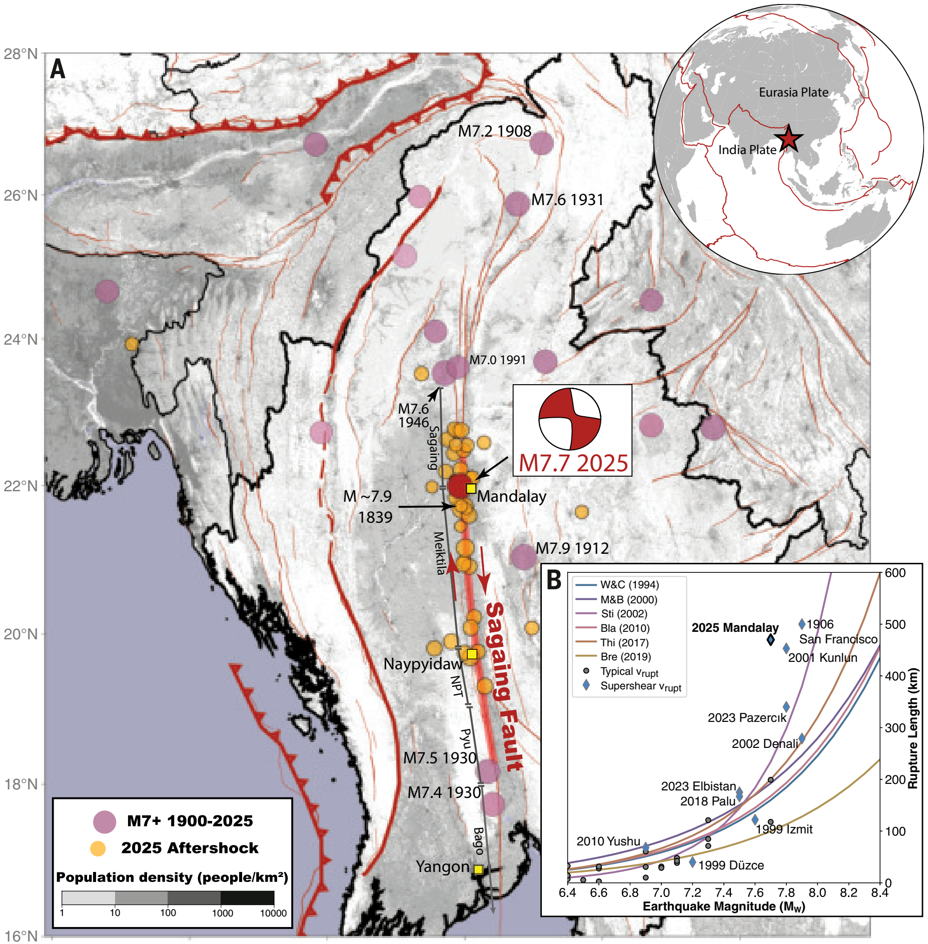

Fig. 1. Tectonic overview and earthquake length scaling. (**A**) Historic M 7 or greater seismicity dating back to 1900 is shown as pink circles. An 1839 earthquake (estimated M ~7.9) is shown at nearly the same location of the 2025 M_w 7.7 earthquake (red circle and red W-phase centroid moment tensor). The ~475-km-long rupture length of the 2025 mainshock is indicated in red along the Sagaing Fault. Aftershocks of the 2025 mainshock are indicated with orange circles. The populous cities of Mandalay, Naypyidaw, and Yangon are indicated with yellow squares. Major tectonic boundaries are indicated in dark red, with smaller mapped faults as thin red lines (*29*). Labeled gray lines indicate the approximate bounds of the five segments of the southern Sagaing Fault. The basemap shows population density (*30*). (Inset) Major tectonic boundaries as red lines, with the location of the 2025 M_w 7.7 earthquake indicated with the red star. (**B**) Comparison of fault rupture lengths from ruptures known to have any period of supershear rupture (blue diamonds) and sub- to shear-velocity ruptures (gray circles) (*31*–*33*) with common earthquake scaling relationships for continental strike slip faults. W&C (1994), M&B (2000), Sti (2002), Bla (2010), Thi (2017), and Bre (2019) refer to (*6*), (*22*), (*23*), (*7*), (*24*), and (*8*), respectively.

largely at subshear-wave velocities (Fig. 3D); however, the rupture front in the southern propagation direction quickly reached supershear speeds of at least 5 km/s before briefly slowing to shear speeds (~3.5 km/s) about 100 km south of the epicenter. From there, supershear velocities resumed until ~325 km south of the epicenter before decreasing to roughly shear wave speeds beyond 330 km south of the epicenter (Fig. 3D). The modeled source-time function determined the rupture duration to be ~85 s, with later moment attributed to fitting waveform noise (Fig. 2B). Because we calculated a lower bound on the maximum rupture speed, some areas indicate rupture velocity in excess of the Eshelby speed (~5.0 km/s for a shear wave velocity of 3.5 km/s). Our model indicates that more than 53% of the seismic moment of this earthquake occurred before the arrival of the shear wave from the hypocenter; south of the hypocenter, this fraction was more than 68%.

Numerical modeling suggests that supershear rupture can result from vertically polarized shear wave (SV) to P-diffracted wave conversions at the free surface (*16*). This mechanism leads to rupture velocities that are greatest near the surface, despite crustal seismic velocities being lesser near the surface than at depth. As shown in Fig. 2A, we observed this effect prominently in our rupture model, with the shallow rupture front persistently preceding deeper rupture during supershear propagation south of the hypocenter. This effect may also lead to surface-slip displacements that are larger than slip at depth, in contrast to a coseismic shallow slip deficit that is commonly observed in earthquake ruptures (*17*). This pattern can be observed in Fig. 3A, in which measured surface rupture (*18*) and modeled shallow slip exceeds slip at medium depths in places where rupture speeds are high, particularly between 110 and 200 km south of the hypocenter and again between 250 and 350 km south of the hypocenter. Still, slip at medium depth exceeds shallower slip at the north end of rupture, where subshear to shear-velocity rupture occurred. Generally, measured surface rupture and modeled shallow (<7 km) slip follow similar trends, which provides confidence in the model. Perfect correlation between the two is not expected because of the model's depth-averaging of slip over each subfault, model smoothing, and the lack of guarantee that the surface slip displacements are fully coseismic.

Our modeling of supershear rupture is confirmed by direct observation of a Rayleigh Mach wave, which is analogous to the sonic boom generated by objects that exceed the speed of sound in the atmosphere (SM, materials and methods). Theory predicts that surface waves from all sections of a supershear segment will constructively interfere in Mach cones, the angle of which is dependent on the supershear rupture velocity and the Rayleigh wave phase velocity (*19*). This interference results in surface waves that lack the complexity typically observed for large earthquakes, which would be considered as line sources. At these azimuths, surface-wave waveforms of the mainshock instead match scaled waveforms of smaller aftershocks that can be considered as point sources. By comparing the distribution of Rayleigh waves generated by the mainshock with those of multiple large aftershocks (*20*, SM, materials and methods), we confirmed the presence of a Rayleigh Mach wave (Fig. 4).

Areas of faults that undergo supershear rupture often have a dearth of aftershocks, with aftershocks preferentially occurring on adjacent structures or in subshear velocity portions of the fault (*21*). For the first 16 days after the rupture, we observed a paucity of aftershocks in supershear zones (Fig. 3C). We included earthquakes located within 20 km of the rupture trace, with the understanding that more precise relocations might confirm these to be on the same fault as that of the main rupture. We found denser aftershock cluster along the Sagaing Fault in the epicentral region and northward, the region that experienced subshear velocity rupture, as compared with south of the epicenter, where rupture reached supershear velocities. A small cluster of four aftershocks between ~90 and 130 km south of the epicenter

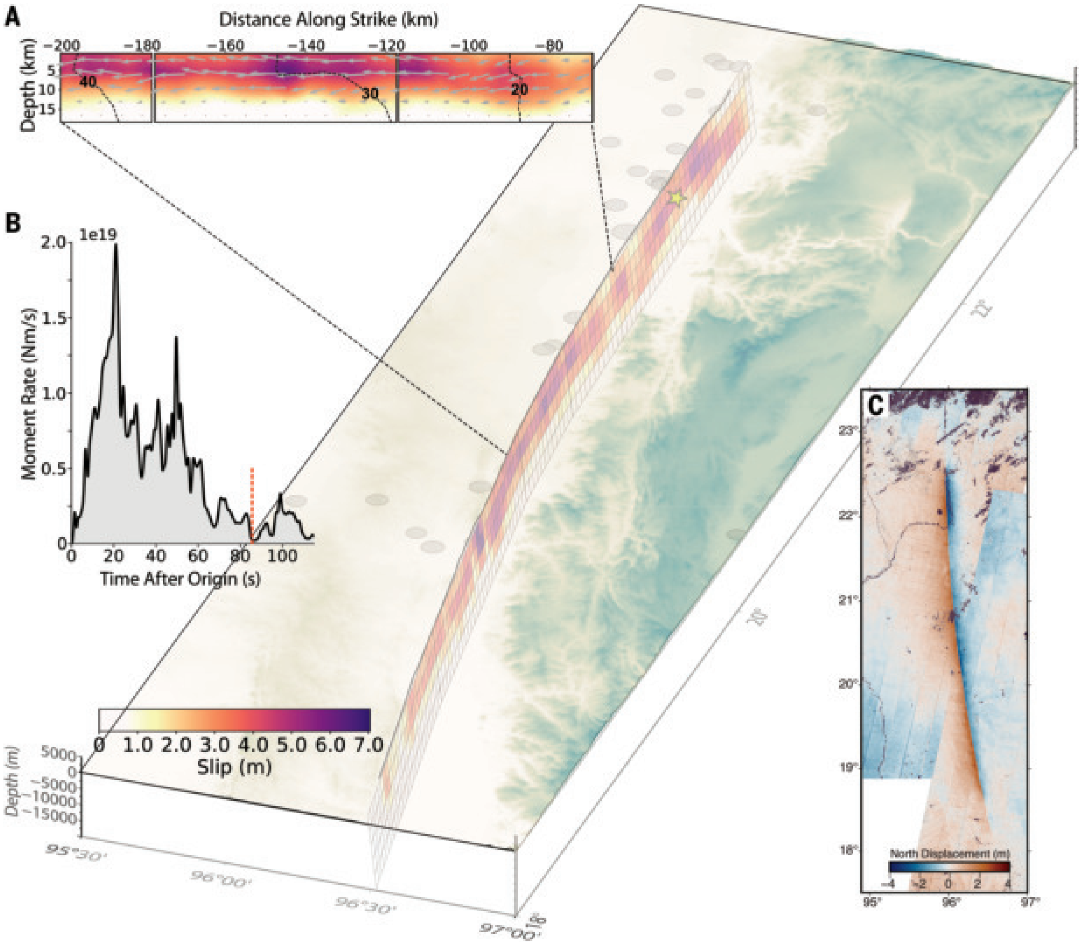

Fig. 2. Finite-fault model. Perspective view of the four-segment discretized fault plane is shown to align with a simplified fault trace (black line). The yellow star indicates the hypocenter location. Aftershock locations are indicated with gray circles. The color bar denotes amplitude of slip. Basemap topography is from (*34*). (**A**) Selected portion of the rupture shown in fault-perpendicular view, with slip smoothed across subfaults. Color indicates slip amplitude as on the central image. Gray arrows indicate the rake direction, scaled by amplitude of slip. Black dashed lines indicate the rupture onset time, labeled in increments of 10 s from 20 to 40 s after origin time. (**B**) The source time function, with slip after 85 s (dashed red line) attributed to fitting waveform noise. (**C**) Pixel-tracking displacements in the north-south direction (primary direction of motion) from Sentinel-2 orbit 46. Positive displacements (red) indicate northward motion; negative displacements (blue) indicate southward motion. Model fits to teleseismic body waves, teleseismic surface waves, local strong-motion accelerometer observations, and Sentinel-2 optical pixel tracking displacements are available in figs. S2, S3, S4, and S5 to S8, respectively.

(Fig. 3C) potentially corresponds to a small region of slower rupture velocity seen in the finite-fault results in the same region (Fig. 3D).

Is the Mandalay rupture anomalous?

The Mandalay earthquake stands out among continental strike slip earthquakes with well-documented rupture lengths (Fig. 1B). The earthquake exhibited one of the longest documented surface ruptures. With respect to earthquake scaling relationships (*6–8*, *22–24*), the Mandalay earthquake is a clear outlier among continental ruptures, comparable only with the ~450-km-long 2001 M_w 7.8 Kunlun and the ~500-km-long 1906 M_w 7.9 San Francisco earthquakes (Fig. 1B). Most other documented supershear ruptures do not strongly deviate from published magnitude-length scaling relationships (Fig. 1B). Moreover, our conservative estimate that ~65% of the southern moment release occurred during supershear rupture indicates that this rupture velocity was sustained in a manner not typical of other documented supershear ruptures. Thus, the extreme length of the Mandalay earthquake is likely related to the persistence of supershear rupture throughout the earthquake. The sustained high rupture velocities allowed the earthquake to propagate over a longer distance as compared with that of other M 7 or greater earthquakes, thus increasing exposure of population centers along the Sagaing Fault to near-source strong shaking. USGS PAGER reports based on a ~200-km-long rupture (the expected rupture length from scaling relationships) indicated that ~7.7 million people were exposed to MMI VII (very strong) and stronger shaking (PAGER version 6) (*3*). This exposure more than doubled to 18.6 million people when the underlying shaking model included the full 475-km-long rupture (PAGER version 22) (*3*). As an example, the city of Nay Pyi Taw (population ~925,000) was expected to experience strong shaking for a ~200-km-long rupture, with moderate damage to vulnerable structures but light damage to resistant structures (PAGER version 6). By the time the full extent of rupture was understood, Nay Pyi Taw was expected to have experienced violent shaking, accompanied by heavy damage to even resistant structures (PAGER version 22).

Seismic hazard considerations for continental strike-slip fault systems

Satellite imagery indicates that the Mandalay earthquake ruptured the Sagaing, Meiktila, and Nay Pyi Taw fault segments and at least partially ruptured the Pyu segment. On the basis of the earthquake magnitude (M_w 7.7) and previous estimates of accumulated slip (*4*), we can surmise that the Nay Pyi Taw and Pyu segments together stored the interseismic moment of a ~M_w 7.4 earthquake. However, in absence of interseismic strain accumulation estimates in these segments, we cannot discern whether the 2025 earthquake fully or partially ruptured these segments. Because the Bago segment was unruptured in this earthquake, previously reported strain conditions of this segment may remain (*4*).

The longer-than-expected rupture length observed in the 2025 Mandalay earthquake has important implications for probabilistic seismic hazard analysis and impact assessment. Analysis based on established scaling relationships [for example, (*6*)], reported by Wang *et al.* (*5*) determined that the ~220-km-long Meiktila and ~180-km-long Sagaing sections of the Sagaing Fault could host earthquakes of M_w 7.9 and M_w 7.7, respectively, but their combined rupture (totaling ~400 km) could generate a M_w 8.1 to 8.3 earthquake. These authors suggested that return times of such earthquakes would be on the order of 500 to 1000 years. However, the 2025 event ruptured ~475 km [equivalent to more than three fault sections, as defined by Wang *et al.* (*5*)] and did so with a much smaller total seismic moment, equivalent to M_w 7.7. Although a M_w 7.7 may be less damaging than a potential M_w 8 or greater event over the same area, the shorter recurrence interval of smaller events may make these lesser-magnitude events more influential in the magnitude-frequency relationships used in probabilistic seismic hazard analyses.

The Mandalay earthquake is an important analog for other major earthquakes, such as the 1906 M_w 7.9 San Francisco earthquake (*25*, *26*). California's San Andreas Fault system, which hosted the 1906 earthquake, is tectonically similar to the Sagaing Fault; both are

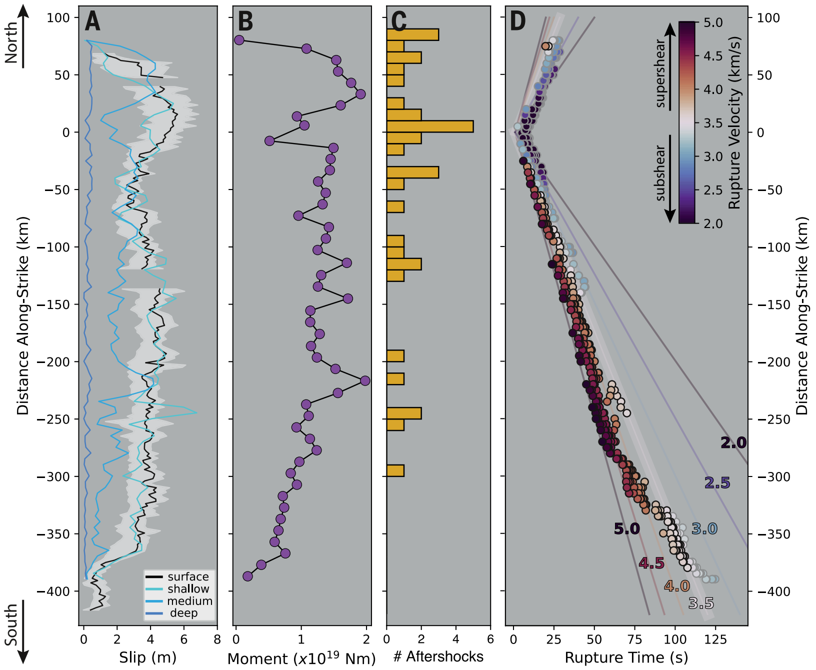

Fig. 3. Fault slip and approximate rupture velocity. (**A**) Slip as a function of depth. Surface slip was measured from satellite observations (*18*), where the light gray area indicates the range of minimum to maximum estimated surface slip, with the average value indicated in black. Modeled shallow (<7 km), medium (7 to 16 km), and deep (>16 km) slip are indicated with shades of blue. (**B**) Moment along-strike, as indicated by the finite fault model solution. Circles indicate measurement in 10-km bins along-strike, connected with black lines for visual clarity. (**C**) Histogram of aftershocks, within 16 days and 20 km of the fault, along-strike. (**D**) Rupture time versus distance along-strike for each subfault (circles) in the finite fault model. Each point is colored by the average rupture velocity from the hypocenter (Eq. 1). Colored lines indicate different rupture velocities, with 3.5 km/s indicated with a thicker line to emphasize the approximate shear wave velocity.

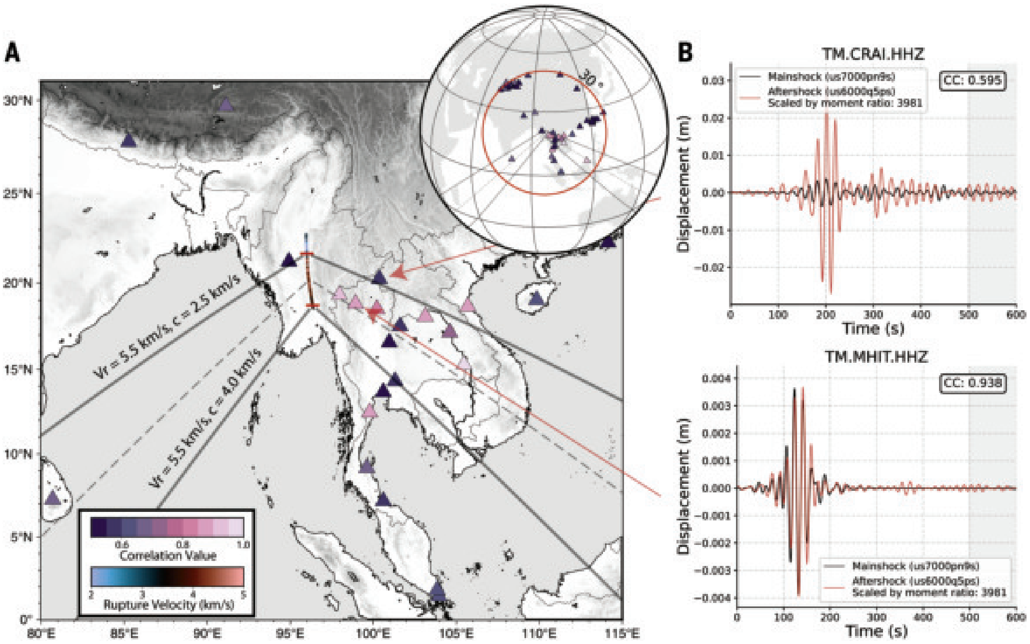

Fig. 4. Mach wave analysis. (**A**) Map view of study region with fault colored by surface rupture velocity. Basemap topography is from (*34*). The Rayleigh Mach wave angles assuming phase velocities (c) of 2.5 and 4.0 km/s and a rupture velocity (V_r) of 5.5 km/s are indicated with gray lines. The top and bottom of the supershear rupture are indicated with red lines. Broadband seismic stations are indicated with triangles, colored by the waveform average correlation value (CC) with the selected aftershock. (Inset) A larger view of the seismic stations considered, on the same color scale. (**B**) Example waveforms from stations (top) TM.CRAI and (bottom) TM.MHIT. At station TM.CRAI, outside the Rayleigh Mach wave regions, mainshock waveforms (black) have low correlation with the lesser-magnitude event (red). Station TM.MHIT, in the Mach region, has high correlation. Aftershock waveforms (red) are scaled by 3981, derived from the moment ratio of the mainshock to aftershock. USGS event page identification numbers for the mainshock and aftershocks are shown parenthetically in the legends.

right-lateral, geometrically simple continental faults capable of hosting M 8 or greater earthquakes. The 1906 earthquake produced a similar anomalously long surface rupture (~500 km) (Fig. 1B) (*25*, *26*) where earthquake scaling relationships predicted a ~220-km-long rupture. The 1906 earthquake additionally likely ruptured with sustained supershear velocities north of San Francisco (*26*).

The San Andreas Fault also shares societal similarities to the Sagaing Fault. Both pierce major cities with large populations and critical infrastructure. Earthquake rupture forecasts for the San Andreas Fault generally follow common magnitude scaling laws (*27*); these scaling laws are used with a single prescribed seismogenic width, which likely limits the occurrence of extremely long (high aspect ratio) ruptures such as the 2025 Mandalay earthquake. Of the $\leq$1-million-year recurrence interval right-lateral ruptures of M_w 7.65 to 7.75 considered in the USGS National Seismic Hazard Model 2023, the longest rupture is 382 km long (*28*), which is nearly 100 km shorter than the 2025 Myanmar rupture.

However, as more supershear ruptures are identified with associated atypical source characteristics, it becomes clear that seismic hazard analyses may be incomplete without these outlier events. Although we do not speculate here on the net effect that such outlier events have on overall modeled seismic hazard, the larger exposure area of an outlier event could potentially lead to a broader economic and humanitarian impact because of the quantity of affected infrastructure and population. The 2025 Mandalay earthquake affected multiple populous cities simultaneously, highlighting that the exposure area of lesser-magnitude, sustained supershear ruptures can be comparable with that of an average, greater-magnitude event. Because lesser-magnitude events are more frequent than their greater-magnitude counterparts, quantifying the probability of anomalously long, lesser-magnitude events is critical for constraining overall risk. The range of impacts estimated by the USGS PAGER system, which varied as a function of inferred rupture length, underscores the continued need for resources to rapidly estimate the true and full extent of earthquake shaking to support efficient and effective humanitarian relief.

REFERENCES AND NOTES

1. D. J. Wald, V. Quitoriano, C. B. Worden, M. Hopper, J. W. Dewey, *Ann. Geophys.* **54**, 5 (2012).
2. D. J. Wald, K. S. Jaiswal, K. D. Marano, D. B. Bausch, M. G. Hearne, *U.S. Geol. Surv. Fact Sheet* **2011**, 2010–2036 (2011).
3. M. G. Hearne, libcomcat, version 2.1.7. *US Geological Survey software release* (2025); https://doi.org/10.5066/P91WN1UQ.
4. T. Z. H. Tin *et al.*, *J. Asian Earth Sci.* **228**, 105125 (2022).
5. Y. Wang, K. Sieh, S. T. Tun, K. Y. Lai, T. Myint, *J. Geophys. Res. Solid Earth* **119**, 3767–3822 (2014).
6. D. L. Wells, K. J. Coppersmith, *Bull. Seismol. Soc. Am.* **84**, 974–1002 (1994).
7. L. Blaser, F. Krüger, M. Ohrnberger, F. Scherbaum, *Bull. Seismol. Soc. Am.* **100**, 2914–2926 (2010).
8. C. M. Brengman, W. D. Barnhart, E. H. Mankin, C. N. Miller, *Bull. Seismol. Soc. Am.* **109**, 1701–1715 (2019).
9. M. D. Petersen *et al.*, *Earthq. Spectra* **40**, 5–88 (2024).
10. C. T. Mon *et al.*, *Geophys. Res. Lett.* **47**, e2019GL086236 (2020).
11. W. Fadil *et al.*, *Bull. Seismol. Soc. Am.* **113**, 613–635 (2023).
12. D. P. Robinson, S. Das, M. P. Searle, *Tectonophysics* **493**, 236–243 (2010).
13. A. Socquet, J. Hollingsworth, E. Pathier, M. Bouchon, *Nat. Geosci.* **12**, 192–199 (2019).
14. H. Bao *et al.*, *Nat. Geosci.* **12**, 200–205 (2019).
15. P. Koch *et al.*, Wavelet Inversion for Slip (WISP), version 1.1.0. US Geological Survey software release (2025); https://doi.org/10.5066/P14RVF65.
16. Y. Kaneko, N. Lapusta, *Tectonophysics* **493**, 272–284 (2010).
17. J. M. Nevitt *et al.*, *Sci. Rep.* **10**, 5031 (2020).
18. N. G. Reitman *et al.*, Remote surface rupture observations for the M7.7 2025 Mandalay, Burma (Myanmar) earthquake. US Geological Survey data release (2025); https://doi.org/10.5066/P1RYMWCK.
19. M. Vallée, E. M. Dunham, *Geophys. Res. Lett.* **39**, 2011GL050725 (2012).
20. W. L. Yeck, neic-supershear-analysis, version 1.0.0. US Geological Survey software release (2025); https://doi.org/10.5066/P1BQPVIV.
21. M. Bouchon, H. Karabulut, *Science* **320**, 1323–1325 (2008).
22. P. M. Mai, G. C. Beroza, *Bull. Seismol. Soc. Am.* **90**, 604–615 (2000).
23. M. Stirling, D. Rhoades, K. Berryman, *Bull. Seismol. Soc. Am.* **92**, 812–830 (2002).
24. K. K. S. Thingbaijam, P. M. Mai, K. Goda, *Bull. Seismol. Soc. Am.* **107**, 2225–2246 (2017).
25. W. Thatcher, G. Marshall, M. Lisowski, *J. Geophys. Res.* **102** (B3), 5353–5367 (1997).
26. S. G. Song, G. C. Beroza, P. Segall, *Bull. Seismol. Soc. Am.* **98**, 823–831 (2008).
27. B. E. Shaw, *Bull. Seismol. Soc. Am.* **113**, 924–947 (2023).
28. E. H. Field *et al.*, *Bull. Seismol. Soc. Am.* **114**, 523–571 (2023).
29. E. Zelenin, D. Bachmanov, S. Garipova, V. Trifonov, A. Kozhurin, *Earth Syst. Sci. Data* **14**, 4489–4503 (2022).
30. V. Lebakula *et al.*, *Sci. Data* **12**, 495 (2025).
31. A. Sarmiento *et al.*, Flatfiles and related digital products for the fault displacement hazard initiative database, version 1. UCLA Dataverse (2024); https://doi.org/10.25346/S6/Y4F9LJ.
32. H. Bao *et al.*, *Nat. Geosci.* **15**, 942–949 (2022).
33. M. Abdelmeguid *et al.*, *Commun. Earth Environ.* **4**, 456 (2023).
34. B. Tozer *et al.*, *Earth Space Sci.* **6**, 1847–1864 (2019).

ACKNOWLEDGMENTS

We thank the USGS National Earthquake Information Center (NEIC) 24/7 Duty Seismologists who are critical to the USGS NEIC's global earthquake monitoring. We also acknowledge R. Briggs, W. Mooney, R. Gold, B. Shiro, K. Marra, A. Hesser, and three anonymous reviewers for their valuable comments. **Funding:** The US Geological Survey Earthquake Hazards Program supported this work. **Author contributions:** Conceptualization: D.E.G., W.L.Y., W.D.B., D.R.S., P.S.E. Methodology: D.E.G., W.L.Y., C.E.H., J.A., H.K., N.G.R., W.D.B. Investigation: D.E.G., W.L.Y., C.E.H., J.A., H.K., N.G.R., W.D.B., D.R.S., A.E.H., P.S.E., D.W. Visualization: D.E.G., W.L.Y., W.D.B. Writing – original draft: D.E.G., W.L.Y., C.E.H., J.A., H.K., N.G.R., W.D.B., D.R.S., A.E.H., P.S.E., D.W. Writing – review & editing: D.E.G., W.L.Y., C.E.H., J.A., H.K., N.G.R., W.D.B., D.R.S., A.E.H., P.S.E., D.W. **Competing interests:** The authors declare that they have no competing interests. **Data and materials availability:** The USGS event webpage contains up-to-date information of USGS event characterization (https://earthquake.usgs.gov/earthquakes/eventpage/us7000pn9s/executive), including origin information, moment tensor modeling, finite-fault modeling, DYFI, and PAGER. Earlier versions of these products (for example, PAGER) can be accessed using libcomcat (*3*). The facilities of EarthScope Consortium were used for access to waveforms and related metadata for modeling performed outside of NEIC's real-time system (*4*). These services are funded through the Seismological Facility for the Advancement of Geoscience (SAGE) Award of the National Science Foundation under Cooperative Support Agreement EAR-1851048. Sentinel-2 observations are Copernicus Sentinel data processed by the European Space Agency (ESA). The finite fault modeling software is available at https://doi.org/10.5066/P14RVF65 (*15*). The Mach wave detection software is available at https://doi.org/10.5066/P1BQPVIV (*20*), A tagged version of this Mach wave software used can be found at https://code.usgs.gov/ghsc/neic/research/neic-supershear-analysis/-/tags/version_in_publication. Any use of trade, firm, or product names is for descriptive purposes only and does not imply endorsement by the US government.

SUPPLEMENTARY MATERIALS

science.org/doi/10.1126/science.ady3581
Materials and Methods; Figs. S1 to S8; References (*35–44*)

Submitted 18 April 2025; resubmitted 16 June 2025; accepted 19 August 2025

10.1126/science.ady3581

2025 MANDALAY EARTHQUAKE

RESEARCH ARTICLE

Direct estimation of earthquake source properties from a single CCTV camera

Soumaya Latour[1]†, Mathias Lebihain[2], Harsha S. Bhat[3], Cédric Twardzik[4], Quentin Bletery[4], Kenneth W. Hudnut[5], François Passelègue[4]*†

We present a direct measurement of the slip-rate function from a natural coseismic rupture, recorded on 28 March 2025, during the moment magnitude (M_w) 7.7 Mandalay earthquake (Myanmar). This measurement was made using video footage of the surface rupture captured by a closed-circuit television (CCTV) security camera located only meters away from the fault trace. Using direct image analysis, we measured the relative slip at each time step and deduced the slip rate. Our results show a local slip duration of 1.4 seconds and a cumulative slip of ~3 meters, during which surface slip velocity peaked at ~3.5 meters per second with passage of the rupture front. These findings demonstrate the pulse-like nature of the seismic rupture at the location of the recording. Using slip-pulse elastodynamic rupture models, we obtained the complete mechanical properties of this pulse, including the energy release rate.

Estimating the spatial and temporal evolution of slip along fault interfaces is critical for understanding the physics of deformation processes in Earth's crust throughout the seismic cycle (*1*). Because slip typically occurs at depth under extreme conditions, direct in situ observations are, in most cases, impossible. Reconstructions of slip history rely on inverse modeling (*2*). Consequently, our understanding of earthquake physics is fundamentally limited by the resolution and coverage of the data used in these inversions, as well as the inherent complexity of the forward problem (*3*–*6*). As a result, many key aspects of earthquake rupture, particularly the local dynamics of slip and the associated stress evolution at the fault interface, remain poorly constrained.

On 28 March 2025, a devastating moment magnitude (M_w) 7.7 earthquake struck Myanmar along the Sagaing fault (*7*) near Mandalay. The earthquake caused catastrophic damage: more than 5400 fatalities, >11,000 injuries, and hundreds to thousands reported missing. Infrastructure losses included 120,000 homes, 2500 schools, numerous temples, and key transportation networks such as bridges and airports. Several historic sites, particularly in Inwa, suffered extensive damage. This right-lateral strike-slip event ruptured more than 450 km of the fault, with slip reaching the surface on long segments and horizontal displacements up to 6 m [Fig. 1A; (*8*)]. The moment source function derived from the US Geological Survey (USGS) (*9*) indicates that the rupture propagation lasted ~120 s (Fig. 1B), in agreement with the SCARDEC solution (*10*), and likely included supershear phases (*11*).

Beyond its societal impact, the earthquake offered an unprecedented scientific opportunity: For the first time, a closed-circuit television (CCTV) security camera located just meters from the surface rupture captured the real-time deformation of the ground during seismic faulting (*12*). This footage provides a direct observation of coseismic surface displacement, enabling us to extract the time history of slip and slip rate at a specific fault point, measurements that, until now, were only accessible through laboratory experiments or inferred indirectly through modeling. In this study, we analyzed the footage to obtain a direct measurement of the slip-rate function during a natural earthquake (*13*) and, additionally, to invert the evolution of shear stress, energy dissipation (breakdown work), and rupture dynamics. Our results provide ground-truth constraints on seismic rupture physics, offering a critical benchmark for validating numerical models and seismic inversions and helping to close a long-standing observational gap in earthquake science.

Measurement of local slip rate during the earthquake

The camera was positioned on the east side of the fault and was approximately oriented in the southwest direction. To estimate the local slip rate, we tracked distinct visual landmarks located on both sides of the fault (Fig. 2A). The primary landmark was a concrete or metallic pillar (*R*0) located on the west side of the fault; two additional landmarks, *R*1 and *R*2, were small poles located adjacent to a road and behind a fence composed of vertical bars. Throughout the video, these features display predominantly horizontal motion relative to the foreground, consistent with right-lateral strike-slip faulting.

To quantify this motion, we defined two fault-parallel lines intersecting the vertical landmarks (Fig. 2A) and tracked the pixel intensity along these lines over the entire duration of the observable rupture propagation (Fig. 2, B to E). We defined $t = 0$ s as the approximate onset of fault slip [corresponding to the time stamp 12:46:34.633 of the video and not synchronized to universal time coordinated (UTC)]. Ground shaking began at $t = -4.5$ s, which is evident as coherent motion across the frame due to camera motion. A secondary seismic phase was observed at approximately $t = -1.8$ s. The onset of fault slip was identified as the moment when the tracked landmarks began to move relative to nearby, foreground features. This relative motion continued until approximately $t = 1.6$ s (Fig. 2C).

For each landmark, we selected a nearby visually stable reference point on the east side of the fault, as shown in Fig. 2A: *R*0′ (a vertical wall) and *R*1′ and *R*2′ (vertical bars of the fence). We tracked the motion of both the landmark and its corresponding reference feature over time (Fig. 2, C and E). The difference in their pixel positions provided a measure of relative displacement that was corrected for camera motion. We determined the temporal and spatial resolutions using the method described in the supplementary materials (fig. S1), and we applied a spatial scaling using an estimate of the final slip. This approach yielded a temporal resolution of 0.033 s and a spatial resolution with a relative uncertainty of approximately ±20%.

The slip history derived from the three measurements is shown in Fig. 3A. The curve obtained from *R*0 provides the most reliable estimate, as both the onset and arrest of motion were clearly visible in the video. The timing and slope of estimates from *R*1 and *R*2 are consistent with that of *R*0. The slip increased smoothly from 0 to 3 m over ~1.4 s, after which it ceased. We obtained the slip-rate function (Fig. 3B) by numerically differentiating the slip history after resampling it at 90 Hz. We then applied a moving average with a 0.33-s time window, as we interpreted the oscillations in the raw curve to result from uncertainties in manual tracking and camera-motion correction. The slip-rate function is slightly asymmetric: The slip rate rose rapidly from 0 to 3.5 m s^{-1} within 0.6 s, then decreased more gradually to 0 m s^{-1} over ~1 s. These values correspond to an average slip acceleration of 5.8 m s^{-2} and a slip deceleration of 3.5 m s^{-2}.

The total slip duration is best estimated using the rise time of the slip function, as the smoothing applied during signal processing tends to artificially broaden the slip-rate pulse. The most robust estimate of

---

[1] Université de Toulouse, CNRS, Observatoire Midi-Pyrénées, IRAP, Toulouse, France. [2] Navier, ENPC, Institut Polytechnique de Paris, Université Gustave Eiffel, CNRS, Marne-la-Vallée, France. [3] Laboratoire de Géologie, École Normale Supérieure, CNRS, UMR 8538, PSL Université, Paris, France. [4] Université Côte d'Azur, CNRS, Observatoire de la Côte d'Azur, IRD, Géoazur, Sophia Antipolis, France. [5] Southern California Edison, Rosemead, CA, USA. ***Corresponding author. Email: francois.passelegue@cnrs.fr** †These authors contributed equally to this work.

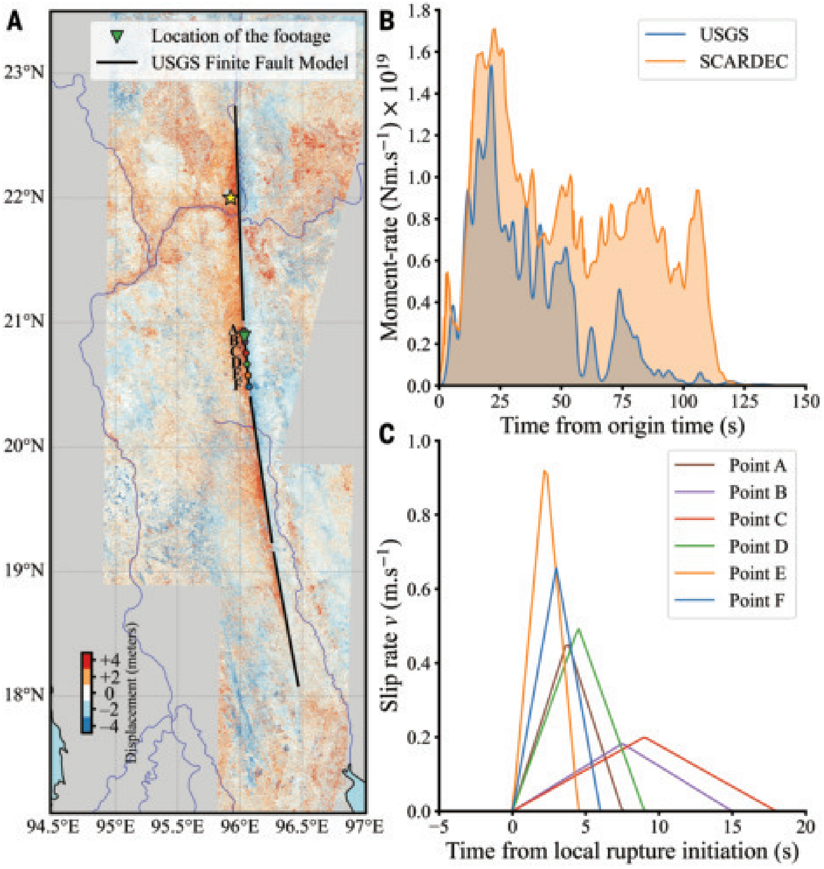

Fig. 1. Displacement field, moment-rate functions, and local slip-rate functions for the 2025 Mandalay earthquake. (**A**) North-south displacement field derived from the subpixel correlation of Sentinel-2 optical imagery. The yellow star indicates the location of the epicenter, and the green triangle marks the location of the footage, as given in the YouTube video description. The black lines show the surface trace of the finite fault model obtained from the USGS. Dots labeled A to F show the locations of the shallowest subfaults of the USGS finite fault model, which were used to extract the local slip-rate functions shown in (C). (**B**) Moment-rate functions from the USGS and SCARDEC. (**C**) Local slip-rate functions derived from the USGS finite fault model. This was only done for the shallowest subfaults of the segment highlighted in (A). Note that we use a triangular function to display the local slip-rate function instead of the asymmetric cosine function used by the USGS kinematic inversion.

slip duration is $\Delta t = 1.4$ s (Fig. 3A), independent of any assumptions related to spatial scaling. By contrast, our estimates of total and intermediate slip must consider a relative uncertainty of approximately ±20% in the spatial scaling factor. The uncertainty in total slip also affects absolute values of the slip rate.

Duration and shape of the slip-rate function

Our results highlight the much shorter local slip duration (1.4 s) compared with the total rupture duration of 100 to 120 s (Fig. 1B). This clearly shows that the rupture had a pulse-like nature, also called a self-healing pulse, at least at the surface along this segment of the fault. Self-healing pulses have long been identified as a possible mode of earthquake rupture (*14*). Indeed, pulse-like behavior appears to be a fairly common feature of rupture models for large earthquakes (*15*, *16*). The origin of this pulse-like behavior can be attributed to (i) the elongated geometry of the rupture or (ii) the structure of the fault damage zone (*17*). In the case of the Mandalay earthquake, the rupture was expected to have quickly saturated the seismogenic width, resulting in a large length-to-width ratio at the footage location. Under these conditions, it is expected that a pulse-like rupture would emerge naturally (*18*, *19*). However, alternative slip-healing mechanisms may also account for the short 1.4-s slip duration observed here. In particular, thermal pressurization of pore fluids within a thin gouge layer can induce rapid restrengthening behind the rupture tip. Using representative values for hydrothermal diffusivity ($\alpha = 10^{-4}$ to 10^{-6} m^2 s^{-1}) and a gouge thickness h ranging from 10^{-2} to 10^{-3} m (*20*, *21*), the expected slip duration scales to $\Delta t \approx h^2/\alpha \approx$ 1 s (*22*), consistent with our observations. This mechanism does not rely on rupture aspect ratio and could explain the relatively small pulse width compared with the total rupture depth. Our results, however, are agnostic to various healing mechanisms simply because of the lack of additional in situ physical measurements.

The slip-rate values are consistent with the coseismic slip rates expected during large earthquakes. Particle velocity in the vicinity of the fault was predicted to be capable of reaching several meters per second for self-healing pulse ruptures (*14*). Note that our direct measurements of the fault slip rate are much higher than those estimated from inverted teleseismic data (*9*), which indicated a peak slip rate on the order of 0.2 m s^{-1} at the footage location (Fig. 1C). In addition, the recorded duration of local slip is much shorter than the inverted estimate: 1.4 s compared with ≈16 s for the USGS kinematic model. However, it is well known that modeling the rupture process involves substantial uncertainty (*6*, *23*). Indeed, the inverted slip duration just 10 km north of the footage location is much shorter (~6 s), and the peak slip rate is higher (0.45 m s^{-1}) (Fig. 1C). This discrepancy underscores the value of direct observation of slip during a natural earthquake as an empirical benchmark for validating and refining seismic source models of large earthquakes.

The shape of the slip-rate function is a key parameter in kinematic slip models (*24*) and plays an important role in ground motion prediction (*25*). In this study, the smoothed slip-rate function exhibits a simple form that can be described as an asymmetric triangle, with the duration of the acceleration phase being ~60% that of the deceleration phase. A similarly smooth, asymmetric, and triangular slip-rate function has been observed in friction experiments involving self-healing slip pulses propagating at 0.76 times the Rayleigh wave speed (*26*).

An analytical form of the slip-rate function was proposed for mode III self-healing pulses (*27*). This form, sometimes referred to as the Yoffe function, is characterized by an infinitely steep onset, a sharply peaked maximum, and a long tail with a variable slope. Although the Yoffe function qualitatively captures the asymmetry observed in our data, its overall shape is more peaked and strongly asymmetric. A regularized version of the Yoffe function, derived from dynamic rupture models (*28*), more closely resembles the slip-rate function observed in our measurements, though it still exhibits greater asymmetry.

Estimate of dynamic source parameters from the fault slip rate

We applied the elastodynamic equilibrium condition to infer the evolution of shear stress from a slip-based model. Assuming a two-dimensional plane strain shear (mode II) rupture propagating at a constant sub-Rayleigh rupture velocity V_r along the fault, the shear stress $\tau(x)$ is related to the spatial distribution of slip rate $v(x)$ through the singular integral equation (*22*, *29*, *30*)

$$\tau(x) = \tau_0 - \frac{\bar{\mu}}{2\pi V_r} PV \int_0^L \frac{v(\xi)}{x - \xi} \mathrm{d}\xi \tag{1}$$

where τ_0 is the background stress; $\bar{\mu}$ is a scaled shear modulus, which depends on the rupture velocity V_r; x is the distance to the rupture tip; $L = V_r\Delta t$ is the length of the slip pulse, which defines the spatial extent of the actively slipping region; ξ is the integration variable; and *PV* denotes the Cauchy principal value of the integral.

To compute the shear-stress evolution $\tau(x) - \tau_0$ along the fault, we interpolated $v(x)$ using a Chebyshev-based fit (Fig. 4, A and B), which captures the asymptotic behavior of slip and slip rate expected from fault mechanics, at both the leading and trailing edges of the pulse (see figs. S4 and S5 and supplementary materials for more details).

Once $v(x)$ was known, we inferred the shear stress evolution from Eq. 1 (Fig. 4C). Because the exact value of V_r was not known at this stage, we present results for two representative cases in Fig. 4C: $V_r/C_s = 0.75$ and $V_r/C_s = 0.90$. These ratios correspond to the two end-member rupture velocities of a rupture propagation scenario accounting for the ground motion and arrival times of the first and second seismic-wave arrivals as observed in the footage (Fig. 2B), implying a local sub-shear rupture velocity (see supplementary materials and fig. S3).

As anticipated for pulse-like ruptures, we observed that the stress drop was followed by a restrengthening phase (Fig. 4D) that spanned ~17% of the pulse length. The dependence of the shear-stress evolution on the rupture velocity V_r was also expected: A lower rupture velocity V_r requires a larger strength drop $\Delta\tau$, defined as the difference between the maximum and the minimum shear stress, to match the measured cumulative slip and slip rate. In addition, the size of the cohesive zone X_c, which corresponds to the distance over which the frictional strength of a fault degrades from its peak to residual level, increases linearly with V_r. Specifically, we found $\Delta\tau = 5.7$ MPa and $X_c = 3749$ m for $V_r = 0.90C_s$, compared with $\Delta\tau = 28.2$ MPa and $X_c = 3124$ m for $V_r = 0.75C_s$. Examining the apparent stress-slip relationship in Fig. 4D, we observed a decay of shear stress τ with slip δ, up to a critical slip value $D_c = 2.94$ m, which is consistent for both rupture velocities.

We then calculated the breakdown work $W_b = \int_0^{D_c} [\tau(\delta) - \tau_{\min}]\, d\delta$ associated with the slip pulse, integrating up to the point of minimum stress $\tau_{\min}$, defined spatially at X_c and in cumulative slip at D_c (Fig. 4, C and D). Because this estimate is strongly dependent on final slip D_{fin} and rupture velocity V_r, we conducted a sensitivity analysis to characterize the uncertainty on these parameters (fig. S6 and supplementary materials). For the assumed final slip of 3.0 m, W_b ranges from 7.7 MJ m^{-2} for $V_r = 0.90C_s$ to 38.2 MJ m^{-2} for $V_r = 0.75C_s$.

To better constrain V_r and provide an independent direct measurement of the energy release rate G during the rupture pulse of the M_w 7.7 Mandalay earthquake, we fitted a classical two-dimensional steady-state rupture pulse model (*29*) to the observed slip pulse. The model assumes a steady-state sub-Rayleigh rupture velocity V_r and a constant-width cohesive zone in which the friction linearly decreases from the peak to the residual frictional strength ($f_p = 0.6$ and $f_r = 0.1$, respectively) behind the rupture front (fig. S7A). Unlike the direct slip-based model used previously, this model imposes a cohesive zone friction law and no healing within the pulse. Therefore, the energy released during

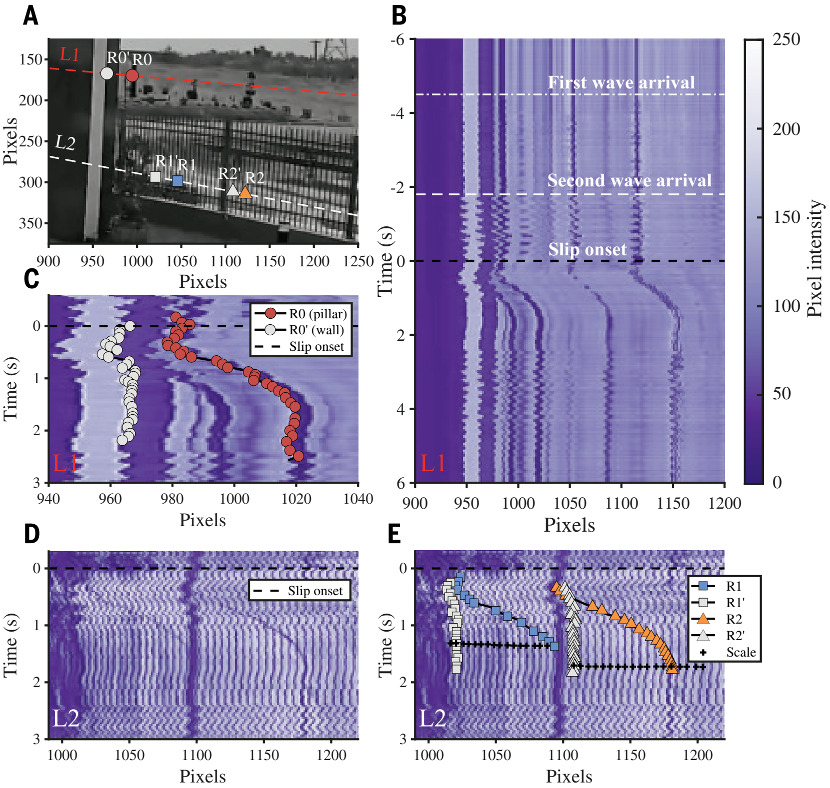

Fig. 2. Landmark tracking method. (**A**) Zoomed-in video frame showing tracked landmarks and their corresponding reference objects. The landmarks are as follows: *R*0 (red circle) is the front-side pillar, *R*1 (blue square) is the pole visible behind the fence, and *R*2 (orange diamond) is the second pole behind the fence. The reference points are as follows: *R*0′ (gray circle) is the arch wall, and *R*1′ and *R*2′ (gray square and diamond, respectively) are fence bars near the initial positions of *R*1 and *R*2. The red dashed line (L1) indicates the axis used for projections in (B) and (C). The white dashed line (L2) indicates the axis used for projections in (D) and (E). (**B**) Motion tracking with annotations showing the arrival of the first seismic wave, second wave, and slip onset. (**C**) Pixel displacement time series for *R*0 and *R*0′, measured along L1. (**D**) Pixel displacement time series for *R*1, *R*1′, *R*2, and *R*2′, measured along L2. (**E**) Same as (D), with additional annotations showing the tracking of each landmark and associated reference for *R*1 and *R*2 as well as a motion scale (black crosses).

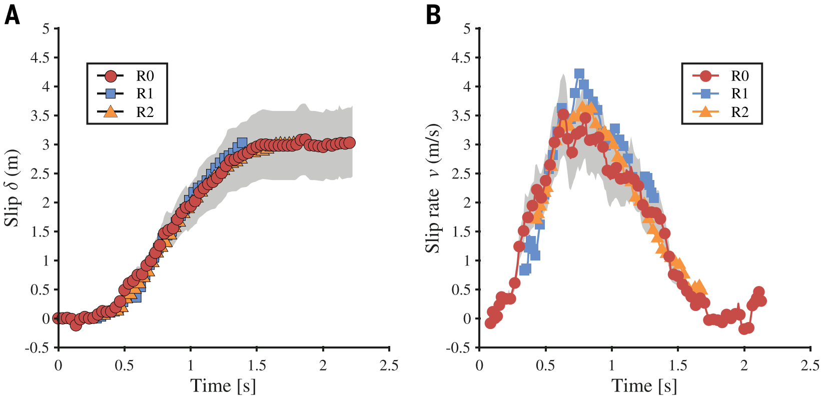

Fig. 3. Slip and slip-rate functions measured at the camera location. (**A**) Evolution of the fault slip during the rupture propagation modeled using the three landmark-reference pairs (Fig. 2A). (**B**) Slip-rate function derived from (A) for the three pairs. The gray shaded areas in (A) and (B) represent the effect of the 20% uncertainty in our slip estimate on the measurements derived from *R*0, which is the landmark used in the modeling. The symbols correspond to those described in Fig. 2.

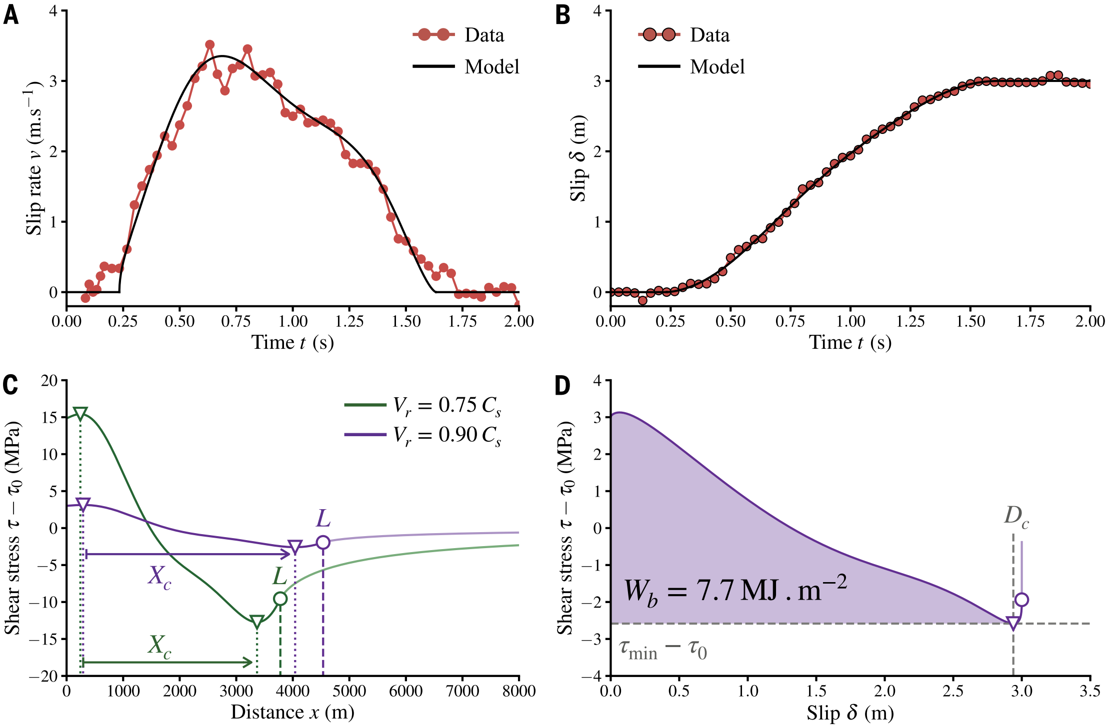

Fig. 4. Stress evolution and stress-slip relationship inferred from the slip-rate function. (**A** and **B**) Direct measurement (red circles) and Chebyshev-based fit (solid black curve) of (A) fault slip rate and (B) fault slip at the footage location. (**C**) Solution of the evolution of shear-stress change as a function of the distance from the rupture tip during slip-pulse propagation for rupture scenarios $V_r = 0.75C_s$ (solid green curve) and $V_r = 0.90C_s$ (solid purple curve). Cohesive zone size X_c is defined as the distance between the maximum and minimum of the shear-stress change (triangles), whereas the pulse length L corresponds to the extent of the actively sliding region (circles). (**D**) Evolution of stress variation $\tau - \tau_0$ with slip, including the healing stage for $V_r = 0.90C_s$. The breakdown work W_b (in shaded purple area) is defined from an integral of the shear-stress change $\tau - \tau_{min}$ up to the critical slip distance $\delta = D_c$.

the weakening contributes entirely to the rupture propagation and corresponds to G as described in fracture mechanics. Whereas the direct slip-based approach is applicable in this study because of the availability of true on-fault slip measurements from CCTV footage, the linear cohesive zone model is a more general framework that can be applied to conventional seismic observations, including data recorded at stations located away from the fault (*31*). We assumed a nominal normal traction of $\sigma_0 = 10$ MPa, consistent with the shallow nature of the rupture. The slip pulse duration was fixed at $\Delta t = 1.4$ s, as estimated previously. We performed a grid search on the scaled cohesive zone size to X_c/L and scaled rupture velocities V_r/C_s, identifying the parameters that produce the largest signal similarity index (SSI), which is a Euclidean-norm measure of how well the predicted slip-rate evolution matches that measured from image analysis. As seen in Fig. 5A, the optimal SSI corresponds to $X_c/L = 0.71$ and $V_r/C_s = 0.903$, which provides the fit of the curve in Fig. 5B. This X_c/L value is lower than the elastodynamic estimate of 0.83, as the pulse model prohibits restrengthening within the pulse, reducing the effective weakening (cohesive) zone. Nevertheless, the result supports $V_r = 0.90C_s = 3240$ m s^{-1} as the most consistent rupture scenario.

We have now obtained a complete mechanical characterization of the slip pulse observed in the CCTV data. The inferred strength drop was $\tau_p - \tau_r = 5$ MPa, the stress drop was $\tau_0 - \tau_r = 2$ MPa, and the corresponding slip-weakening distance was $X_c \approx 2.5$ m. These values are consistent with the slip-based model estimates ($\tau_p - \tau_r = 5.7$ MPa, $\tau_0 - \tau_r = 2.6$ MPa), except for $D_c = 2.94$ m, which was slightly overestimated because of the larger cohesive zone size. Ultimately, the energy release rate G was computed as $\int_0^{D_c} \left[\tau_f(\delta) - \tau_r\right] d\delta = 5.8\,\mathrm{MJ/m^2}$, where $\tau_f(\delta)$ is the strength evolution with slip δ (Fig. 5C). Assuming that $G = G_c$, our analysis here provides a direct estimate of the local fracture energy G_c of a natural fault. The energy release rate is of the same order of magnitude as our elastodynamic estimate of the breakdown work $W_b = 7.7$ MJ m^{-2}. Although related, the two quantities are not equivalent: G_c is expected to be smaller than W_b for ruptures that have undergone complete frictional weakening (*32*–*34*). Our value of G_c is consistent with expectations for an earthquake of the size and geometry of the Mandalay event (*35*–*38*), but it is substantially larger than values typically reported for experimental faults, both in analog materials (*39*, *40*) and in crustal rock samples (*41*, *42*). This difference is primarily attributed to the larger slip-weakening distance D_c inferred here, compared with the much smaller values typically observed during laboratory earthquakes (*40*, *41*). Nevertheless, such large values of D_c remain compatible with those measured during high-velocity friction experiments under upper-surface stress conditions (*43*–*45*) and are expected from seismic kinematics inversion of large earthquakes (*46*). Beyond the specific case of the Mandalay earthquake, these direct measurements offer a rare, empirical benchmark for earthquake source modeling. Unlike traditional kinematic and dynamic inversions, which are limited by data coverage and modeling assumptions, the video-derived slip and slip-rate functions provide ground-truth constraints on the physical processes behind large earthquakes, such as fault weakening, energy dissipation, and rupture dynamics.

Discussion

Our study highlights the potential for a new observational approach in earthquake science: strategically deploying CCTV or high–frame rate cameras near active, shallow-fault zones. Such installations could capture not only rapid, coseismic fault slip, as demonstrated here, but also slower aseismic deformation or postseismic creep. Compared with

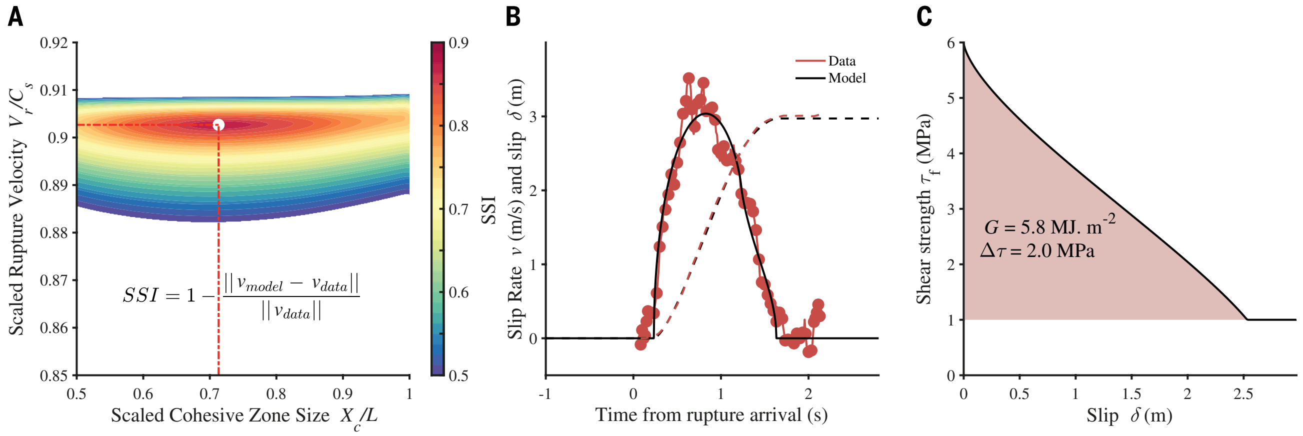

Fig. 5. Evaluation of rupture velocity and energy release rate. (**A**) Grid search for the best-fitting scaled cohesive zone size, X_c/L, and scaled rupture velocity, V_r/C_s. The fit is measured using the SSI, as defined in the text. v_{model} and v_{data} are slip rates from the model and the data, respectively. (**B**) Comparison of slip (dashed lines) and slip rate (solid lines) between the observed and best-fitting model slip pulse. (**C**) Evolution of friction strength, τ_f, with slip, δ.

traditional instrumentation such as broadband seismological stations or continuous GPS networks, video monitoring systems are relatively low cost, widely available, and easy to deploy, making them an attractive complementary tool for expanding fault-monitoring capabilities. With appropriate placement and calibration, these instruments could provide direct, high-resolution constraints on fault behavior across the full spectrum of slip modes, opening new avenues for studying earthquake physics.

REFERENCES AND NOTES

1. J.-P. Avouac, *Annu. Rev. Earth Planet. Sci.* **43**, 233–271 (2015).
2. A. Tarantola, B. Valette, *Rev. Geophys.* **20**, 219–232 (1982).
3. A. Saraò, S. Das, P. Suhadolc, *J. Seismol.* **2**, 1–25 (1998).
4. I. A. Beresnev, *Bull. Seismol. Soc. Am.* **93**, 2445–2458 (2003).
5. S. Hartzell, P. Liu, C. Mendoza, C. Ji, K. M. Larson, *Bull. Seismol. Soc. Am.* **97**, 1911–1934 (2007).
6. P. M. Mai *et al.*, *Seismol. Res. Lett.* **87**, 690–708 (2016).
7. G. Bertrand, C. Rangin, *J. Asian Earth Sci.* **21**, 1139–1157 (2003).
8. N. G. Reitman *et al.*, Remote surface rupture observations for the M7.7 2025 Mandalay, Burma (Myanmar) earthquake. USGS Data Release (2025); https://doi.org/10.5066/P1RYMWCK.
9. US Geological Survey, Finite Fault – M 7.7 - 2025 Mandalay, Burma (Myanmar) earthquake (2025); https://earthquake.usgs.gov/earthquakes/eventpage/us7000pn9s/finite-fault [accessed 16 May 2025].
10. M. Vallée, J. Charléty, A. M. Ferreira, B. Delouis, J. Vergoz, *Geophys. J. Int.* **184**, 338–358 (2011).
11. N. Inoue *et al.*, *Seismica* **4**, 1 (2025).
12. H. Richter, "Watch an earthquake split a hillside in two," *Science*, 22 July 2025.
13. J. Kearse, Y. Kaneko, *Seismic Record* **5**, 281–288 (2025).
14. T. H. Heaton, *Phys. Earth Planet. Inter.* **64**, 1–20 (1990).
15. D. Melgar, G. P. Hayes, *Geophys. Res. Lett.* **44**, 9691–9698 (2017).
16. V. Lambert, N. Lapusta, S. Perry, *Nature* **591**, 252–258 (2021).
17. F. Barras, E. Aharonov, F. Renard, *Geophys. Res. Lett.* **52**, e2024GL111189 (2025).
18. H. Weng, J.-P. Ampuero, *J. Geophys. Res. Solid Earth* **124**, 8584–8610 (2019).
19. H. Weng, J.-P. Ampuero, *Nat. Commun.* **13**, 7327 (2022).
20. J. R. Rice, *J. Geophys. Res. Solid Earth* **111**, B05311 (2006).
21. A.-A. Gabriel, D. I. Garagash, K. H. Palgunadi, P. M. Mai, *Science* **385**, eadj9587 (2024).
22. D. I. Garagash, *J. Geophys. Res. Solid Earth* **117**, B04314 (2012).
23. S. Minson, M. Simons, J. Beck, *Geophys. J. Int.* **194**, 1701–1726 (2013).
24. H. N. Razafindrakoto, P. M. Mai, *Bull. Seismol. Soc. Am.* **104**, 855–874 (2014).
25. I. A. Beresnev, *Pure Appl. Geophys.* **181**, 1859–1869 (2024).
26. G. Lykotrafitis, A. J. Rosakis, G. Ravichandran, *Science* **313**, 1765–1768 (2006).
27. S. Nielsen, R. Madariaga, *Bull. Seismol. Soc. Am.* **93**, 2375–2388 (2003).
28. E. Tinti, E. Fukuyama, A. Piatanesi, M. Cocco, *Bull. Seismol. Soc. Am.* **95**, 1211–1223 (2005).
29. J. R. Rice, C. G. Sammis, R. Parsons, *Bull. Seismol. Soc. Am.* **95**, 109–134 (2005).
30. N. Brantut, D. I. Garagash, H. Noda, *J. Geophys. Res. Solid Earth* **124**, 8998–9020 (2019).
31. E. M. Dunham, R. J. Archuleta, *Bull. Seismol. Soc. Am.* **94** , S256–S268 (2004).
32. F. Paglialunga, F. Passelegue, M. Lebihain, M. Violay, *Earth Planet. Sci. Lett.* **626**, 118550 (2024).
33. D. S. Kammer *et al.*, *Nat. Commun.* **15**, 4736 (2024).
34. B. Fryer, M. Lebihain, C. Noel, F. Paglialunga, F. Passelègue, *J. Mech. Phys. Solids* **193**, 105876 (2024).
35. R. E. Abercrombie, J. R. Rice, *Geophys. J. Int.* **162**, 406–424 (2005).
36. E. Tinti, P. Spudich, M. Cocco, *J. Geophys. Res. Solid Earth* **110**, B12303 (2005).
37. S. Nielsen *et al.*, *J. Seismol.* **20**, 1187–1205 (2016).
38. M. Cocco *et al.*, *Annu. Rev. Earth Planet. Sci.* **51**, 217–252 (2023).
39. I. Svetlizky, J. Fineberg, *Nature* **509**, 205–208 (2014).
40. F. Paglialunga *et al.*, *Earth Planet. Sci. Lett.* **584**, 117442 (2022).
41. D. S. Kammer, G. C. McLaskey, *Earth Planet. Sci. Lett.* **511**, 36–43 (2019).
42. S. Xu, E. Fukuyama, F. Yamashita, *J. Geophys. Res. Solid Earth* **124**, 766–787 (2019).
43. A. Tsutsumi, T. Shimamoto, *Geophys. Res. Lett.* **24**, 699–702 (1997).
44. T. Hirose, T. Shimamoto, *J. Geophys. Res. Solid Earth* **110**, B05202 (2005).
45. G. Di Toro *et al.*, *Nature* **471**, 494–498 (2011).
46. T. Mikumo, K. B. Olsen, E. Fukuyama, Y. Yagi, *Bull. Seismol. Soc. Am.* **93**, 264–282 (2003).
47. F. Passelègue *et al.*, Data and model for Direct Estimation of Earthquake Source Properties from a Single CCTV Camera. Zenodo (2025); https://doi.org/10.5281/zenodo.16785672.

ACKNOWLEDGMENTS

We thank those who uploaded and shared the analyzed footage on social media. F.P. thanks B. Fryer, N. Calza, and F. Paglialunga for discussions and for proofreading the manuscript. S.L. and F.P. thank J.-P. Ampuero and F. Courboulex for valuable discussions. We thank D. Garagash and an anonymous reviewer for their constructive remarks, which helped to enhance this paper. **Funding:** F.P. acknowledges support from the European Union (ERC Starting Grant HOPE, no. 101041966). H.S.B. acknowledges support from ERC Consolidator Grant PERSISMO (no. 865411) for partial support of this work. Q.B. acknowledges support from ERC Starting Grant EARLI (no. 949221) for partial support of this work. **Author contributions:** S.L. and F.P. conceived the study; S.L. and K.W.H. conducted the frame analysis based on satellite imaging; M.L. developed the elastodynamic inversion; F.P., H.S.B., and M.L. estimated the rupture properties; C.T. and Q.B. analyzed the kinematic inversion from USGS and provided estimates of the wave speeds; S.L. and F.P. wrote the first draft of the manuscript; and K.W.H. provided critical data for spatial scaling and validation. All authors contributed to discussions, interpretation of results, and review of the manuscript. **Competing interests:** The authors declare no competing interests. **Data and materials availability:** All data and code necessary to directly reproduce our results are available online at Zenodo (*47*).

SUPPLEMENTARY MATERIALS

science.org/doi/10.1126/science.adz1705
Supplementary Text; Figs. S1 to S7; References (*48–54*)

Submitted 20 May 2025; accepted 29 August 2025

10.1126/science.adz1705

2025 MANDALAY EARTHQUAKE

RESEARCH ARTICLE

Supershear rupture sustained through a thick fault zone in the 2025 M_w 7.8 Mandalay earthquake

Shengji Wei[1,2,3]*†, Xin Wang[4,5]†, Chenglong Li[6], Hongyu Zeng[2], Zhangfeng Ma[2], Qibin Shi[7], Han Chen[3,6], Yihe Huang[8], Mingzhe Lyu[2,3], Jiangtao Liao[3,9], Shun Yang[10], Yiming Bai[11], Phyo Maung Maung[2], Kyawmoe Oo[12], Yin Myo Min Htwe[12], Jianyong Zhang[13], Luca Dal Zilio[2,3], Xinjian Shan[5], Ling Chen[14,5]

On 28 March 2025, a moment magnitude (M_w) 7.8 earthquake ruptured a seismic gap along the Sagaing fault in Myanmar, generating a surface rupture 480 km in length and causing widespread damage. With holistic geodetic and seismic techniques, we resolved its rupture dynamics and fault zone structure. The rupture initiated as bilateral subshear and transitioned to supershear (~5.3 km/s) about 100 km south of the epicenter, sustaining this velocity for more than 200 km. The supershear segment aligns with a ~2-km–thick low-velocity fault zone exhibiting ~45% shear wave speed reduction. We suggest that the thick fault zone, aided by fault geometry and basin structure, enabled prolonged supershear propagation. Our findings emphasize that observations and models encompassing the entire fault zone are crucial for advancing both specific-event and earthquake-cycle simulations.

The largest continental crustal earthquakes—capable of producing ruptures stretching hundreds of kilometers and affecting multiple populated centers—pose considerable seismic threats. Such events often develop into supershear ruptures in which the rupture speed exceeds crustal shear wave velocity, as reported for recent strike-slip events such as the 2001 M_w 7.8 Kokoxili earthquake (*1*–*3*), the 2002 M_w 7.9 Denali earthquake (*3*–*5*), and the 2023 M_w 7.8 Turkey earthquake (*5*–*8*). Notably, the supershear rupture portion of these events often take place on relatively simple fault geometries (*1*, *9*, *10*) or "superhighways" (*11*) and therefore have reduced energy dissipation into secondary fault branches, allowing the rupture to develop to supershear speed and form long surface ruptures (*9*). Continental strike-slip faults at plate boundaries, such as the North Anatolian (Türkiye), Sagaing (Myanmar), and San Andreas (USA) faults, are particularly concerning due to their relatively simple geometries and historical occurrence of large events.

During an earthquake rupture, part of the released energy contributes to creating damage zones or/and fault zones, characterized by diffuse inelastic coseismic deformation or substantial reduction of seismic wave speeds, as increasingly reported for active continental faults (*12*–*19*). Here, we term them coseismic damage zones when created during earthquake ruptures, primarily constrained by near-fault geodetic and field deformation observations (*15*, *17*, *20*, *21*), or low-velocity fault zones (LVFZ) when indicating the cumulative effects of historical ruptures (*19*, *22*–*26*).

However, clarity is still lacking regarding the connection between these fault zones and large strike-slip ruptures, and the role of fault zones in long, sustained supershear ruptures. The recent M_w 7.8 earthquake on 28 March, 2025 in Mandalay, Myanmar, provides a valuable case to address these questions. The event took place on the Sagaing fault, which forms the eastern boundary of the Burma microplate, a sliver block created by oblique collision between the Indian Ocean and the Sunda plates (*27*) (Fig. 1A). The fault accommodates a tectonic slip rate of 20 to 23 mm/yr (*28*) (Fig. 1B). Over the past 200 years, the Sagaing fault has hosted more than 10 $M > 6.5$ earthquakes. However, a ~250-km seismic gap between the cities of Mandalay and Naypyidaw had remained unruptured since at least 1897—until the 2025 M_w 7.8 event (Fig. 1C) (*29*). In Myanmar, the 2025 event has so far directly resulted in at least 5352 fatalities, 7108 injuries, and 538 missing individuals (*30*). The impacts extended beyond Myanmar, including a tall building collapse in Bangkok, Thailand, located ~1000 km from the epicenter (*31*), and substantial building damage in Yunnan province, China (*32*). Early reports showed that the event produced a >450-km surface rupture and supershear rupture speed (*33*, *34*) and also triggered seismicity in Shan-Thai plateau and southern China (*35*).

Through the application of multiple techniques to both seismic and geodetic datasets, we investigated the events of its surface deformation, resulting coseismic damage zone, detailed rupture process, and the associated fault zone structures. These results offer new insights into the interrelationship between supershear rupture and fault zone structure.

3D surface deformation and damage zone

To characterize surface deformation and the ruptured fault associated with the earthquake, we first analyzed multiple sets of satellite observations. We employed three independent remote sensing techniques: differential interferometric synthetic aperture radar, aperture interferometry, and pixel offset on Sentinel-1/2 and ALOS-2 satellite imagery, to obtain fourteen coseismic surface displacement images (figs. S1 and S2 and methods in the supplementary materials). These datasets, acquired from multiple viewing geometries, provide complementary sensitivity to different components of ground deformation, with an effective spatial resolution of ~200 m. We integrated these observations to reconstruct the full three-dimensional (3D) coseismic displacement field produced by the earthquake (fig. S3). The results reveal a rupture length of ~480 km, characterized by predominant right-lateral strike-slip motion (Fig. 2 and fig. S3). Vertical displacements are minor (Fig. 2C), indicating that the rupture was nearly pure strike-slip.

The coseismic surface displacements exhibit clear along-strike variations. To the first order, the north–south component of displacement (Fig. 2A) reveals a three-segment pattern. The northern segment, located north of Mandalay, shows the largest displacement for the event—up to ~5.5 m. Deformation was greater to the east of the fault, suggesting an east-dipping fault geometry. The central segment, extending approximately 80 km southward from Sagaing, had the smallest displacement magnitude among the three segments and near-symmetric deformation across the fault. The southern segment shows larger displacement than the middle segment but the amplitude on the western side of the fault gradually increases compared with the eastern side, implying a transition to a west-dipping fault geometry.

Fault slip and coseismic damage-zone width derived from high-resolution (10-m) Sentinel-2 displacements also reveal distinct along-strike variations (Fig. 3A and methods). North of the epicenter, sharp

---

[1]Key Laboratory of Deep Petroleum Intelligent Exploration and Development, Institute of Geology and Geophysics, Chinese Academy of Sciences, Beijing, China. [2]Earth Observatory of Singapore, Nanyang Technological University, Singapore. [3]Asian School of the Environment, Nanyang Technological University, Singapore. [4] Key Laboratory of Planetary Science and Frontier Technology, Institute of Geology and Geophysics, Chinese Academy of Sciences, Beijing, China. [5]College of Earth and Planetary Sciences, University of Chinese Academy of Sciences, Beijing, China. [6]State Key Laboratory of Earthquake Dynamics and Forecasting, Institute of Geology, China Earthquake Administration, Beijing, China. [7]Department of Environmental and Planetary Sciences, Rice University, Houston, TX, USA. [8]Department of Earth and Environment Sciences, University of Michigan, Ann Arbor, MI, USA. [9]Key Laboratory of Earth Exploration and Information Technology of Ministry of Education, Chengdu University of Technology, Chengdu, China. [10]Marine Science and Technology College, Zhejiang Ocean University, Zhoushan, China. [11]School of Physical and Mathematical Sciences, Nanyang Technological University, Singapore. [12]Department of Meteorology and Hydrology, Naypyitaw, Myanmar. [13]China Earthquake Networks Center, Beijing, China. [14]State Key Laboratory of Lithospheric and Environmental Coevolution, Institute of Geology and Geophysics, Chinese Academy of Sciences, Beijing, China.
***Corresponding author. Email: shjwei@gmail.com** †These authors contributed equally to this work.

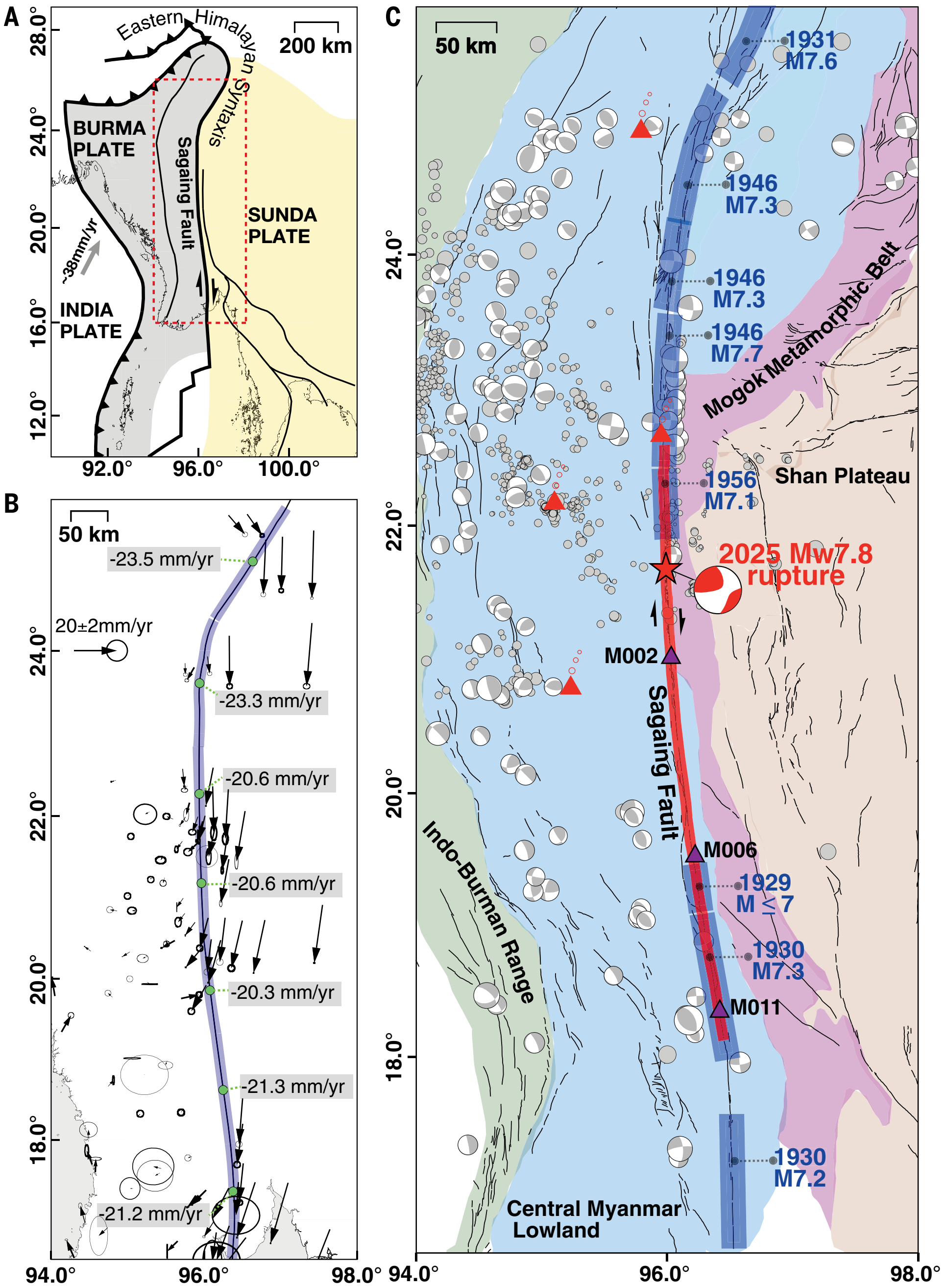

Fig. 1. Seismotectonic background. (**A**) Tectonic setting for the study region. The red dashed rectangle marks the locations of (**B** and **C**). (B) Slip rate distribution along the Sagaing Fault along with the GNSS observations used to derive these rates (*28*). GNSS velocities are relative to the Burma plate. (C) Historical earthquakes in the region. Gray beach balls represent focal mechanisms from the global centroid moment tensor (GCMT) catalog and (*60*). Gray dots are earthquake epicenters from the USGS catalog. Red triangles indicate locations of Quaternary volcanoes (*61*). The detailed fault inventory map is from (*27*) and the dark red line is our mapped ruptured fault trace of the 2025 event. The red star is our refined epicenter and the red beach ball is the GCMT solution.

fault-parallel offsets suggest a highly localized rupture zone with a narrow damage zone. South of the epicenter, the gradient progressively broadens across the fault, marking a transition to a wider damage zone (fig. S4). The measured fault total slip is ~1 to 6 m (Fig. 3C), distributed within a coseismic damage zone ~20 to 800 m wide (Fig. 3D). Along the fault segment north of the epicenter, where maximum coseismic slip occurred, the narrowest damage zone is ~60 m wide (Fig. 3D and fig. S4). The coseismic damage zone to the south broadens to between 90- and 190-m wide and can be divided into three sections by thickness (Fig. 3D): ~120 m from ~20 km north to ~210 km south of the epicenter, ~90 m from ~210 to 330 km south, and ~190 m further south.

Overall, the average width of these coseismic damage zones is ~100 m (Fig. 3D), which lies at the lower end of the observed range compared with other continental strike-slip earthquakes (*15*, *17*, *18*, *36*). This is due to the relatively simple geometry of the Sagaing fault, characterized by considerably fewer stepovers, bends, and branches. The segmented variation in damage zone width is more pronounced than the total slip. This contrast suggests that coseismic damage width is more strongly influenced by other factors, such as rock properties, compared with slip amplitude (*18*, *21*). Indeed, south of the epicenter, sediment thickness increases and near-surface shear wave velocities (top 1 km) decrease (Fig. 3, D and E), as revealed by detailed shallow velocity structure imaged along the Sagaing fault (*37*).

Static slip model

We constrained the fault geometry and coseismic slip distribution by inverting the 3D surface deformation fields (see methods). Our preferred model resolved nine fault segments along the ~480-km rupture, achieving a variance reduction of 99.6% (figs. S5 and S6). The simple fault geometry—requiring no bifurcations or branches (black line in Fig. 3A)—contrasts with the fault branching mechanisms proposed for large strike-slip events (*38*). This simple geometry also deviates from the empirical relationship between rupture length and number of fault segments, as summarized for other events (*39*, *40*), although the number of asperities may match the relationship better. Based on (*39*), a continental strike-slip event with a 480-km rupture length should correspond to 27 fault segments, much more than that observed for the 2025 event. Modest dip variations are evident along the strike, with the fault dipping ~70° eastward in the north, near-vertical in the central section, and slightly (~80°) west-dipping in the south (fig. S5).

The static slip model reveals that most coseismic slip is concentrated shallower than 12 km (Fig. 3B), consistent with the depth extent of interseismic locking inferred from global navigation satellite system (GNSS) observations (*28*). The slip distribution exhibits pronounced along-strike heterogeneity. The longest, also the largest, slip patch is located north of the epicenter and extended more than ~100 km with a peak slip of ~6 m. Southward, slip decreased to ~2.5 to 3 m along a ~70-km section, then increased again to ~4 m and remained relatively uniform over the remaining ~230 km of rupture. Superimposed on this broad pattern are short-wavelength (~10 to 20 km) variations, which are also independently detected in fault-crossing offsets from Sentinel-2 optical imagery.

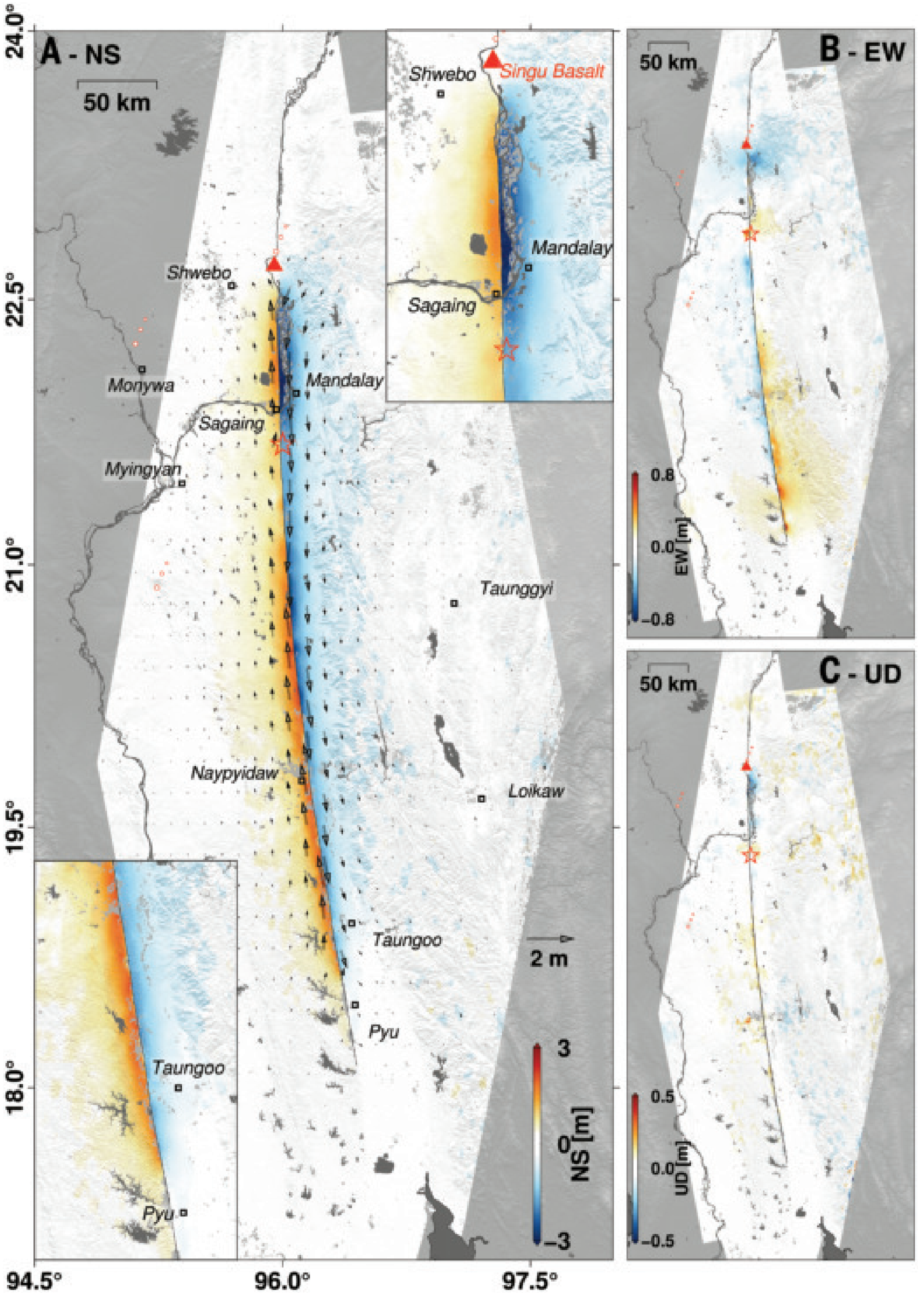

Fig. 2. 3D coseismic surface deformation map derived from satellite observations. (**A**) North-South direction deformation; (**B**) East-West; (**C**) up-down. The vectors in (A) represent horizontal motion and the black line is our mapped fault trace. Our refined epicenter is indicated by the red star. ALOS2 and Sentinel-1/2 images acquired from February to April 2025 were used to derive these 3D deformation maps (*62*) (see tables S1 and S2 for more details).

The measured total slip closely matches the near-surface slip estimated by our static slip model (Fig. 3, A and C). Checkerboard resolution tests confirmed the model's ability to resolve slip asperities across a range of spatial wavelengths (fig. S7). The averaged static stress drop estimated from our slip model was ~3 megapascals (MPa), which is consistent with that inferred for other major strike-slip faults (*41*).

Distinct rupture terminations were identified at both ends of the fault. To the north, the rupture terminated abruptly south of the Singu Basalt (*42*), coinciding with the southern limit of the 2012 M_w 6.8 Thabeikkyin earthquake rupture (Fig. 3B and fig. S8). We infer that a strong stress shadow posed by the 2012 event, combined with the mechanical contrast between basalt and the surrounding crust, formed an effective barrier to further rupture propagation. Toward the southern end, slip amplitude and rupture depth gradually diminished, suggesting a more distributed termination process. This segment overlaps the rupture zone of the 1929 and 1930 earthquakes (Fig. 3B), although the absence of detailed historical slip models precludes further constraints. These observations explain the displacement contrast patterns shown at the northern and southern termini, shown in the insets of Fig. 2A.

Shallow slip deficit (SSD) across the rupture was overall negligible, with slip on the near-surface subfault (~1 km depth) exhibiting only ~1% deficit relative to peak slip at depth (fig. S9). This value is substantially lower than the SSD observed in previous large strike-slip earthquakes (*43*–*45*), but closer to that reported for more recent events (*16*). The negligible SSD is robustly resolved by the dense and near-fault geodetic coverage for the 2025 event, as also suggested by recent studies of other earthquakes (*44*, *46*, *47*). However, along-strike variations occurred: On the fault segment south of Mandalay, where the coseismic slip amplitude was less, SSD (~7%) was larger than along the other fault segments (near 0%) (fig. S9). Reanalysis of interseismic GNSS velocity fields reveals that this segment is partially creeping, with a shallow creep rate of approximately 2.3 mm/yr extending to a depth of ~9.5 km (fig. S10), in contrast to the nearly fully locked behavior of adjacent fault segments. This contrast between SSD and coseismic slip suggests that depth-dependent and laterally varying fault frictional properties contributed to observed coseismic slip variations.

Kinematic and supershear rupture

We characterized the first-order rupture evolution using a path-calibrated teleseismic back-projection (BP) (*5*) technique on high-frequency [(HF), 0.3 to 1.0 Hz, fig. S11] seismic data from the Australian (AU) and European (EU) arrays (fig. S12A and methods). Locations of the HF radiators from BP align closely with the fault trace (Fig. 4A). The size of the BP radiators is proportional to the power of the stacked teleseismic waveforms. Our result shows that the rupture initially propagated bilaterally, with northward and southward segments each rupturing ~100 km at subshear speeds (~3 km/s). The southward rupture then accelerated to a supershear speed of ~5.3 km/s, maintaining this speed for at least 200 km (Fig. 4C). The robustness of the result is verified by BP applications to smaller nearby events consistent with their locations in a refined catalog (fig. S12). Synthetic tests mimicking mainshock rupture further confirmed the robustness of the result (figs. S13 and S14), which also shows that the array located away from the rupture directivity had less sensitivity (fig. S13, methods).

The evolution of rupture speed is further supported by the location and timing of subevents from a multiple point source (*48*) (MPS)

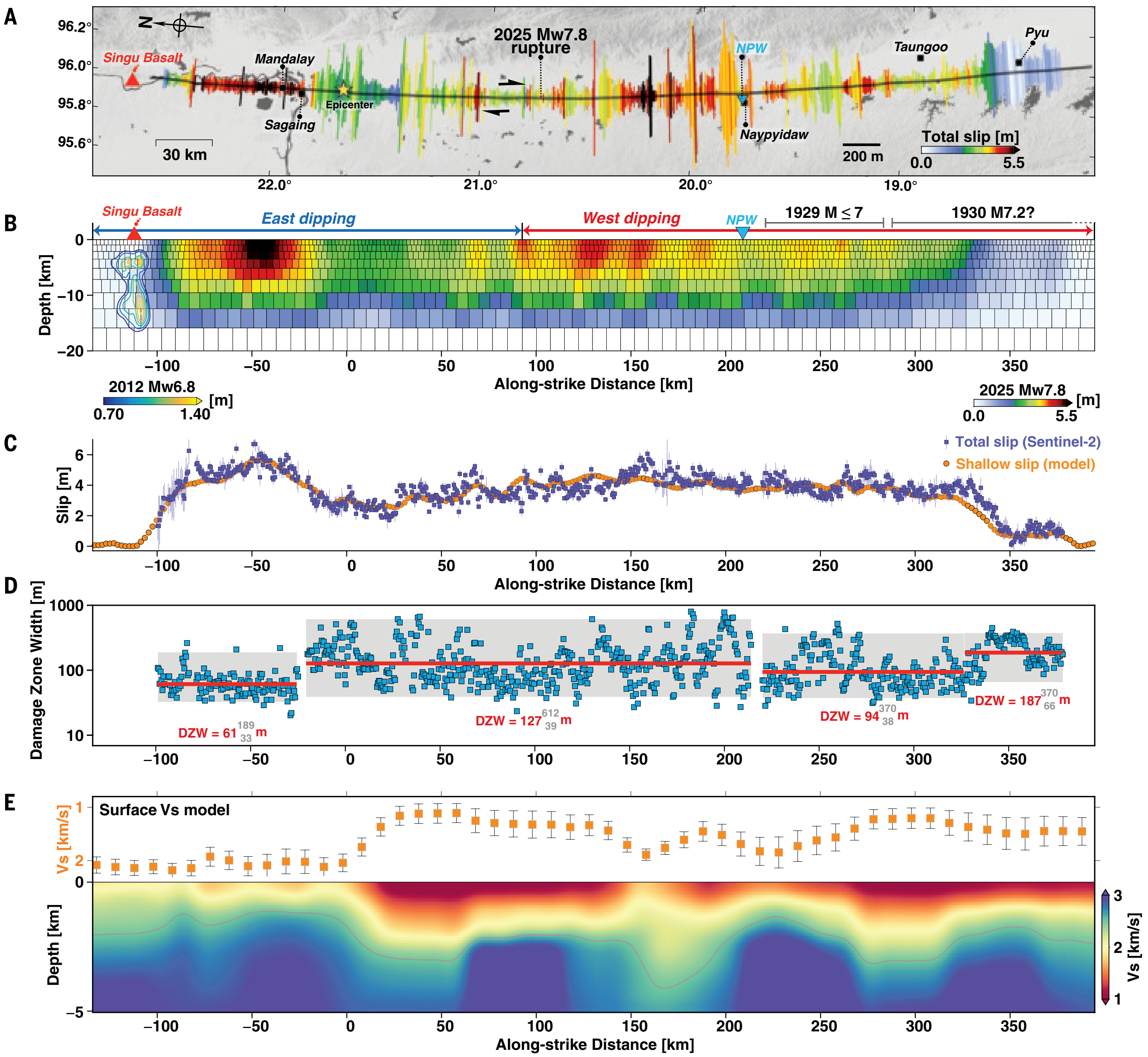

Fig. 3. Coseismic damage zone width and slip model, in comparison with velocity model. (**A**) Coseismic damage zone width and surface slip (*62*) estimated from Sentinel-2 image correlation. The length of the fault-perpendicular lines represents the width of the coseismic damage zone and the colors indicate the total slip magnitude. (**B**) Depth view of geodetic slip distribution for the 2025 M_w 7.8 event and the slip model of the 2012 M_w 6.8 event are shown in color-coded contours. Rupture extent for the 1929 and 1930 earthquakes is indicated at the southern end of the rupture. The purple triangle indicates the location of the NPW strong motion station. (**C**) Comparison between fault total slip from Sentinel-2 displacement [purple squares with uncertainty defined as standard deviation (one-sigma) between fault-parallel displacement (10 m binned mean) and fitting displacement] and shallow (≤1 km depth) slip amplitudes in the static slip model (orange dots). (**D**) Damage zone width (blue squares). The red lines are the averaged damage zone width of four segments. (**E**) Shear wave speed model in the top 5 km from (*37*). Orange squares represent the numerical average of uppermost 1-km surface shear wave velocity and uncertainty, in which the uncertainty is defined in (*37*). The gray line in (E) indicates the sedimentary base.

inversion using local-to-regional strong motion waveform and teleseismic body waves (Fig. 4B, fig. S16, and methods). MPS results fit the observations closely, with an average waveform cross-correlation coefficient of 0.8 across all components and stations (fig. S17). The result consists of 10 subevents (fig. S18), and the spatiotemporal evolution of these subevents shows that the mainshock began with a bilateral rupture that transitioned to supershear propagation ~100 km south of the epicenter (Fig. 4C). The overall source time function captures the low-frequency component of the moment-rate function derived from the finite fault inversion (Fig. 4D, inset; see details below).

Strong-motion waveforms recorded at the Naypyidaw (NPW) station (*49*), located 2.6 km from the fault trace at 19.779°N (blue triangle in Fig. 4A), provide independent evidence for supershear rupture propagation. To ensure the reliability of the absolute timing and waveform data from this station, we verified the accuracy of its GNSS time synchronization by comparing teleseismic arrival times with those recorded globally (fig. S15 and methods).

We then refined the mainshock epicenter and origin time using a nearby, well-located calibration event (fig. S19 and methods). Our analysis yields a revised epicenter at the latitude of 21.641°N, ~37 km

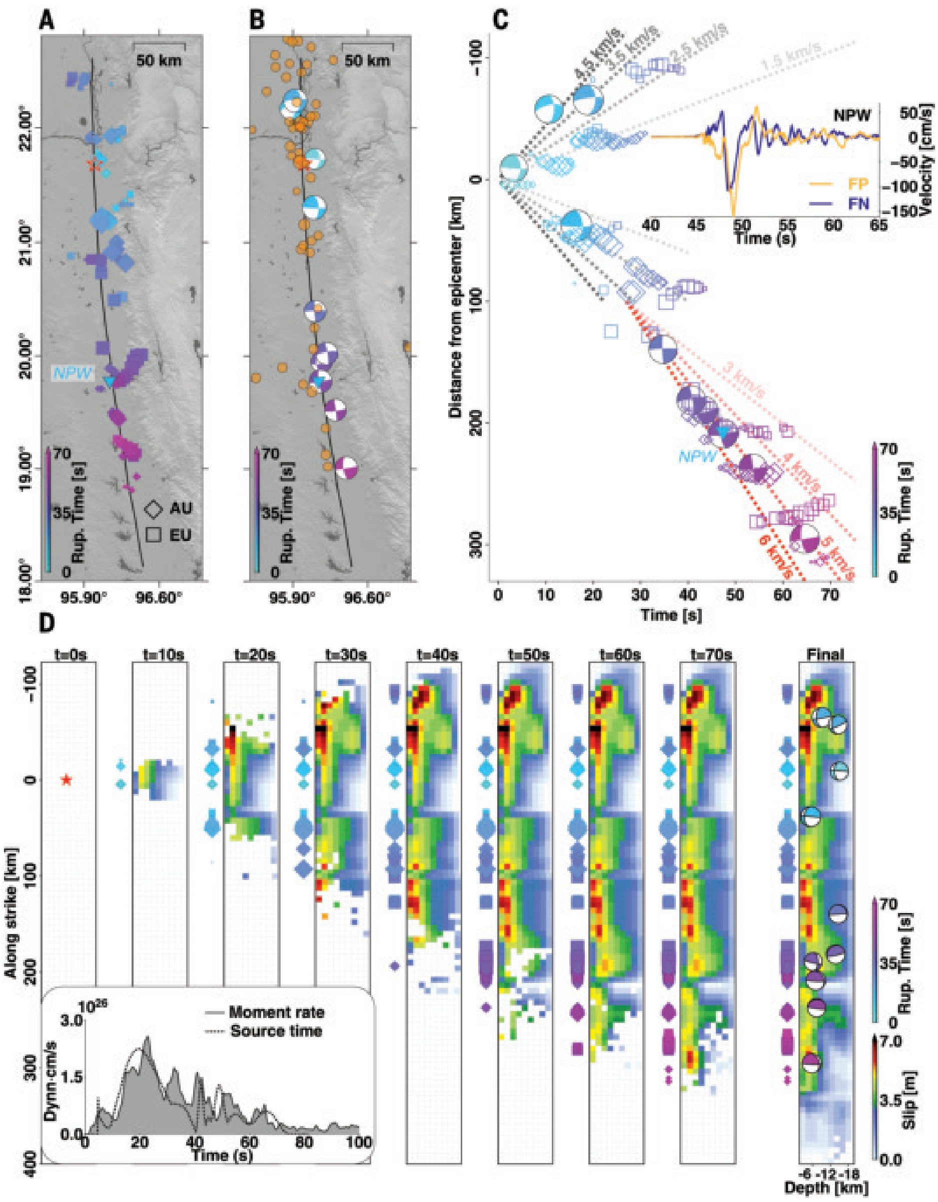

Fig. 4. Kinematic rupture models. (**A**) Map view of the back-projection (BP) results (*62*) from the EU array (squares) and the AU array (diamonds), color coded by time and sized by the power of stacked teleseismic waveforms. (**B**) MPS results (*62*) in map view, in which beach balls are color-coded by peak time in the source time function, projected to the low hemisphere. Orange dots indicate aftershocks provided by the USGS catalog. The blue triangles in (A) and (B) represent the location of the NPW station. (**C**) Rupture speed analysis and horizontal component velocity waveform at the NPW station. Fault-parallel (FP) and fault-normal (FN) directions are relative to the fault azimuth angle of 173 degrees. (**D**) Finite fault model with time (10 s) (*62*). Inset shows the moment rate function of the finite fault model (gray shaded area) and the total source time function of the MPS solution, with focal mechanism solutions projected to the western hemisphere.

south of that in the initial United States Geological Survey (USGS) report (22.013°N) (https://www.usgs.gov/programs/earthquake-hazards/earthquakes), but in closer agreement with the Thailand catalog (21.68°N). The refined origin time (2025-03-28 06:20:55.209 coordinated universal time) is 2.5 s later than the USGS report, again aligning more closely with the Thailand catalog (https://www.tmd.go.th/en/EarthQuake).

The supershear rupture pulse recorded at the NPW station, identified as the onset of the largest amplitude in the velocity waveform, arrived at ~48 ± 0.5 s (Fig. 4C inset). Given the station's distance of 206 km from the refined epicenter—closely approximating the rupture distance along the fault—the inferred average rupture speed was ~4.3 km/s, exceeding the local shear-wave velocity and thus indicating supershear propagation. Notably, the rupture phase arrival time at NPW closely matches the rupture timing derived from BP and MPS results at the same location (blue triangle in Fig. 4C). Further evidence for supershear rupture propagation is provided by the NPW waveform characteristics. Theoretical asymptotic analyses and laboratory rock experiments (*50*) demonstrate that when the Mach cone front generated by a sustained supershear rupture sweeps a near-fault station, the resulting ground motion is dominated by fault-parallel (FP) particle velocity relative to the fault-normal (FN) component. This pattern is clearly observed at the NPW station (Fig. 4C, inset, and fig. S20A). Moreover, the observed FP-to-FN velocity amplitude ratio suggests a rupture velocity of 5.0 to 5.3 km/s (fig. S20B and methods), consistent with estimates from BP and MPS.

Using the refined epicenter and rupture speed constraints from the preceding analyses, we performed a finite fault inversion that jointly fits teleseismic body waves, near-fault strong-motion records, and the 3D surface displacement field (methods). The resulting finite fault model (Fig. 4D) provides excellent fits to all datasets (figs. S21 to S23) and yields a moment-rate function consistent with that derived from the MPS source time function (Fig. 4D, inset), lending high confidence to key features of the model. These include the fault-geometry transition from east-dipping in the north to west-dipping in the south, the spatial distribution of slip, and the supershear rupture velocity observed along the central segment of the rupture. Collectively, multiple independent analyses and inversions corroborate a sustained supershear rupture propagating southward from ~100 km to at least 310 km along the strike from the epicenter (Fig. 4).

Thick LVFZ for supershear segment

We used passive seismic measurements to investigate the influence of the internal structure of the Sagaing fault zone. Along the supershear rupture segment of the 2025 event, three broadband seismic stations were located within 1 km of the surface rupture (Fig. 5A and fig. S24). Teleseismic P-waves recorded at these stations exhibited major time shifts between the vertical and radial components (fig. S24A). Notably, earthquakes originating from the western side of the fault show larger time shifts than those from the eastern side, indicating a clear back-azimuthal variation (fig. S24B). These time shifts resulted in delayed arrivals in receiver function (RF) waveforms, and when the shift exceeded a threshold (e.g., >1s), a negative phase was observed at the zero time (Fig. 5B, figs. S25 to S27, and methods).

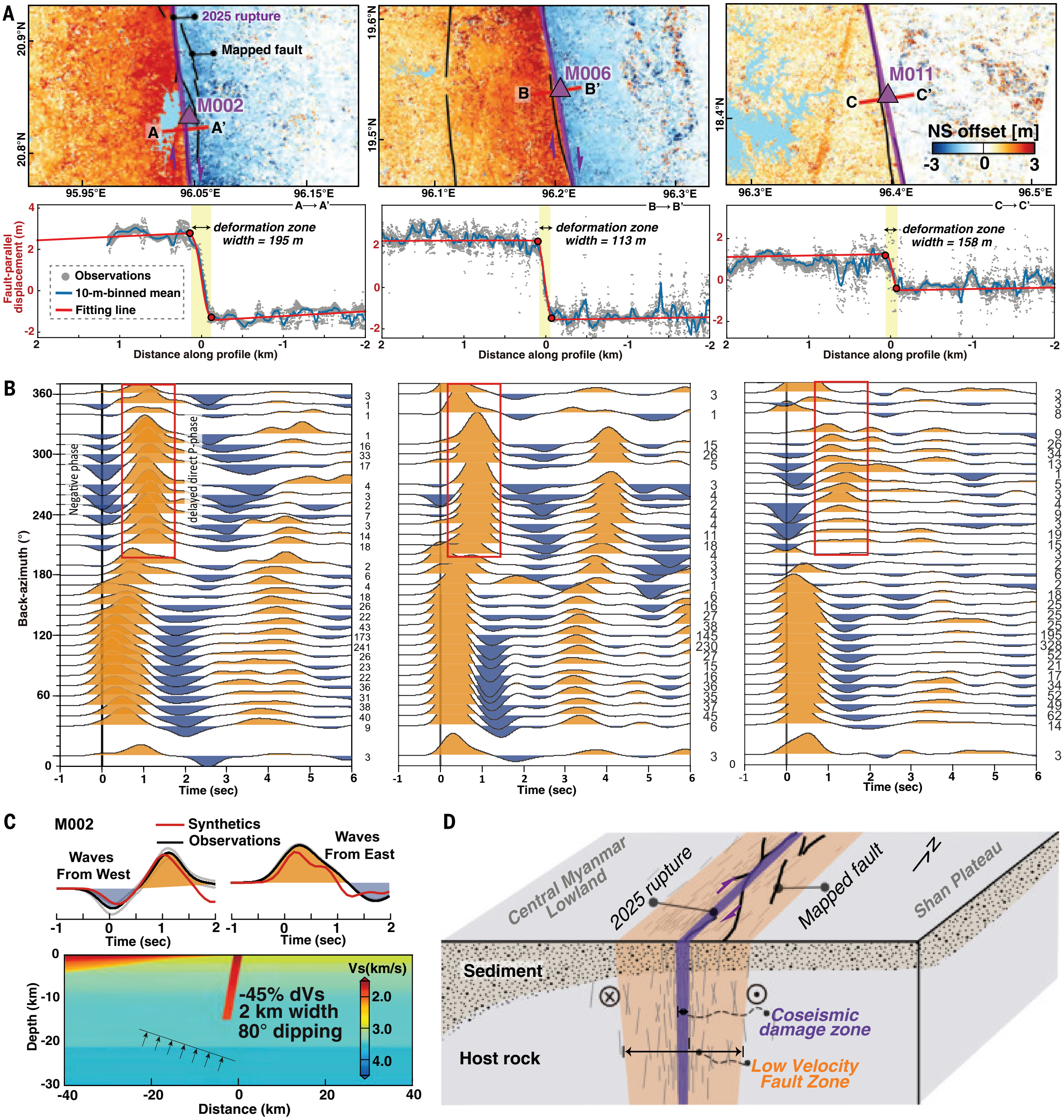

Fig. 5. Relationship between the coseismic damage zone and the low-velocity fault zone sustaining supershear rupture. (**A**) North-South displacement and across-fault profiles at the three broadband stations (M002, M006, and M011; Fig. 1C). Black and purple lines represent mapped faults and the 2025 rupture. (**B**) Stacked RF waveforms at M002, M006, and M011, grouped by the back-azimuth of incoming waves, with the number of stacked traces indicated on the right side of each panel. A clear transition is observed from a positive to negative zero-lag phase at back-azimuths near 180°. (**C**) 2D synthetic modeling results illustrating the effect of a dipping low-velocity fault zone on RF waveforms. A west-dipping fault zone produces a negative zero-lag phase for waves coming from the west, while maintaining a positive first P-phase for waves from the east, consistent with the observations. (**D**) Schematic illustration showing the relationship between the coseismic damage zone and the low-velocity fault zone.

These negative zero-lag phases in RFs cannot be explained by a 1D layered velocity model and are often neglected in conventional RF studies (*51*). Here, we argue that the negative zero-lag phase represents true structural signals caused by 2D effects of low-velocity fault zone structure. Through synthetic tests we show that basin models (*37*) are unable to reproduce the negative phase at time zero (fig. S28B). The negative zero-lag phase occurs only within specific back-azimuth ranges (Fig. 5B), which rules out sensor misorientation. It is observed when a different frequency band (fig. S27A) and deconvolution method (fig. S27B) are used. Therefore, the signal is not caused by sidelobe effects during filtering nor is it an artifact of RF calculation. The transition from a positive to a negative zero-lag phase occurred at back-azimuths near 180°—consistent with the polarity reversal observed in Fig. 5B—and closely aligns with the strike of the Sagaing fault, supporting an interpretation of a west-dipping fault zone structure.

We modeled the observed polarity reversal of the zero-lag phase with a west-dipping low-velocity fault zone structure (Fig. 5C and methods). A grid search was performed on the dipping angle, fault zone width, and velocity reduction, to find the best combined fit to observed RF waveforms. The velocity reduction ranged from 25 to 45% with 10% intervals; fault zone width varied from 1 to 3 km with 0.5 km intervals; and the dip angle ranged from 60° to 90° with 10° intervals. For each grid point, we calculated the amplitude ratio between the negative phase near time zero and the subsequent positive phase, then computed the misfit between observed and synthetic waveforms. The search shows that a west-dipping fault zone with a dip angle of 70° to 80°, a thickness of ~2 km, and a shear-wave velocity reduction of approximately 45% is needed to achieve the negative zero-lag phase and corresponding amplitude (figs. S28 and S29). The grid search results also indicate an uncertainty of ~0.5 km in fault width and ~10% in velocity reduction (fig. S30 and methods). The inferred west-dipping fault geometry is also consistent with that derived from geodetic inversions (fig. S31). The ~2-km width of the fault zone exceeds those of other well-studied faults such as the San Andreas, Ridgecrest, Landers, and Calico faults (table S3), although the observed velocity reduction is comparable (fig. S32 and methods).

The drivers of supershear rupture

The simple fault geometry and thick fault zone probably provide the most essential conditions behind the supershear and subshear-to-supershear transition distance of the 2025 event. A fault zone produces strong head waves that travel faster than the initial rupture front, creating dynamic fault stress perturbations that promote the development of a new supershear rupture front, as confirmed by dynamic earthquake simulations (*12*, *52*, *53*). Fault zones need to be sufficiently thick to facilitate a supershear transition. Damic rupture simulations show that the critical fault zone width should be at least 2 to 3 times the critical nucleation size of earthquakes $L_c = \frac{GD_c}{\Delta\tau_s}$, where G is shear modulus, D_c is the critical slip distance in slip-weakening friction law, and $\Delta\tau_s$ is the fault strength drop, i.e., the difference between fault static and dynamic shear strength. Assuming $G = 30$ GPa, $D_c = 1$ m, and $\Delta\tau_s = 50$ MPa (methods), and yielding a L_c of 600 m, the observed Sagaing fault zone width would be ~3 to 4 L_c. Such thick fault zones allow the transition to supershear rupture even with low background stress. Given the estimated static stress drop of 3 MPa, the relative stress drop—defined by the ratio of static stress drop to the strength drop—is likely <0.1 in this region, substantially lower than the relative stress drop needed for supershear transition in homogeneous media (*12*). Another feature of supershear rupture in thick fault zones is the increase in the supershear transition length with the fault zone width (*12*). A relative stress drop of <0.1 and a fault zone width of 3 to 4 L_c indicate that the transition length is >100 L_c (*12*), which matches the ~100-km transition length observed from the seismological analysis.

Other factors may also have facilitated the supershear rupture transition in the 2025 event. The observed supershear transition occurred near an along-strike fault-geometry transition, where the fault dip changes from eastward to subvertical (slightly west-dipping, Fig. 3B and fig. S5). Dynamic simulations demonstrated that geometrical kinks, such as dip changes or bends, can act as stress concentrators that temporarily slow and then reaccelerate the rupture, favoring supershear transition once the accumulated energy is released (*54*). As the rupture propagated onto the west dipping fault, the smooth fault geometry provided the "superhighway" to help sustain the supershear rupture, similar to what may have happened for other supershear events (*9*, *11*). The relatively thick (~2 to 3 km) sedimentary basin along the southern fault segment (Fig. 3E) serves as another favorable condition to sustain supershear rupture, as the waves reflected from the bottom of the basin could have increased shear stress on the fault and promoted rupture propagation (*55*, *56*).

In contrast to the relatively simple surface rupture of the 2025 event, fault traces mapped by earthquake geologists reveal secondary fault branches and bifurcations (Figs. 5D and 1C). These deviations from the straight 2025 rupture likely reflect past earthquakes that created more complex geomorphological signatures (*27*). The considerable fault zone thickness (~2 km) further suggests that ruptures in the past may have involved both the main fault and secondary strands. Observations indicate that fault zones may take hundreds or thousands of years for faults to heal from coseismic damages of large events (*57*). Dynamic simulations also show that coseismic rupture can produce off-fault plastic deformation that leads to permanent damage in the fault zone (*58*). Therefore, cumulative fault damage from previous events, including events similar to the 2025 event, have likely formed the observed thick fault zone (Fig. 5D).

Our observations and models reconcile the coseismic fault geometry, supershear rupture, and fault damage zone in a region where supershear rupture may have been governed by the cumulative imprint of past earthquakes. This inherited complexity appears to have guided the rupture dynamics for the 2025 M_w 7.8 Mandalay event. The Sagaing fault thus exemplifies how long-term fault zone evolution may influence earthquake behavior, a pattern that might apply to other plate boundary–type strike-slip faults. Specifically, supershear rupture along these faults may be more likely to occur where the fault zones are wide and fault geometry is simple. These findings highlight the need for both specific-event and earthquake-cycle models to incorporate more comprehensive and accurate fault zone structures (*59*), which may critically control rupture mode, speed, and size across successive earthquake generations. The results also provide new insight into assessing the potential hazard of major earthquakes along continental faults with recognized seismic gaps, such as those associated with the southern San Andreas fault in CA and the North Anatolian fault near İstanbul, Türkiye.

REFERENCES AND NOTES

1. M. Bouchon, M. Vallée, *Science* **301**, 824–826 (2003).
2. Y. Klinger *et al.*, *Bull. Seismol. Soc. Am.* **95**, 1970–1987 (2005).
3. K. T. Walker, P. M. Shearer, *J. Geophys. Res. Solid Earth* **114**, 2008JB005738 (2009).
4. E. M. Dunham, R. J. Archuleta, *Bull. Seismol. Soc. Am.* **94**, S256–S268 (2004).
5. H. Zeng, S. Wei, A. Rosakis, *J. Geophys. Res. Solid Earth* **127**, e2022JB024359 (2022).
6. D. Melgar *et al.*, *Seismica* **2**, v2i3.387 (2023).
7. C. Ren *et al.*, *Science* **383**, 305–311 (2024).
8. Z. Jia *et al.*, *Science* **381**, 985–990 (2023).
9. M. Bouchon *et al.*, *Tectonophysics* **493**, 244–253 (2010).
10. J. Jara *et al.*, *Proc R Soc Lond A.* **477**, 20210364 (2021).
11. D. P. Robinson, S. Das, M. P. Searle, *Tectonophysics* **493**, 236–243 (2010).
12. Y. Huang, J.-P. Ampuero, D. V. Helmberger, *Earth Planet. Sci. Lett.* **433**, 109–115 (2016).
13. A. Vallage, Y. Klinger, R. Grandin, H. S. Bhat, M. Pierrot-Deseilligny, *Geology* **43**, 1079–1082 (2015).
14. K. Okubo *et al.*, *J. Geophys. Res. Solid Earth* **124**, 11771–11801 (2019).

15. C. W. D. Milliner *et al.*, *Geochem. Geophys. Geosyst.* **16**, 1577–1598 (2015).
16. S. L. Antoine, Y. Klinger, K. Wang, R. Bürgmann, *Geophys. Res. Lett.* **51**, e2024GL110798 (2024).
17. X. Xi *et al.*, *Commun. Earth Environ.* **6**, 103 (2025).
18. C. Li, T. Li, X. Shan, G. Zhang, *Seismol. Res. Lett.* **94**, 39–51 (2022).
19. Y. Ben-Zion, C. G. Sammis, *Pure Appl. Geophys.* **160**, 677–715 (2003).
20. C. Pelties, J. de la Puente, J.-P. Ampuero, G. B. Brietzke, M. Käser, *J. Geophys. Res. Solid Earth* **117**, 2011JB008857 (2012).
21. C. Li, Z. Ma, X. Xi, G. Zhang, X. Shan, *Geophys. Res. Lett.* **51**, e2024GL108169 (2024).
22. Y. Huang, J.-P. Ampuero, *J. Geophys. Res. Solid Earth* **116**, 2011JB008684 (2011).
23. Y. Huang, J.-P. Ampuero, D. V. Helmberger, *J. Geophys. Res. Solid Earth* **119**, 3133–3154 (2014).
24. M. Abdelmeguid, M. S. Mia, A. Elbanna, *Geophys. Res. Lett.* **51**, e2023GL108060 (2024).
25. V. Lyakhovsky, Y. Ben-Zion, A. Agnon, *J. Geophys. Res.* **106**, 4103–4120 (2001).
26. L. Valoroso, L. Chiaraluce, C. Collettini, *Geology* **42**, 343–346 (2014).
27. Y. Wang, K. Sieh, S. T. Tun, K.-Y. Lai, T. Myint, *J. Geophys. Res. Solid Earth* **119**, 3767–3822 (2014).
28. E. O. Lindsey *et al.*, *Earth Planet. Sci. Lett.* **622**, 118384 (2023).
29. N. Hurukawa, P. Maung Maung, *Geophys. Res. Lett.* **38**, 2010GL046099 (2011).
30. Earthquake survivors in Mandalay face sanitation crisis in temporary shelters (Mizzima, 2025); https://bur.mizzima.com/2025/04/09/52626.
31. Strong earthquake in central Myanmar felt as far as Bangkok (Reuters, 2025); https://www.reuters.com/world/asia-pacific/strong-earthquake-central-myanmar-panic-bangkok-2025-03-28.
32. Myanmar earthquake caused damage to 847 households in Ruili, Yunnan [in Chinese] (Xinhua News Agency, 2025); https://www.xinhuanet.com/20250329/b3bcf429bdb544bb966b28c93a96bd5a/c.html.
33. N. Inoue *et al.*, *Seismica* **4**, v4i1.1691 (2025).
34. D. Melgar *et al.*, *Seismica* **4**, v4i2.1771 (2025).
35. Z. Peng *et al.*, Earthquake Research Advances, 100413 (2025).
36. S. L. Antoine, Y. Klinger, A. Delorme, R. D. Gold, *J. Geophys. Res. Solid Earth* **127**, e2022JB024480 (2022).
37. Y. Bai *et al.*, *Earth Planet. Sci. Lett.* **610**, 118105 (2023).
38. R. S. Stein, P. Bird, *Seismol. Res. Lett.* **95**, 3406–3415 (2024).
39. Y. Klinger, *J. Geophys. Res. Solid Earth* **115**, 2009JB006550 (2010).
40. H. S. Bhat, M. Olives, R. Dmowska, J. R. Rice, *J. Geophys. Res. Solid Earth* **112**, 2007JB005027 (2007).
41. P. Bird, R. S. Stein, *Seismol. Res. Lett.* **95**, 3306–3315 (2024).
42. G. Bertrand *et al.*, *Comptes Rendus Académie Sci. - Ser. IIA - Earth. Planet. Sci.* **327**, 479–484 (1998).
43. Y. Fialko, D. Sandwell, M. Simons, P. Rosen, *Nature* **435**, 295–299 (2005).
44. X. Xu *et al.*, *Geophys. J. Int.* **204**, 1867–1886 (2016).
45. Z. Jin, Y. Fialko, *Geophys. Res. Lett.* **48**, e2021GL095213 (2021).
46. Z. Ma *et al.*, *Geophys. Res. Lett.* **51**, e2023GL107788 (2024).
47. K. Jiang, W. Xu, L. Xie, *J. Geophys. Res. Solid Earth* **129**, e2024JB028826 (2024).
48. Q. Shi, S. Wei, M. Chen, *Geophys. J. Int.* **215**, 737–752 (2018).
49. S.-T. Lai *et al.*, *Earth Syst Sci Data Discuss* **2025**, 1–23 (2025).
50. M. Mello, H. S. Bhat, A. J. Rosakis, *J. Mech. Phys. Solids* **93**, 153–181 (2016).
51. X. Yang, G. L. Pavlis, Y. Wang, *Bull. Seismol. Soc. Am.* **106**, 1948–1962 (2016).
52. S. P. Hicks *et al.*, *Nat. Geosci.* **13**, 647–653 (2020).
53. H. Weng, J.-P. Ampuero, *J. Geophys. Res. Solid Earth* **124**, 8584–8610 (2019).
54. L. Bruhat, Z. Fang, E. M. Dunham, *J. Geophys. Res. Solid Earth* **121**, 210–224 (2016).
55. H. Weng, H. Yang, Z. Zhang, X. Chen, *J. Geophys. Res. Solid Earth* **121**, 4446–4457 (2016).
56. Y. Kaneko, N. Lapusta, *Tectonophysics* **493**, 272–284 (2010).
57. E. S. Cochran *et al.*, *Geology* **37**, 315–318 (2009).
58. P. Zhai, Y. Huang, C. Liang, J.-P. Ampuero, *Geophys. J. Int.* **242**, ggaf274 (2025).
59. Y. Ben-Zion, *Rev. Geophys.* **46**, 2008RG000260 (2008).
60. W. Fadil *et al.*, *Bull. Seismol. Soc. Am.* **113**, 613–635 (2023).
61. L. Y. Zhang *et al.*, *Geochem. Geophys. Geosystems* **21**, e2020GC009091 (2020).
62. S. Wei, Data and model files of "Supershear Rupture Sustained Through a Thick Fault Zone in the 2025 Mw 7.8 Mandalay Earthquake", Zenodo (2025); https://doi.org/10.5281/zenodo.17077559.

ACKNOWLEDGMENTS

We thank Y. Wang of the Department of Geology, National Taiwan University for the discussion on the earthquake geology and acknowledge Center for Geohazard Observations and Department of Meteorology and Hydrology of Myanmar for their work in seismic data acquisition. We thank the China Earthquake Networks Center for providing continuous waveform data. We acknowledge the Department of Meteorology and Hydrology in Naypyitaw and the GFZ Helmholtz Center for Geosciences (GFZ) for their collaborative efforts to install the strong motion station at Naypyitaw and make the data available. **Funding:** Funding for this work was provided by the Chinese Academy of Sciences (grant E4515401), the National Natural Science Foundation of China (grants 42494861 and NSFC92355001), the Postdoctoral Fellowship Program of CPSF (grant GZB20250098), the Tier 2 project "Integrating space geodesy and dense array seismology to reveal fundamental earthquake physics" supported by the Singapore Ministry of Education (MOE) (MOET2EP50124-0011). **Author contributions:** Conceptualization: S.W., X.W., Z.M.; Methodology: S.W., X.W., Z.M., C.L., H.Z., Q.S., H.C., M.L., Y.H.; Investigation: S.W., Z.M, X.W., C.L., H.Z., Q.S., H.C., M,L., Y.H.; Visualization: Z.M., C.L., X.W., H.C., S.W., Q.S., H.Z., Y.B., S.Y.; Funding acquisition: S.W., X.S.; Project administration: S.W.; Supervision: S.W.; Writing – original draft: S.W., M.Z., X.W., H.Z., C.L., Q.S.; Writing – review & editing: All authors. **Competing interests:** Authors declare that they have no competing interests. **Data and materials availability:** The ALOS-2 PALSAR images are owned by the Japanese Space Agency (JAXA) and provided to Z.M. under grant ER4A2N150. All Sentinel-1 SAR images are provided by the European Space Agency (ESA). All Sentinel-2 optical images are downloaded from the Google Earth engine applications (https://code.earthengine.google.com/_ah/conflogin?continue=https://code.earthengine.google.com/). The teleseismic data and strong motion waveforms are from the IRIS-DMC. Our SAR/InSAR. Part of earthquake source parameters (e.g., mainshock epicenter, moment tensor solutions) are downloaded from https://www.globalcmt.org/CMTsearch.html and https://www.usgs.gov/programs/earthquake-hazards. 3D surface deformation map, multiple-point-source solution, back-projection results, finite fault model, static slip model, total slip along the rupture and damage zone width can be downloaded from Zenodo (*62*). Strong motion waveform data were downloaded from strongmotioncenter.org. The raw teleseismic waveform data from the Earth Observatory of Singapore–Myanmar (EOS–Myanmar) seismic array and the processed receiver function (RF) waveforms are available for download at the World Data Center for Geophysics, Beijing (http://www.geophys.ac.cn/ArticleDataInfo.asp?MetaId=727).

SUPPLEMENTARY MATERIALS

science.org/doi/10.1126/science.adz2101
Methods and materials; figs. S1 to S32; Tables S1 and S3; References (*63–122*)

Submitted 22 May 2025; accepted 8 September 2025

10.1126/science.adz2101

RESEARCH ARTICLE

Bimaterial effect and favorable energy ratio enabled supershear rupture in the 2025 Mandalay earthquake

Liuwei Xu[1], Lingsen Meng[1]*, Zhang Yunjun[2,3], Yanchen Yang[4,5], Yidi Wang[2,3], Changyang Hu[2,3], Huihui Weng[6], Wenbin Xu[7], Elizabeth Su[1], Chen Ji[8]

Joint seismic and geodetic analyses revealed that the 2025 moment magnitude (M_w) 7.8 Mandalay, Myanmar, earthquake ruptured ~510 km of the Sagaing fault, with a sustained supershear rupture extending ~450 km on the southern branch. Far-field Mach waves and near-field ground motion confirmed the supershear nature. This exceptionally long supershear rupture caused building collapse and soil liquefaction, as observed in satellite imagery, offering insights into the damage potential of such ruptures in urban areas. Sustained supershear propagation was facilitated by the fault's linear geometry, prolonged interseismic quiescence, favorable energy ratio, and pronounced bimaterial contrasts across the fault interface. These findings underscore the roles of fault structure, stress accumulation, and material contrasts in governing rupture dynamics, demonstrating that large-scale supershear propagation can occur in interplate continental fault systems.

At 12:51 p.m. local time on 28 March 2025, a moment magnitude (M_w) 7.8 earthquake struck near the city of Mandalay, Myanmar. Situated at the junction of three tectonic plates—the Indian (IN), Eurasian (EU), and Burma (BU) plates (*1, 2*)—Myanmar is subject to high seismicity. The central longitudinal axis of the country, home to both the major economic center of Mandalay and the political capital NayPyiDaw, coincides with the boundary between the BU and EU plates (Fig. 1A). The right-lateral strike-slip Sagaing fault, which marks the boundary, spans ~1400 km and accommodates a relatively high slip rate of ~20 mm/year (*3, 4*). In the 20th century, the Sagaing fault generated at least seven magnitude (M) ≥ 7 earthquakes along different segments (Fig. 1A), with the exception of a seismic gap between Mandalay and NayPyiDaw (Fig. 1A) (*2, 5*). The 2025 Mandalay earthquake ruptured this long-standing seismic gap. The epicenter was located near Mandalay, and early reports indicated a bilateral, north-south (N-S)–oriented rupture (*6*). According to data compiled by the Democratic Voice of Burma, the earthquake resulted in 4355 confirmed fatalities, 210 people reported missing, and 7830 injured.

To obtain timely and comprehensive fault rupture details about the earthquake, we collected global seismic data and applied the slowness-enhanced back-projection (SEBP) method (*7*). SEBP enabled us to resolve the spatiotemporal evolution of high-frequency (HF) radiators along the fault during the mainshock. We also derived coseismic ground deformation using synthetic aperture radar (SAR) and optical imagery from the Sentinel-1, LuTan-1, ALOS-2, and Sentinel-2 satellites. These deformation observations, in combination with global and local seismic datasets, were jointly inverted through finite fault inversion (FFI) (*8, 9*) to reconstruct the slip distribution, rupture history, and slip vectors across the fault. Our integrated analysis of SEBP and joint FFI results revealed that the earthquake ruptured the subvertical Sagaing fault in a bilateral manner along the N-S direction. The northern branch rupture was relatively minor, with an approximate length of 60 km and an average rupture speed of 0.9 km/s. By contrast, the southern branch exhibited an unusually fast rupture, propagating ~450 km at a speed of 5.0 km/s, exceeding the local shear wave velocity and therefore classifying it as a supershear rupture. We confirmed the supershear nature of the southern segment by identifying Mach waves and Mach cones in the seismic wavefield and by analyzing ground motions recorded at a near-fault station.

Owing to the ongoing civil conflict in Myanmar, field investigations and postevent damage assessments have been substantially constrained. To address this limitation, we generated damage proxy maps (DPMs) and analyzed them in conjunction with other satellite radar imagery. DPMs highlight regions where the radar backscattering characteristics changed anomalously relative to their typical background variation, indicative of potential structural damage (*10, 11*). Optical satellite images revealed building collapses in urban areas and widespread secondary hazards (e.g., soil liquefaction, landslides), which aligned with regions of high DPM values. This study offers a detailed characterization of the prolonged and devastating earthquake, providing a set of observations that can serve as a reference for postevent hazard assessment.

Rupture kinematics resolved by SEBP and joint FFI

The SEBP analysis revealed an asymmetrical bilateral rupture propagating in the N-S direction. The HF radiators closely followed the surface trace of the Sagaing fault (Fig. 1A and figs. S1 to S9). All three arrays consistently indicated a fast rupture speed of 4.8 to 5.0 km/s on the southern branch (Fig. 1C; figs. S2B, S4B, and S6B; and movies S1 to S3). The length of the southern rupture segment was ~450 km. The speed substantially exceeded the local shear wave speed in the crust above depths of 20 km (2.5 to 3.7 km/s; fig. S10 and table S1) (*5*), suggesting supershear rupture. By contrast, the northern branch exhibited a shorter and slower rupture. Based on SEBP results, the northern rupture extended ~60 km with an estimated average speed of 0.9 km/s (*12*). The rupture speeds resolved by the three arrays showed greater variability, ranging from 0.9 to 1.7 km/s (figs. S2B, S4B, and S6B). This variation likely reflects uncertainties introduced by the relatively weak HF radiation from the northern branch, attributable to its slower rupture speed and interference from the southern branch's signal (*13*). We validated the speed measurements by applying back-projection to synthetic seismograms generated by a bilateral model with a subshear northern branch and a supershear southern branch (*12*) (figs. S11 to S13). The recovered southern speeds were 8 to 20% lower than the input value, whereas those of the northern branch were underestimated by 30% (figs. S11 and S12). Although such underestimation may be less pronounced in real earthquake back-projection, it suggests greater uncertainty in back-projection results for the northern branch. Nevertheless, the synthetic back-projection confirmed the supershear nature of the southern rupture and the subshear nature of the northern one.

The joint FFI results indicated that the rupture was predominantly right-lateral strike-slip (Fig. 2C and movie S4). The coseismic slip distribution aligned well with the HF radiators (Fig. 1C); north of the epicenter, slip extended ~60 km, whereas the southern rupture extended

---

[1]Department of Earth, Planetary and Space Sciences, University of California Los Angeles, Los Angeles, CA, USA. [2]National Key Laboratory of Microwave Imaging, Aerospace Information Research Institute, Chinese Academy of Sciences, Beijing, China. [3]School of Electronic, Electrical and Communication Engineering, University of Chinese Academy of Sciences, Beijing, China. [4]National Engineering Research Center for Remote Sensing Satellite Applications, Aerospace Information Research Institute, Chinese Academy of Sciences, Beijing, China. [5]School of Resources and Environment, University of Chinese Academy of Sciences, Beijing, China. [6]State Key Laboratory for Mineral Deposits Research, School of Earth Sciences and Engineering, Nanjing University, Nanjing, China. [7]School of Geoscience and Info-Physics, Central South University, Changsha, China. [8]Department of Earth Science, University of California, Santa Barbara, Santa Barbara, CA, USA. ***Corresponding author. Email: lsmeng@g.ucla.edu**

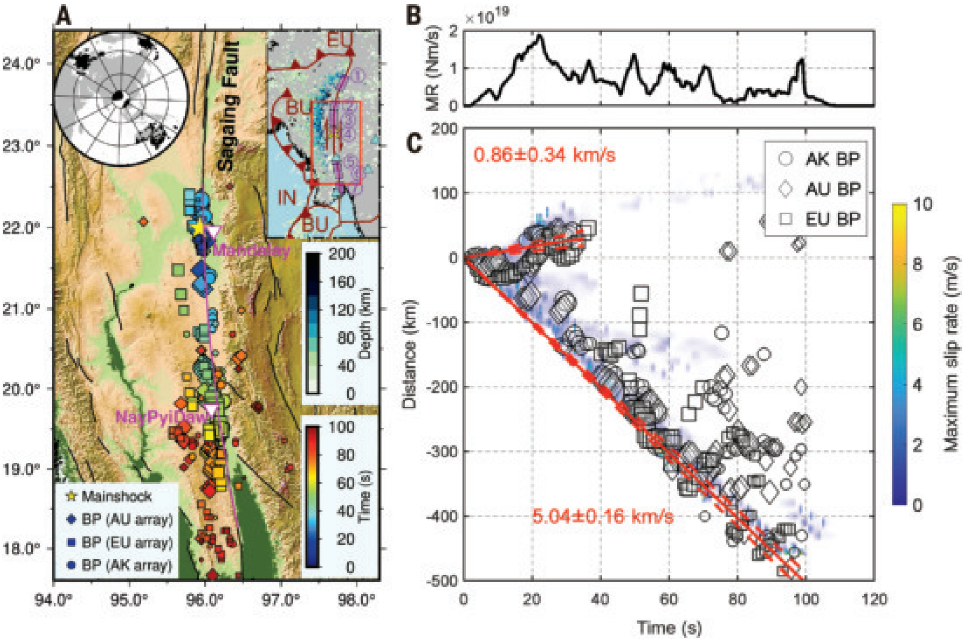

Fig. 1. Overview map and rupture process. (**A**) Back-projection (BP) results and active faults (black lines). (*2*). Colored symbols represent HF radiators imaged by three seismic arrays (see legend). Symbol size is proportional to beam power, and color indicates rupture time relative to the mainshock origin time (the lower legend). White triangles denote the major cities along the Sagaing fault. The magenta line denotes the surface rupture identified according to the ground deformation. (Inset, upper left) Locations of the three arrays. (Inset, upper right) The regional tectonic map. Colored dots indicate historical seismicity from 1 January 1990 to 3 April 2025, color-coded by hypocenter depth (the upper legend). Dark red lines mark plate boundaries (*1*, *2*). The red box highlights the source region shown in the main image. Cyan triangles denote strong motion stations. Purple bars denote rupture zones of historical *M* 7 earthquakes in the 20th century, with event names and magnitudes listed in table S3 (*2*). BU, Burma plate; IN, Indian plate; EU, Eurasian plate. (**B**) Moment rate function illustrating the temporal evolution of seismic moment release. (**C**) Rupture velocity from SEBP and comparison to the FFI. Symbols mark the timing and location of HF radiators. Locations are shown as along-fault distance relative to the hypocenter, with positive values to the north and negative values to the south. The red solid line indicates the best-fit rupture front, with standard deviation (±1 σ) outlined by dashed lines. The background colormap represents the maximum slip rate at each along-strike position from the FFI.

~450 km. Near the hypocenter, the fault dips 65° to the east, whereas along the southern branch, it steepens to 80° [see also (*12*)]. Slip was concentrated at shallow depths: About 75% of the seismic moment was released between 0- and 15-km depth, with a peak slip of ~7.9 m. The total seismic moment was 6.37×10^{20} N·m, corresponding to a moment magnitude of M_w 7.8. Most of the moment release occurred within the first 100 s (Fig. 1B). Rupture duration exceeded the typical value predicted by the global scaling relationship [~40 s (*14*)] but was comparable to that of some M_w 7.8 strike-slip events, such as the 2001 Kunlun (*15*), 2013 Scotia (*16*), and 2023 Türkiye earthquakes (*17*). Our model successfully reproduced static displacements observed in SAR and optical satellite data (figs. S14 to S16) and provided good fits to teleseismic and local strong-motion recordings (figs. S17 to S22), including at station NPW, located just 2 to 3 km from the fault (figs. S21 and S22). Nine additional inversions using different initial models yielded minor standard deviations in both objective function values and coseismic slip distributions [(*12*); fig. S23], confirming the robustness of our solution.

In the back-projection images, we observed that the HF radiators extended farther along the southern branch than mapped surface fault traces (Fig. 1A). The slip model revealed that the southern segment between 420 and 460 km hosted coseismic slip that did not reach the surface, thereby accounting for the discrepancy in rupture extent. Additionally, several southern radiators observed after 90 s exhibited a westward spatial bias relative to the fault trace, likely caused by coda-wave contamination during the rupture's terminal phase. The distribution of northern HF radiators was consistent with both the mapped surface traces and the slip model after calibration (*12*). The northern surface rupture terminated near ~22.5°N, coinciding with the southern edge of a M_w 6.8 strike-slip earthquake in 2012 (fig. S24) (*18*). This termination may reflect prior stress release from the 2012 event that impeded rupture propagation.

Aftermath estimation by satellite damage proxy maps

The DPMs derived from Sentinel-1A satellite imagery have served as a key tool for systematically assessing the mainshock and its impacts in the absence of on-ground postevent damage assessments (Fig. 3) (*10*–*12*, *19*). We found that areas exhibiting high DPM values closely align with the spatial orientation of fault traces, consistently forming a 2- to 3-km-wide zone along the fault (Fig. 3 and fig. S25). This pattern helps delineate the extent of off-fault damage and reveals widespread surface destruction beyond the primary rupture zone. By integrating building footprint data with hazard models from the US Geological Survey (USGS) and using a causal Bayesian network to model seismic multihazards and their impacts (*12*, *20*), we generated three high-resolution (45 m) hazard probability maps for building damage, liquefaction, and landslides, respectively (Fig. 3 and figs. S26-S28). Building collapses were observed in Mandalay, with high landslide potential identified at Sagaing Hill and high soil liquefaction potential in the Irrawaddy floodplain and the city's southeastern areas (Fig. 3). These findings underscore the multiscale mechanisms underlying seismic impacts and demonstrate the effectiveness of satellite-based seismic multihazard and impact assessments, particularly in regions where on-the-ground access is limited.

Validation of supershear rupture

We further validated the southern supershear rupture using surface wave observations. As proposed by (*21*), a supershear rupture exhibits distinct characteristics in the far-field surface wave field: within specific regions, waves from different parts of the rupture arrive simultaneously and interfere constructively, simplifying the Rayleigh and Love waveforms. This results in a high degree of similarity between the waveforms of the large supershear rupture and those of a smaller, colocated event (hereinafter referred to as an empirical Green's function, EGF). These regions of constructive interference are known as Mach cones, with the recorded surface waves referred to as Mach waves, and the angles between the Mach cones and the rupture direction termed Mach angles (*12*). We collected 76 Rayleigh waveforms to identify Mach waves and cones. To minimize surface wave dispersion, seismograms were bandpass filtered to 15 to 25 s following (*21*, *22*). The EGF was a M_w 5.1 event that occurred north of the mainshock epicenter with a similar focal mechanism (EGF 2, table S2 and fig. S24). We quantified waveform similarity using standard cross-correlation

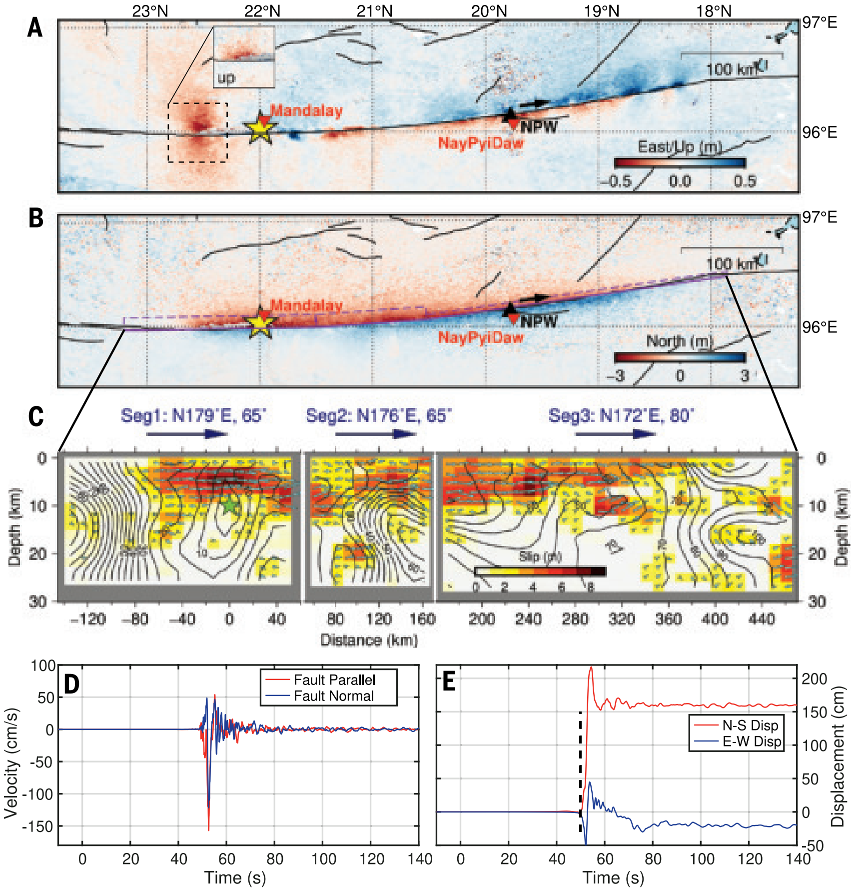

Fig. 2. Ground deformation and slip model. (**A**) East-west (E-W) ground deformation. The zoomed-in inset presents the vertical ground deformation with full coverage shown in fig. S32C. Inverted triangles denote major cities along the fault. The black triangle indicates the seismic station GE.NPW, and the arrow shows the FP direction (N172°E). The deformation reference point is set at (N20.0°, E94.6°), outside the figure extent. (**B**) N-S ground deformation. Purple boxes outline the boundaries of the fault model used in the joint FFI, with solid lines denoting the upper fault boundaries and dashed lines representing other boundaries. (**C**) Spatial distribution of final slip (color scale), rupture initiation time (black contours in seconds), and rake angle (cyan arrows) along the fault. Strike and dip angles for each fault segment are labeled at the top. (**D**) Comparison of FP (red) and FN (blue) velocity seismograms recorded at GE.NPW. Waveforms are obtained by integrating the raw acceleration data and removing baseline drifts. The time axis is referenced to the earthquake origin time (28 March 2025, 06:20:52 UTC). (**E**) Ground displacement time series at GE.NPW. N-S (red) and E-W (blue) components are shown. The bold dashed line marks the onset of substantial ground deformation, occurring 50 s after the origin time. Displacements are calculated by integrating the velocity seismograms and applying drift corrections.

coefficients (CCs) (*12*). On the southeast side of the epicenter, waveforms from the mainshock and the EGF exhibited high similarity (CCs > 0.85) at several Australian stations (e.g., AU.GVL, AU.STKA; Fig. 4C). On the southwest side, Mach waves were observed at stations in South Africa and Madagascar (e.g., II.SUR, II.ABPO; Fig. 4C). The Mach angle was 30° to 60°, which, assuming a local S wave speed (V_S) of 3.2 km/s, suggests a rupture speed of 3.4 to 5.8 km/s. This range is consistent with the rupture speed measured by SEBP, though minor uncertainties may arise from V_S variations, rupture complexity, and rupture speed fluctuations.

Theoretical analyses and laboratory experiments (*23*, *24*) have shown that a key characteristic of supershear ruptures is a dominant fault-parallel (FP) component in the near-fault ground velocity field, which exceeds the fault-normal (FN) component. This FP dominance has been observed in several reported supershear events, including the 2002 Denali, 2020 Caribbean, and 2023 Türkiye earthquakes (*25*–*29*). The seismic station GE.NPW, located 2 to 3 km from the fault trace (Fig. 2, A and B), recorded ground accelerations during the mainshock. After integrating the acceleration to velocity and removing the drift (*30*), we observed a larger peak ground velocity in the FP direction (~160 cm/s) than in the FN direction (~120 cm/s) (Fig. 2D). This amplitude pattern is consistent with the aforementioned supershear signature. Recent observations on the 2023 Türkiye earthquake (*31*) showed that a rupture propagating at 3 km/s could also generate the FP dominance, with this speed exceeding the V_s of 2.83 km/s in their model. Dynamic simulations (*32*) further demonstrated that an FP/FN > 1 indicates supershear rupture once the front stabilizes after the transition, though this ratio may fluctuate if the rupture front remains unsteady immediately following the supershear onset. To provide further constraint on rupture speeds, we integrated the acceleration waveforms twice to obtain displacement time series (Fig. 2E). Near-fault displacement records are known to be sensitive to slip on nearby fault segments (*33*). We identified the onset of significant horizontal ground displacement and interpreted it as the approximate arrival of the rupture front at the fault patch near the station. Motions in the N-S component began as early as ~50 s (Fig. 2E and fig. S29), corresponding to an estimated rupture speed of 4.9 km/s, given the station's epicentral distance of 246 km. This represents a lower bound on the average rupture velocity from the hypocenter, as we ignored undetectable fault slip, the 2- to 3-km distance from the fault to the station, and the vertical rupture propagation within the fault. Taken together, these complementary observations, including SEBP imaging, far-field Mach wave detection, near-field amplitude characteristics, and displacement-based rupture timing, collectively support the existence of a fast-propagating supershear rupture along the southern segment of the fault.

Supershear ruptures controlled by bimaterial effect, energy ratio, and fault geometry

The 2025 Mandalay earthquake exhibited two remarkable features: an exceptionally early transition to supershear rupture and a prolonged supershear propagation spanning at least 400 km, making it one of the longest documented supershear earthquakes to date. Several mechanisms have been proposed to explain supershear transition, i.e., how rupture accelerates to the supershear regime. The classic Burridge-Andrews mechanism (*34*, *35*) suggests that the rupture front at a sub-Rayleigh speed is preceded by a daughter crack, whose speed is the S wave speed at the beginning and accelerates to a stable supershear speed after a certain distance. Given a high initial shear stress and/or a weak fault, rupture can also directly transition to the supershear regime before apparent formation of a daughter crack (*36*). In addition to the assumption of uniform properties, the heterogeneities of fault strength and stress (*36*–*38*), free surface (*39*), fault roughness, curvature, or bending (*40*, *41*), fault step-overs (*42*), damage zones (*43*), and bimaterial effects (*44*–*46*) may also promote supershear transition. The southern segment of the Mandalay earthquake shared several similarities with the 2018 M_w 7.5 Palu event but exhibited a higher rupture speed (5 km/s compared with 4.1 km/s in the Palu event). This exceptionally long and fast rupture offers a valuable opportunity to assess theoretical and numerical models of supershear propagation.

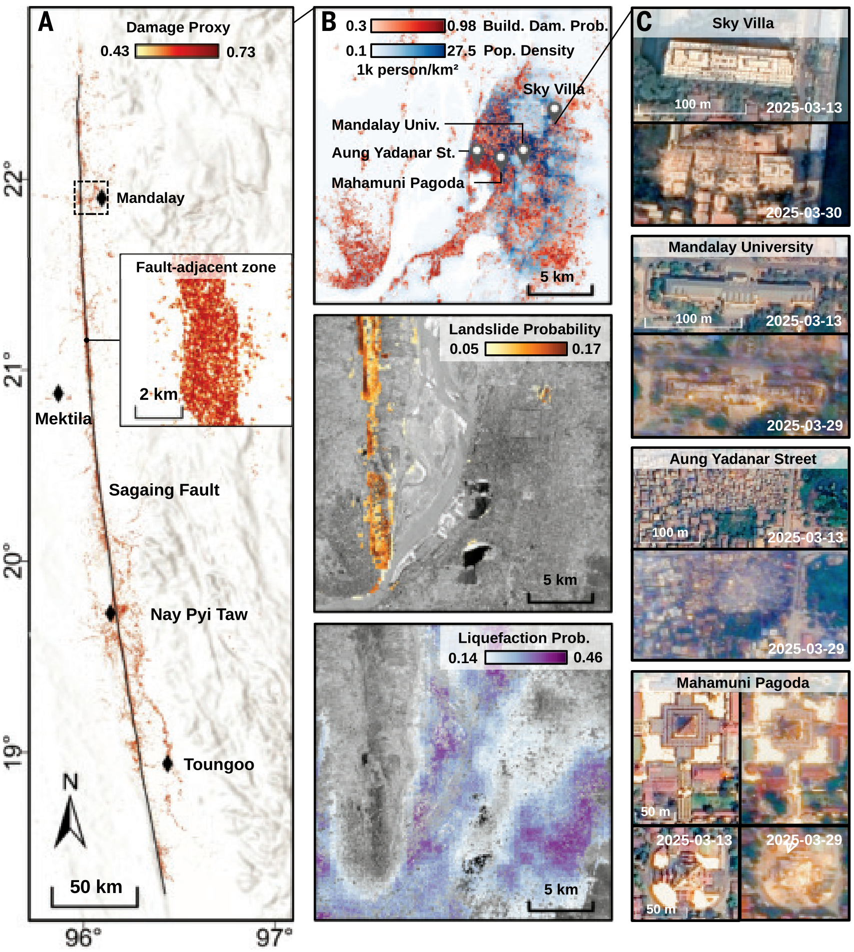

Fig. 3. Multihazard analysis of the earthquake region along the Sagaing fault. (**A**) DPM with white-to-red scale indicating increasing damage probability along the fault. (Inset) An enlarged view of a high-DPM zone near the fault. (**B**) Hazard probability distribution in Mandalay (light-to-dark scale), including building damage (top), landslides (middle), and liquefaction (bottom). Background layers show population density (white-to-blue scale) and Gaofen-1 optical imagery. (**C**) Damage interpretation in Mandalay derived from Jilin-1 optical imagery.

The Sagaing fault separates the Central Myanmar Basin to the west from Shan-Thai Block to the east (figs. S30 and S31). The former is characterized by a thick (~15 km) low-velocity layer consisting of Cenozoic basin sediments, and the latter features granite and the Mogok metamorphic belts with minimal sediment cover (*5*, *47*). The V_s structure along the Sagaing fault (*5*) reveals a pronounced material contrast across the fault within the shallowest 10 km, where most coseismic slip occurred. The eastern side exhibits V_s values of 2.8 to 3.7 km/s, whereas the western side shows lower V_s values of 2.2 to 3.3 km/s. By estimating the average velocity within the top 10 km as $V_{s\_mean}=10/\Sigma(dz/V_s)$, we obtained a V_{s_mean} of 2.9 and 3.3 km/s for the western and eastern sides, respectively. The difference in V_s suggests a difference in rock stiffness (*48*), a bimaterial contrast that influences rupture speed (*44*–*46*, *49*). Given the right-lateral strike-slip nature of the Sagaing fault, the southward rupture propagated in the negative direction, i.e., the moving direction of the stiff medium. Laboratory experiments and numerical simulations have shown that, in this direction, normal stress initially increases behind the rupture tip and decreases ahead of it. As the rupture propagates, the normal stress reduction becomes more pronounced, causing a broader region ahead of the rupture tip to yield simultaneously and accelerating the rupture to supershear speed. Once the rupture reaches supershear, the normal stress perturbation behind the crack tip reverses and becomes extensional rather than compressional (*44*–*46*, *50*). Conversely, rupture propagating in the positive direction (the moving direction of compliant medium) tends to experience increased normal stress ahead of the rupture tip, which favors subshear or nonsustained supershear behavior, explaining the slow rupture observed along the northern segment. However, dynamic simulations also predict a longer rupture extension in the positive direction compared with that in the negative direction (*51*, *52*), contrasting with the shorter northern branch of the Mandalay earthquake. This discrepancy could be explained by the five $M \geq 6.8$ events that occurred in the north between 1946 and 2012, which reduced stress accumulation (*2*) (Fig. 1A, table S3).

The observed rupture speed of 5 km/s was anomalously fast, corresponding to rupture speed/shear wave speed (V_r/V_s) ratios of 1.6 to 1.8, exceeding the Eshelby speed of $\sqrt{2} * V_s$ expected for rupture in a homogeneous medium (*53*). It also surpassed the predicted upper limit—the compliant side's compressional wave speed (V_p)—suggested by numerical simulations for the material contrast level across the Sagaing fault [$V_{s\_compliant}/V_{s\_stiff} = 0.85$; (*46, 50*)] (fig. S31). These observations imply that factors beyond the bimaterial effect may have also contributed to the extreme rupture acceleration. One potential contributor is the poroelastic effect. Along the bimaterial Sagaing fault, the compliant side consists of porous sedimentary rocks, whereas the stiffer side comprises less porous metamorphic rocks (*54*). This material contrast could enhance the bimaterial effect and further promote rupture acceleration (*55*). Additionally, an elevated stress level due to the long period of seismic quiescence as well as the free-surface effect (*39*, *56*) may have played roles. Near-fault investigations, including mapping of distributed deformation, rock sampling from boreholes, and cross-fault seismic reflection experiments, will help evaluate these possibilities.

The ratio between the dissipated and potential energies (G_c/G_0) is another key factor controlling rupture propagation (*57*). Here, G_c represents the fracture energy dissipated near the rupture front, whereas G_0 denotes the static elastic energy release rate for strike-slip rupture with a finite rupture width (*12*). Theory and numerical simulations have demonstrated that persistent supershear propagation is permitted when $G_c/G_0 < 0.7$ is satisfied on a purely strike-slip fault (*57*). The southern segment of the Sagaing fault, between Mandalay and NayPyiDaw, has remained seismically quiescent without experiencing any $M \geq 7$ earthquakes since 1839 (Fig. 1A) (*2*). This prolonged interseismic period results in considerable prestress accumulation and slip deficit. Because G_0 depends more strongly than G_c on slip deficit (*12*, *56*), the energy ratio G_c/G_0 decreases with longer interseismic intervals. Thus, the extended seismic quiescence led to another favorable condition for sustained supershear rupture.

Fault geometry also has an important influence on earthquake rupture propagation. We found that the southern segment of the Sagaing fault exhibits a remarkably simple and linear geometry, which is conducive to persistent supershear propagation (*58*). The three-segment fault model used in the joint FFI incorporated a total strike variation of only 9° (Fig. 2). From the epicenter to (21.51°N, 95.99°E), the first segment extends ~55 km with a strike of 179°. The following 110-km segment to the south adopts a strike of 176°, and then the strike shifts

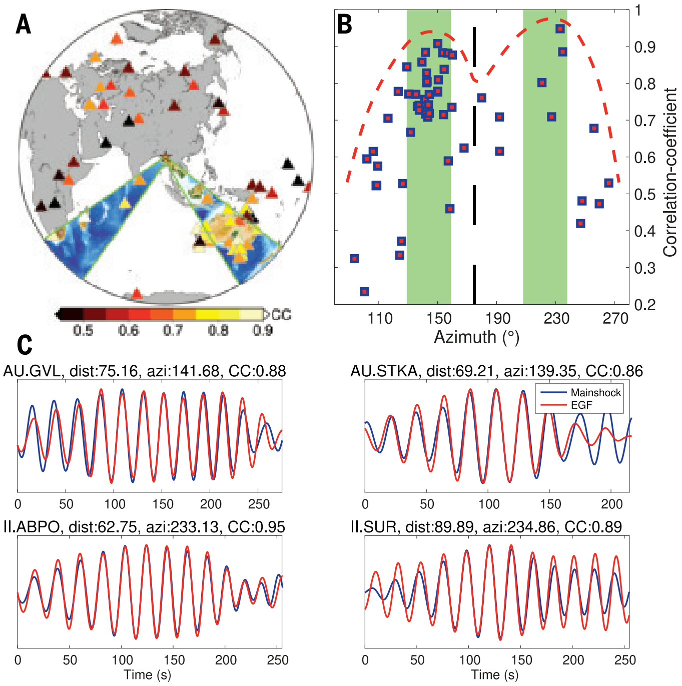

Fig. 4. Far-field Rayleigh wave Mach cones and waves. (**A**) Mach cone distribution. Colored areas within the green boundaries mark the Mach cones, where Mach waves have been identified. Seismic station locations are shown as triangles, with color indicating the CCs between 15- and 25-s Rayleigh wave displacement seismograms from the M_w 7.8 Mandalay mainshock and the M_w 5.1 EGF event. (**B**) Azimuthal distribution of waveform similarity. CCs between 15- and 25-s Rayleigh waveforms of the mainshock and EGF, plotted as a function of station azimuth. The black dashed line marks the rupture direction of the southern segment. Green bands denote the azimuthal extent of the identified Mach cones, accounting for uncertainties in Rayleigh wave phase and rupture velocities. The red dashed curve indicates the envelope that delineates the distribution pattern of CCs. (**C**) Representative Mach waves. Bandpass-filtered vertical displacement Rayleigh wave seismograms for the mainshock (blue) and EGF (red) at selected stations. Station name, azimuth (azi), and epicentral distance (dist; in degrees) are annotated.

to 172° for the next 220 km. Near the southern terminus, the strike rotates slightly to 170°. Whereas this three-segment model is a simplified representation of the fault based on ground deformation (Fig. 2B), detailed inspection of the surface trace indicates that the curve of the fault is continuous without any sizeable kinks or step-overs (fig. S32). Numerical simulations and laboratory experiments by (*59*, *60*) demonstrated that ruptures can propagate at supershear speeds across fault bends of 10°, whether on the extensional or compressional side, without any reduction in propagation velocity. Therefore, the geometrically simple and linear structure of the Sagaing fault likely helped to sustain supershear rupture propagation, consistent with observations in other large events (*58*).

REFERENCES AND NOTES

1. P. Bird, *Geochem. Geophys. Geosyst.* **4**, 2001GC000252 (2003).
2. Y. Wang, K. Sieh, S. T. Tun, K.-Y. Lai, T. Myint, *J. Geophys. Res. Solid Earth* **119**, 3767–3822 (2014).
3. G. Bertrand *et al.*, *C. R. Acad. Sci. II* **7**, 479–484 (1998).
4. C. Vigny *et al.*, *J. Geophys. Res.* **108** (B11), 2002JB001999 (2003).
5. X. Wang *et al.*, *J. Geophys. Res. Solid Earth* **124**, 504–526 (2019).
6. Z. Peng *et al.*, Mainshock rupture properties, aftershock activities and remotely triggered seismicity associated with the 2025 Mw 7.7 Sagaing Fault earthquake in Myanmar. EarthArXiv X5BQ7D (2025); https://doi.org/10.31223/X5BQ7D.
7. L. Meng, A. Zhang, Y. Yagi, *Geophys. Res. Lett.* **43**, 628–636 (2016).
8. C. Ji, D. J. Wald, D. V. Helmberger, *Bull. Seismol. Soc. Am.* **92**, 1192–1207 (2002).
9. G. Shao, X. Li, C. Ji, T. Maeda, *Earth Planets Space* **63**, 559–564 (2011).
10. S.-H. Yun *et al.*, *Seismol. Res. Lett.* **86**, 1549–1556 (2015).
11. Z. E. Ross *et al.*, *Science* **366**, 346–351 (2019).
12. Materials and methods are available as supplementary materials.
13. L. Xu *et al.*, *J. Geophys. Res. Solid Earth* **128**, e2022JB025936 (2023).
14. D. Melgar, G. P. Hayes, *Geophys. Res. Lett.* **44**, 9691–9698 (2017).
15. D. Wang, J. Mori, K. Koketsu, *Earth Planet. Sci. Lett.* **440**, 115–126 (2016).
16. L. Ye *et al.*, *Earth Planet. Sci. Lett.* **401**, 215–226 (2014).
17. L. Xu *et al.*, *Commun. Earth Environ.* **4**, 379 (2023).
18. L. T. Aung *et al.*, The 2012 Mw 6.8 Thabeikkyin earthquake in central Myanmar: A widely felt strong event with unilateral rupture through the Singu basalt on the Sagaing fault." in AGU Fall Meeting, 12 to 16 December 2022, Chicago, IL (AGU, 2022).
19. Y. Yang *et al.*, *Int. J. Appl. Earth Obs. Geoinf.* **133**, 104133 (2024).
20. S. Xu, J. Dimasaka, D. J. Wald, H. Y. Noh, *Nat. Commun.* **13**, 7793 (2022).
21. M. Vallée, E. M. Dunham, *Geophys. Res. Lett.* **39**, L05311 (2012).
22. H. Bao *et al.*, *Nat. Geosci.* **12**, 200–205 (2019).
23. M. Mello, H. S. Bhat, A. J. Rosakis, *J. Mech. Phys. Solids* **93**, 153–181 (2016).
24. V. Rubino, A. J. Rosakis, N. Lapusta, *J. Geophys. Res. Solid Earth* **125**, e2019JB018922 (2020).
25. E. M. Dunham, R. J. Archuleta, *Bull. Seismol. Soc. Am.* **94** (6B), S256–S268 (2004).
26. H. Bao *et al.*, *Nat. Geosci.* **15**, 942–949 (2022).
27. M. Abdelmeguid *et al.*, *Commun. Earth Environ.* **4**, 456 (2023).
28. C. Ren *et al.*, *Science* **383**, 305–311 (2024).
29. A. Rosakis, M. Abdelmeguid, A. Elbanna, *Nat. Geosci.* **18**, 534–541 (2025).
30. D. M. Boore, *Bull. Seismol. Soc. Am.* **91**, 1199–1211 (2001).
31. B. Delouis, M. van den Ende, J.-P. Ampuero, *Bull. Seismol. Soc. Am.* **114**, 726–740 (2023).
32. S. Yao, H. Yang, *Sci. Adv.* **11**, eadq0154 (2025).
33. H. Kanamori, E. E. Brodsky, *Rep. Prog. Phys.* **67**, 1429–1496 (2004).
34. R. Burridge, *Geophys. J. Int.* **35**, 439–455 (1973).
35. D. J. Andrews, *J. Geophys. Res.* **81**, 5679–5687 (1976).
36. Y. Liu, N. Lapusta, *J. Mech. Phys. Solids* **56**, 25–50 (2008).
37. E. M. Dunham, P. Favreau, J. M. Carlson, *Science* **299**, 1557–1559 (2003).
38. J. N. Hayek *et al.*, *Geophys. Res. Lett.* **51**, e2024GL110128 (2024).
39. Y. Kaneko, N. Lapusta, *Tectonophysics* **493**, 272–284 (2010).
40. L. Bruhat, Z. Fang, E. M. Dunham, *J. Geophys. Res. Solid Earth* **121**, 210–224 (2016).
41. X. Ma, A. Elbanna, *Earth Planet. Sci. Lett.* **523**, 115702 (2019).
42. K. J. Ryan, D. D. Oglesby, *J. Geophys. Res. Solid Earth* **119**, 5814–5829 (2014).
43. Y. Huang, J. P. Ampuero, D. V. Helmberger, *Earth Planet. Sci. Lett.* **433**, 109–115 (2016).
44. S. Langer, L. Olsen-Kettle, D. Weatherley, *Geophys. J. Int.* **190**, 1169–1180 (2012).
45. H. Shlomai, J. Fineberg, *Nat. Commun.* **7**, 11787 (2016).
46. H. Shlomai, M. Adda-Bedia, R. E. Arias, J. Fineberg, *J. Geophys. Res. Solid Earth* **125**, e2020JB019829 (2020).
47. A. Mitchell, The Shan Plateau West of the Salween, *Geological Belts, Plate Boundaries, and Mineral Deposits in Myanmar*, A. Mitchell, Ed. (Elsevier, 2018), pp. 19–76.
48. D. Boore, *Bull. Seismol. Soc. Am.* **106**, 316–320 (2016).
49. K. Xia, A. J. Rosakis, H. Kanamori, J. R. Rice, *Science* **308**, 681–684 (2005).
50. Z. Shi, Y. Ben-Zion, *Geophys. J. Int.* **165**, 469–484 (2006).
51. M. Abdelmeguid, A. Elbanna, *Earth Planet. Sci. Lett.* **593**, 117648 (2022).
52. D. J. Andrews, Y. Ben-Zion, *J. Geophys. Res.* **102** (B1), 553–571 (1997).
53. K. Xia, A. J. Rosakis, H. Kanamori, *Science* **303**, 1859–1861 (2004).
54. Z. Zhou *et al.*, *J. Oceanol. Limnol.* **42**, 1074–1086 (2024).
55. E. M. Dunham, J. R. Rice, *J. Geophys. Res.* **113** (B9), 2007JB005405 (2008).
56. J. Xu, H. Zhang, X. Chen, *Geophys. J. Int.* **202**, 2194–2206 (2015).
57. H. Weng, J. P. Ampuero, *Nat. Geosci.* **13**, 817–821 (2020).
58. M. Bouchon *et al.*, *Tectonophysics* **493**, 244–253 (2010).
59. C.-E. Rousseau, A. J. Rosakis, *J. Geophys. Res.* **108** (B9), 2002JB002310 (2003).
60. E. L. Templeton *et al.*, *J. Geophys. Res.* **114** (B8), 2008JB006174 (2009).
61. R. Burns, piyushrpt, Z. Yunjun, B. Marfito, C. Liang, H. Fattahi, E. Fielding, Microwave Remote Sensing Laboratory, G. Manipon, S. Mirzaee, S. Staniewicz, Andy CA6JAU, V. Schut, asolarte, mzzhong, dbekaert, S. S. Sangha, Russell, G. H. X. Shiroma, L. Zhu, shitong01, hbparache, J. H. Kennedy, F. Amelung, bbuzz31/isce2: Buzzanga et al., 2023, (v2.6.3), Zenodo (2023); https://doi.org/10.5281/zenodo.8157051.
62. L. Xu, Z. Yunjun, Y. Yang, Y. Wang, C. Hu, Geodetic Deformation, DPM products, and source imaging results in "Bimaterial Effect and Favorable Energy Ratio Enabled Supershear Rupture in the 2025 Mandalay Earthquake", Zenodo (2025); https://doi.org/10.5281/zenodo.17113746.
63. L. Xu, L. Meng, Codes for Slowness-Enhanced Back-Projection (SEBP), Zenodo (2024); https://doi.org/10.5281/zenodo.12801968.
64. U.S. Geological Survey, Earthquake Hazards Program, Advanced National Seismic System (ANSS) Comprehensive Catalog of Earthquake Events and Products: Various (2017); https://doi.org/10.5066/F7MS3QZH.
65. G. Ekström, M. Nettles, A. M. Dziewonski, *Phys. Earth Planet. Inter.* **200-201**, 1–9 (2012).

66. R. Newman *et al.*, Wilber 3: A Python-Django Web Application For Acquiring Large-scale Event-oriented Seismic Data, Incorporated Research Institutions for Seismology (2013); https://ds.iris.edu/wilber3/.
67. A. Strollo *et al.*, *Seismol. Res. Lett.* **92**, 1788–1795 (2021).
68. GEOFON Data Centre, GEOFON Seismic Network (GFZ Helmholtz Centre for Geosciences, 1993). https://doi.org/10.14470/TR560404.
69. M. Beyreuther *et al.*, *Seismol. Res. Lett.* **81**, 530–533 (2010).
70. WorldPop, WorldPop Global Project Population Data; https://hub.worldpop.org/.
71. U.S. Geological Survey, Earthquake Hazards Program; https://earthquake.usgs.gov/earthquakes/eventpage/us7000pn9s/ground-failure/about.
72. Changguang Satellite, Jilin-1 Repository; https://www.jl1mall.com/resrepo/.
73. D. Gansu, *RSC: Comparative Analysis Data Before and After the Myanmar Earthquake on March 28, 2025* (National Tibetan Plateau / Third Pole Environment Data Center, 2025).
74. P. Wessel, W. H. F. Smith, *Eos* **79**, 579 (1998).
75. R. B. Lohman, W. D. Barnhart, *J. Geophys. Res. Solid Earth* **115**, 12413 (2010).

ACKNOWLEDGMENTS

We thank reviewer M. Abdelmeguid and the two anonymous reviewers for their constructive comments. We thank China Earthquake Networks Center (CENC) for providing the aftershock catalog. We thank Y. Wang for providing the fault dataset of Myanmar. We thank the US Geological Survey for providing Sentinel-2 and surface rupture data. We thank the European Space Agency, China Centre for Resources Satellite Data and Application, and Aerospace Exploration Agency for providing the Sentinel-1, LuTan-1, and ALOS-2 SAR imagery. We thank Google Maps for providing topography and world street maps. **Funding:** This work is supported by the NSF grant EAR-2506181 (L.X., L.M.) and the National Natural Science Foundation of China grants 42388102 and 42174023 (W.X.). **Author contributions:** Conceptualization: L.M., C.J., Z.Y., L.X.; Methodology: L.X., C.J., L.M., Z.Y., Y.Y.; Investigation: L.X., Z.Y., Y.Y., Y.W., C.H., H.W., C.J., E.S.; Visualization: L.X., Z.Y., Y.Y., Y.W., C.H., W.X.; Supervision: L.M., C.J., Z.Y.; Writing – original draft: L.X., H.W., Z.Y., C.J., Y.Y.; Writing – review & editing: all authors. **Competing interests:** The authors declare that they have no competing interests. **Data and materials availability:** All data are available in the main text or the supplementary materials. The SAR processing is performed using the ISCE-2 software, available at (*61*). The geodetic dataset, DPM products, and source imaging results of this study are available at (*62*). The MATLAB code for SEBP is available at (*63*). The moment tensor solutions came from the USGS (http://earthquake.usgs.gov) (*64*) and the Global Centroid Moment Tensor project (http://www.globalcmt.org) (*65*). All teleseismic data can be downloaded through the IRIS Wilber 3 system (https://ds.iris.edu/wilber3/) (*66*) and ORFEUS (www.orfeus-eu.org) (*67*). The local strong motion data can be downloaded from IRIS Wilber 3 system (https://ds.iris.edu/wilber3/) (*66*) and GFZ Helmholtz Centre for Georesearch (https://geofon.gfz.de/) (*68*). The Python software package Obspy (www.obspy.org) (*69*) was used for seismic data requesting and waveform filtering. Some of the images in the figures were based on optical images from Google Map, World Hillshade, OpenStreetMap, Jilin-1, and GaoFen series of satellites. Population density data was from the WorldPop Global Project Population Data (https://hub.worldpop.org/) (*70*). The hazard model and fault traces data are available on USGS (https://earthquake.usgs.gov/earthquakes/eventpage/us7000pn9s/executive) (*71*). The Jilin-1 imagery source is available at https://www.jl1mall.com/resrepo/ (*72*). The Gaofen series datasets are provided by National Tibetan Plateau/Third Pole Environment Data Center (http://data.tpdc.ac.cn) (*73*). Figures were produced using Generic Mapping Tools (*74*), Obspy, and Matlab. The static displacement data was downsampled by InSamp (https://github.com/williamBarnhart/InSamp) (*75*).

SUPPLEMENTARY MATERIALS

science.org/doi/10.1126/science.ady6100
Materials and Methods; Figs. S1 to S40; Tables S1 to S6; References (*76–118*);
Movies S1 to S4

Submitted 28 April 2025; accepted 8 September 2025

10.1126/science.ady6100

PRIZE ESSAY

NEUROSCIENCE

Respecifying partners

Neural circuits are rewired by manipulating cell surface combinatorial code

Cheng Lyu

Imagine being an axon during brain development. Your task is to find the correct synaptic partner in a brain filled with billions of neurons (*1*). It is a daunting challenge. The billion neurons in our brains form approximately 10^{14} synapses. That means that each axon must somehow identify the right partner from a vast number. How does the developing brain accomplish this feat of precision? And what happens to us when it fails?

One strategy that nature uses to make this complex problem more manageable is dimensionality reduction—essentially, it narrows down the search space. In some neural tissues, such as the layered vertebrate retina (*2*–*4*), the process is staged: First, neurons target a specific layer [a one-dimensional (1D) search], and then they look for the correct partner within that layer (a 2D search). But this simplification does not apply everywhere. For example, in adult fruit flies (*Drosophila melanogaster*), approximately 50 types of olfactory receptor neurons (ORNs) synapse with 50 types of projection neurons (PNs) in a one-to-one fashion at 50 discrete glomeruli, which together occupy stereotyped 3D positions in the antennal lobe. How is this feat achieved?

DA1-ORN axons rewired to VA1v-PN dendrites

Confocal images of four fly antennal lobes (each column shows the same lobe) showing DA1-ORN axons (top row), DA1-PN or VA1v-PN dendrites (middle row), and their merge with glomerular staining in gray (bottom row). PN dendrite borders are indicated with a dashed line. Wild-type flies (left two columns) and DA1-ORN–rewired flies (right two columns) are shown.

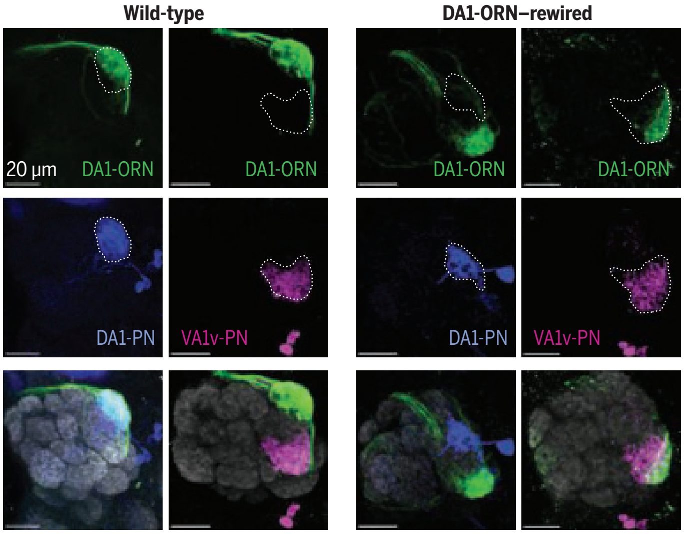

GRAPHIC: ADAPTED FROM (*12*) BY A. FISHER/*SCIENCE*

To answer this developmental question, it is necessary to study development dynamically, watching it unfold in real time. This is tricky: Gene expression in neurons changes rapidly as brains mature, which makes it difficult to track specific cell types using traditional genetic tools. To get around this hurdle, my colleagues and I developed a framework that allowed us to genetically label individual ORN and PN types consistently across developmental stages (*5*).

We discovered that although the adult antennal lobe is a 3D structure, the most critical phase of partner selection between ORNs and PNs occurs on a temporary 2D surface. During this period, ORN axons grow along the lobe surface, and PN dendrites extend outward to meet them—even those PNs that eventually settle deeper inside. This finding means that the initial partner search is effectively constrained to a 2D space.

The simplification does not stop there. We observed that each ORN type follows a genetically hardwired trajectory along the lobe surface, and this trajectory intersects with dendrites of its destined PN partner. This process further narrows the search from two dimensions to essentially one dimension. Each ORN "walks" a predetermined path and selects its partner from just a handful of candidate PN types along the way.

Although this model was largely built from observations of normal development across many ORN and PN types, it was also supported by cell type–specific perturbation experiments. When we genetically rerouted ORN axons away from their usual paths, their intended PN partners failed to migrate inward as usual. Instead, they remained stalled on the surface, as if waiting for their missing axonal partner. Moreover, the more that we rerouted the ORN trajectories, the more mismatched their connections became, which revealed a strong correlation between trajectory deviation and partner mismatch.

How does an ORN axon choose one synaptic partner out of a handful of potential candidates? Decades of research point to the role of cell surface proteins—ligands and receptors—that mediate attraction and repulsion between specific neuron types (*6*–*8*). But disrupting a single gene often yields only partial defects. Even null mutations, which completely eliminate gene function, typically produce only subtle or incomplete phenotypes. This result suggests that these proteins operate combinatorially or redundantly, which makes the system robust but also harder to decode using traditional "one-gene-at-a-time" methods.

An alternative approach to testing an understanding of a system is to rebuild it from key components. As the physicist Richard Feynman once said, "What I cannot create, I do not understand." So we investigated whether we could rewire an ORN to form a new connection with a different PN by changing its cell surface molecular profile.

We focused on rewiring a group of ORNs that normally targets the DA1 glomerulus (DA1-ORNs) to instead form synapses with a group of PNs that normally receives input from the VA1v glomerulus (VA1v-PNs). We began by identifying candidate cell surface proteins using single-cell RNA sequencing (*9*, *10*) followed by genetic screening (*11*). We found dozens of proteins that, when manipulated, partially altered wiring patterns. We then performed systematic tests using RNA interference and gene overexpression tools to probe different combinations.

After extensive trials, we successfully rewired DA1-ORN axons to VA1v-PN dendrites by manipulating just five key proteins in one cell type (DA1-ORNs; see the figure), all in a fly engineered with 11 transgenes (*12*). We grouped our manipulations into three strategic categories: (i) increase repulsion between DA1-ORNs and their original DA1-PN partners, (ii) decrease repulsion between DA1-ORNs and the new VA1v-PN targets, and (iii) match attraction between DA1-ORNs and VA1v-PNs. No single manipulation resulted in major rewiring. A combination of two strategies produced intermediate effects. But when all three were applied, the rewiring was robust and consistent. Even more, this same strategy could be used to rewire other ORN-PN pairs, demonstrating the generalizability of the approach.

But do these anatomical changes translate to changes in function and behavior? To find out, we used calcium imaging to measure neuronal activity in live flies. We found that the rewired VA1v-PNs now responded to 11-*cis*-vaccenyl acetate (cVA), a pheromone typically only detected by DA1-ORNs (*13*, *14*). In wild-type flies, cVA detection suppresses male-male courtship (*14*). Meanwhile, odorants that activate VA1v-ORNs promote courtship (*15*). So, if VA1v-PNs now receive inputs from DA1-ORNs, the response to cVA might be misinterpreted or perhaps even reversed. We tested this idea by measuring courtship activity between males. As predicted, the rewired male flies appreciably increased courtship toward other males—a notable behavioral shift. This finding confirmed that altering neural wiring can indeed change how sensory information drives behavior.

Our study shows that synaptic specificity in developing brains can be determined by a small set of cell surface proteins acting in combination. These proteins orchestrate a combinatorial usage of attraction and repulsion that guides axons to their correct partners. By tweaking just a few of these components, we were able to respecify both neural and behavioral partners, opening doors for exploring how changes in circuit wiring contribute to neurodevelopmental disorders and how similar principles may have shaped the evolution of brain circuits across species. □

REFERENCES AND NOTES

1. F. A. C. Azevedo *et al.*, *J. Comp. Neurol.* **513**, 532 (2009).
2. J. R. Sanes, S. L. Zipursky, *Neuron* **66**, 15 (2010).
3. J. R. Sanes, S. L. Zipursky, *Cell* **181**, 536 (2020).
4. E. Agi *et al.*, *Science* **383**, 1084 (2024).
5. C. Lyu *et al.*, *Science* **388**, 538 (2025).
6. R. W. Sperry, *Proc. Natl. Acad. Sci. U.S.A.* **50**, 703 (1963).
7. B. J. Dickson, *Science* **298**, 1959 (2002).
8. A. L. Kolodkin, M. Tessier-Lavigne, *Cold Spring Harb. Perspect. Biol.* **3**, a001727 (2011).
9. C. N. McLaughlin *et al.*, *eLife* **10**, e63856 (2021).
10. Q. Xie *et al.*, *eLife* **10**, e63450 (2021).
11. Z. Li *et al.*, bioRxiv 10.1101/2025.03.01.640985 (2025).
12. C. Lyu, Z. Li, C. Xu, J. Kalai, L. Luo, bioRxiv 10.1101/2025.03.01.640986 (2025).
13. T. S. Ha, D. P. Smith, *J. Neurosci.* **26**, 8727 (2006).
14. A. Kurtovic, A. Widmer, B. J. Dickson, *Nature* **446**, 542 (2007).
15. H.-H. Lin *et al.*, *Neuron* **90**, 1272 (2016).

10.1126/science.aeb5128

Department of Biology, Stanford University, Stanford, CA, USA. Email: chenglyu@stanford.edu

PHOTOS: (TOP TO BOTTOM) COURTESY OF JUNJIE ZHANG; RYUJI SUZUKI; CLAIRE BALLARD

GRAND PRIZE WINNER

Cheng Lyu received an undergraduate degree from Peking University and a PhD from Rockefeller University. After completing his postdoctoral fellowship at Stanford University, he will start his laboratory in the School of Life Sciences at Westlake University in 2026. His research focuses on exploring how developmental changes in neural circuits shape animal behavior in ethologically meaningful ways. **www.science.org/doi/10.1126/science.aeb5128**

FINALISTS

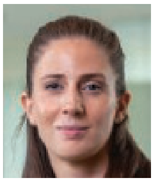

Constanze Depp received an undergraduate degree from the Ruprecht Karl University of Heidelberg and a PhD from the Georg August University of Göttingen and the Max Planck Institute for Experimental Medicine. She is completing her postdoctoral fellowship in Beth Stevens's laboratory at Boston Children's Hospital and the Broad Institute of the Massachusetts Institute of Technology and Harvard University. Her research focuses on glia cell aging as a risk factor for Alzheimer's disease. **www.science.org/doi/10.1126/science.aeb5153**

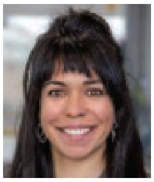

Sara Mederos received an undergraduate degree from the Autonomous University of Madrid and a PhD from the Cajal Institute (CSIC) and the Complutense University of Madrid. She is currently a Wellcome Trust Early-Career Fellow at the Sainsbury Wellcome Centre (University College London) and will start her laboratory in the Neurosciences Programme at the Hospital del Mar Research Institute Barcelona in 2026. Her research investigates the brain circuits that enable flexible choices under changing internal states and external contexts. **www.science.org/doi/10.1126/science.aeb5165**

eppendorf
& Science
PRIZE FOR
NEURO
BIOLOGY

REVIEW SUMMARY

MATERIALS SCIENCE

Porous materials: The next frontier in energy technologies

Eliyahu M. Farber, Nicola M. Seraphim, Kesha Tamakuwala, Andreas Stein, Maja Rücker, David Eisenberg*

Full article and list of author affiliations:
https://doi.org/10.1126/science.adn9391

BACKGROUND: Porous materials, with pores ranging from angstroms to centimeters, consist of two phases—void and matter. These phases allow the transfer of multiple energy vectors, such as mass, charge, heat, radiation, and pressure. The high-area interface between the phases allows for these energy vectors to meet and interconvert by various processes, ranging from desired catalytic conversions between light, heat, electricity, and chemical streams to undesired events, such as cracking, passivation, or quenching of excited states. Thanks to their energy transfer capabilities, porous materials are increasingly adopted in a broad range of energy applications, driving performance breakthroughs in solar, nuclear, electrochemical, thermal, and subsurface energy extraction and conversion.

ADVANCES: By considering energy conversion devices or fuel extraction techniques in terms of energy vectors being simultaneously transferred and interconverted in the solid and void phases of a porous material, it is possible to design better porous components for a variety of applications. Such a view highlights the constraints and reveals new opportunities for optimization, simulation, and cross-disciplinary fertilization. For instance, the simultaneous tuning of mass and charge transfer in porous electrodes where the total volumetric surface area has been maximized leads to higher power density in electrochemical devices, such as supercapacitors, fuel cells, batteries, and electrolyzers. All energy streams are constrained by the geometry (size, shape, and orientation) and spatial distribution (ordering, hierarchy, and directionality) of the pores. Thus, heat storage in pore-embedded phase change materials (such as paraffin in carbons) is boosted by tuning pore sizes and apertures—improving heat conductivity while retaining the active matter. In thermochemically reactive materials that store solar heat at high temperatures, the porous structure can be tuned across multiple length-scales, enhancing the simultaneous absorption of light, distribution of heat, and evolution of the reaction front in time and space. Pores can also be used for selective blocking of energy streams: In thermoelectric generators, disconnected pores are introduced to disperse phonons but not electrons, reducing heat conductivity while maintaining the temperature difference and electronic conductivity needed for efficient thermoelectric energy conversion. Porous structures can evolve over time: Pores are formed inside nuclear fuel pellets by the action of evolved gases; by nanometric cracking of battery particles; or in the soil during unconventional extraction of oil, gas, and geothermal heat from low-porosity rocks (such as hydraulic fracturing).

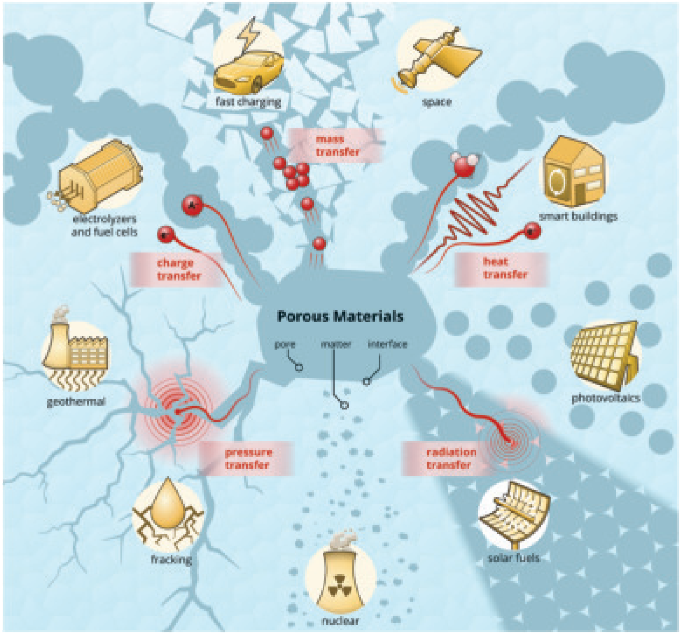

Porous materials are key components of most energy conversion and extraction technologies. With pores ranging from angstroms to centimeters, porous materials can conduct the transfer of mass, charge, heat, radiation, and pressure, enabling energy conversion across many length-, time-, and energy scales.

OUTLOOK: The ultimate goal in porosity design—a task-specific porous architecture for each application—calls for great advances in analysis, synthesis, and material characterization. Better mathematical and computational models are needed for studying energy transfer processes in porous materials. These, in turn, require the complete three-dimensional visualization of porous structures on all length-scales, using tomographic, spectroscopic, and diffraction techniques. These will guide synthetic advances, leading to fuller control of the distribution of pore sizes, shapes, and connectivity patterns in materials. By taking a broader view of porous materials, commonalities between porosity subfields must be recognized, leading to the exchange of synthetic strategies, analytical tools, and inspiration sources. For example, biomimetically inspired design strategies could tackle challenges such as the simultaneous control of the internal (e.g., hierarchical) porosity of a material and its external morphology (determining textural porosity and roughness) or the synthesis of precise pore architectures without wasteful sacrificial templates. Tomographic and computational methods used for understanding fluid flow in subsurface energy extraction should be embraced even more by researchers in the fields of catalysis or heat storage. Overall, a deeper understanding of energy streams will drive new generations of porous components for our expanding energy landscape. ☐

---

*Corresponding author. Email: eisenberg@technion.ac.il Cite this article as E. M. Farber *et al.*, *Science* **390**, eadn9391 (2025). DOI: 10.1126/science.adn9391

RESEARCH

IN *SCIENCE* JOURNALS

Edited by **Michael Funk**

DEVELOPMENT

Cells whisper to each other in the ear

The organ of Corti contains a highly organized epithelium with ciliated (hairy) cells that sense sounds and transmit them to the brain. Sound intensity and pitch sensing rely on the precise alignment of alternating rows of various types of hair cells and supporting cells. Considering that each row contains 3500 hair cells, understanding how the hearing epithelium acquires its precise pattern is a long-standing challenge. García-Gómez *et al.* now show that extensive local communication between cells underlies this precision. Messages between cells are multiple and diverse, including instructions about alternative fate choices, cell type induction, cell density, and cell attraction. These mechanisms explain patterning robustness and help in understanding congenital and acquired sensorineural hearing deficits. —Miguel Torres Sci. Adv. (2025) 10.1126/sciadv.adz3944

Ciliated cells (yellow and red) in the organ of Corti, seen in a colored scanning electron microscopy image

MOLECULAR BIOLOGY

Boosting telomerase at chromosomes' ends

Human replication protein A (RPA), long recognized as an essential factor in DNA replication and repair, has now been found to play a critical role at chromosome ends. Agrawal *et al*. demonstrated that RPA directly enhances the processivity of telomerase, the enzyme responsible for extending telomeres. By boosting telomerase's ability to add repeated DNA sequences, RPA proves vital for maintaining telomere length and genomic stability. This repurposing of a fundamental single-stranded DNA-binding complex provides fresh insights into telomere regulation and has implications for aging, cancer, and telomere-related disorders. —Di Jiang

Science p. 495, 10.1126/science.ads5297

POLYMER RECYCLING

Uncovering a urethanase

There have been major advances recently in the discovery and engineering of hydrolase enzymes for degradation of ester linkages in polymers such as polyethylene terephthalate. However, more resistant chemical linkages, such as those found in urethane polymers, present additional challenges. Chen *et al*. developed a computational pipeline for screening enzymes with potential activity and identified a highly active urethanase. The authors report a kilogram-scale chemo-enzymatic depolymerization of commercial polyurethane foam and show enzymatic degradation of *N*-aryl carbamates with nearly complete conversion within 8 hours. This discovery framework may be useful in identifying enzymes for the chemical and polymer recycling industry. —Michael A. Funk

Science p. 503, 10.1126/science.adw4487

COMPARATIVE COGNITION

Rational chimps

The ability of humans to think rationally and weigh the evidence when making a choice is well known. Such decision-making requires a metacognitive process in which an individual can evaluate an overall set of evidence and make the best supported choice. Whether other animals can also do this has been unknown. Schleihauf *et al*. tested whether our closest relatives, chimpanzees, were able to evaluate weak and strong evidence regarding the location of a food reward (see the Perspective by Hare). They found that the chimps correctly inferred the most rational location based on the strength of the evidence that they received about the reward's location. —Sacha Vignieri

Science p. 521, 10.1126/science.adq5229; see also p. 444, 10.1126/science.aeb7565

IMAGE: G. BREDERG/SCIENCE SOURCE

EPIDEMIOLOGY

COVID-19's traveling companions

The massive range and costs of interventions undertaken to limit the harms caused by severe acute respiratory syndrome coronavirus 2 (SARS-CoV-2) had many side effects. Using surveillance data from the Centers for Disease Control and Prevention for notifiable infectious diseases, Brett and Rohani made a comprehensive statistical analysis of the indirect impact of the pandemic on a range of infections occurring in the US (see the Perspective by Durrheim). Although several endemic infections have rebounded to prepandemic levels of notification since 2020, the overall burden from infectious disease has been reduced. —Caroline Ash

Science p. 510, 10.1126/science.adw4964;
see also p. 442, 10.1126/science.aeb5722

NEUROINFLAMMATION

Unsilencing neurons with BTKi's

Bruton's tyrosine kinase inhibitors (BTKi's) suppress overreactive B cell signaling and could potentially curtail disease progression in multiple sclerosis. To investigate the signaling pathways involved in B cell–mediated neuronal impairment and the effects of BTKi's, Shin *et al.* performed pharmacological experiments in mouse and human coculture models. They demonstrated that lymphotoxin-α (LTα) released from proinflammatory B cells triggered necroptotic signaling in neurons, leading to neuronal depolarization and silencing. BTKi's mitigated these effects by inhibiting LTα release. Patient data demonstrating that LTα correlated with a neuronal injury marker in cerebrospinal fluid suggested that the signaling pathways characterized in vitro could be relevant for the human condition. —Daniela Neuhofer

Sci. Transl. Med. (2025)
10.1126/scitranslmed.adx2652

IMMUNOMETABOLISM

Organelle cross-talk in lymphocytes

Lymphocytes, including regulatory T (T_{reg}) cells, tune their metabolism to support their immunological functions. However, the molecular events controlling T_{reg} cell metabolic reprogramming during inflammation are not fully understood. Using a mouse model of acute inflammation, Saravia *et al.* found that activated T_{reg} cells undergo mitochondrial metabolic reprogramming dependent on Opa1, a protein that controls mitochondrial dynamics from the inner mitochondrial membrane. Loss of Opa1 triggered T_{reg} cell mitochondrial bioenergetic stress, severe inflammation, and aberrant activation of transcription factor EB (TFEB), which led to excessive lysosomal biogenesis. These findings identify a pathway of interorganelle communication between mitochondria and lysosomes that supports T_{reg} cell–suppressive functions during inflammation. —Claire Olingy

Sci. Immunol. (2025)
10.1126/sciimmunol.ads9456

GUT MICROBIOTA

Protection by sorbitol digestion

Excess dietary intake of fructose can lead to steatotic liver disease. In zebrafish depleted of gut microbiota, Jackstadt *et al.* found that dietary glucose was converted to sorbitol in the intestine, and was then converted to a fructose intermediate in the liver, resulting in hepatic steatosis. This effect was mimicked by high levels of exogenous sorbitol and attenuated by intestinal repopulation with sorbitol-degrading bacteria. These results suggest that excessive dietary intake of sorbitol, which is used as a sugar substitute, may increase the risk of steatotic liver disease. —Wei Wong

Sci. Signal. (2025)
10.1126/scisignal.adt3549

IN OTHER JOURNALS

Edited by **Corinne Simonti** and **Jesse Smith**

SEPSIS

A clearer sepsis diagnosis

Sepsis is a deadly condition caused by severe infection and the host response to it, leading to acute dysfunction of multiple organs. It is difficult to predict and it progresses rapidly, so the standard of care is to urgently start broad antibiotic coverage until the diagnosis is ascertained, which results in overtreatment with antibiotics and the spread of drug-resistant bacteria. By using machine learning to evaluate a set of mRNAs in the blood of patients presenting for emergency care, Liesenfeld *et al.* were able to identify those with incipient sepsis and distinguish bacterial infections from viral ones that would not need antibiotic treatment, all with greater accuracy than currently available laboratory testing. —Yevgeniya Nusinovich

Nat. Med. (2025)
10.1038/s41591-025-03933-y

BEHAVIOR

Seeking food

Animals facing food scarcity and caloric deficit need to modulate their behavior to maximize the chances of finding food. Kamath *et al.* studied the brain mechanisms underlying hunger-induced behavioral changes in mice. Hunger enhanced exploratory behavior and modulated risk assessment such that hungry animals were willing to spend more time and collect more food in a threatening environment compared with satiated animals. Mechanistically, Agouti-related peptide (AgRP)–expressing neurons in the arcuate nucleus of the hypothalamus reduced dopamine release in the tail of the striatum, thus increasing exploratory behavior. These results show that dopaminergic signaling is responsible for translating an internal state in behavioral changes. —Mattia Maroso

Neuron (2025)
10.1016/j.neuron.2025.09.009

IMMUNOLOGY

Interfering with an interferon dogma

Type I and III interferons (IFN-I and IFN-III) are small proteins that signal the presence of pathogens and trigger the transcription of IFN-stimulated genes (ISGs). Ngo *et al.* used genetic tools to deplete IFN-I/IFN-III–producing plasmacytoid dendritic cells (pDCs) in mice and study their contribution to host defense. In the absence of pDCs, mice could still induce ISGs through IFN-I/IFN-III production by other cell

IMAGE: NASA, ESA, STSCI; IMAGE PROCESSING: ALYSSA PAGAN (STSCI)

GALAXIES

Simulated flybys form galaxy bars

Some spiral galaxies, including the Milky Way, contain a galactic bar structure, a linear arrangement of stars that extends between the spiral arms through the galaxy center. Galactic dynamics studies have shown how bars can be stable and self-sustaining, but it is less clear how they initially form. Łokas has investigated barred galaxies in cosmological simulations, finding multiple cases in which a bar structure formed immediately after a galaxy experienced a close flyby with another more massive galaxy. These results demonstrate a mechanism for the rapid formation of at least some bars, particularly in dense galaxy cluster environments where flybys are common. —Keith T. Smith

Astron. Astrophys. (2025)
10.1051/0004-6361/202555503

The nearby galaxy NGC 5335 has a prominent central bar structure.

types and control the dissemination of mouse cytomegalovirus. In addition, mice that lacked pDCs showed less lung tissue damage and improved survival after severe influenza virus infections. This suggests that the ability of pDCs to produce IFN-I/IFN-III is not essential for animals to mount an effective immune response and might even be detrimental in some circumstances. —Sarah H. Ross

Nat. Immunol. (2025)
10.1038/s41590-025-02288-3

CONDENSED MATTER

Electrons dancing on liquid helium

A thin layer of liquid helium provides a pristine environment for electrons trapped on the surface. Being isolated from external noise, these single electrons can act as spin or charge qubits with long coherence times. Castoria *et al.* describe a device that allows the detection and control of single electrons trapped on helium at temperatures around 1 K. Combining a superconducting coplanar waveguide with an electron trap region, the authors demonstrated the ability to load and unload the trap with single electrons from an adjoining electron reservoir. Such single-electron sensing and control will be useful for the development of quantum technologies based on electrons on helium. —Ian S. Osborne

Phys. Rev. X (2025)
10.1103/vcl7-73ms

PLASTIC RECYCLING

Deconstructing polyurethane

Polyurethane, which is used in a wide variety of foams and spongy materials, is currently difficult to recycle. Part of the trouble is that it is constructed from two types of building blocks, respectively bearing oxygen- and nitrogen-linking groups, and most breakdown methods tend to cleanly recover just one of them. Hosgor *et al.* report that heating the foams in diethyl carbonate, which functions as both a reagent and solvent, together with zinc acetate as a catalyst, can deliver both the polyol (oxygen) and dicarbamate (nitrogen) components in 90 and 70% of respective yields. —Jake S. Yeston

Green Chem. (2025)
10.1039/D5GC02533H

NEUROSCIENCE

Profiling individual hippocampal ripples

Ripples are transient neural network events characterized by high-frequency oscillations in the local field potentials of hippocampal area CA1. Hippocampal ripples have been linked to a variety of brain functions, but they have typically been treated as homogeneous, raising the question of how they can support such diverse functions. Castelli *et al.* investigated local field potentials underlying individual ripples across the CA1 layers. They found two ripple profiles that exhibited distinct laminar currents across the CA1 somatodendritic axis and differentially recruited hippocampal neurons during periods of sleep and rest. This indicates that there may be different types of ripples with distinct population activity levels, structural organization, and neuronal content serving different brain functions. —Peter Stern

Neuron (2025)
10.1016/j.neuron.2025.09.012

RESEARCH ARTICLE SUMMARY

SOLAR CELLS

Electron accumulation across the perovskite layer enhances tandem solar cells with textured silicon

Oussama Er-raji* *et al.*

Full article and list of author affiliations:
https://doi.org/10.1126/science.adx1745

INTRODUCTION: To realize terawatt-scale photovoltaic deployment, achieving both resource and cost efficiency are imperative. Perovskite/silicon tandem solar cells present a compelling solution by surpassing the power conversion efficiency (PCE) of single-junction silicon solar cells, with only marginal additional production costs. Today, this technology achieves up to 34.85% PCE, establishing it as the most efficient dual junction. Moving toward commercialization, the adoption of industry-compatible fabrication processes and solar cell architectures becomes increasingly essential. In this context, monolithic fully textured perovskite/silicon tandem solar cells leverage the use of textured silicon substrates with industry-standard pyramid heights (>1 μm), which does not necessitate modifications to existing silicon manufacturing lines. The perovskite top cell is conformally grown on the large silicon pyramids via the evaporation–spin-coating route for the perovskite absorber, resulting in a structured perovskite/air interface that minimizes reflection losses. Despite its theoretically high PCE, substantial photovoltage and charge-transport losses limit the PCE to <32%, primarily because of inadequate interface passivation at the perovskite/electron transport layer (C_{60}) junction.

RATIONALE: Building on an optoelectrical simulation study, we identified two approaches to mitigate photovoltage losses at the perovskite/C_{60} interface: (i) chemical passivation strategies aimed at lowering surface recombination velocity, and (ii) work function engineering strategies designed to modulate charge carrier concentrations at the contact interface (i.e., field-effect passivation). Focusing on the latter, we proposed that—unlike traditional semiconductors such as silicon—owing to the intrinsic property of the perovskite film, not only the interface properties are improved by majority charge carrier (electron) accumulation at the interface. Instead, the induced electron accumulation region extends across the entire perovskite absorber, raising the electron concentration, and thus absorber conductivity. Consequently, this strategy not only reduces photovoltage losses but also mitigates transport losses, leading to improvements in both open-circuit voltage (V_{OC}) and fill factor (FF).

RESULTS: To implement the work function engineering strategy, we deposited 1,3-diaminopropane dihydroiodide on the perovskite surface, leading to a positive dipole formation (see the figure). Optoelectronic characterization revealed a reduction in the energy offset between the perovskite conduction band minimum (CBM) and the C_{60} lowest unoccupied molecular orbital, decreasing from 180 meV in the reference to 70 meV in the passivated system. Additionally, an increase of 80 mV was observed in the implied V_{OC} of perovskite/C_{60} stacks. A FF loss analysis showed that transport losses were halved, partly owing to mitigation of the non-ohmic resistance component. Consequently, passivated tandem solar cells achieved PCEs of up to 33.1%, with a V_{OC} of 2.01 V, and enhanced outdoor stability.

CONCLUSION: Minimizing energy band offsets at the perovskite/charge transport interfaces has proven effective not only in mitigating photovoltage losses through modulation of charge carrier concentrations at the interface but also in enhancing charge transport via a deep field-effect passivation mechanism. Applied to fully textured perovskite/silicon tandems, this strategy yielded a V_{OC} improvement of 100 mV compared to previous devices with identical architecture. Notably, the results confirmed that increased perovskite surface area—stemming from the large pyramid heights in industrial silicon substrates—does not pose a fundamental barrier to effective interfacial passivation in the perovskite top cell. □

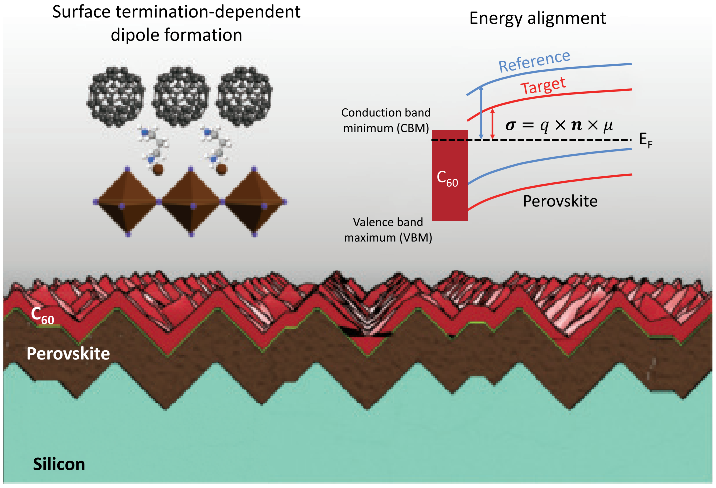

Interface passivation at the perovskite/C_{60} electron transport layer for efficient fully textured perovskite/silicon tandem solar cells. Perovskite surface treatment with 1,3-diaminopropane dihydroiodide reveals that the termination chemistry of the perovskite critically influences the orientation of the resulting dipole. This dipole minimizes the CBM energy offset between C_{60} and the perovskite (target versus reference). This effect facilitates electron accumulation both at the perovskite/C_{60} interface, which reduces interfacial recombination, and across the entire perovskite layer, which enhances conductivity, where σ is conductivity, q is elementary charge, n is electron density, and μ is mobility.

---

*Corresponding author. Email: oussama.er-raji@ise.fraunhofer.de (O.E.); stefaan.dewolf@kaust.edu.sa (S.D.W.); stefan.glunz@ise.fraunhofer.de (S.W.G.) Cite this article as O. Er-raji *et al.*, *Science* **390**, eadx1745 (2025). DOI: 10.1126/science.adx1745

MOLECULAR BIOLOGY

FIGNL1 inhibits homologous recombination in BRCA2 deficient cells by dissociating RAD51 filaments

Raviprasad Kuthethur *et al.*

Full article and list of author affiliations:
https://doi.org/10.1126/science.adt1210

INTRODUCTION: Homologous recombination (HR) is essential for DNA double-strand break (DSB) repair, and Breast Cancer Gene 2 (BRCA2) facilitates RAD51 nucleofilament formation crucial for strand exchange in DSB repair. Cells lacking BRCA2 show defects in RAD51 loading, leading to impaired HR and genomic instability and predisposing them to cell death, drug sensitivity, and tumorigenesis. RAD51 loading requires stringent regulation as excessive RAD51 on chromatin causes genome instability. This regulation occurs through RAD51 dissociation from DNA, mediated by helicases during HR, suggesting a balance between RAD51 loading and removal.

RATIONALE: Pathogenic BRCA2 mutations are viable chemotherapy targets through synthetic lethal strategies targeting HR deficiency. However, some BRCA2-deficient patients develop resistance through unknown HR restoration mechanisms. We hypothesized that HR restoration might result from inactivating mechanisms dissociating RAD51 from DSBs. We investigated the role of the AAA+ ATPase Fidgetin Like 1 (FIGNL1) in facilitating the dissociation of RAD51 and assessed its impact on the restoration of homologous recombination in the context of BRCA2 deficiency.

RESULTS: Our findings demonstrate that the loading of RAD51 at DSBs in BRCA2-deficient cells can be restored through the loss of the anti-recombinase FIGNL1. The genetic knockout of FIGNL1 in both mouse and human BRCA2-deficient cells reverses HR defects and mitigates genome instability, which correlates with increased chemoresistance to PARPi and platinum-based drugs. Additionally, the loss of FIGNL1 results in the synthetic viability of BRCA2-deficient mouse embryonic stem cells, with restored RAD51 loading at DSBs. These findings suggest that HR defects in BRCA2-deficient cells arise from the unregulated removal of RAD51 by FIGNL1, rather than from defective RAD51 loading.

We also show that FIGNL1 can dissociate RAD51 when assembled into a hexameric form, with initial interaction facilitated by FIGNL1's RAD51 binding domain (FRBD). The hexameric interactions between RAD51 and FIGNL1 are crucial for RAD51 removal from DSBs. We identified the MMS22L-TONSL complex as responsible for loading RAD51 in cells deficient in BRCA2 and FIGNL1. MMS22L-TONSL and RAD51 compete for the same binding site on FIGNL1's FRBD region. FIGNL1 loss results in increased MMS22L loading at DSBs, suggesting that FIGNL1 facilitates removal of RAD51 loaded by MMS22L-TONSL. The absence of MMS22L-TONSL in BRCA2/FIGNL1 double-deficient cells leads to HR defects, genome instability, and re-sensitization to chemotherapeutic agents.

CONCLUSION: Our findings define a pathway for modulating RAD51 levels during homologous recombination (HR), thereby refining the prevailing notion that HR defects in BRCA2-deficient cells are primarily attributable to RAD51 loading deficiencies. Our data suggest that the removal of RAD51 by FIGNL1 is responsible for HR defects in BRCA2-deficient cells. Furthermore, the identification of the MMS22L-TONSL complex as a potential mediator of RAD51 loading holds implications for understanding chemoresistance in BRCA2-deficient tumors and for developing strategies to re-sensitize these tumors to chemotherapy. ☐

---

*Corresponding author. Email: petr.cejka@irb.usi.ch (P.C.); a.raychaudhuri@erasmusmc.nl (A.R.C.) Cite this article as R. Kuthethur *et al.*, *Science* **390**, eadt1210 (2025). DOI: 10.1126/science.adt1210

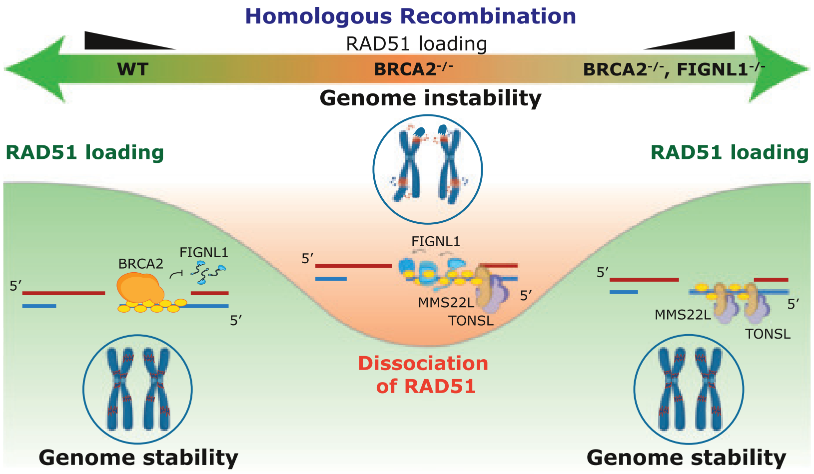

Modulating regulation of RAD51 during homologous recombination. BRCA2 facilitates the loading and stabilization of RAD51 and suppresses the anti-recombinase function of FIGNL1. In cells lacking BRCA2, FIGNL1 dissociates RAD51 from double-strand breaks (DSBs), leading to a deficiency in homologous recombination and resulting in genomic instability. In BRCA2-deficient cells, the absence of FIGNL1 can restore RAD51 loading through the MMS22L-TONSL complex, thereby re-establishing homologous recombination and genomic stability.

RESEARCH ARTICLE SUMMARY

PROTEIN CHAPERONES

Structural dissection of αβ-tubulin heterodimer assembly and disassembly by human tubulin-specific chaperones

Yeonjae Seong†, Hyunmin Kim†, Kyumi Byun, Yeon-Woo Park, Soung-Hun Roh*

Full article and list of author affiliations:
https://doi.org/10.1126/science.ady2708

INTRODUCTION: Microtubules are essential cytoskeletal polymers critical for cell division, intracellular transport, and maintenance of cell shape. They are composed of αβ-tubulin heterodimers, each consisting of an α-tubulin and a β-tubulin monomer. Assembly and disassembly of tubulin heterodimers are assisted by tubulin binding cofactors (TBCs): TBCA, TBCB, TBCC, TBCD, and TBCE. In addition, a small guanosine triphosphatase (GTPase), Arl2, is involved in this pathway.

RATIONALE: TBCs can mediate both guanosine triphosphate (GTP)–independent disassembly and GTP-dependent assembly of αβ-tubulin heterodimers. Although this process is essential for maintaining cytoskeletal homeostasis, the mechanisms involved remain poorly understood. We used cryo–electron microscopy (cryo-EM) to analyze reconstituted human TBC complexes under defined nucleotide conditions and captured structural snapshots of the disassembly and assembly pathway.

RESULTS: We purified human TBCDE-Arl2 complex and TBCC from mammalian cells and expressed TBCA and TBCB individually in *Escherichia coli*. These components were reconstituted with αβ-tubulin under defined GTP conditions, yielding six cryo-EM structures with 2.1- to 2.5-Å resolution. In the absence of GTP, we captured State I (TBCD–Arl2–β-tub) and State II (TBCDE–Arl2–β-tub), in which only β-tubulin was resolved, indicating disassembly of the heterodimer. In these states, β-tubulin is stabilized through electrostatic complementarity, as its highly negatively charged surface engages positively charged regions on TBCD (Armadillo-repeat domains AD1 and AD3), which compensates for the loss of α-tubulin. These interactions remodel the S9-H10 motif of β-tubulin, forming a new interface that mitigates its intrinsic instability. Upon addition of GTP, Arl2 undergoes a major conformational change in State III (TBCDE–Arl2_{GTP}–β-tub), which displaces the AD2 domain of TBCD, enabling α-tubulin binding. This leads to State IV (TBCDE–Arl2_{GTP}–αβ-tub), in which α-tubulin is resolved, revealing a partially reassembled heterodimer. With the addition of TBCC and a post–GTP hydrolysis mimic (GTP-AlFx), we resolved State V (TBCDEC–$\text{Arl2}_{\text{GDP-AlFx}}$–αβ-tub) and State VI (TBCDC–$\text{Arl2}_{\text{GDP-AlFx}}$–αβ-tub). In State V, the regulatory protein domain (RPD) of TBCC binds the GTP-bound Arl2 and contributes to the catalytic site, whereas in State VI, the coiled-coil domain (CCD) acts as a molecular clamp bridging α- and β-tubulin and displacing TBCE. These transitions complete formation of the native αβ-tubulin interface and finalize heterodimer assembly. Lastly, our structural analysis revealed that TBCD functions as a GTPase-activating protein for β-tubulin. β-Tubulin GTP hydrolysis is coupled to Arl2's GTPase activity, establishing a coordinated checkpoint that ensures that only fully assembled and mature αβ-tubulin heterodimers are released.

CONCLUSION: Based on our structures, we propose a mechanism by which TBCs mediate both the GTP-independent disassembly and GTP-dependent reassembly of αβ-tubulin heterodimers. Arl2 acts as a central regulator that switches the complex between these opposing states, and the coordinated GTPase activities of Arl2 and β-tubulin provide quality control that ensures precise regulation of tubulin heterodimer homeostasis. ☐

Schematic overview of the αβ-tubulin heterodimer assembly-disassembly cycle. In the disassembly state, αβ-tubulin is dissociated and monomeric β-tubulin is stabilized by TBCDE-Arl2. GTP binding induces the assembly priming state, enabling α-tubulin recruitment. TBCC engagement completes the assembly of native αβ-tubulin heterodimer and facilitates the release of TBCE. Coupled GTP hydrolysis in Arl2, and β-tubulin ensures the release of a functionally competent αβ-tubulin heterodimer through a quality control checkpoint.

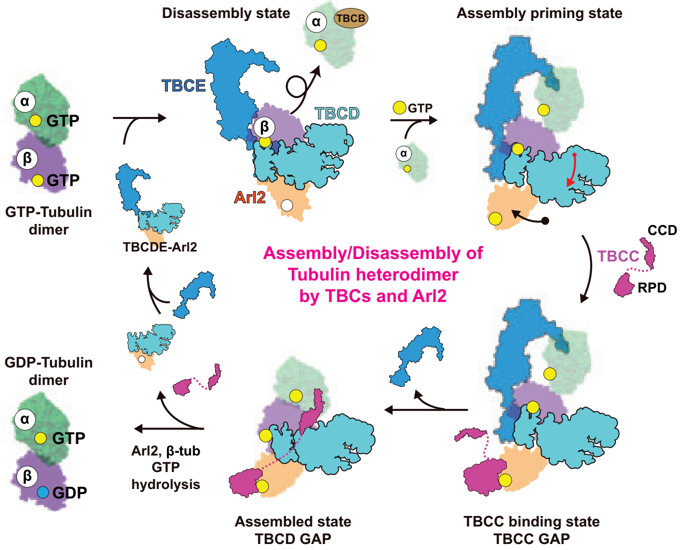

---

*Corresponding author. Email: shroh@snu.ac.kr †These authors contributed equally to this work. **Cite this article as Y. Seong *et al.*, *Science* 390, eady2708 (2025). DOI: 10.1126/science.ady2708**

RESEARCH ARTICLE SUMMARY

GREENHOUSE GASES

Global methane action pays for itself at least six times over

Thomas Stoerk*, James Rising, Drew Shindell, Simon Dietz

Full article and list of author affiliations:
https://doi.org/10.1126/science.adu7392

INTRODUCTION: Methane is a powerful but short-lived greenhouse gas, responsible for about one-third of the warming caused by well-mixed greenhouse gases since the 19th century. Its concentration in the atmosphere is once again rising rapidly owing to emissions from fossil fuels, agriculture, and waste, as well as anthropogenic and natural emissions from wetlands. Because of these two factors, reducing methane emissions has been identified as one of the most effective ways to curb near-term global warming. In response, the Global Methane Pledge, launched at COP26 in 2021, set an international target to reduce anthropogenic methane emissions by at least 30% from 2020 levels by 2030. Understanding the economic case for such action is crucial, especially given concerns about costs and the distribution of climate impacts across countries.

RATIONALE: We provide a comprehensive economic assessment of global methane abatement, quantifying both benefits and costs. Our study improves on prior work by incorporating recent climate modeling, country-level damage estimates, and the effects of climate tipping points. We anchor our analysis on methane scenarios consistent with the Global Methane Pledge, using an integrated assessment model (IAM) to capture the impact of methane abatement on global temperatures, economic damages, and key tipping elements such as ice sheets and ocean currents. In addition to modeling climate-related benefits, we include improved air quality from reduced methane-driven ozone, and we evaluate abatement costs using detailed sectoral estimates from the Global Methane Assessment.

RESULTS: Our findings show that global methane abatement yields large net economic benefits. Achieving the Global Methane Pledge results in more than $1 trillion in annual avoided market damages by 2050. Benefits are greater in lower-income countries because of their higher vulnerability to climate change. Methane action also reduces climate risk, including the likelihood and severity of extreme damage outcomes (climate tail risk). It lowers the intensity of several key tipping points: For example, by 2050, the likelihood of Amazon rainforest dieback drops by 8% and Indian monsoon disruption by 13%. Even using conservative assumptions about costs, the benefit-cost ratio of methane action is at least three—rising to more than six when health cobenefits are included. Some cost estimates suggest that methane mitigation could even be profitable owing to energy recovery and other gains. Finally, we provide estimates of the “social cost of methane” [the monetary value of future damages from 1 metric ton of methane emissions (tCH_4)], finding a global average of $7381/$tCH_4$, with higher domestic values for economies such as the US, EU, China, and India—implying strong economic self-interest in methane reductions.

CONCLUSION: Our analysis shows that global methane mitigation is not only feasible but also economically compelling. The benefits—spanning avoided climate damages and improved air quality—consistently outweigh the costs under a wide range of scenarios. The gains are especially pronounced for low- and middle-income countries, underscoring the policy’s equity-enhancing potential. Given that major economies also stand to gain considerably on their own, global cooperation is not strictly necessary for substantial methane action to be in their national interest. □

---

*Corresponding author. Email: t.a.stoerk@lse.ac.uk Cite this article as T. Stoerk *et al*., *Science* **390**, eadu7392 (2025). DOI: 10.1126/science.adu7392

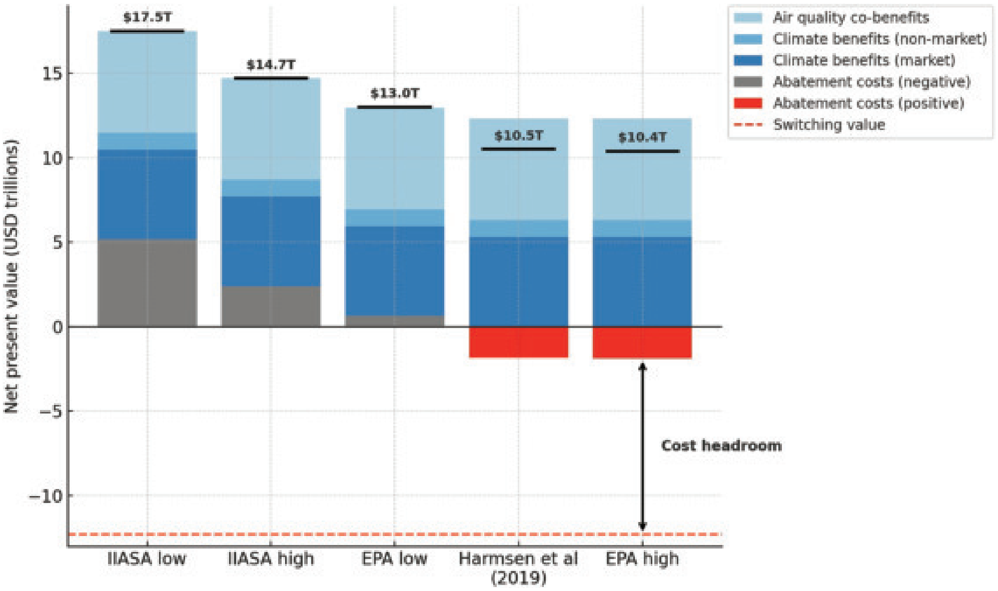

Net economic benefit of global methane action from 2020 to 2050. Net present value of climate benefits (market and nonmarket), air-quality cobenefits, and abatement costs under five methane abatement cost scenarios. Horizontal black lines show net benefits. The dashed line indicates the switching value threshold and available cost headroom before net present value is reduced to zero. The discount rate is 2.5%. IIASA, International Institute for Applied Systems Analysis; EPA, US Environmental Protection Agency; Harmsen *et al*., M. Harmsen *et al*., *Environ. Sci. Policy* **99**, 136–149 (2019).

RESEARCH ARTICLE SUMMARY

NEUROIMMUNOLOGY

Regional encoding of enteric nervous system responses to microbiota and type 2 inflammation

Peng Tan†, Alok Jaiswal†, Shane P. Murphy, Eric M. Brown, Hailey Wheeler, Chien-Wen Su, Emily P. Finan, Guadalupe J. Jasso, Hai Ning Shi, Daniel B. Graham, Toni M. Delorey, Jacques Deguine*, Ramnik J. Xavier*

Full article and list of author affiliations:
https://doi.org/10.1126/science.adr3545

INTRODUCTION: The enteric nervous system (ENS) is a branch of the autonomous nervous system composed of neurons located across two plexi of the intestinal tract. The ENS can function semiautonomously to regulate digestion and peristalsis, through a circuit involving five main neuronal types: (i) sensory neurons activate (ii) excitatory and (iii) inhibitory motor neurons through (iv) ascending and descending interneurons, which concomitantly activate (v) secretomotor and vasodilator neurons to regulate epithelial secretion and absorption. Accumulating evidence suggests that, in addition to working through this core circuit, the ENS plays a key role in responses to bacteria, allergens, and parasites through extensive cross-talk with the immune system.

RATIONALE: The gastrointestinal tract is constantly exposed to environmental changes driven by the microbiota, pathogens, and immunity, yet our understanding of the ENS's adaptation to these fluctuations remains limited, in part because of difficulties in isolating and profiling enteric neurons. To address this gap, we generated gnotobiotic mouse reporters and colonized them with distinct microbiomes, and in parallel, studied the ENS of animals exposed to type 2 inflammation, including food allergy and *Heligmosomoides polygyrus* infection. In each of these settings, we deeply profiled the ENS across distinct segments of the intestine—duodenum, jejunum, ileum, and colon—to define its response to perturbation.

RESULTS: Plate-based single-nucleus RNA profiling of the ENS captured a total of 7640 enteric neurons with more than 6000 median genes per cell. This atlas highlights two main axes of diversity across enteric neurons. First, we observed a functional specification of sensory neurons across distinct cell types characterized by distinct neuropeptides and receptors, including neuromedin U (Nmu)–expressing neurons that respond to type 2 cytokines and leukotrienes. Second, we observed transcriptomic gradients across both subsets of motor neurons (inhibitory and excitatory), likely encompassing distinct cell states that can be modulated by environmental challenges. Notably, these changes were highly coordinated across distinct perturbations, with changes in the frequency of Nmu^+ neurons and a shift of inhibitory motor neurons between *Bglap* and *Dcc*/*Aldh1a3* populations occurring in animals that were allergic, parasite-infected, and born germ-free.

To define the programs that contribute to neuronal adaptation, we next used adeno-associated virus (AAV)–PHP.S viral vectors—which efficiently target all peripheral neurons—to delete genes of interest in *Cas9*-expressing animals. We first delivered pools of guides and performed single-nucleus RNA sequencing of infected neurons to identify genes associated with changes in neuronal cell states. Lastly, we deleted candidate regulators in individual animals and validated two genes, *Edf1* and *Mitf*, as regulators of both inhibitory motor neuron cell state and total gastrointestinal transit time. More specifically, deletion of *Edf1* resulted in an expansion of $BGLAP^+$ neurons among infected cells and increased transit time, whereas deletion of *Mitf* expanded DCC^+ neurons and shortened transit time.

CONCLUSION: Our studies provide a detailed transcriptomic atlas of the ENS during distinct environmental challenges and reveal a set of coordinated responses to perturbations. This work directly links ENS cell states to changes in intestinal physiology and provides a blueprint for future functional studies of the ENS in health and disease. ☐

---

*Corresponding authors: jdeguine@broadinstitute.org (J.D.); xavier@molbio.mgh.harvard.edu (R.J.X.) †These authors contributed equally to this work.
Cite this article as P. Tan *et al.*, *Science* **390**, eadr3545 (2025). DOI: 10.1126/science.adr3545

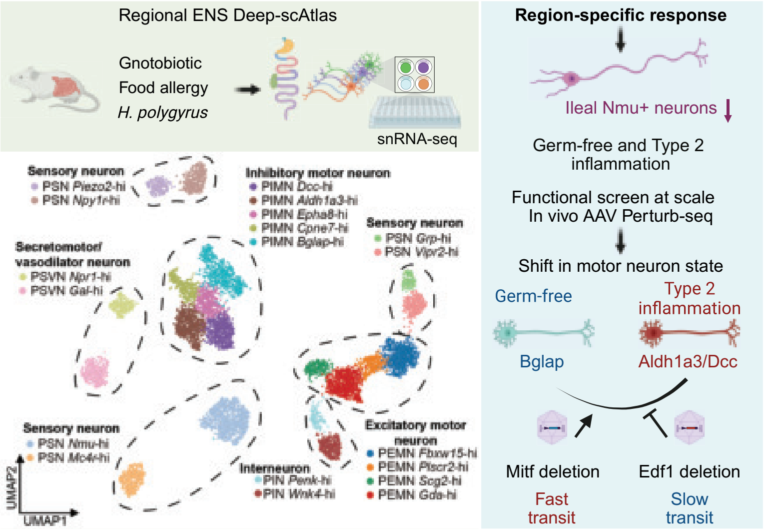

Enteric neurons across sites and perturbations. Enteric neuron single-nucleus RNA sequencing (snRNA-seq) was performed on the indicated segments and models, resulting in a single-cell (sc) atlas of 7640 deeply profiled neurons (bottom left). *Nmu*-hi sensory neurons and inhibitory motor neuron states were highly responsive to perturbations (top right), and AAV-based gene deletions demonstrated a role for *Mitf* and *Edf1* in modulating inhibitory motor neurons and gastrointestinal transit time (bottom right). PSN, putative sensory neurons; PEMN, putative excitatory motor neurons; PIMN, putative inhibitory motor neurons; PIN, putative interneurons; PSVN, putative secretomotor/vasodilator neurons.

RESEARCH ARTICLE SUMMARY

NEUROSCIENCE

Diverse somatic genomic alterations in single neurons in chronic traumatic encephalopathy

Guanlan Dong†, Chanthia C. Ma†, Shulin Mao‡, Katherine Sun-Mi Brown‡, Samuel M. Naik, Gannon A. McDonough, Samadhi P. Wijethunga, Junho Kim, Samantha L. Kirkham, Diane D. Shao, Jonathan D. Cherry, Madeline Uretsky, Elizabeth Spurlock, Ann C. McKee, August Yue Huang*, Michael B. Miller*, Eunjung Alice Lee*, Christopher A. Walsh*

Full article and list of author affiliations:
https://doi.org/10.1126/science.adu1351

INTRODUCTION: Chronic traumatic encephalopathy (CTE) is a neurodegenerative disease that develops years after exposure to repetitive head impacts (RHI) in some individuals. It is most often observed in individuals with a history of playing contact sports. Clinically, CTE is diagnosed through postmortem neuropathological examination of brain tau deposition, a hallmark it shares with Alzheimer's disease (AD). However, CTE is distinct in its tau accumulation patterns and clinical symptoms. Moreover, not everyone exposed to RHI develops CTE, and little is known about how head trauma can lead to CTE pathogenesis.

RATIONALE: While somatic mutations are well established as drivers for cancer progression, they also accumulate in noncancer cells and even in nondividing cells such as neurons. Recent advances in single-cell whole-genome sequencing (scWGS) technology have enabled the detection of private somatic mutations that accumulate in each nondividing neuron. Previous studies of single neurons showed that private somatic single-nucleotide variants (SNVs) increase during normal aging and more so in neurodegenerative diseases. However, the profiles of other mutation types have not been investigated in disease, and the role of somatic mutations in CTE is unknown.

RESULTS: Here we show that somatic mutations significantly increase in neurons of CTE patients and present specific disease-related patterns. We applied two scWGS methods to hundreds of neurons isolated from the prefrontal cortex of 15 individuals with CTE and 4 individuals with RHI but without CTE and compared mutational burdens and signatures with neurons from neurotypical controls and AD patients. In addition to the conventional strand-agnostic method, we included a strand-aware duplex sequencing modality that can distinguish between double-stranded mutations and single-stranded DNA lesions. We found a significant elevation of mostly double-stranded somatic SNVs in CTE that resembles a pattern previously reported in AD. Furthermore, we discovered high burdens of short deletions in both CTE and AD, resembling a known pattern of COSMIC signature ID4. Notably, the high burdens are only found in a subset of CTE and AD patients with a prominent signal from single-stranded events. Furthermore, somatic mutations in protein-coding genes are consistently enriched in essential neuronal functions, which, coupled with increased burdens in CTE, may lead to a dysregulated neuronal transcriptome and contribute to neurodegeneration. In contrast, somatic mutational burdens in individuals exposed to RHI but without a CTE diagnosis are similar to those of neurotypical controls, suggesting that the development of CTE involves mechanisms beyond those caused by RHI alone.

CONCLUSION: In this study, we characterized two types of somatic mutations in CTE neurons using both strand-agnostic and strand-specific methods of scWGS. Our results reveal that neurons in the CTE brain are exposed to stereotyped mutational processes shared with AD, implying potentially common pathogenic mechanisms. Specifically, increased SNVs resemble a pattern previously linked to oxidative damage, and increased short deletions resemble a pattern associated with topoisomerase 1 (TOP1) activity. In addition, the absence of similar changes in neurons exposed to RHI but without CTE highlights the complexity of CTE pathogenesis. Further study on the mechanisms leading to the short deletion pattern in certain CTE and AD patients may contribute to identifying novel therapeutic targets for neurodegenerative diseases. ☐

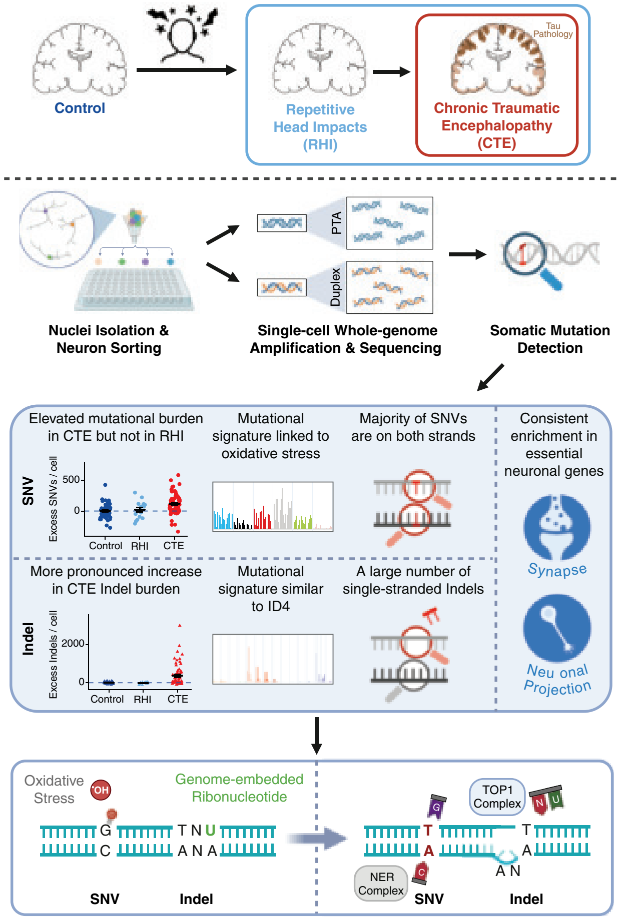

Excess of somatic mutations in single neurons in CTE. CTE develops after exposure to RHI in some individuals. Somatic mutations were profiled from single neurons in CTE brains using two scWGS methods. An excess of somatic SNVs and short deletions was found in CTE, resembling patterns associated with distinct mutagenic mechanisms that may contribute to CTE pathogenesis.

---

*Corresponding author. Email: christopher.walsh@childrens.harvard.edu (C.A.W.); ealice.lee@childrens.harvard.edu (E.A.L.); mbmiller@bwh.harvard.edu (M.B.M.); yue.huang@childrens.harvard.edu (A.Y.H.) †These authors contributed equally to this work. ‡These authors contributed equally to this work. **Cite this article as G. Dong *et al*., *Science* 390, eadu1351 (2025). DOI: 10.1126/science.adu1351**

RESEARCH ARTICLE SUMMARY

CATALYSIS

Conversion of syngas into olefins with high hydrogen atom economy

Chang Gao†, Wenlong Song†, Huiqiu Wang†, Xiao Chen, Chaojie Cui*, Wangshu Hao, Ning Yan, Yuan Yang, Shenglong Yang, Hao Lv, Mingyu Ma, Xinli Lian, Ruixia Zhang, Weizhong Qian*

Full article and list of author affiliations:
https://doi.org/10.1126/science.aea0774

INTRODUCTION: The synthesis of olefins from syngas through methanol has long been hindered by a low hydrogen atom economy (HAE), primarily due to the formation of water by-products and the requirement for high H_2/CO ratios. This limitation not only increases production costs but also raises environmental concerns, prompting the need for innovative catalytic solutions in the emerging technology of direct syngas to olefins.

RATIONALE: To address this challenge, we developed a sodium-modified FeCx@Fe_3O_4 core-shell catalyst that integrates the water-gas shift (WGS) and syngas-to-olefins (STO) reactions. By coupling these two processes, the catalyst enables in situ conversion of water generated during STO into hydrogen through the WGS reaction, thereby reducing the dependence on external hydrogen sources and improving HAE.

RESULTS: Under the conditions of 623 K and 2 MPa with a low H_2/CO ratio feedstock, the catalyst achieved outstanding performance: a CO conversion rate of ~95%, an olefin selectivity exceeding 75% (based on hydrocarbon products), and a hydrocarbon yield of 33 wt % (based on feedstock). The catalyst performance was stable over 500 hours of testing. Its HAE reached ~66 to 86% within an H_2/CO ratio range of 1 to 3, far surpassing the ~43 to 47% of the traditional WGS–methanol synthesis–methanol to olefins (MTO) route (at an H_2/CO ratio of ~2 to 2.05). Isotope-tracing and WGS-blocking experiments validated the coupling mechanism, and the contribution of the WGS reaction was quantitatively determined.

CONCLUSION: This study represents a substantial breakthrough in enhancing HAE for syngas conversion. The new WGS-STO coupling route of the developed catalyst reduces steam consumption, wastewater generation, and CO_2 emissions, with a 46% reduction in complete environmental factor compared with the WGS-MTO route. It also provides a sustainable alternative to existing olefin production technologies, offering great potential for the resource-efficient transformation of the olefin industry and contributing to the achievement of carbon neutrality goals. ☐

---

*Corresponding author. Email: qianwz@tsinghua.edu.cn (W.Q.); cuicj06@tsinghua.edu.cn (C.C.) The list of author affiliations is available in the full article online. †These authors contributed equally to this work. **Cite this article as C. Gao *et al.*, *Science* 390, eaea0774 (2025). DOI: 10.1126/science.aea0774**

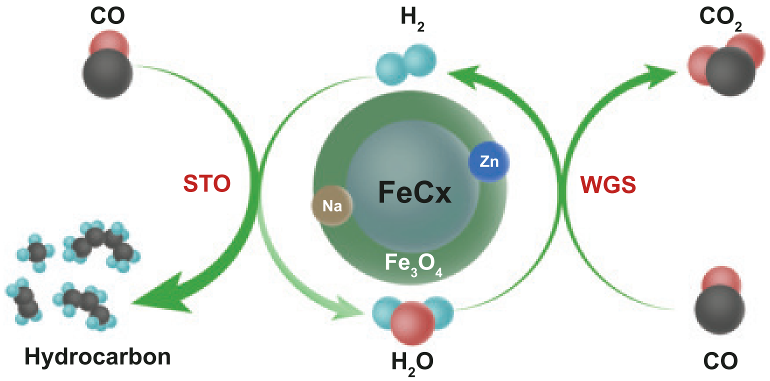

Improvement of hydrogen atom economy and olefin yield under the WGS-STO coupling effect.

MOLECULAR BIOLOGY

Human RPA is an essential telomerase processivity factor for maintaining telomeres

Sourav Agrawal[1]†, Xiuhua Lin[1]†, Vivek Susvirkar[1]†, Michael S. O'Connor[2,3], Bianca L. Chavez[1], Victoria R. Tholkes[1], Grace P. Tauber[1], Qixiang He[1], Kaitlyn M. Abe[1], Xuhui Huang[2,3], Ci Ji Lim[1]*

Telomerase counteracts telomere shortening by repeatedly adding DNA repeats to chromosome ends. We identified the replication protein A (RPA) heterotrimer as a telomerase processivity factor critical for telomere maintenance. RPA stimulates telomerase processivity in vitro, and AlphaFold modeling predicts that RPA engages a telomerase surface distinct from the one bound by the shelterin subunit TPP1. Guided by these predictions, we engineered separation-of-function telomerase reverse transcriptase (TERT) mutants and found that the loss of RPA-mediated stimulation impairs telomere elongation, even when TPP1–POT1–mediated stimulation remains intact. Furthermore, short-telomere disease–associated TERT mutations reduce RPA-dependent telomerase stimulation, revealing a mechanistic link between impaired processivity and telomeropathies. Together, our findings establish human RPA as a key regulator of telomerase and offer molecular insights into telomere-related disease mechanisms.

Telomeres, the natural ends of linear chromosomes, are crucial for maintaining genome stability (*1*). In humans, telomere maintenance (*2*, *3*) involves the extension of the G-rich single-stranded DNA (ssDNA) by telomerase (*4*–*7*) and the synthesis of the complementary C-strand by DNA polymerase α-primase (Polα-primase) in conjunction with the CTC1-STN1-TEN1 (CST) complex (*8*, *9*). Telomerase is recruited to telomeres by the shelterin protein TPP1 (*10*–*12*), which together with POT1 also stimulates telomerase repeat addition processivity (RAP) in vitro (*13*). However, the role of this stimulatory function in telomere maintenance in vivo remains unclear.

Replication protein A (RPA) is a highly conserved heterotrimeric complex involved in DNA replication and repair (*14*). In ciliates and yeast, RPA-like complexes are implicated in telomerase regulation and telomere maintenance (*15*–*19*). In human cell extracts, RPA has been reported to modulate telomerase activity and processivity (*20*). However, whether RPA directly stimulates telomerase processivity and supports telomere maintenance in human cells remained unknown.

RPA stimulates telomerase processivity through ssDNA and TERT interactions

Using primer-extension assays, we found that recombinant human RPA (fig. S1) increased telomerase RAP approximately sixfold, an effect similar to although less potent than that of the TIN2-TPP1-POT1 (TPT) complex (Fig. 1, A and B). Like TPT (*13*), RPA specifically stimulated RAP without affecting overall telomerase activity (Fig. 1C). This function required the complete heterotrimer because individual subunits and subcomplexes were inactive (Fig. 1D and fig. S2). These results establish the RPA heterotrimer as a telomerase processivity factor in vitro.

To understand the mechanism of RPA stimulation, we investigated the role of RPA's ssDNA binding domains (Fig. 1D) (*14*). Deletion of the OB-A and OB-B domains, which are crucial for ssDNA binding (*21*), abolished the stimulatory effect, whereas removal of the OB-F domain involved in protein-protein interactions (*14*) did not (Fig. 1E and fig. S2). This suggests that RPA's interaction with ssDNA is critical for stimulating telomerase RAP. To further test the importance of ssDNA binding, we used a polyT oligonucleotide (T36) as a competitor. Titration of T36 sequestered RPA and led to a dose-dependent reduction in telomerase RAP stimulation by RPA but not by TPT (Fig. 1F). This differential effect occurs because RPA binds nonspecifically to any ssDNA (*14*), including the polyT competitor, whereas TPT (POT1) requires a specific telomeric sequence for binding through its POT1 subunit (*22*, *23*). This result further highlights the necessity of RPA's ssDNA binding for telomerase RAP stimulation.

TPP1–POT1 requires both protein-protein and protein-DNA interactions for telomerase RAP stimulation (*24*). We therefore examined whether RPA also has direct interactions with telomerase reverse transcriptase (TERT). We used AlphaFold2 multimer (*25*) to screen for potential protein-protein interactions between RPA subunits and TERT. AlphaFold2 predicted that the RPA32 OB-D domain interacts with TERT TEN domain (Fig. 1, G to I).

To test this prediction, we performed stoichiometric titrations of RPA to a fixed 1 μM DNA primer concentration in the direct telomerase assay. By titrating RPA from substoichiometric to equimolar levels, we assessed whether telomerase processivity enhancement by RPA arises purely from ssDNA binding or involves an additional TERT–RPA interaction, as predicted with AlphaFold2 and demonstrated for TPP1–POT1 (*24*). A purely ssDNA binding–dependent mechanism would yield a linear increase in processivity with increasing RPA concentration, whereas an additional TERT–RPA interaction should produce a nonlinear response.

We observed a nonlinear, hyperbolic increase in telomerase RAP, with near-maximal stimulation at substoichiometric RPA binding concentrations (Fig. 1, J and K). This response resembles the in vitro stimulation reported for TPP1–POT1 (*24*) and is consistent with the AlphaFold2 prediction that RPA directly interacts with TERT. A separate binding assay by using fluorescence polarization under the same conditions showed a linear correlation between RPA concentration and DNA primer occupancy (Fig. 1K), indicating that the nonlinear processivity enhancement is not due to binding inefficiency or miscalculated protein concentration.

To test for an in vivo interaction, we performed coimmunoprecipitation (co-IP) assays using mCherry-tagged baits (Fig. 1L and fig. S3). Tagged RPA subunits coprecipitated TERT, unlike the mCherry-RAP1 negative control. Specifically, mCherry-RPA14 produced a robust signal comparable with that of the TPP1 positive control, whereas the pull-down by mCherry-RPA32 was significant but more modest, a difference we attribute to potential steric hindrance from its N-terminal tag. Furthermore, co-overexpression of all three subunits with the tag on RPA14 [superRPA (*26*)] reduced the pull-down signal, likely because of competition from the elevated level of RPA complexes. RPA70 could not be assessed owing to poor expression. This pull-down by multiple RPA baits, which is consistent with mass spectrometry data detecting all three RPA subunits in purified telomerase holoenzyme (*27*), provides strong evidence for an in vivo interaction between telomerase and the RPA heterotrimer.

Together, these results demonstrate that RPA stimulates telomerase RAP through both ssDNA binding and protein-protein interactions, similar to TPP1–POT1.

---

[1]Department of Biochemistry, University of Wisconsin–Madison, Madison, WI , USA. [2]Department of Chemistry, University of Wisconsin–Madison, Madison, WI , USA. [3]Theoretical Chemistry Institute, University of Wisconsin–Madison, Madison, WI , USA. ***Corresponding author. Email: ciji.lim@wisc.edu** †These authors contributed equally to this work.

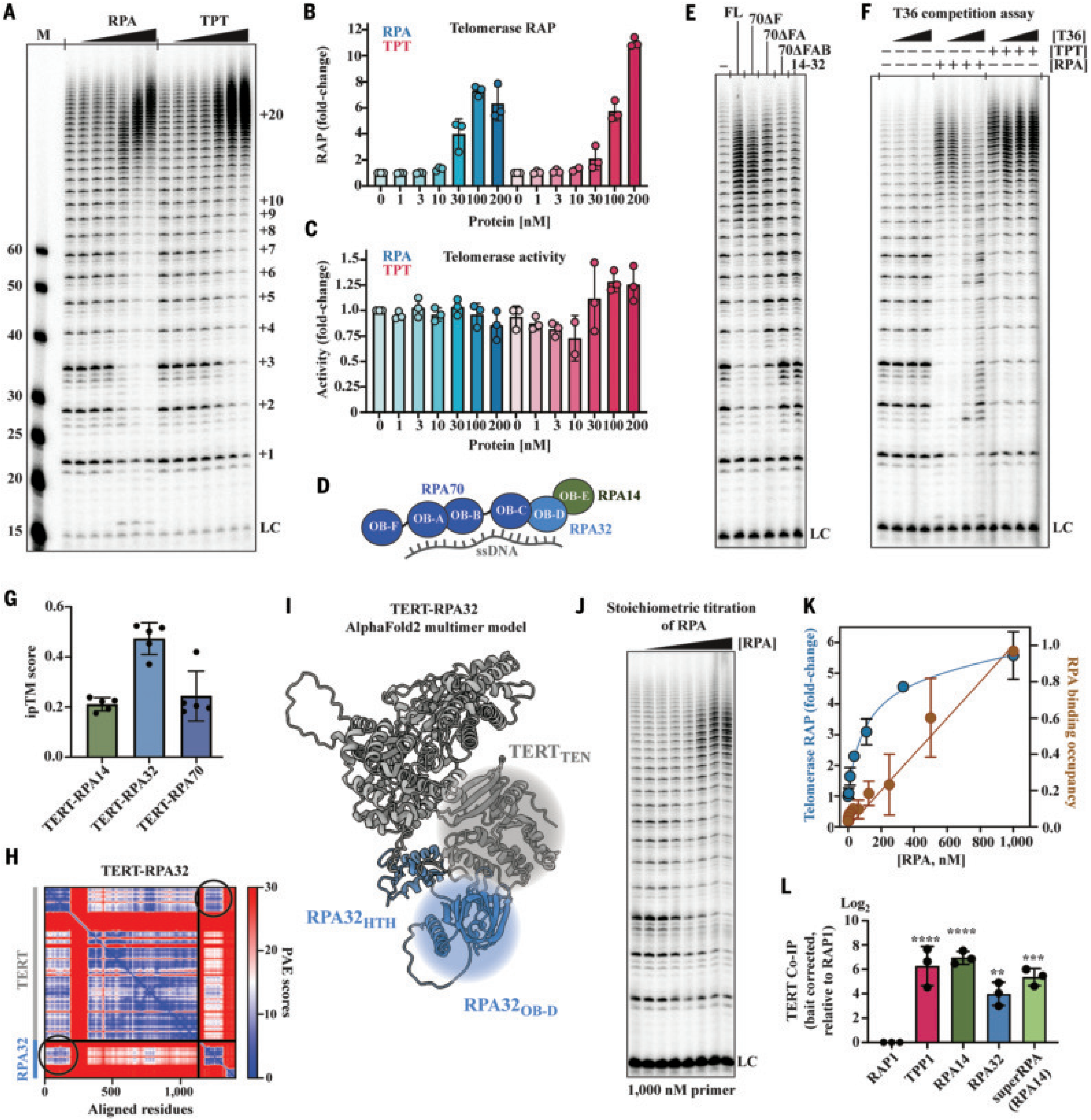

Fig. 1. Human RPA stimulates telomerase processivity through ssDNA and TERT interactions. (**A**) Direct telomerase assay showing repeat addition products from reactions with increasing concentrations of RPA or TPT (TIN2-TPP1-POT1). Numbers at right indicate the number of telomere repeats added. M, molecular weight markers; LC, loading control. (**B**) Quantification of telomerase RAP from experiments as in (A), shown as fold-change relative to the no-protein control. (**C**) Quantification of total telomerase activity from experiments as in (A), shown as fold-change. (**D**) Schematic of the human RPA heterotrimer highlighting its known ssDNA binding OB-fold domains (*14*). (**E**) Direct telomerase assay comparing full-length (FL) RPA with various RPA70 truncation mutants and the RPA14-32 heterodimer. Protein and protein complexes are used at 200 nM. (**F**) Competition assay showing the effect of a nontelomeric dT$_{36}$ oligo (T36) on telomerase stimulation by TPT and RPA. (**G**) AlphaFold2-predicted integrated TM-score (ipTM) for TERT interactions with individual RPA subunits. (**H**) Predicted aligned error (PAE) plot for the TERT–RPA32 interaction, showing the expected distance error (angstroms) between residue pairs. Lower values (blue) indicate higher confidence. (**I**) AlphaFold2 multimer model showing the predicted interaction between the TERT TEN domain (gray) and the RPA32 OB-D domain (blue). (**J**) Stoichiometric titration of RPA (0 to 1000 nM protein concentration) in a direct telomerase assay using 1000 nM primer. (**K**) Quantification of telomerase RAP from (J) (blue, left *y* axis) and RPA binding occupancy determined by means of fluorescence polarization (brown, right *y* axis). (**L**) Co-IP results quantifying TERT pull-down by mCherry-tagged baits, normalized to bait input (mCherry–bait/mCherry–RAP1) and expressed relative to the RAP1 negative control. In all graphs, error bars indicate SD from $n = 3$ independent experiments. ****$P \le 0.0001$; ***$P \le 0.001$; **$P \le 0.01$.

RPA32 OB-D and TPP1 OB domains bind telomerase at separate sites

To determine whether RPA and TPP1 engage the same surface on telomerase, we docked our AlphaFold2-predicted TERT_{TEN}–RPA32 model onto a cryo–electron microscopy (cryo-EM) structure of TPP1-bound telomerase (Fig. 2A). This analysis revealed two distinct, nonoverlapping interfaces: RPA32 contacts the TEN domain, whereas the TPP1 OB domain spans both the TEN and IFD–TRAP regions, as previously described (*28*–*30*). The prediction of this distinct RPA32 interface remained consistent across models of increasing complexity, from AlphaFold2 simulations including TPP1 OB domain (fig. S4) to AlphaFold3 (*31*) predictions of the entire telomerase-RPA-TPP1-POT1-ssDNA assembly (fig. S5).

The predicted separation of the RPA32 and TPP1 binding sites suggested that we could create separation-of-function (SOF) TERT mutants to probe the distinctive functional roles of each factor (Fig. 2B). To test the stability of the predicted interactions, we performed all-atom molecular dynamics simulations. The simulations showed that highly conserved TERT residues (E79, R83, R87, T116, T117, D146, and D147) maintained stable contacts with RPA32 (Fig. 2, C to E, and fig. S6A), raising our confidence in selecting them for mutagenesis. (Single-letter abbreviations for the amino acid residues are as follows: A, Ala; C, Cys; D, Asp; E, Glu; F, Phe; G, Gly; H, His; I, Ile; K, Lys; L, Leu; M, Met; N, Asn; P, Pro; Q, Gln; R, Arg; S, Ser; T, Thr; V, Val; W, Trp; and Y, Tyr. In the mutants, other amino acids were substituted at certain locations; for example, E79R indicates that glutamate at position 79 was replaced by arginine.)

We reconstituted telomerase [by overexpressing TERT and telomerase RNA (TR) in human embryonic kidney (HEK) 293T cells] with a panel of TERT mutations at the predicted RPA-binding interface (E79A, R83A, R87A, T116A/T117A, and D146A/D147A), hereafter termed TERT_{RPA}. In direct telomerase assays, all TERT_{RPA} mutants retained wild-type (WT) basal activity. However, three mutants—R83A, T116A/T117A, and D146A/D147A—selectively abolished RPA-mediated processivity stimulation while retaining stimulation by TPT (Fig. 2F and fig. S7), defining them as SOF mutants for RPA stimulation.

As a complementary approach, we tested previously reported TERT_{TPT} mutants, K78E (*32*) and Y772A (*28*), which disrupt the TERT–TPP1 interaction. As predicted with AlphaFold modeling, both TERT_{TPT} mutants disrupted TPT-mediated processivity stimulation, whereas RPA-mediated stimulation was only weakly affected (Fig. 2F). Y772A had little to no effect, whereas K78E caused a modest but detectable reduction in RPA stimulation, possibly because of its proximity to the predicted RPA32–TERT_{TEN} interface. These findings further support the model that RPA32 and TPP1 OB domains bind distinct surfaces on TERT.

We next sought to validate the interaction by mutating the predicted contact residues on RPA32. Guided by the compact (~940 Å^2) interface, we introduced alanine substitutions at six predicted and conserved contact residues in the RPA32 OB-D domain (T88, W107, H131, R133, F135, and F144) (fig. S6B), which pair in the model with TERT residues D147, R83, T116/T117, E79, Q73, and T117, respectively (Fig. 2, C to E). The model predicted a key π-cation interaction between TERT R83 and RPA32 W107. Direct telomerase assays revealed a spectrum of effects on processivity (Fig. 2G and fig. S8); the W107A mutation markedly reduced RPA stimulation, whereas T88A, F135A, and F144A caused more modest losses, and H131A and R133A had little to no negative impact.

To ensure these effects were specific to the TERT–RPA32 interaction, we confirmed (by means of mass photometry) that each mutant RPA complex purified as an intact heterotrimer and (by means of fluorescence polarization assay) bound telomeric ssDNA with near-WT affinity (fig. S9). These results suggest that the observed loss in RPA stimulation is consistent with disruptions at the predicted binding interface, rather than protein misfolding or impaired DNA binding. Together, our findings indicate that several residues on the RPA32 OB-D surface contribute to telomerase stimulation.

RPA localizes to telomeres by means of telomerase without triggering a DNA damage response

We next used immunofluorescence (IF) to validate the TERT–RPA32 interaction in cells. We found that endogenous RPA32 colocalized with telomeres upon transient expression of both TERT and TR, indicating that telomerase is required to recruit or stabilize RPA at telomeres (Fig. 3A). To test whether the predicted interface was necessary, we analyzed cells expressing TERT_{RPA} mutants (E79A, R83A, R87A, T116A/T117A, and D146A/D147A). All tested mutants reduced RPA signal at telomeres, with single-residue substitutions lowering colocalization by ~50% and double-residue substitutions abolishing it almost completely (Fig. 3B), demonstrating the TERT–RPA32 interaction is important for RPA accumulation at telomeres.

Because the TERT_{RPA} mutations are distant from the known TERT–TPP1 interaction site (*28*, *29*), we next sought to confirm that they do not affect telomerase recruitment. Our IF imaging showed that key TERT_{RPA} mutants, including R83A and T116A/T117A, were indeed recruited to telomeres as efficiently as WT TERT (Fig. 3C and fig. S10). Because these mutants retain intact recruitment but specifically lack RPA-mediated stimulation, they are true SOF mutants.

By contrast, the D146A/D147A mutation was an exception. Despite its distance from the TERT–TPP1 interaction site (fig. S11, A and B), the mutant exhibited a telomere recruitment defect, causing telomerase to accumulate in Cajal bodies (fig. S11C). However, it retained normal TPP1–POT1–mediated stimulation in vitro (Fig. 2F and fig. S7). How this mutant uncouples these two TPP1-mediated functions presents an interesting mechanistic question that warrants future investigation.

To confirm the TERT–RPA32 interaction at physiological levels, we performed a proximity ligation assay (PLA) (*33*) using probes for endogenous TR and RPA32. The assay detected discrete nuclear foci in HeLa cells, indicating that endogenous telomerase and RPA are in close proximity (Fig. 3, D and E). The PLA signal increased approximately threefold in cells expressing TERT from the AAVS1 safe-harbor locus (*34*), which is consistent with the estimated upper limit of fully assembled telomerase RNPs (approximately fourfold above parental) (*35*). Introducing the T116A/T117A mutation reduced the PLA signal by ~50 to 60%, confirming that the TERT–RPA32 interface mediates this proximity in cells.

Our biochemical assays established a dual requirement for RPA-mediated stimulation: TERT interaction and ssDNA primer engagement. To determine whether this dual requirement applies to RPA localization in cells, we analyzed a catalytically dead TERT mutant (D712A) (*36*) that prevents the formation of a nascent 3′ overhang for RPA to engage (fig. S12A). IF analysis showed that this mutant abolished RPA32 accumulation at telomeres, an outcome that mirrors the effect of our interface-disrupting mutants (fig. S12, B and C). This demonstrates that stable RPA localization at telomeres requires engagement with both TERT and telomeric ssDNA, confirming the dual requirement in a cellular context.

We investigated whether telomerase-mediated RPA localization triggers a DNA damage response (DDR), which occurs when RPA accumulates at telomeres upon POT1 depletion (*37*). We checked for two DDR markers: RPA32 phosphorylation (*38*) and 53BP1 foci (*37*). Unlike etoposide-treated controls, telomerase-overexpressing cells showed no RPA32 phosphorylation band shift on Western blots (Fig. 3F). Similarly, telomerase-overexpressing cells showed no increase in 53BP1 foci at telomeres (Fig. 3G and fig. S13). Together, these results demonstrate that telomerase-mediated RPA recruitment to telomeres occurs without activating DDR.

TERT SOF RPA mutants are defective in telomere maintenance in cells

To investigate RPA's physiological function in telomere maintenance, we used our SOF TERT_{RPA} mutants (R83A and T116A/T117A), which retain telomerase recruitment to telomeres (Fig. 3C) but lack RPA-mediated

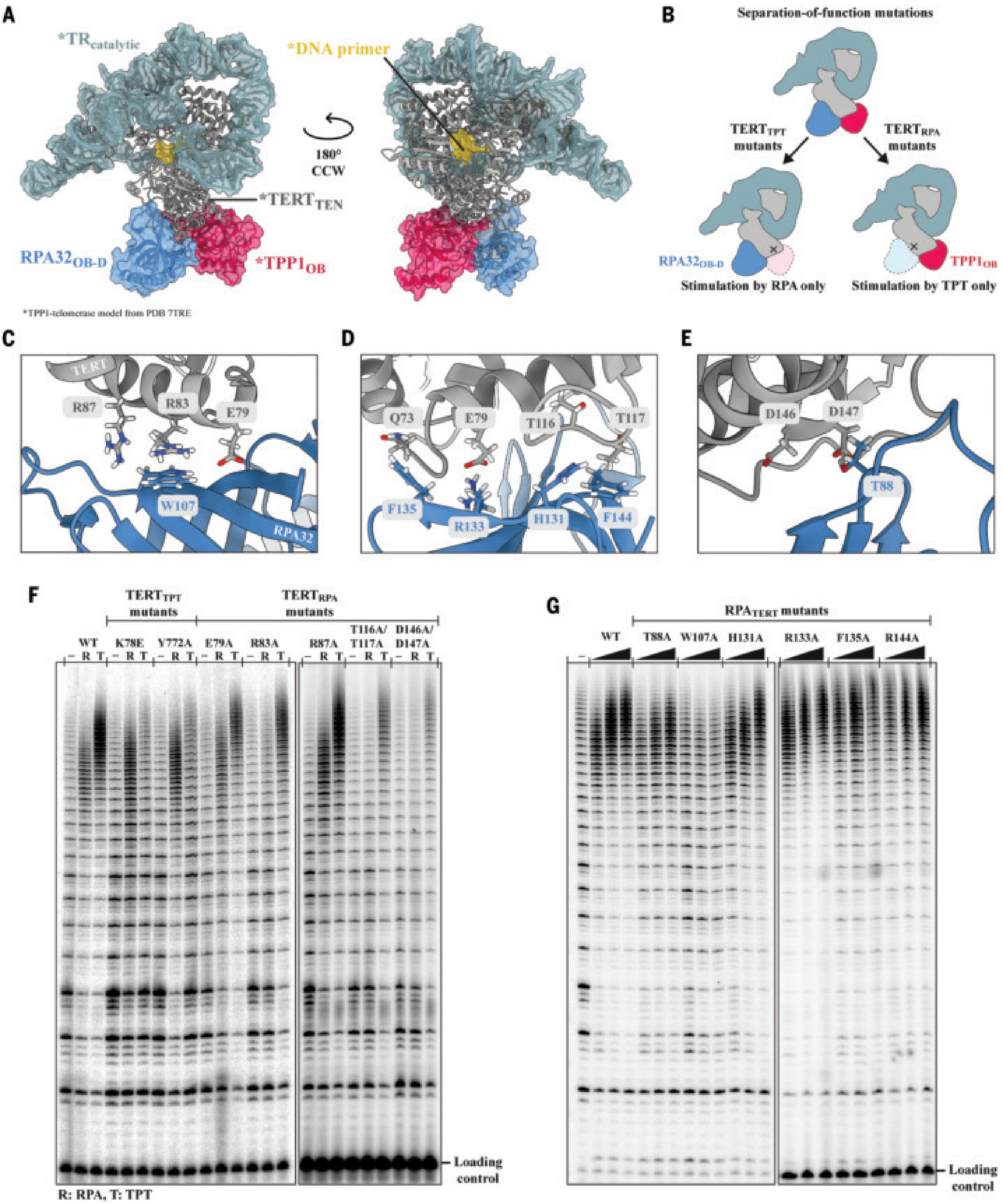

Fig. 2. Distinct TERT binding sites for RPA32 OB-D and TPP1 OB domains enable SOF mutations. (**A**) Hybrid structural model, shown in two views rotated 180° counterclockwise (CCW), showing the AlphaFold-predicted RPA32 OB-D domain (blue) docked onto the TPP1-bound telomerase cryo-EM structure [Protein Data Bank (PDB) ID 7TRE; asterisked components]. This illustrates the non-overlapping binding sites of RPA32 (blue) and TPP1 (red) OB domains on the TERT TEN domain. (**B**) Schematic illustrating the principle of TERT SOF mutants that are selectively stimulated by either RPA or TPT. (**C** to **E**) Close-up views of the predicted TERT–RPA32 interface highlighting key interacting residues. (**F**) Direct telomerase assay comparing WT TERT with TERT$_{TPT}$ mutants (K78E and Y772A) and TERT$_{RPA}$ mutants (E79A, R83A, R87A, T116A/T117A, D146A/D147A). Reactions were performed with no added protein (–), 200 nM RPA (R), or 200 nM TPT (T). (**G**) Direct telomerase assay testing WT TERT activity with increasing concentrations (50, 100, and 200 nM) of RPA complexes containing the indicated RPA32 mutations. A loading control is indicated for both gels.

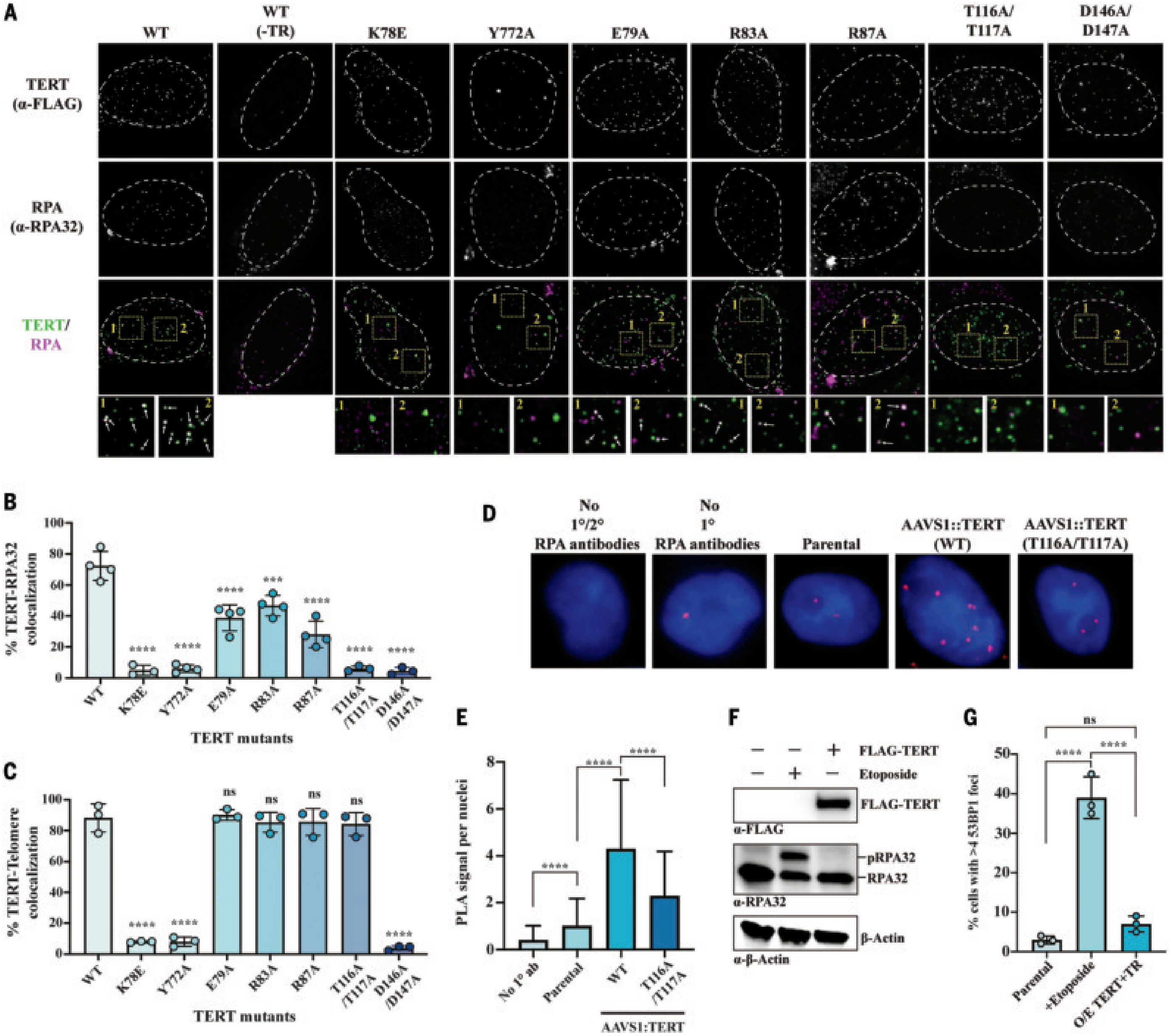

Fig. 3. RPA localizes to telomeres by means of telomerase without triggering a DDR. (**A**) Representative IF images of HeLa cells expressing WT TERT with or without TR, or the indicated TERT mutants. TERT (α-FLAG, green) and RPA32 (α-RPA32, magenta) are shown. Merged images display colocalization, with insets showing magnified views of the boxed regions where colocalization is indicated with arrows. Dashed lines indicate nuclei. (**B**) Quantification of the percentage of TERT foci that colocalize with RPA32 foci for WT and the indicated TERT mutants, based on images as in (A). Statistical significance was determined relative to the WT sample. (**C**) Quantification of the percentage of TERT foci that colocalize with telomeres for WT and the indicated TERT mutants. Statistical significance was determined relative to the WT sample. (**D**) Representative images from a PLA showing TERT–RPA32 association (magenta foci) in parental HeLa cells and in cells with WT or T116A/T117A TERT integrated at the AAVS1 locus. (**E**) Quantification of the PLA signal per nucleus from (D). (**F**) Western blot analysis of cell lysates probed for phosphorylated RPA32 (pRPA32), a marker of DDR. Etoposide treatment serves as a positive control. β-Actin is a loading control. (**G**) Quantification of the percentage of cells with 53BP1 foci, a DDR marker. The analysis compares parental cells, etoposide-treated cells, and cells overexpressing TERT and TR (O/E TERT+TR). In all graphs, error bars indicate SD. Data points in (B) and (C) are from biological replicates, with >100 total nuclei analyzed per sample. ns, not significant; ****P* ≤ 0.001; *****P* ≤ 0.0001.

stimulation (Fig. 2F). This system allows a direct probe of RPA's processivity function in cells. We used CRISPR-Cas9 to insert expression cassettes for WT or mutant TERT into the AAVS1 safe-harbor locus (*34*) in HEK293T cells (Fig. 4A). The resulting polyclonal cell lines, verified with polymerase chain reaction (PCR) and Western blot (Fig. 4B), express exogenous TERT that dominates telomerase assembly, leading to a dominant phenotype (*32*, *35*).

Southern blot analysis of telomere length revealed the functional consequences of these mutations (Fig. 4C). Whereas WT TERT expression caused telomere lengthening, several mutants led to telomere shortening. These included the recruitment-defective $\mathrm{TERT_{TPT}}$ mutants (K78E and Y772A) and D146A/D147A mutant. The SOF $\mathrm{TERT_{RPA}}$ mutants (R83A and T116A/T117A), which are recruited to telomeres but cannot be stimulated by RPA, also caused telomere shortening.

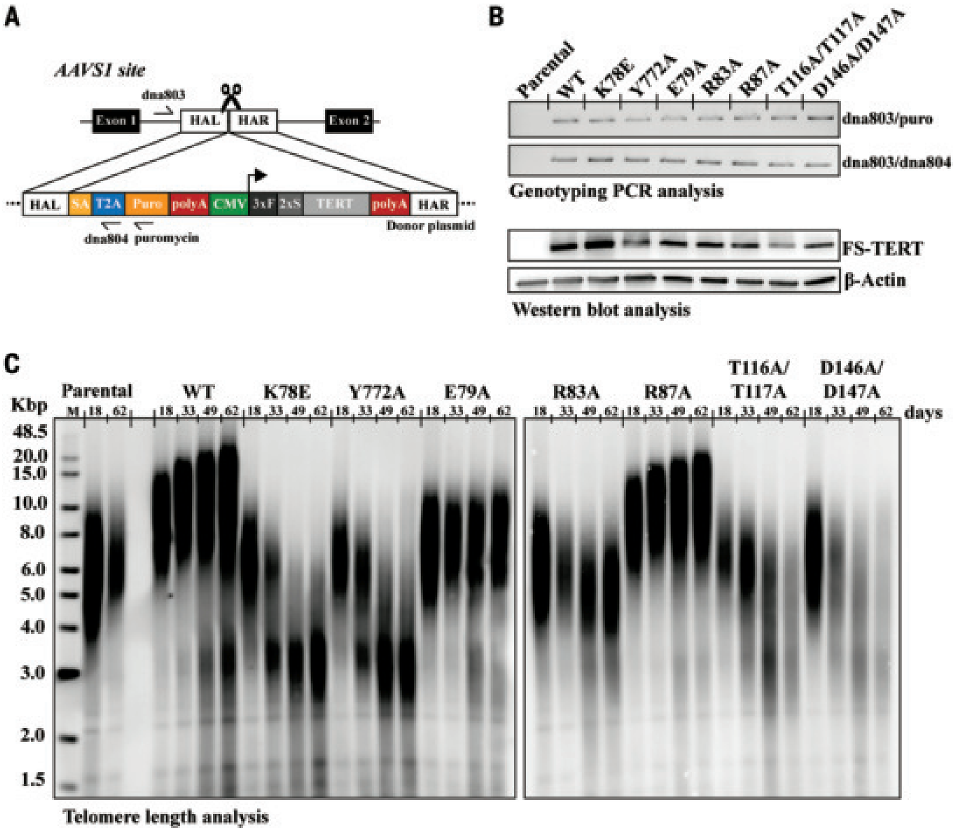

Fig. 4. TERT SOF RPA mutants are defective in telomere maintenance in cells. (**A**) Schematic of the strategy for CRISPR-Cas9–mediated insertion of a TERT expression cassette into the AAVS1 safe-harbor locus. HAL/HAR, homology arms; Puro, puromycin resistance; 2xS, Twin-Strep tag; 3xF, 3xFLAG tag. (**B**) Genotyping PCR analysis confirming successful insertion at the AAVS1 locus (top) and Western blot analysis of FLAG-Strep–tagged TERT (FS-TERT) expression in the indicated cell lines (bottom). β-Actin serves as a loading control. (**C**) Telomere length analysis by Southern blot of the indicated cell lines cultured over several time points (days). M, molecular weight marker in kilobase pairs (Kbp).

Conversely, mutants that did not disrupt stimulation by either RPA or TPT (E79A and R87A) maintained or elongated telomeres.

These findings collectively highlight the role of RPA in telomere maintenance. The key observation is that the TERT R83A and T116A/T117A mutants cannot support telomere elongation despite retaining their ability to be stimulated by TPP1–POT1. Whereas TPP1 is essential for telomerase recruitment and may contribute to processivity stimulation when partnered with POT1, RPA provides a distinctive and indispensable enhancement of RAP during telomere extension.

Connections to short telomeres human diseases

To connect our findings to telomere-related diseases, we examined several short-telomere syndrome mutations—TERT R83P (*39*), F115L (*40*), and T116I (*41*)—that map to the predicted TERT–RPA32 interface (Fig. 5A). Direct telomerase assays showed that all three mutants impaired RPA-mediated RAP stimulation (Fig. 5B and fig. S14, A and B). Whereas the R83P mutation disrupts stimulation by both RPA and TPT, likely by destabilizing the helical structure between residues 76 to 92, F115L and T116I selectively impair only RPA stimulation, which is consistent with a disruption at the RPA interface. In cells, the R83P mutant failed to localize to telomeres, which is consistent with its TPT stimulation defect (Fig. 5, C and D). By contrast, F115L and T116I localized normally, fulfilling the criteria for SOF mutants (Fig. 3C). As predicted from their impaired RPA stimulation, all three disease mutants showed a significant drop in TERT–RPA colocalization in cells (Fig. 5E and fig. S14C).

Telomere length assays in HEK293T cells revealed the functional consequences of these mutations (Fig. 5F). Unlike WT TERT, which robustly lengthened telomeres, all three disease mutants failed to support elongation. R83P caused rapid telomere shortening, which is consistent with its recruitment defect. T116I also led to shortening despite its normal localization, supporting the model that loss of RPA-mediated stimulation impairs telomerase activity in cells. The F115L mutant maintained initial telomere length but failed to promote elongation, suggesting a partial loss of function.

Recent studies have also linked short-telomere syndromes to mutations in RPA70 (*42*) and RPA32 (*43*). We investigated whether these mutations impair telomerase processivity stimulation, which would suggest additional RPA–telomerase contacts. However, direct assays showed that RPA complexes with these disease-associated variants stimulate telomerase normally (fig. S15). This suggests that the telomere defects associated with these particular mutations arise from functions distinct from the direct telomerase stimulation we described here.

Discussion

Our work demonstrates that the human RPA heterotrimer directly enhances telomerase RAP. This stimulation requires RPA to bind both the TERT TEN domain and the 3′ telomeric overhang and that disrupting this interaction causes telomere shortening in our cellular assays. We propose a sequence in which telomerase is first recruited to telomeres by TPP1 (*10*–*12*, *44*–*46*) and subsequently engaged by RPA for processive extension of the telomere overhang. Whether TPP1–POT1 contributes to processivity in cells remains to be determined. The inactivation of DDR at telomeres despite the presence of RPA can be explained by POT1 capping the telomere duplex–ssDNA junction (*47*), preventing the activation of RPA by ATR.

The idea that an RPA-family complex stimulates telomerase was foreshadowed by findings in other systems (*15*–*19*). In *Tetrahymena*, Teb2 and Teb3 are the RPA32 and RPA14 subunits, respectively, and together with Teb1 form the TEB complex (*18*). Teb2 binds the same TERT surface predicted here for RPA32 OB-D, and an intact TEB complex is required for maximal telomerase stimulation activity (*17*). While this manuscript was in revision, a genetic study in budding yeast suggested that RPA interacts with the telomerase subunit Est3 in vivo and stimulates activity (*19*). Taken together with our results, these observations suggest that RPA-family complexes play an evolutionarily conserved role as direct modulators of telomerase RAP.

Comparison of our TERT–RPA32 AlphaFold model with the telomerase–TPP1–POT1 cryo-EM structure (*29*) suggests a potential steric clash between POT1 and RPA32 because they bind overlapping surfaces on TERT (fig. S16). This implies that the initial TPP1–POT1 complex may need to be displaced for RPA to engage telomerase. To explore this possibility, we used AlphaFold3 (*31*) to model the complete assembly. AlphaFold3 predicted a “hand-over” conformation that repositioned POT1, with RPA70 instead binding the 5′ overhang, while TPP1 and RPA32 simultaneously engage the TERT TEN domain (fig. S5).

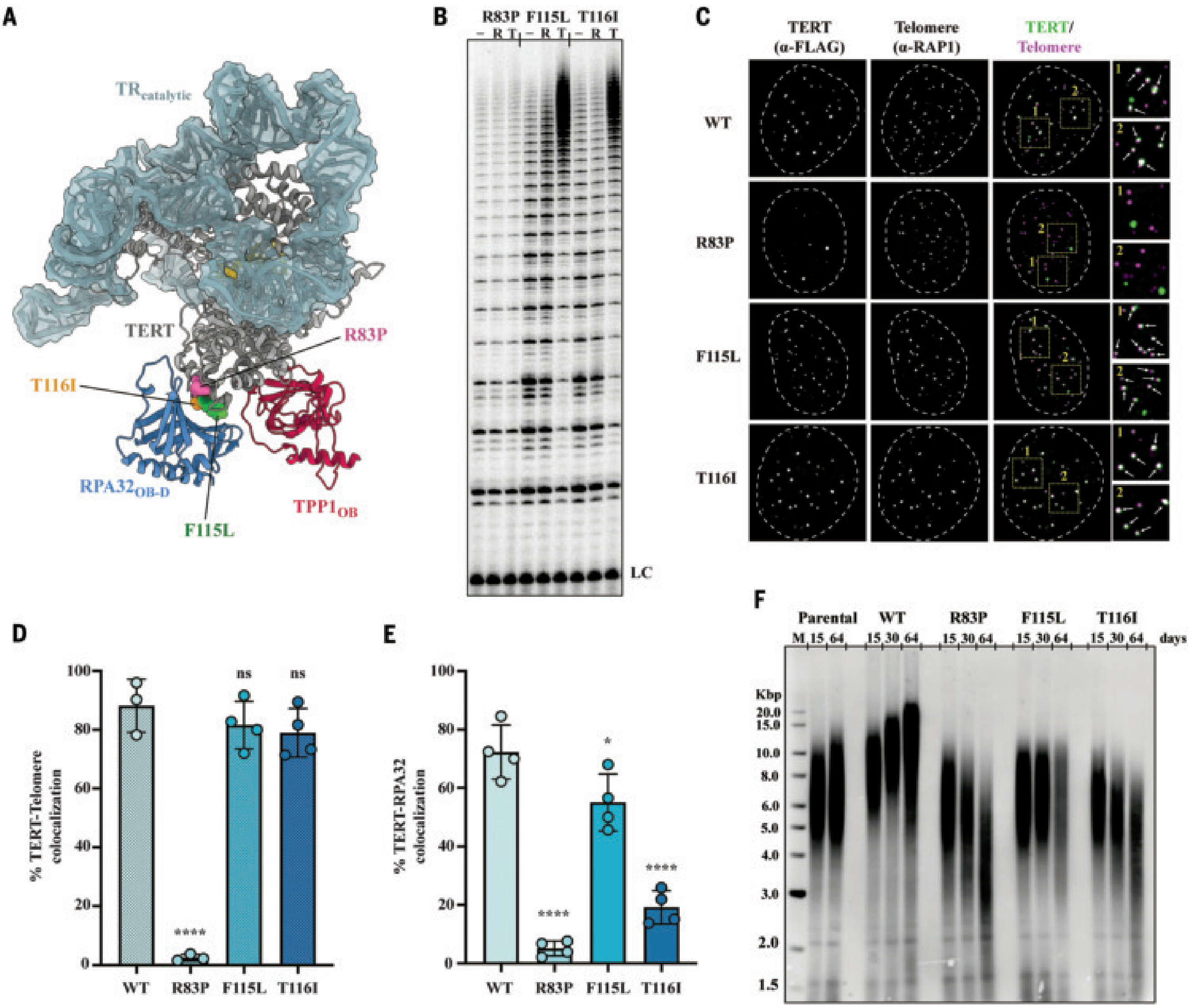

Fig. 5. Loss in telomerase RAP stimulation by RPA provides an explanation for short telomere disease TERT mutations. (**A**) Short-telomere disease–associated TERT mutations mapped onto the structural model of the telomerase-RPA32-TPP1 complex. R83P (pink) (*39*), F115L (green) (*40*), and T116I (orange) (*41*) are highlighted. (**B**) Direct telomerase assay comparing WT TERT with the indicated disease mutants in the presence of no added protein (–), 200 nM RPA (R), or 200 nM TPT (T). (**C**) Representative IF images showing localization of TERT (α-FLAG, green) and telomeres (α-RAP1, magenta) in cells expressing WT TERT or the indicated mutants. Dashed lines indicate nuclei. (**D**) Quantification of TERT and telomere colocalization from images as in (C). (**E**) Quantification of TERT and RPA32 colocalization for the indicated mutants. (**F**) Telomere length analysis by means of Southern blot of parental cells and cells expressing WT or mutant TERT at different time points (days). M, molecular weight marker in kilobase pairs (Kbp). In bar charts, error bars indicate the SD from $n = 3$ independent experiments, with >100 nuclei analyzed per condition for IF quantifications in (D) and (E). ns, not significant; $*P \leq 0.05$; $****P \leq 0.0001$.

Our biochemical data are consistent with this proposed hand-over model. The AlphaFold3 model predicts that RPA70 OB-A and -B domains bind the 5′ end of the telomeric overhang, which agrees with our finding that these ssDNA binding domains are essential for stimulation (Fig. 1E). Furthermore, RPA displaced a prebound TPP1–POT1 complex from ssDNA regardless of POT1's binding position (fig. S17, A and B), which is consistent with a previous report (*48*). Adding both factors together did not further increase processivity, suggesting that only one factor is used at a time (fig. S17, C to E). Collectively, these results support a two-step mechanism in which RPA replaces POT1 to engage the overhang and stimulate telomerase processivity. Although this model fits our biochemical data and AlphaFold predictions, alternative coordination mechanisms involving POT1—with or without TPP1—remain possible. Future studies will be necessary to clarify the precise sequence of events and the potential roles of other telomere-associated factors (*48*).

Our findings have implications for understanding neo-telomere formation and telomere-related diseases. Because RPA is a major component at double-stranded DNA breaks, our discovery that it stimulates telomerase processivity raises the possibility that this mechanism facilitates telomere formation at these sites (*49*, *50*). Furthermore, identifying disease-associated TERT mutations that disrupt this RPA-mediated stimulation provides a direct mechanistic link to short-telomere syndromes and highlights the RPA–telomerase axis as a potential therapeutic target. Future studies should delineate how shelterin, RPA, and telomerase coordinate to regulate telomere maintenance.

REFERENCES AND NOTES

1. R. J. O'Sullivan, J. Karlseder, *Nat. Rev. Mol. Cell Biol.* **11**, 171–181 (2010).
2. C. Lim, T. R. Cech, *Nat. Rev. Mol. Cell Biol.* **22**, 283–298 (2021).
3. H. Takai, V. Aria, P. Borges, J. T. P. Yeeles, T. de Lange, *Nature* **627**, 664–670 (2024).
4. C. W. Greider, E. H. Blackburn, *Cell* **51**, 887–898 (1987).
5. C. W. Greider, E. H. Blackburn, *Nature* **337**, 331–337 (1989).
6. J. Lingner *et al.*, *Science* **276**, 561–567 (1997).
7. T. M. Nakamura *et al.*, *Science* **277**, 955–959 (1997).
8. Q. He, C. Lim, *Trends Biochem. Sci.* **48**, 860–872 (2023).
9. S. W. Cai, T. de Lange, *Genes Dev.* **37**, 555–569 (2023).
10. H. Xin *et al.*, *Nature* **445**, 559–562 (2007).
11. E. Abreu *et al.*, *Mol. Cell. Biol.* **30**, 2971–2982 (2010).
12. A. M. Tejera *et al.*, *Dev. Cell* **18**, 775–789 (2010).
13. F. Wang *et al.*, *Nature* **445**, 506–510 (2007).
14. M. S. Wold, *Annu. Rev. Biochem.* **66**, 61–92 (1997).
15. V. Schramke *et al.*, *Nat. Genet.* **36**, 46–54 (2004).
16. P. Luciano *et al.*, *EMBO J.* **31**, 2034–2046 (2012).
17. J. Jiang *et al.*, *Science* **350**, aab4070 (2015).
18. H. E. Upton, H. Chan, J. Feigon, K. Collins, *J. Biol. Chem.* **292**, 217–228 (2017).
19. C. A. Moeller-McCoy *et al.*, *Proc. Natl. Acad. Sci. U.S.A.* **122**, e2419309122 (2025).
20. M. P. Rubtsova *et al.*, *Biochemistry (Mosc.)* **74**, 92–96 (2009).
21. A. Bochkarev, R. A. Pfuetzner, A. M. Edwards, L. Frappier, *Nature* **385**, 176–181 (1997).
22. P. Baumann, T. R. Cech, *Science* **292**, 1171–1175 (2001).
23. D. Loayza, H. Parsons, J. Donigian, K. Hoke, T. de Lange, *J. Biol. Chem.* **279**, 13241–13248 (2004).
24. C. M. Latrick, T. R. Cech, *EMBO J.* **29**, 924–933 (2010).
25. J. Jumper *et al.*, *Nature* **596**, 583–589 (2021).
26. L. I. Toledo *et al.*, *Cell* **155**, 1088–1103 (2013).
27. G. E. Ghanim *et al.*, *Nature* **593**, 449–453 (2021).
28. B. Liu *et al.*, *Nature* **604**, 578–583 (2022).
29. Z. Sekne, G. E. Ghanim, A.-M. M. van Roon, T. H. D. Nguyen, *Science* **375**, 1173–1176 (2022).
30. S. Padmanaban, V. M. Tesmer, J. Nandakumar, *Life Sci. Alliance* **6**, e202201727 (2023).
31. J. Abramson *et al.*, *Nature* **630**, 493–500 (2024).
32. J. C. Schmidt, A. B. Dalby, T. R. Cech, *eLife* **3**, e03563 (2014).
33. O. Söderberg *et al.*, *Nat. Methods* **3**, 995–1000 (2006).
34. R. C. DeKelver *et al.*, *Genome Res.* **20**, 1133–1142 (2010).
35. L. Xi, T. R. Cech, *Nucleic Acids Res.* **42**, 8565–8577 (2014).
36. T. L. Beattie, W. Zhou, M. O. Robinson, L. Harrington, *Mol. Cell. Biol.* **21**, 6151–6160 (2001).
37. E. L. Denchi, T. de Lange, *Nature* **448**, 1068–1071 (2007).
38. S. Din, S. J. Brill, M. P. Fairman, B. Stillman, *Genes Dev.* **4**, 968–977 (1990).
39. T. J. Vulliamy *et al.*, *PLOS ONE* **6**, e24383 (2011).
40. K. E. Schratz *et al.*, *Blood* **135**, 1946–1956 (2020).
41. S. Feurstein *et al.*, *Blood Adv.* **4**, 4873–4886 (2020).
42. R. Sharma *et al.*, *Blood* **139**, 1039–1051 (2022).
43. R. Kochman *et al.*, *Genes Dev.* **38**, 755–771 (2024).
44. F. L. Zhong *et al.*, *Cell* **150**, 481–494 (2012).
45. J. Nandakumar *et al.*, *Nature* **492**, 285–289 (2012).
46. A. N. Sexton *et al.*, *Genes Dev.* **28**, 1885–1899 (2014).
47. V. M. Tesmer, K. A. Brenner, J. Nandakumar, *Science* **381**, 771–778 (2023).
48. R. L. Flynn *et al.*, *Nature* **471**, 532–536 (2011).
49. A. O. M. Wilkie, J. Lamb, P. C. Harris, R. D. Finney, D. R. Higgs, *Nature* **346**, 868–871 (1990).
50. C. G. Kinzig, G. Zakusilo, K. K. Takai, L. R. Myler, T. de Lange, *Science* **383**, 763–770 (2024).
51. M. A. Cianfrocco, M. Wong-Barnum, C. Youn, R. Wagner, A. Leschziner, "COSMIC2: A Science Gateway for Cryo-Electron Microscopy Structure Determination" in *Practice and Experience in Advanced Research Computing 2017: Sustainability, Success and Impact* (Association for Computing Machinery, 2017), pp. 1–5; https://dl.acm.org/doi/10.1145/3093338.3093390.
52. S. Agrawal *et al.*, Human RPA is an essential telomerase processivity factor for maintaining telomeres. Zenodo (2025); https://doi.org/10.5281/zenodo.17100911.

ACKNOWLEDGMENTS

We thank V. Lundblad, D. Wuttke, M. Stone, J. Schmidt, S. Cohen, and T. Bryan for their constructive suggestions and discussions and T. Record and colleagues in the Lim and Huang laboratories for their valuable input. We thank K. Nguyen for generously providing the hTR expression plasmid and K. Mehta for the superRPA plasmid. For computational support, we acknowledge the COSMIC^2 platform (*51*) for our initial AlphaFold work and thank J. Herr and the departmental IT team for their assistance in setting up our computational workflow. We acknowledge the use of facilities and equipment supported by the University of Wisconsin–Madison Biophysics Instrumentation Facility, which was established with support from the University of Wisconsin–Madison and grants BIR-9512577 (NSF) and S10 RR13790 (NIH). **Funding:** Support for this research was provided to C.J.L. by the National Institutes of Health; the National Institute of General Medical Sciences (R01GM153806 and DP2GM150023); and the University of Wisconsin–Madison, Office of the Vice-Chancellor for Research and Graduate Education with funding from the Wisconsin Alumni Research Foundation and the Department of Biochemistry. X.H. acknowledges the support from the Hirschfelder Professorship Fund. In addition, individual support was provided to M.S.O. and K.M.A. by a NIH T32 predoctoral fellowship (T32GM130550), to S.A. by the William H. Peterson Graduate Fellowship, to B.L.C. by the Arthur B. Michael Biochemistry Graduate Fellowship, and to Q.H. by the Louis and Elsa Thomsen Wisconsin Distinguished Graduate Fellowship. **Author contributions:** Conceptualization: C.J.L. Methodology: S.A., X.L., V.S., M.S.O., B.L.C., V.R.T., X.H., and C.J.L. Investigation: S.A., X.L., V.S., M.S.O., B.L.C., G.P.T., V.R.T., Q.H., K.M.A., and C.J.L. Visualization: V.S. and C.J.L. Funding acquisition: C.J.L. and X.H. Project administration: C.J.L. Supervision: S.A., C.J.L., and X.H. Writing – original draft: C.J.L. and S.A. Writing – review & editing: C.J.L, S.A., X.L., V.S., M.S.O., B.L.C., V.R.T., Q.H., K.M.A., and X.H. **Competing interests:** The authors declare no competing interests. **Data and materials availability:** Plasmids and cell lines generated are available upon request. All AlphaFold predicted models and MD simulation–related files are archived at Zenodo (*52*). All other data are available in the main text or supplementary materials.

SUPPLEMENTARY MATERIALS

science.org/doi/10.1126/science.ads5297
Materials and Methods; Figs. S1 to S17; Tables S1 to S3; References (*53*–*76*)

Submitted 17 August 2024; resubmitted 8 June 2025; accepted 11 September 2025

10.1126/science.ads5297

POLYMER RECYCLING

Glycolysis-compatible urethanases for polyurethane recycling

Yanchun Chen[1]†, Jinyuan Sun[1,2]†, Kelun Shi[1,2]†, Tong Zhu[1], Ruifeng Li[1], Ruiqiao Li[2,3], Xiaomeng Liu[1,2], Xinying Xie[1], Chao Ding[1], Wen-Chao Geng[1,4], Jinwei Ren[5], Wenyu Shi[6], Yinglu Cui[1,5,7]*, Bian Wu[1]*

Recycling thermoset polyurethanes is hindered by their cross-linked structures and chemically stable urethane bonds. Although chemo-enzymatic approaches offer promise, known urethanases remain inefficient under industrial glycolysis conditions. Here, we present GRASE [graph neural network (GNN)–based recommendation of active and stable enzymes], a GNN-based framework that integrates self-supervised and supervised learning to identify efficient, glycolysis-compatible urethanases. Among these, *Ab*PURase exhibited two orders of magnitude greater activity than previously known enzymes in 6 molar diethylene glycol, enabling near-complete depolymerization of commercial polyurethane at kilogram scale within 8 hours. Structural analysis revealed that a tightly packed hydrophobic core and proline-stabilized lid loop may confer *Ab*PURase's stability and efficiency in harsh solvents. This work highlights how deep learning accelerates the discovery of biocatalysts with industrial potential and addresses a critical barrier in polyurethane recycling.

Advances in biocatalytic polyester recycling (*1*) have illuminated the potential of enzymatic depolymerization for developing alternatives, especially hydrolyzable polymers. Polyurethane, with an annual global consumption of 22 million metric tons in 2024, constitutes the second largest category of hydrolyzable plastics (*2*, *3*). Its production process is energy intensive and heavy in terms of greenhouse gas emissions, requiring 331 MJ/kg of energy and 12.3 kg-CO_2e/kg of greenhouse gas emissions (*4*). Polyurethanes are classified as polyester or polyether based depending on the polyol segment, although all contain urethane linkages. Recent biodegradation efforts have focused on ester hydrolases such as cutinases, which cleave ester bonds in the polyol segment (*5*–*9*). By contrast, polyether polyurethanes, which constitute ~75% of the polyurethane foam market (*10*), remain highly resistant to biodegradation because of the lack of enzymes that are capable of cleaving urethane linkages (*11*).

Compounding this challenge, commercial polyurethane materials are predominantly thermoset with extensive cross-linked networks that impede enzymatic penetration. Unlike thermoplastics such as polyethylene terephthalate (PET), which can be remolded into amorphous states through melt extrusion, thermoset polyurethanes cannot be reshaped to enhance susceptibility to enzymatic attack (*12*, *13*). Therefore, alternative recycling techniques are needed to overcome the depolymerization challenges posed by thermoset materials.

Currently, glycolysis represents the most promising industrial-scale chemical recycling method for polyurethane. During this process, polyols undergo transesterification with alcohol reagents such as diethylene glycol (DEG) (*14*–*16*), resulting in an upper phase enriched with recovered polyols that are suitable for straightforward reuse in new polyurethane syntheses. The bottom phase, constituting >60% (w/w) of glycolysis products, accumulates excess DEG along with a mixture of *N*-aryl carbamates [toluenediamine-DEG (TDA-DEG) or 4,4′-methylenedianiline-DEG (MDA-DEG)] and their related derivatives. Although the polyol-rich upper phase is routinely reclaimed, the bottom phase is seldom valorized and would be incinerated as hazardous waste, imposing environmental and economic burdens. The aromatic mixture can increase the viscosity of the bottom phase, which severely impedes the DEG recovery, so ongoing research has focused on valorizing the aromatic mixture (*11*, *17*). Although hydrolytic recovery offers a potential route for recovering monomeric components from these carbamate by-products, the process currently requires energy-intensive conditions (200°C, 16 bar, pH > 12), diminishing the ecological advantages provided by glycolysis (*17*) (fig. S1, tables S1 and S2, and supplementary text 1). A recent advancement by Branson *et al.* introduced a chemo-enzymatic process for polyurethane foam recycling using urethanases (UMG-SPs, including SP1, SP2, and SP3) to hydrolyze *N*-aryl carbamates (*11*). Despite considerable interest, these enzymes retain unresolved limitations in organic solvent compatibility, a longstanding challenge in chemo-enzymatic systems (*18*). A phase change from the organic phase to the aqueous phase is necessary for facilitating enzymatic depolymerization, which requires a substantial amount of solvent evaporation that compromises industrial feasibility (table S2 and supplementary text 1). Further protein engineering efforts to enhance the performance of SP1 have yielded limited gains (*19*), raising demands for more efficient glycolysis-compatible enzymes.

Distinct regioselectivity across diverse urethanases

With various potential PURases described, we initially explored the hydrolytic activity of 14 literature-claimed PURases on *N*-aryl carbamates, encompassing carbamate-degrading amidases from *Agrobacterium tumefaciens* d3 (AmdA) (*20*), *Rhodococcus erythropolis* MP_{50} (ReMP50) (*21*), *Candida parapsilosis* NBRC 708 (CPUTNase) (*22*), *Aspergillus oryzae* (AmdS) (*22*), and *Lysinibacillus fusiformis* SCO2 (SCO2) (*23*), as well as SP1 (*11*) and seven metagenomic urethanases from a patent (GatA or Aes urethanases) (*24*). LCC^{ICCG} (*1*), a cutinase known for its activity on PET, was also evaluated. For benchmarking, we used aromatic carbamates derived from the glycolysis of toluene diisocyanate (TDI)–based polyurethane with DEG. The bottom-phase products included bis[2-(2-hydroxyethoxy)ethyl] (4-methyl-1,3-phenylene) dicarbamate (2,4-TDA-DEG) and bis[2-(2-hydroxyethoxy)ethyl] (2-methyl-1,3-phenylene) dicarbamate (2,6-TDA-DEG), along with their derivatives. We mapped the *ortho*- versus *para*-hydrolytic specificities of each enzyme given the enzymatic accessibility of either ester group in these carbamates.

Among the 14 enzymes evaluated, only Aes72 (*24*), GatA (*24*), and SP1 demonstrated hydrolytic activity toward these aromatic carbamates, with Aes72 exhibiting the highest specific activity of 0.06 U/mg for the hydrolysis of 2,4-TDA-DEG (Fig. 1). This enzyme preferentially hydrolyzed the *ortho* urethane bond of 2,4-TDA-DEG to generate the intermediate 4-TAC, which subsequently underwent hydrolysis at the *para* position to produce the 2,4-TDA monomer. Although GatA also targeted the *ortho* urethane bond, it exhibited considerably lower efficiency (<60% substrate conversion) and failed to produce any detectable monomers within the reaction period. In contrast to Aes72 and GatA, SP1 demonstrated more promiscuous regioselectivity, hydrolyzing both *ortho* and *para* urethane bonds. Nevertheless, SP1 primarily generated 2-TAC as the intermediate of 2,4-TDA-DEG with low catalytic efficiency, whereas it showed higher activity (0.65 U/mg) toward

---

[1]AIM Center, College of Life Sciences and Technology, Beijing University of Chemical Technology, Institute of Microbiology, Chinese Academy of Sciences, Beijing, China. [2]University of Chinese Academy of Sciences, Beijing, China. [3]State Key Laboratory of Biochemical Engineering, Institute of Process Engineering, Chinese Academy of Sciences, Beijing, China. [4]State Key Laboratory of Green Biomanufacturing, Beijing, China. [5]State Key Laboratory of Microbial Diversity and Innovative Utilization, Beijing, China. [6]College of Biological Sciences, China Agricultural University, Beijing, China. [7]Beijing Key Laboratory of Genetic Element Biosourcing & Intelligent Design for Biomanufacturing, Beijing, China. ***Corresponding author. Email: cuiyinglu@im.ac.cn (Y.Cui); thebianwu@outlook.com (B.W.)** †These authors contributed equally to this work.

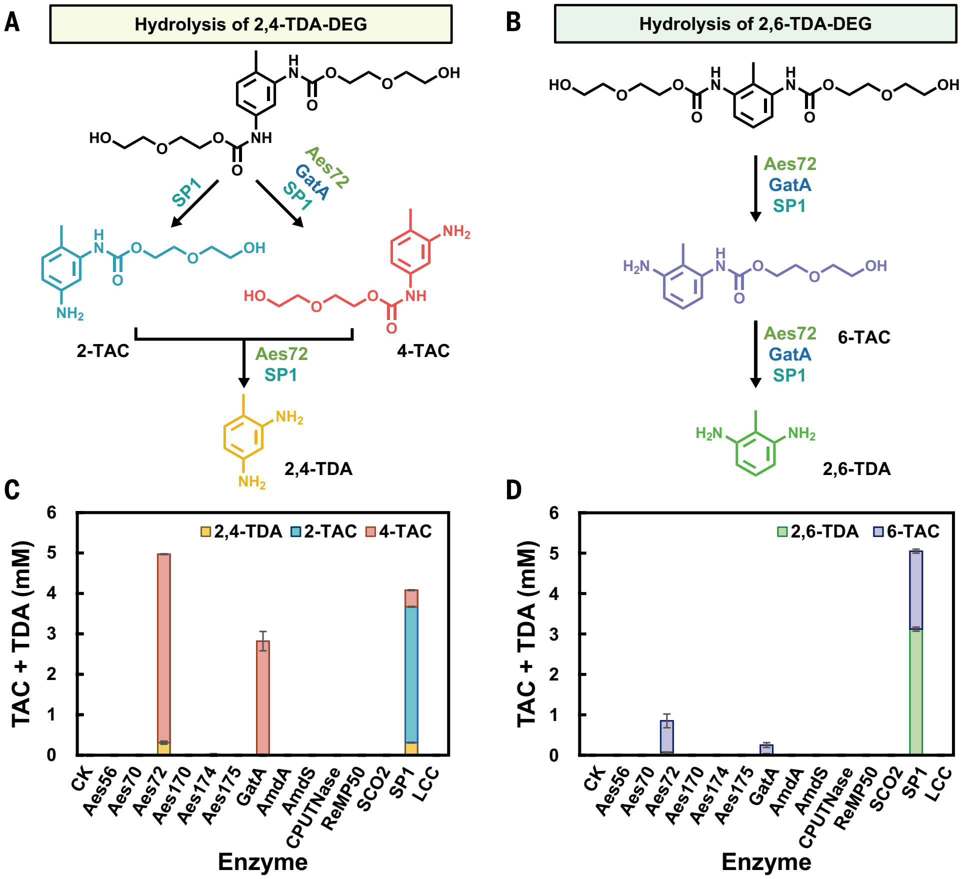

Fig. 1. Hydrolytic pathway of TDA-DEG and the enzymatic activity of literature-claimed PURases. (**A**) The hydrolysis of 2,4-TDA-DEG produces the intermediate compounds 2-TAC and 4-TAC, which are further hydrolyzed to produce 2,4-TDA. (**B**) The hydrolysis of 2,6-TDA-DEG generates the intermediate 6-TAC, which is subsequently hydrolyzed to form 2,6-TDA. (**C** and **D**) Enzymatic hydrolysis of 2,4-TDA-DEG (C) and 2,6-TDA-DEG (D) through published PURases. Reactions were conducted in 100 mM sodium phosphate buffer, pH 7.5, at 50°C for all enzymes except SP1, which was performed at 37°C to prevent thermal inactivation. All data are presented as mean ± SD ($n = 3$).

2,6-TDA-DEG (~44-fold higher activity than that of Aes72). Given the typical 8:2 predominance of 2,4-TDA-DEG over 2,6-TDA-DEG in feedstocks (*25*), preferentially hydrolyzing of 2,4-TDA-DEG is more essential. Therefore, Aes72 has emerged as a promising template for further development.

Machine learning–guided discovery of efficient PURases

We commenced our exploration by performing sequence-based searches with BLASTp against the National Center for Biotechnology Information (NCBI) nonredundant protein database, as well as structure-based retrieval with Foldseek (*26*) against the AlphaFold Protein Structure Database (AlphaFold DB). Candidates identified by these approaches were prioritized on the basis of their sequence or structural identity with respect to Aes72. An experimental validation of the top 10 ranked candidates derived from these approaches demonstrated that only four exhibited urethanase activity for generating TDA monomers, with candidate B1 showing a modest 30% increase in activity compared with that of Aes72 (table S3). Candidates F4 and F5 even failed to generate either TAC intermediates or TDA monomers. We subsequently adopted a clustering approach analogous to that used for exploring the PETase sequence landscape (*27*) and complemented it with an enzyme-substrate complex structure prediction method for substrate-binding analysis (*28*). A total of 216 representative sequences were sampled from 126 clusters through a neighborhood analysis, and the structures were predicted for each in complex with 2,4-TDA-DEG. The 12 top-ranked candidates with the lowest Rosetta energy scores were selected for experimental validation. However, only two candidates generated TDA monomers (table S4). These results show the limitations of relying exclusively on sequence or binding predictions for PURase discovery without extensive experimental characterization.

Recently, deep learning models that learn high-dimensional enzyme representations have demonstrated greater predictive accuracy than that of conventional sequence-similarity metrics, particularly for enzyme commission (EC) number prediction tasks (*29*). Given the absence of specific EC numbers for PURases, we introduced a graph neural network (GNN)–based algorithm using supervised learning frameworks to capture structural representations for function prediction. The pocket residue prediction neural network (named Pythia-Pocket) was trained on the PDB-Bind database to extract the functional features of individual amino acids from protein structures and to predict the probability of each amino acid being a ligand-binding residue (Fig. 2A). Pythia-Pocket used predicted apo structures as its inputs without relying on the additional enzymatic activity data required by other pocket-based approaches (*30*). Protein structures were abstracted as graphs, where amino acid types were encoded as vertex features and backbone atomic distances were encoded as edge features. Neighboring residues were defined using the k-nearest neighbor approach. A message-passing neural network (MPNN) was used to iteratively update the vertex and edge representations. Through multiple MPNN blocks, information propagated across the structure, ultimately generating residue-level embeddings. The embeddings were then compared using cosine similarity to assess their structural similarity. Higher similarity among the catalytic residue representations indicated analogous pocket environments, thereby facilitating the identification of functionally related enzymes. To evaluate the efficiency of Pythia-Pocket, we benchmarked it against the existing PETase identification methods. The results revealed the outstanding performance of Pythia-Pocket in identifying experimentally validated PETases, highlighting the advantage of this approach in pinpointing functionally similar enzymes, especially within underrepresented enzyme classes (fig. S2, table S5, and supplementary text 2.1 and 2.2). The stability of the candidates was evaluated by Pythia (*31*), our previously developed neural network, which predicts the likelihood of an individual residue on the base of its local structural context, to estimate protein stability through a negative log-likelihood (NLL) metric (fig. S3 and supplementary text 2.3 and 2.4). In light of the inherent trade-off between activity and stability, we integrated both Pythia and Pythia-Pocket into a unified framework called GRASE (GNN-based recommendation of active and stable enzymes) to identify candidates that optimally balanced the structural robustness and target functionality of the NCBI nonredundant protein database and the AlphaFold DB (Fig. 2B). We stratified the cosine similarity between

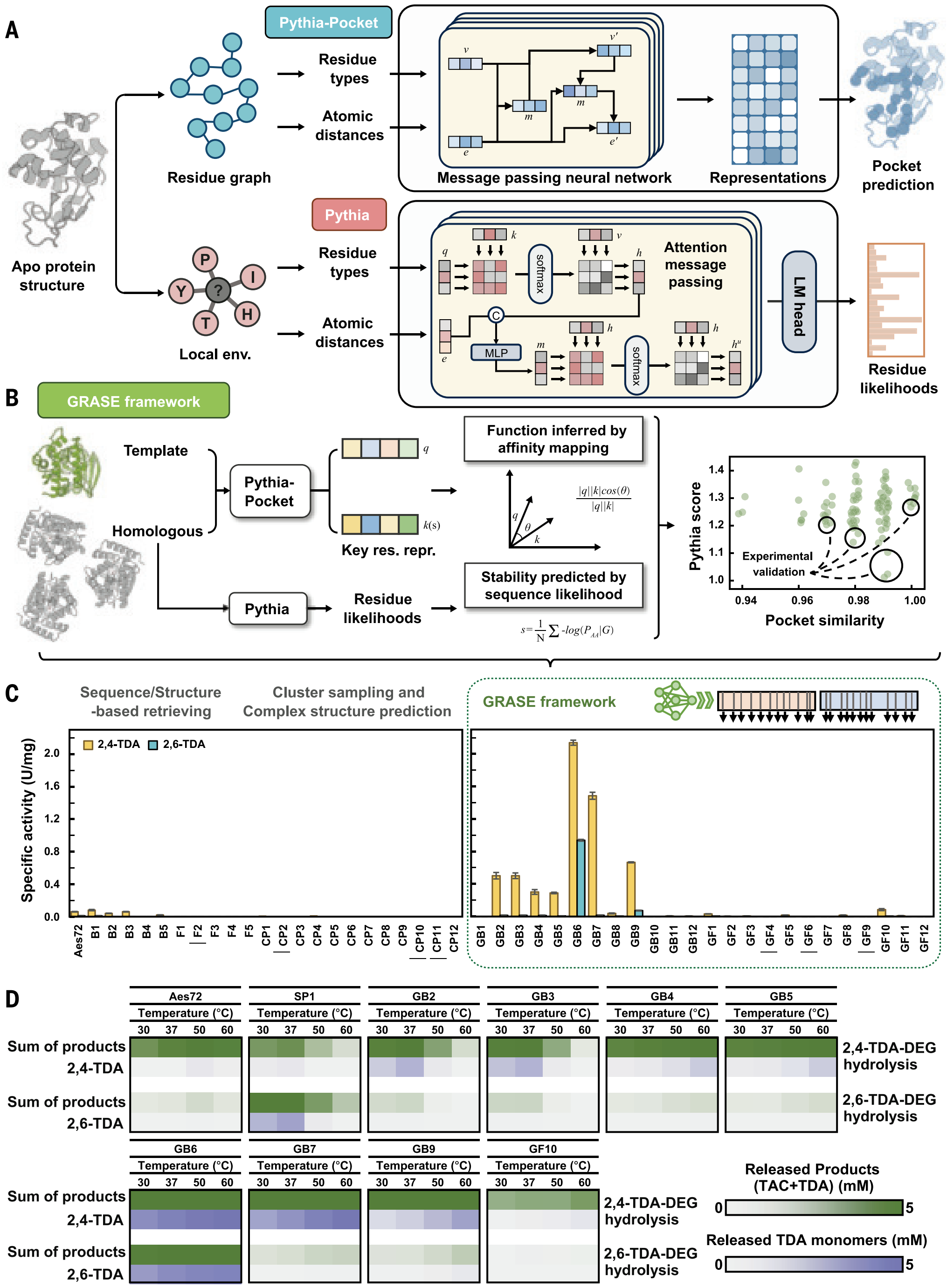

Fig. 2. Architecture of the models and functional validation of GRASE-identified enzymes. (**A**) Architectures of Pythia-Pocket and Pythia. Both models abstract protein structures as graphs, starting with the apo protein structure. In Pythia-Pocket, the entire protein graph is used as the input for an MPNN, generating vertex representations (v) for each residue. These representations are then passed through a linear layer to predict the probability of each residue being part of the ligand-binding pocket. Conversely, Pythia uses the local structure context of each amino acid as an input, updating residue-specific interactions through attention-based message passing. The final output predicts probability distributions for each amino acid type at the central residue. (**B**) Overview of the GRASE workflow. Pythia-Pocket generates residue-level embeddings for the key catalytic residues of the query protein (e.g., Aes72) and candidate structures. The cosine similarity between the key residue representations is calculated to quantify the functional similarity between the active sites of the query and candidate proteins. Concurrently, protein stability is evaluated using Pythia by calculating the NLL of each candidate sequence, where lower NLL values indicate higher predicted stability. (**C**) Enzyme hydrolysis of 2,4-TDA-DEG and 2,6-TDA-DEG. The candidates identified through a sequence-based search (B1 to B5), structure-based retrieving (F1 to F5), and sequence clustering (CP1 to CP12), along with GRASE-curated enzymes (GB1 to GB12 and GF1 to GF12) were evaluated for their catalytic activity toward 2,4-TDA-DEG and 2,6-TDA-DEG. Enzymes that failed to express (F2, CP2, CP10, CP11, GF4, GF6, and GF9) are underlined. The specific activities of these enzymes were measured at their optimal temperatures. One unit of PURase activity is defined as the amount of enzyme that hydrolyze 2,4-TDA-DEG equivalent to 1.0 μmol of 2,4-TDA monomers per minute. All data are presented as mean ± SD ($n = 3$). (**D**) Heatmaps of each product after TDA-DEG hydrolysis with GRASE-curated enzymes performed from 30° to 60°C over 1 hour in 100 mM sodium phosphate buffer, pH 7.5. Enzymes with specific activities lower than 0.05 U/mg are not shown. The heatmap gradient represents the sum of the released products (TAC intermediates + TDA monomers) (green) and TDA monomers (purple) from 0 to 5 mM.

the key catalytic residues of the candidates and Aes72 derived from Pythia-Pocket into four distinct tiers ranging from 1.00 to 0.97. Within each tier, the three sequences with the highest Pythia-predicted stability values were selected. This approach established functional similarity as a baseline while maximizing stability, allowing for a more comprehensive exploration of the sequence-function landscape.

By applying GRASE without any expert curation, we experimentally evaluated the 24 top-ranked candidates (tables S6 and S7). Among them, 21 were successfully expressed and exhibited urethanase activity toward *N*-aryl carbamates, with 17 generating both TAC intermediates and TDA monomers and the remaining four yielding only TAC (Fig. 2, C and D). Eight outperformed the benchmark (Aes72), with five (GB2, GB3, GB6, GB7, and GB9) achieving activities greater than 0.5 U/mg (table S8). GB6 (*Ab*PURase) exhibited the highest activity, with a 32-fold increase in activity against 2,4-TDA-DEG (2.14 U/mg) and a 62-fold enhancement against 2,6-TDA-DEG (0.94 U/mg) relative to Aes72. A similar performance was observed for GB7, which demonstrated activity toward 2,4-TDA-DEG at 1.49 U/mg but significantly reduced activity toward 2,6-TDA-DEG at only 0.02 U/mg. When exposed to 6 M DEG, the activity of *Ab*PURase was even more pronounced, with 465- and 170-fold improvements over Aes72 at 50° and 37°C, respectively (figs. S4 and S5). Coupled with its high expression level, these results highlighted the considerable potential of *Ab*PURase for degradation in the postglycolysis phases of polyurethane recycling. Beyond the identification of *Ab*PURase, the enzymes filtered by GRASE outperformed those ranked by overall structural similarity, because all soluble GRASE candidates produced TAC, and seven of them could further produce TDA monomers. These enzymes retained the key catalytic functions despite their low overall sequence identity levels (as low as 34%). These results illustrate that the similarity of local structural motifs may preserve the essential catalytic functions in distantly related enzymes, offering valuable perspectives on functional domains that may inform evolutionary diversification.

Chemo-enzymatic depolymerization of commercial polyurethane foams at kilogram scale

We subsequently conducted chemo-enzymatic depolymerization on commercial polyurethane foams. Given that BASF is one of the major global suppliers of polyurethane (*32*), its products are well suited for use as standardized substrates for chemo-enzymatic degradation. We embarked on the glycolysis of a TDI-based flexible polyurethane foam from BASF, resulting in an apolar upper phase enriched with polyols, an intermediate phase concentrated in styrene-acrylonitrile (*33*), and a polar bottom phase containing DEG and diverse aromatic compounds (Fig. 3A). Because of the water added during the foaming process, the polyurethane foam contained not only carbamates but also *N*,*N*′-diarylurea functional groups, leading to the formation of a small amount of diphenylurea derivatives in the bottom phase (fig. S6).

Before enzymatic treatment, the reaction parameters were optimized (figs. S7 and S8) with consideration of process-modeled operating costs for polyurethane recycling (tables S9 and S10 and supplementary text 1). An enzyme loading of 8 mg/g (milligrams of enzyme per gram of polyurethane) was estimated as the economical compromise between productivity and cost, reducing the incurred operating expenses by \$47 tons^{-1} compared with those required at 16 mg/g while achieving near-complete conversion within 12 hours (fig. S7 and table S10). After optimization, we evaluated the hydrolytic performance of *Ab*PURase, Aes72, and SP1 on the bottom phase derived from glycolysis of 30 g of BASF foam at temperatures ranging from 30° to 60°C (fig. S9 and tables S11 and S12). *Ab*PURase showed a maximal initial conversion (37% at 0.5 hours) at 60°C, but enzyme inactivation curtailed the overall depolymerization to 91% after 12 hours. At 50°C, *Ab*PURase maintained robust activity, obtaining 33% conversion at 0.5 hours and, ultimately, 98% conversion at 12 hours, with the complete hydrolysis of TAC to TDA, releasing ~385 mM of TDA. By contrast, SP1 and Aes72 achieved only 3 and 5% conversion within the initial 0.5 hours, respectively, at their optimal temperatures (30°C for SP1 and 37°C for Aes72). Prolonged 12-hour incubations led to a modest final conversion of 15% for SP1 and 26% for Aes72, rendering them unsuitable for integration into upstream glycolysis workflows (Fig. 3B). In addition to its operational stability, *Ab*PURase demonstrated notable reusability. Without any immobilization treatment, the enzyme could be recycled and achieve near-complete conversion within 12 hours for at least three cycles (fig. S10).

Building on these bench-scale results, we implemented a kilogram-scale process. One kilogram of BASF polyurethane foam was subjected to glycolysis at 190°C for 3.5 hours with DEG at a ratio of 1:1.5. This reaction afforded an upper phase of 734 g, a bottom phase of 1507 g, and 221 g of insoluble solids (Fig. 3A). Because of the excess of alcohol reagent, the bottom phase was primarily composed of 83% DEG at 8.6 M, along with 14% aromatic compounds (Fig. 3A, fig. S11, and table S13). Consistent with the bench-scale results, *Ab*PURase reached 90% conversion within 2 hours and 98.6% after 8 hours at an enzyme loading of 16 mg/g (Fig. 3C). Reducing this to 8 mg/g for economic considerations resulted in slightly diminished initial efficiency (72% at 2 hours, 90% at 4 hours, and 95% at 8 hours). The reaction progressed more gradually after 4 hours and finally reached 98% conversion after 12 hours. The resulting TDA monomers were efficiently recovered through rectification, achieving TDA and DEG recovery rates of 94.7 and 98.5%, respectively (table S14). On the basis of these results and supporting process modeling, preliminary estimates suggest promising scalability. Nevertheless, further efforts are required to improve enzyme performance through protein engineering, to optimize the conversion of recovered TDA to TDI, and to investigate the repolymerization of recycled monomers.

Molecular origin of the urethanase function toward *N*-aryl carbamates

To investigate the molecular origin of the urethanase function, we conducted a comparative structural analysis. The superimposed structures derived from GRASE and other screening algorithms revealed a conserved overall architecture, with root mean square deviation values consistently <1 Å, reflecting the limitation of global structure searches being unable to discern functional subtleties. Upon applying the GRASE framework, we suggest the variations in the local architecture surrounding the catalytic triad of the active enzymes, particularly within the lid domain (Fig. 4A). As shown in Fig. 4B, the nonfunctional proteins from global structure retrieving (e.g., F4 and F5) appeared to harbor narrow, constricted active sites that might impede the accommodation of bulky *N*-aryl carbamates such as TDA-DEG. By contrast, active proteins curated through GRASE were predicted to feature enlarged binding cavities that may facilitate van der Waals interaction stabilizations and enable more favorable orientations of larger aromatic groups. Those exceeding 1 U/mg in specific activity were predicted to have a highly open lid domain, forming a V-shaped architecture and potentially providing ample space for conducting substrate engagement and efficient catalysis. Certain lower-activity enzymes, although predicted to have enlarged active site pockets, appeared to feature relatively restricted lid domains. Despite the low activity of the enzymes identified through structural retrieval, their inclusion suggested considerable diversity in the architecture of the predicted lid domain. For example, GF5 and GF8, which displayed activities <0.1 U/mg, were predicted to have structurally compromised lid domains. GF5 may contain a single helix instead of the typical two-helix configuration in the lid domain, whereas GF8 was predicted to lack a lid domain. These structural variations suggest that although an open lid domain may be integral for facilitating substrate accommodation, the

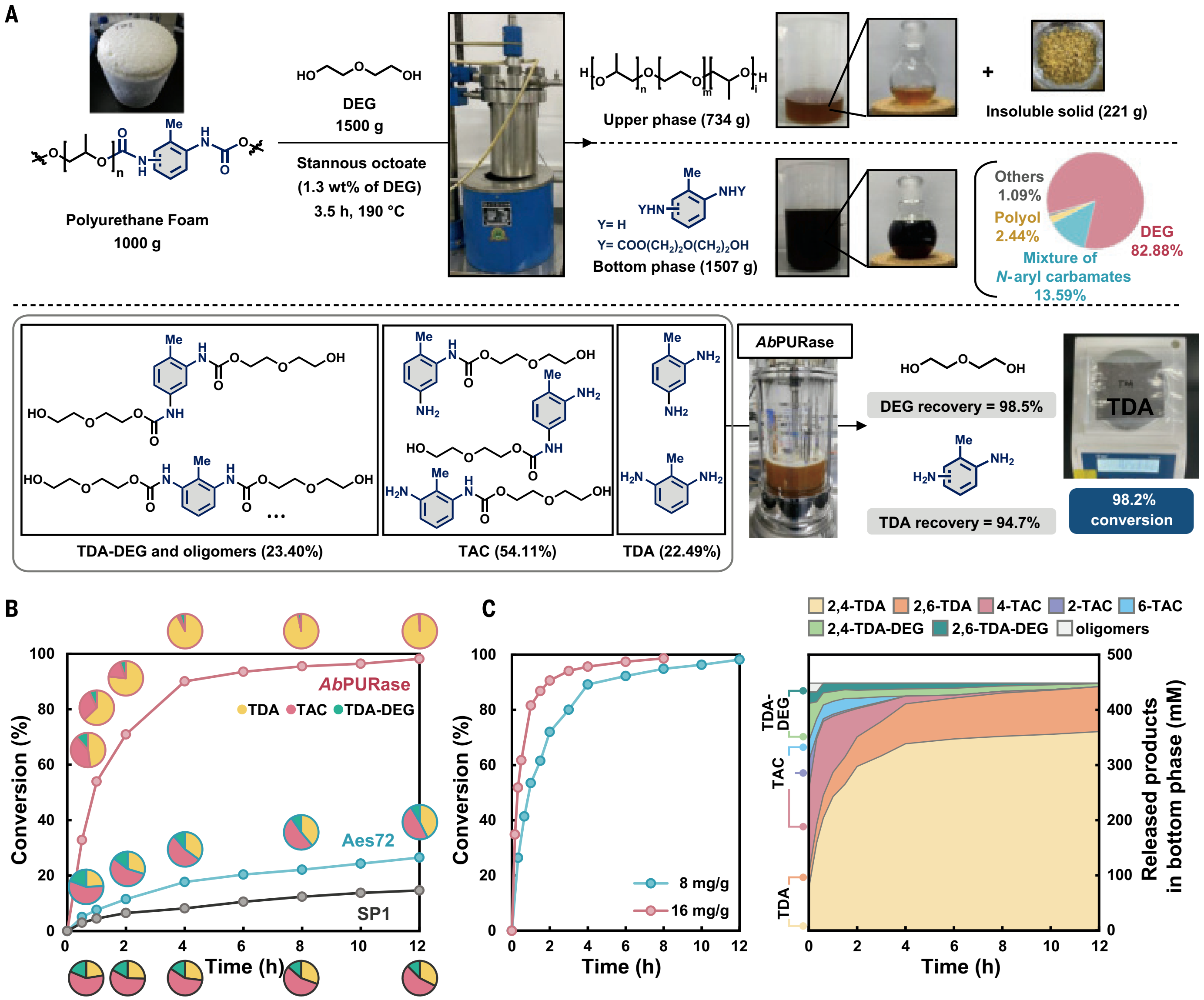

Fig. 3. Chemo-enzymatic depolymerization of BASF polyurethane foam. (**A**) Chemo-enzymatic depolymerization of one kilogram of polyurethane foam. Glycolysis yielded an upper phase enriched with EO-PO-EO copolyether polyols and a bottom phase composed of 8.6 M DEG and low-molecular-weight TDA dicarbamate. The insoluble fraction consisted mainly of additives. The pie chart shows the distribution of the compounds contained in the bottom phase. *Ab*PURase hydrolyzed the TDA dicarbamates in the bottom phase into TDA monomers with an enzyme loading of 8 mg/g. The TDA and DEG products were subsequently purified through rectification. (**B**) Enzymatic hydrolysis of the bottom phase derived from the glycolysis of 30 g of BASF polyurethane foam with 8 mg/g *Ab*PURase (50°C), Aes72 (37°C), and SP1 (30°C) in the bottom phase. Data are from one independent experiment. The pie charts illustrate the relative proportions of TDA-DEG, TAC, and TDA measured at each time point. (**C**) The left panel displays enzymatic hydrolysis of the bottom phase derived from the glycolysis of 1000 g of BASF polyurethane foam with 8 mg/g and 16 mg/g *Ab*PURase at 50°C. The right panel shows temporal variations of the TDA-DEG, TAC, and TDA compositions during enzymatic hydrolysis with 8 mg/g enzyme loading. Data are from one independent experiment.

absence of this critical architecture would severely compromise enzyme functionality.

The critical role of lid domains in modulating functions is commonly seen in the evolutionary adaptations of esterases and lipases, where catalysis in nonaqueous environments is facilitated by a structural transition of the lid domain from a closed to an open conformation (known as interfacial activation) (*34*). Unlike SP1, which belongs to the amidase signature family and uses a Ser-(*cis*)Ser-Lys catalytic triad, *Ab*PURase belongs to the α/β-hydrolase fold-3 (ABH3) superfamily and uses the hydrolase catalytic triad of Ser-His-Asp/Glu. Phylogenetic inference and sequence similarity network analysis suggested phylogenetic independence between these enzymes (fig. S12). Function annotation classified *Ab*PURase and other GRASE-grasped urethanases as carboxylic-ester hydrolases (EC 3.1.1). On the basis of these observations, we validated the esterase activity of *Ab*PURase by hydrolyzing methyl 5-amino-2-methylbenzoate (MAMB) (Fig. 4C). However, *Ab*PURase also exhibited amidase activity, as demonstrated by its cleavage of the C–N bond in *N*-(5-amino-2-methylphenyl)acetamide (NAMA), which was three orders of magnitude greater than its esterase activity (fig. S13). The kinetics analysis suggested that the high performance of *Ab*PURase toward urethane bonds may be attributed primarily to its strong amidase activity.

More crucially, this high activity was retained even in DEG solvents. Up to 6 M DEG, *Ab*PURase exhibited only marginal variation

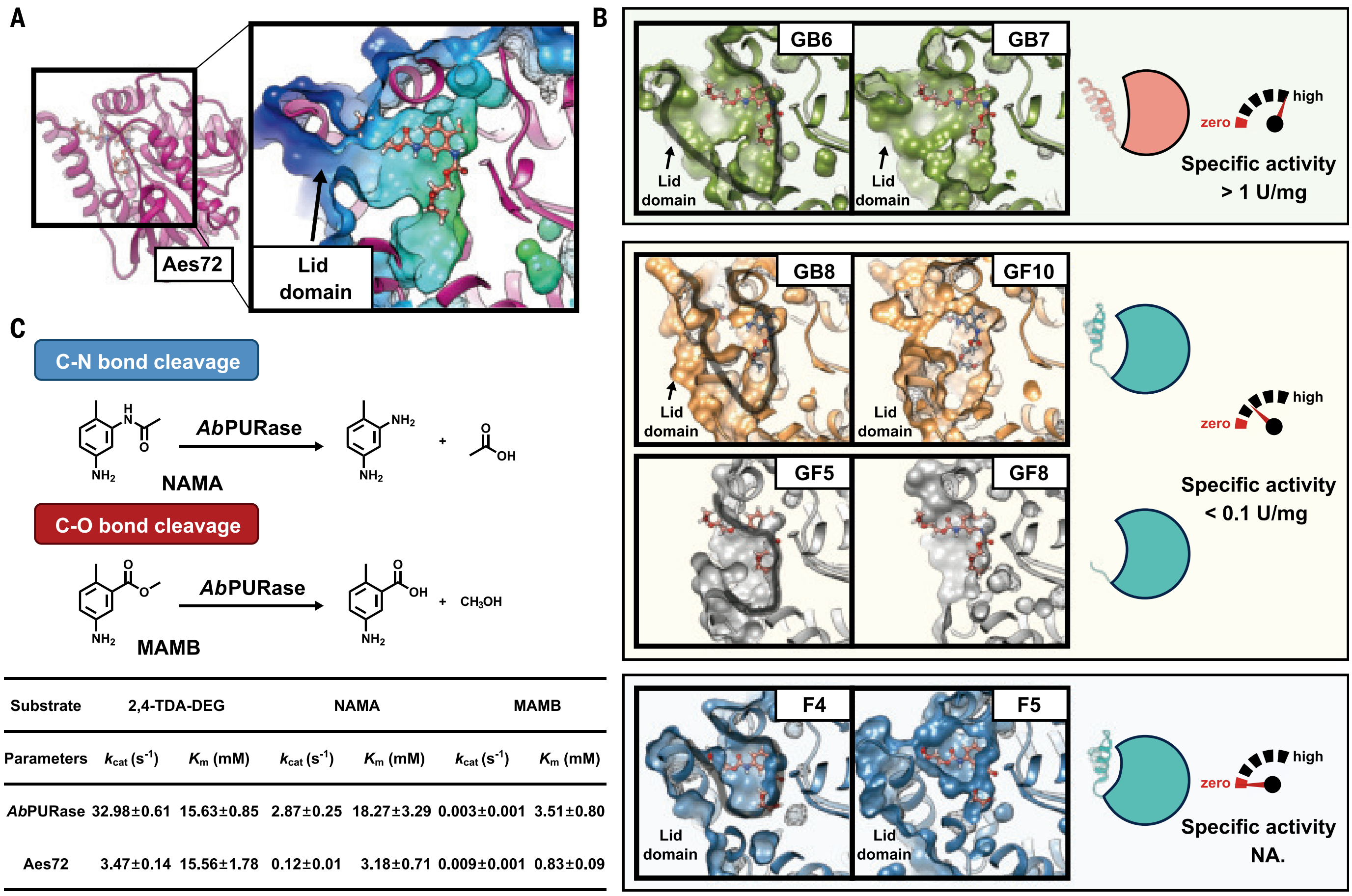

Substrate	2,4-TDA-DEG		NAMA		MAMB	
Parameters	k_{cat} (s^{-1})	K_m (mM)	k_{cat} (s^{-1})	K_m (mM)	k_{cat} (s^{-1})	K_m (mM)
*Ab*PURase	32.98±0.61	15.63±0.85	2.87±0.25	18.27±3.29	0.003±0.001	3.51±0.80
Aes72	3.47±0.14	15.56±1.78	0.12±0.01	3.18±0.71	0.009±0.001	0.83±0.09

Fig. 4. Structural comparison among the enzymes and kinetic parameters. (**A**) Surface structure of Aes72 and its lid region. (**B**) Local structural differences among the active-site pockets of various enzymes highlighting the crucial role of the lid structure in catalytic performance. GF10 structure was obtained from the crystal structure (Protein Data Bank ID: 7NB5), and other enzyme structures were predicted using the AlphaFold3. (**C**) Comparison of Michaelis-Menten kinetic parameters for *Ab*PURase and Aes72 with the substrates 2,4-TDA-DEG, NAMA, and MAMB. All data are presented as mean ± SD ($n = 3$).

in apparent melting temperature (T_m), inferring its structural robustness. By contrast, Aes72 underwent substantial destabilization, with its T_m decreasing by 15°C at 6 M DEG (fig. S14). Consistent with the experimental results, Gaussian accelerated molecular dynamics simulations indicated structural integrity maintenance in *Ab*PURase at 6 M DEG, whereas Aes72 displayed a structural unfolding trend, particularly in the lid region (fig. S15). Detailed structural insights suggest that a tightly packed hydrophobic core in *Ab*PURase formed by residue M38 interacting with lid-domain residues (I9, M12, L13, L35, F197, W271, F277, and I279) could help to prevent DEG infiltration. Conversely, the shorter side chain of the corresponding residue L37 in Aes72 could potentially reduce these interactions, which might facilitate DEG penetration and disruption of the lid domain. Loop$_{\alpha1\text{-}\alpha2}$ in the *Ab*PURase lid domain may be stabilized by multiple proline residues (P24, P25, and P27), whereas Aes72, containing only P25 in loop$_{\alpha1\text{-}\alpha2}$, appears more flexible, potentially promoting partial unfolding of its lid structure. These molecular features provide preliminary insights into the structural stability of *Ab*PURase in DEG-rich environments, although a detailed understanding of the associated mechanism will require further in-depth research.

Discussion

The sequence and structural features underpinning polyurethane hydrolysis have been insufficiently characterized, both within and beyond the currently explored sequence space. The recent successes achieved by representation-based strategies, exemplified by approaches such as CLEAN and Pythia-Pocket, highlight the utility of learned latent embeddings for obtaining more reliable functional inference than conventional sequence- or structure-based comparisons because they capture high-dimensional biochemical features that are often overlooked by the traditional methods. However, subtle differences in catalytic properties may be obscured when embeddings are derived from global representations by using average pooling over the entire protein sequence. Pythia-Pocket addresses this by specifically embedding active-site residues rather than full sequences, enabling finer-grained functional discrimination even among distantly related homologs, as demonstrated by functionally active enzymes identified in this study that shared as little as 34% identity with the reference template. This capability is particularly beneficial for the identification of newly characterized enzymes, as exemplified by plastic-degrading enzymes, directly from a known template without the need for manual expert curation process, thereby accelerating the discovery in functionally underexplored regions of protein spaces. Recognizing that catalytic efficiency is more valuable when accompanied by adequate structural robustness, we integrated Pythia, a neural network that predicts folding stability from the sequence-structure likelihood into the unified GRASE framework, allowing a balance between enzymatic activity and robustness for industrial enzyme discovery.

Enzymes such as *Ab*PURase, which are traditionally classified as esterases, were found to be primarily urethanases in this study. This observation aligns with the broader body of research on enzyme promiscuity and moonlighting, suggesting that many enzymes, rather than being strictly specific, have a range of activities that have often been obscured by conventional classification methods. Therefore, the full functional potential of enzymes may be significantly underappreciated in current annotations. To address this complexity, future studies may focus on efficiently capturing and amplifying the subtle signals that underlie these hidden capabilities. Such efforts will not only deepen our understanding of enzyme function repertoires, but will also contribute to the development of biocatalysts with broad applicability across various industrial challenges.

REFERENCES AND NOTES

1. V. Tournier *et al.*, *Nature* **580**, 216–219 (2020).
2. Plastics Europe, "Plastics – the fast facts 2024" (2024); https://plasticseurope.org/knowledge-hub/plastics-the-fast-facts-2024/.
3. G. Rossignolo, G. Malucelli, A. Lorenzetti, *Green Chem.* **26**, 1132–1152 (2024).
4. S. R. Nicholson, N. A. Rorrer, A. C. Carpenter, G. T. Beckham, *Joule* **5**, 673–686 (2021).
5. J. Liu *et al.*, *Biotechnol. Adv.* **48**, 107730 (2021).
6. A. Raczyńska, A. Góra, I. André, *Biotechnol. Adv.* **77**, 108439 (2024).
7. J. Liu *et al.*, *Appl. Environ. Microbiol.* **90**, e0147723 (2024).
8. F. Di Bisceglie, F. Quartinello, R. Vielnascher, G. M. Guebitz, A. Pellis, *Polymers* **14**, 411 (2022).
9. Z. Jiang *et al.*, *J. Hazard. Mater.* **472**, 134493 (2024).
10. A. Delavarde *et al.*, *Prog. Polym. Sci.* **151**, 101805 (2024).
11. Y. Branson *et al.*, *Angew. Chem. Int. Ed.* **62**, e202216220 (2023).
12. H.-W. Engels *et al.*, *Angew. Chem. Int. Ed.* **52**, 9422–9441 (2013).
13. A. Kemona, M. Piotrowska, *Polymers* **12**, 1752 (2020).
14. D. Simón, A. M. Borreguero, A. de Lucas, J. F. Rodríguez, *Polym. Degrad. Stabil.* **109**, 115–121 (2014).
15. T. Vanbergen *et al.*, *ChemSusChem* **13**, 3835–3843 (2020).
16. G. Kiss, G. Rusu, F. Peter, I. Tănase, G. Bandur, *Polymers* **12**, 1533 (2020).
17. J. del Amo *et al.*, *ACS Sustain. Chem.& Eng.* **12**, 17479–17487 (2024).
18. V. Stepankova *et al.*, *ACS Catal.* **3**, 2823–2836 (2013).
19. T. Bayer *et al.*, *Angew. Chem. Int. Ed.* **63**, e202404492 (2024).
20. S. Trott, R. Bauer, H.-J. Knackmuss, A. Stolz, *Microbiology* **147**, 1815–1824 (2001).
21. S. Trott, S. Bürger, C. Calaminus, A. Stolz, *Appl. Environ. Microbiol.* **68**, 3279–3286 (2002).
22. K. Masaki *et al.*, *J. Biosci. Bioeng.* **130**, 115–120 (2020).
23. Y. Jia, J. Zhou, G. Du, J. Chen, F. Fang, *Food Biosci.* **36**, 100666 (2020).
24. N. Bittner, H. Nefzger, G. Behnken, G. Jaeger, S. Behnken, L. Reisky, "Novel urethanases for the enzymatic decomposition of polyurethanes," EPO Patent EP3587570A1 (2020).
25. N. Azu, A. Chappelle, *Enc. Toxicol.* **9**, 151–156 (2024).
26. M. van Kempen *et al.*, *Nat. Biotechnol.* **42**, 243–246 (2024).
27. H. Seo *et al.*, *Science* **387**, eadp5637 (2025).
28. ByteDance AML AI4Science Team *et al.*, Protenix-advancing structure prediction through a comprehensive AlphaFold3 reproduction. bioRxiv 631937 [Preprint] (2025); https://doi.org/10.1101/2025.01.08.631967.
29. T. Yu *et al.*, *Science* **379**, 1358–1363 (2023).
30. G. Steinkellner *et al.*, *Nat. Commun.* **5**, 4150 (2014).
31. J. Sun, T. Zhu, Y. Cui, B. Wu, *Innovation (Camb.)* **6**, 100750 (2025).
32. A. W. Franz, S. Buchholz, R. W. Albach, R. Schmid, *Green Carbon* **2**, 33–44 (2024).
33. J. del Amo *et al.*, *Materials* **17**, 2844 (2024).
34. M. J. Liszka, M. E. Clark, E. Schneider, D. S. Clark, *Annu. Rev. Chem. Biomol. Eng.* **3**, 77–102 (2012).
35. J. Sun, Y. Cui, B. Wu, "GNN-based Recommendation of Active and Stable Enzymes (GRASE)," Zenodo (2025); https://doi.org/10.5281/zenodo.15549656.

ACKNOWLEDGMENTS

The authors acknowledge the support of the Shanghai BASF Polyurethane Co. Ltd. **Funding:** This work was supported by the National Key R&D Program of China (grant 2024YFC3405500), the Strategic Priority Research Program of the Chinese Academy of Sciences (CAS) (grant XDB0810000), the National Natural Science Foundation of China (grants 32225002, 32170033, and 32422001), Fundamental Research Funds for the Central Universities (grant buctrc202539), the Youth Innovation Promotion Association CAS (grant 2022086), the Postdoctoral Fellowship Program of CPSF (fellowship GZB20240808), and the Beijing Municipal Science & Technology Project, China (grant Z241100007724009). **Author contributions:** Y.Chen and K.S. performed biochemical experiments and collected the data. J.Y.S. developed the Pythia and Pythia-Pocket models. T.Z., X.X., C.D., R.L., and J.R. contributed to data preparation and statistical analyses. R.L., X.L., and W.-C.G. performed process modeling and operating cost analysis. W.S. performed phylogenetic inference and sequence similarity network analysis. Y.C. performed structural modeling and analysis of enzymes and drafted the manuscript with input from all authors. Y.C. and B.W. secured funding, interpreted results, and supervised the study. All authors revised the manuscript and accepted its final version. **Competing interests:** Y.Chen, Y.Cui, and B.W. have filed a patent application that covers the enzyme sequences in the paper. The remaining authors declare no competing interests. **Data and materials availability:** Code for Pythia-Pocket and Pythia are freely accessible at Zenodo (*35*) and GitHub (https://github.com/Wublab/Pythia/). All data used in this analysis are free to access and are available in the main text or the supplementary materials. A complete list of the nucleotide sequences used in this study is provided in data S1.

SUPPLEMENTARY MATERIALS

science.org/doi/10.1126/science.adw4487
Materials and Methods; Supplementary Text S1 to S4; Figs. S1 to S36; Tables S1 to S14; References (*36*–*48*); MDAR Reproducibility Checklist; Data S1

Submitted 2 February 2025; accepted 21 August 2025

10.1126/science.adw4487

EPIDEMIOLOGY

Collateral effects of COVID-19 pandemic control on the US infectious disease landscape

Tobias S. Brett[1]* and Pejman Rohani[1,2,3]

Using data from the United States Centers for Disease Control and Prevention (CDC) disease surveillance systems, we sought to quantify the indirect effects of the COVID-19 pandemic, and the possibility of lack of exposure to common pathogens resulting in immune deficits. Clustering analysis on pandemic-era time-series data identified pathogen groupings according to transmission mechanism. Counterfactual analysis, using Bayesian structural time-series (BSTS) modeling, confirmed that infectious diseases that are directly transmitted via airborne droplets (aerosols) experienced the greatest disruption to transmission. By contrast, sexually transmitted infections (STIs) experienced a smaller transient disruption, and increasing trends in incidence prepandemic appear to have been curtailed. Using epidemiological theory, we demonstrate that the observed magnitudes and durations of notifications deficits were determined by fundamental disease system properties, namely, the serial interval, basic reproductive number, and susceptible recruitment.

The COVID-19 pandemic, caused by the emergence of the novel severe acute respiratory syndrome coronavirus 2 (SARS-CoV-2) coronavirus (*1*), triggered an unprecedented global disruption to human society. Although governmental response measures and individual behavioral changes were targeted at curtailing the spread of SARS-CoV-2 (*2*), they also influenced co-circulating, sympatric infectious diseases (*3–10*). Of particular concern was the prospect that the implementation of social distancing measures would lead to gaps in population immunity against these diseases, with the potential for serious rebound in incidence for some infections after the relaxation of control measures (*11–15*). These fears, motivated by epidemiological theory (*16*, *17*), were borne out in part by the “triple-demic” of SARS-CoV-2, respiratory syncytial virus (RSV), and influenza virus (Fig. 1, A and B) during the winter of 2022–2023 (*18*) and may be contributing to a resurgence of pertussis in 2024 and 2025 (Fig. 1D) (*19*). Additional concerns were raised about potential disruption to disease surveillance efforts, routine vaccination programs (*20*), patient care–seeking behavior (*21*), and health care system capacity (*22*). Ecological competition by a novel pathogen may also have disrupted the community of human infectious diseases (*23*, *24*). The interpretation of post-COVID disease incidence trends is complicated by pandemic-spurred improvements in disease surveillance methodologies (*25*, *26*), spatial variation in disease incidence, and state government responses (Fig. 1, E to J).

The short-term effects of social distancing measures on sympatric infectious diseases have been examined for specific pathogens, including influenza (*11*, *27*, *28*), RSV (*11*, *29*), polio (*30*), tuberculosis (*31*, *32*), pertussis (*10*, *33*, *34*), and enterovirus D68 (*35*). Though valuable in providing epidemiological insights, most of these studies were performed at the height of the pandemic (2020–2021) with the aim of providing “scenario analyses” to project possible postpandemic implications for specific pathogens and diseases. Here, we present a retrospective analysis of surveillance data spanning the pandemic, with the aim of identifying patterns in the impacts of pandemic response measures on a suite of sympatric infectious diseases in the USA.

We carried out a comparative study using time-series data collected by the US Centers for Disease Control and Prevention and made publicly available through the National Notifiable Disease Surveillance System (NNDSS) and FluView (*36*, *37*). From the two sources, we collated a dataset of 24 infectious diseases amenable to statistical analysis.

Clustering analysis

To identify which groupings of diseases were similarly affected by the COVID-19 pandemic, we performed a clustering analysis on the national-level weekly notifications data from the start of 2019 onwards (Fig. 2; full time-series data are shown in fig. S1). We calculated the Spearman’s ρ rank-correlation matrix, finding values of ρ that ranged from -0.47 (between syphilis and mumps) to 0.91 [between campylobacteriosis and Shiga toxin–producing *Escherichia coli* (STEC)] (Fig. 2A). We applied an agglomerative clustering algorithm to the correlation matrix, to construct a dendrogram of the hierarchical clustering of the data (Fig. 2B). On the basis of the silhouette score (fig. S2), we found that the data were most consistent with four clusters.

The clustering is suggestive of factors that might have helped shape the pandemic’s effects on disease transmission (Fig. 2). The first cluster (shaded blue) comprises predominantly pathogens that are spread via airborne or aerosol transmission (with hepatitis B, spread by infected blood or bodily fluids, an outlier); one subgroup consists of vaccine-preventable childhood diseases (mumps, pertussis, invasive *H. influenzae*, and varicella) and the other, influenza A and B. The second (shaded pink) consists of the three sexually transmitted infections (STIs) in the dataset (gonorrhea, chlamydia, and syphilis), with coccidioidomycosis (environmentally transmitted) being an outlier. The third (shaded green) is more disparate but broadly consists of diseases that are not directly transmissible between humans, with one subgrouping consisting of bacteria spread fecal-orally (with malaria an outlier) and a second subgroup of tick-borne pathogens. The final group consists of two apparent outliers: hepatitis A, caused by a virus primarily spread primarily via fecal-oral transmission [which experienced a pronounced multistate outbreak from 2016 to 2019 (*38*)], and notifications of rabies in animals [the only nonhuman disease in the dataset, included for comparative purposes, which is subject to an ongoing vaccination campaign (*39*)]. In what follows, we will focus on the first three clusters, which we label according to predominant transmission mechanism: (i) airborne and aerosol-transmitted infections (ATIs), (ii) STIs, and (iii) environmentally transmitted infections and zoonotic spillover (ETI/Z). To verify that the clustering corresponds to effects of the pandemic and not prepandemic patterns, we repeated the clustering analysis using data pre-2020 (fig. S3). The resulting dendrogram was less reflective of transmission mechanism, although some features were preserved based on seasonal patterns of incidence (e.g., the STI cluster and a high correlation between influenza A and B).

Counterfactual analysis

To quantify the effects of the pandemic on sympatric disease notifications in different US states, we performed a counterfactual Bayesian structural time-series (BSTS) modeling analysis (*40*). The analysis was designed to estimate the discrepancy between observed notifications post-March 2020 and the counterfactual projected notifications predicted to have occurred had no pandemic taken place (see materials and methods). We fit the BSTS model to time-series data for each pairwise combination of US state and disease. Model validation was performed using posterior predictive checks, with 298 pairs passing the check (fig. S4).

---

[1] Odum School of Ecology, University of Georgia, Athens, GA, USA. [2] Department of Infectious Diseases, College of Veterinary Medicine, University of Georgia, Athens, GA, USA. [3] Center for Influenza Disease and Emergence Research (CIDER), Athens, GA, USA. ***Corresponding author. Email: tsbrett@uga.edu**

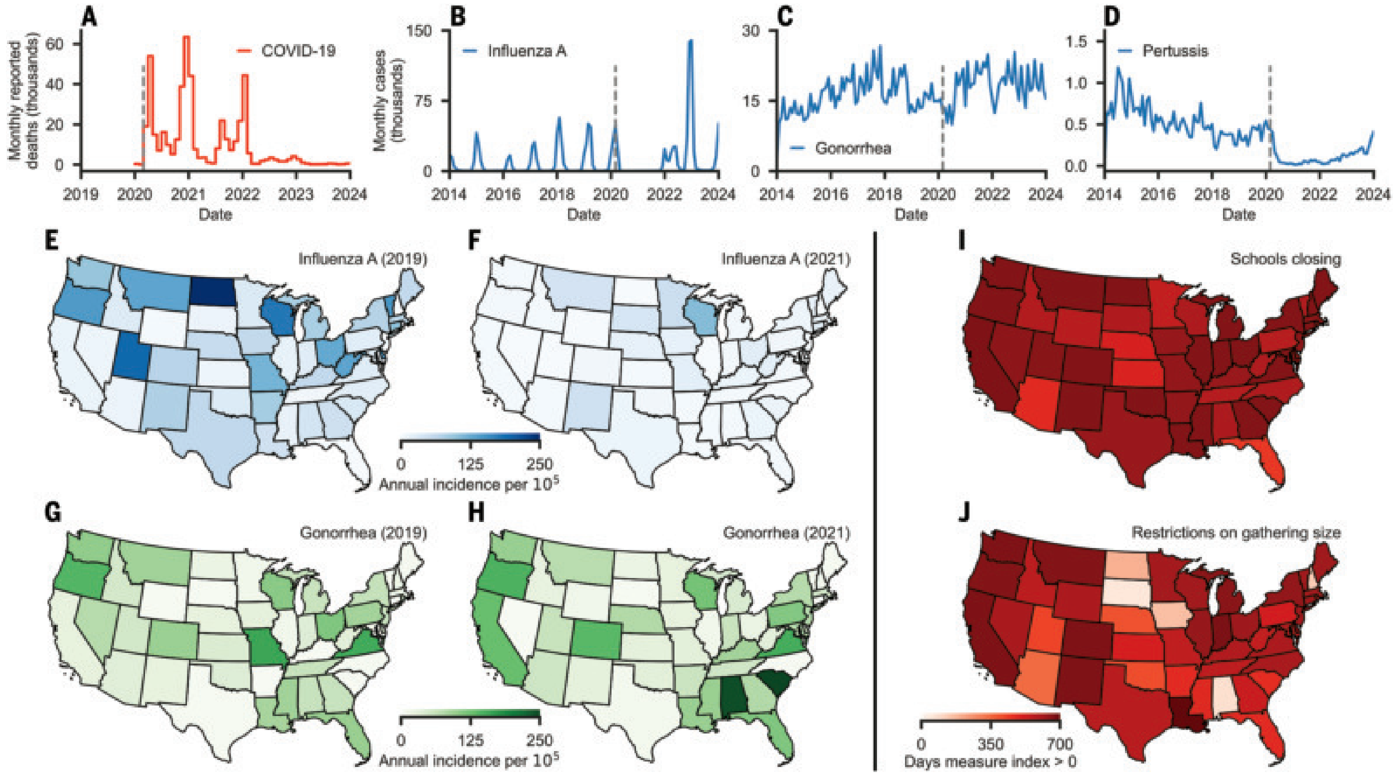

Fig. 1. Overview of pre– and post–COVID-19 notifications for select diseases. (**A**) Monthly recorded COVID-19 mortality. (**B** to **D**) Monthly notifications of cases of influenza A (B) gonorrhea (C), and pertussis (D). (**E** to **H**) On the state level, differences in notifications of influenza A were consistently lower in 2021 compared with 2019 (E and F). By contrast, changes in notifications of gonorrhea varied by state with some up (e.g., Alabama, California, South Carolina) and others down (e.g., Missouri, Nevada, Ohio). (**I** and **J**) The duration of government response measures also varied by state, as quantified by the Oxford COVID-19 Government Response Tracker (OxCGRT; see materials and methods). Although some level of disruption to education in schools remained across much of the country for almost 2 years (I), restrictions on gathering sizes were relaxed more quickly, and with greater spatial variation (J).

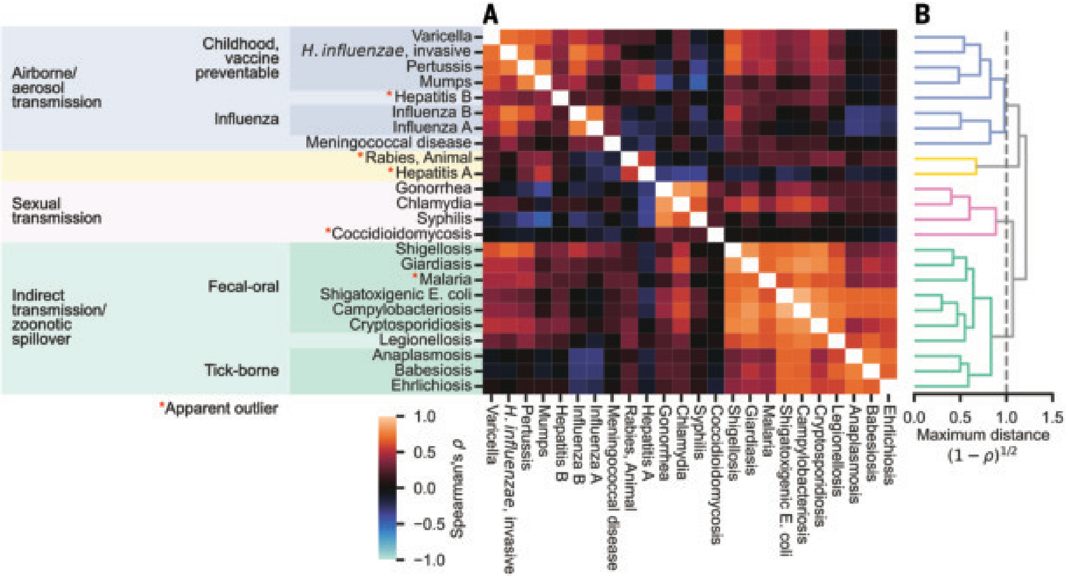

Fig. 2. Clustering analysis of sympatric disease time-series data from the US (2019–2024). (**A**) Spearman's rank correlation matrix for time-series data of weekly national case notifications for 24 infectious diseases (22 from the NNDSS plus lab-confirmed influenza A and B cases; see materials and methods). (**B**) Agglomerative clustering algorithm (*55*) applied to the correlation matrix, with the silhouette score (*56*) identifying four distinct clusters (fig. S2). Of these clusters, one (blue) primarily consists of airborne and aerosol-transmitted infections (ATIs). The second (pink) is of predominantly STIs. The third (green) is a broad cluster, which we label ETI/Z, that includes zoonotic tick-borne infections (anaplasmosis, babesiosis, and ehrlichiosis) and environmentally transmitted infections (ETIs). Diseases in this cluster do not depend on direct human contact for transmission. The final cluster (yellow) consists of two outliers, hepatitis A and rabies in animals.

The key measure used to interpret our results was the relative impact on disease notifications, ψ_t, given by $\psi_t = 100\left(y_t - \tilde{y}_t\right) / \tilde{y}_t$, which quantifies, as a percentage, the deviation of observed notifications y_t from counterfactual model projections, $\tilde{y}_t$ (Fig. 3, A and B). Similarly, the relative net impact, $\chi_t = 100 \sum_{s=0}^{t} \left(y_s - \tilde{y}_s\right) / \sum_{s=0}^{t} \tilde{y}_s$, quantifies the cumulative deviation of observed notifications from counterfactual model projections from the start of the pandemic up to time t. Related approaches have previously been used to quantify excess deaths attributable to the pandemic (*41*).

In Fig. 3, C to J, we present results for four diseases in New York state, representative of the three transmission clusters (Fig. 2A). Results for all other state-disease pairs are presented in figs. S5 to S10. In 2020, notifications of both influenza A (Fig. 3G) and pertussis (Fig. 3H) were substantially below counterfactual projections (posterior median annual relative annual impact −81.5% [−90.5%, −69.7%] and −76.6% [−81.8%, −71.2%], respectively), whereas the relative annual impact on shigellosis notifications (Fig. 3J) was −45.7% [−55.7%, −34.5%]; all ranges correspond to 95% highest density intervals (HDIs). Notifications of all three diseases subsequently rebounded with the annual relative impact 95% HDI containing 0% by the end of 2022. The return of both pertussis and shigellosis to projected levels has been gradual over the course of 2020–2022 (although there were explosive outbreaks of pertussis in New York during 2024, among other locations). By contrast, influenza A was largely absent until a sudden rebound in 2022 (Fig. 3G). Unlike the other three diseases shown, there was no apparent effect on weekly gonorrhea notifications in 2020 (Fig. 3I), with a relative annual impact of −1.2% [−8.5%, 6.5%], although notification reports were absent from early July until late November 2020. Subsequently, there was a small negative impact in 2022 and 2023, as notifications undershot projections that sustained an increasing pre-2020 trend. For all four diseases shown (Fig. 3, G to J), the relative net impact remains below zero at the end of 2023, corresponding to a net deficit in notifications.

Given the large number of state-disease pairs, we summarized our results by aggregating estimates of the relative net impact on each pathogen for each cluster (Fig. 4). We found that the median for all three clusters (with influenza excluded from the ATI cluster) remained below zero at the end of 2023 (Fig. 4A). Although following a similar trajectory to other ATIs, both influenza A and B were most influenced by the pandemic during 2021 (Fig. 4B). Subsequently, during 2022 and 2023, the influenza A rebound was positive in some states (in particular South Dakota, Hawaii, and Nebraska), whereas in others, the influenza seasons were smaller than expected (e.g., Michigan and Louisiana; fig. S11). By contrast, at the start of 2024, influenza B was suppressed in all states apart from Mississippi and South Carolina (fig. S12).

Broadly speaking, the effect of the pandemic and related response measures on other pathogens appears to be more strongly shaped by transmission mechanism of the pathogen concerned than state-level effects (Fig. 4, C to E). To understand whether state-specific differences in COVID-19 response measures could explain the interstate variation in the relative net impact on other pathogens, we formulated a multilevel regression model that we fit to predict the median relative net impact at the end of 2021, 2022, and 2023 using a dataset of government response measures as predictors (figs. S13 to S16). Except for the school closure coefficient for the ATI cluster, the posterior 95% HDI for each coefficient in 2021 included zero (fig. S14B). This indicates that our model was unable to use those predictors to explain interstate variation in relative net impact (χ_t). Our results do not imply that those response measures made no contribution to χ_t, given that the data were standardized and that we estimated nonzero offsets for

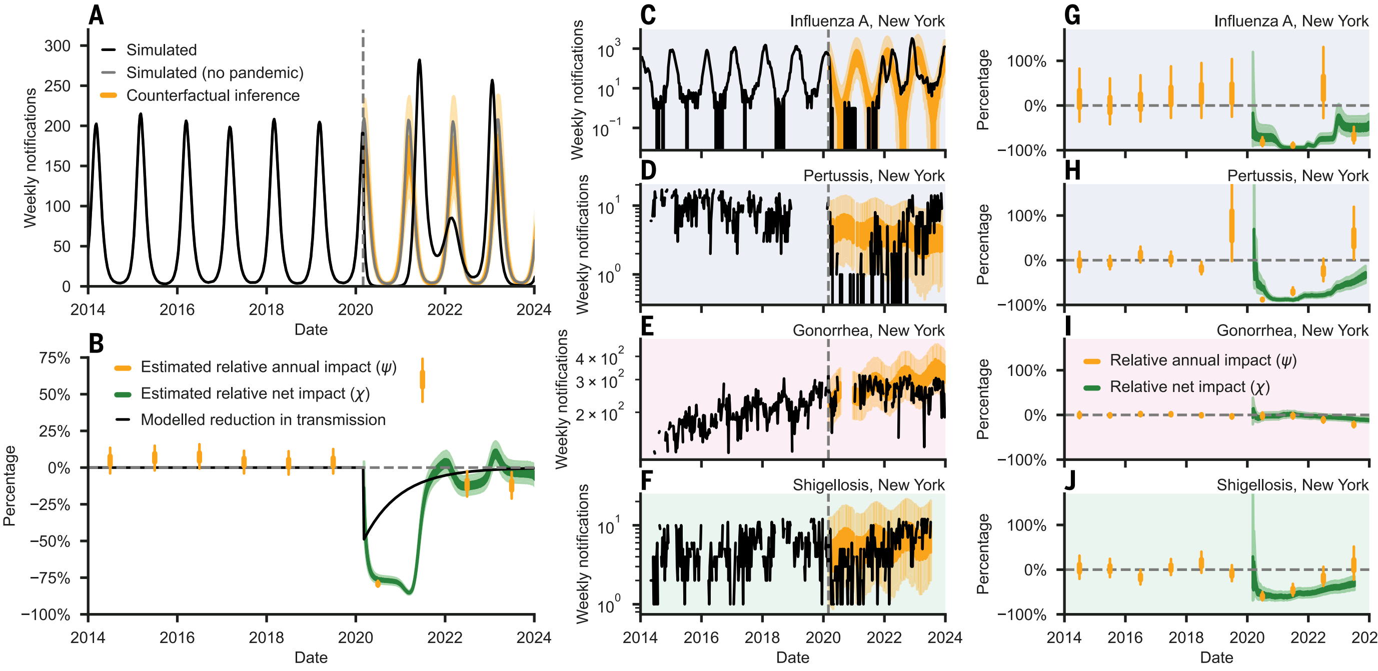

Fig. 3. Results of the counterfactual inference analysis for four diseases in New York. (**A**) Demonstration of counterfactual approach using simulated data. The model was fit to data pre-March 2020, with counterfactual projections (which assumed no pandemic effects) made for subsequent weeks. The counterfactual projections agree with simulated data that assumed no pandemic (gray line) but deviated from the simulated trajectory that assumed an initial 50% reduction in transmission. (**B**) The discrepancy between data post-2020 and the counterfactual projections allow us to quantify the relative impact, which lags the modeled reduction in transmission. Orange intervals show the relative annual impact for a given calendar year; green ribbons show the cumulative relative net impact since the pandemic start (dark and light bars/ribbons correspond to the 50% and 95% HDI, respectively). (**C** to **F**) Weekly observed notifications of influenza A, pertussis, gonorrhea, and shigellosis (black) are compared with counterfactual predictions from the BSTS model. (**G** to **J**) Relative annual and net impact of the pandemic. The annual impact calculations for 2020 only include data post-March.

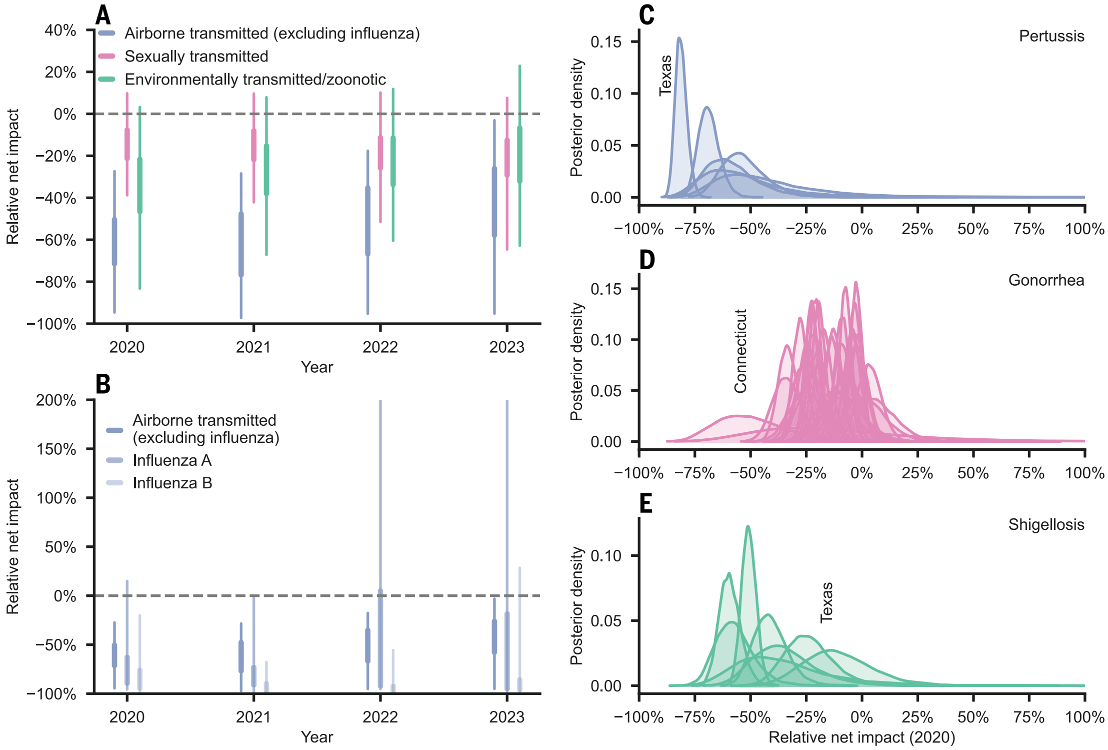

Fig. 4. Relative net impact by year and cluster. (**A**) Relative net impact at the end of each year for each transmission cluster. Densities computed by aggregating posterior samples for all state-disease pairs in a cluster (points indicate the median; bars correspond to 50% and 95% HDIs). Owing to the atypical relative net impact on influenza, we excluded it from the ATI cluster. (**B**) Comparison of the relative net impact on influenza with the rest of the ATI cluster diseases, using the same approach as for (A). For influenza A, the 95% HDI extends to 424% and 435% in 2022 and 2023, respectively. (**C** to **E**) State-level variation in relative net impact for pertussis (C), gonorrhea (D), and shigellosis (E).

each cluster (fig. S14C). Qualitatively similar results were observed for both 2022 and 2023 (figs. S15 and S16).

To explore the possible mechanisms underlying the differences between the two directly transmitted clusters (ATIs and STIs), we formulated and analyzed a simple pathogen transmission model (see materials and methods for details). We modeled the pandemic as causing a reduction in the transmission rate, which followed a decaying exponential, $c(t) = c_0\left(1-e^{-t/\tau}\right)$, where c_0 is the reduction at the start of the pandemic and τ determines the rate of return to the prepandemic transmission level (Fig. 5A). Following the methodology of our counterfactual analysis, we calculated the relative net impact and the return time, defined as the mean time for the relative net impact to return within 10% of zero. Using plausible parameter values, we simulated three diseases: pertussis (Fig. 5, B and C), influenza A (Fig. 5, D and E), and gonorrhea (figs. S17 and S18). We also simulated a set of parameter scenarios (Fig. 5H and figs. S19 and S20). For pertussis, we see a return time of about 4 years, followed by decaying oscillations in the net impact. For influenza, we see greater variation between stochastic replicates, with the net impact returning to zero after about 1 to 2 years. Basic epidemiological theory can explain the observed dynamics. Early in the pandemic, prevalence drops exponentially, $\frac{dI(t)}{dt} \approx -c_0\gamma I(t)$, depending on the severity of control measures, c_0, and the pathogen infectious period, $1/\gamma$. Later, as the transmission rate approaches prepandemic levels, the rebound is shaped by the basic reproductive number, R_0, and the rate of influx into the susceptible pool, κ, approximately following $\frac{dI(t)}{dt} \approx \gamma\kappa R_0 I(t)$. The parameter κ comprises the rate of unvaccinated births and loss of infection- and vaccine-derived immunity. Seasonal infectious diseases with low basic reproductive number, short infectious period, and short-lived immunity, such as influenza, are expected to undergo a sharp decline followed by a volatile rebound before returning to zero. These patterns are broadly in line with observations for influenza A (fig. S11). The return time is sensitive to nonlinearities in the transmission process, analogous to period doubling observed for vaccine-controlled seasonal diseases (*42*). For gonorrhea, we find that the observed relative net impact (for instance in New York; Fig. 3I) is most consistent with a smaller effect of the pandemic compared to the ATIs (both in the magnitude and duration of reductions in transmission rates; fig. S17). Furthermore, to match trends in the data, our modeling required that an increasing trend in transmission rates pre-2020 ended at the start of the COVID-19 pandemic.

Discussion

A limitation of counterfactual analyses is the assumption that data trends can be extrapolated from the training period (the prepandemic period in our study) into the counterfactual projection period (i.e., after March 2020). Therefore, a major caveat to the findings of our BSTS analysis is that it cannot, in isolation, distinguish between effects of the pandemic and other coincidental secular trends in transmission dynamics and surveillance after 2020. For instance, contemporary patterns of incidence may be affected by factors unrelated to the pandemic period, including changes in diagnostic methodology [e.g., increased usage of multiplex assays (*25*, *26*)], behavior [e.g., vaccine hesitancy (*43*)], and pathogen transmissibility and virulence (*44*). Another limitation is our choice of model structure. Given the large number of diseases studied, we opted to use a generalized linear model; however, appropriate disease-specific mechanistic transmission models could provide better interpretations of the data. Furthermore, as we were fitting to 6 years of data pre-2020, diseases with long interepidemic periods [such as mumps (*45*)] were difficult to fit with

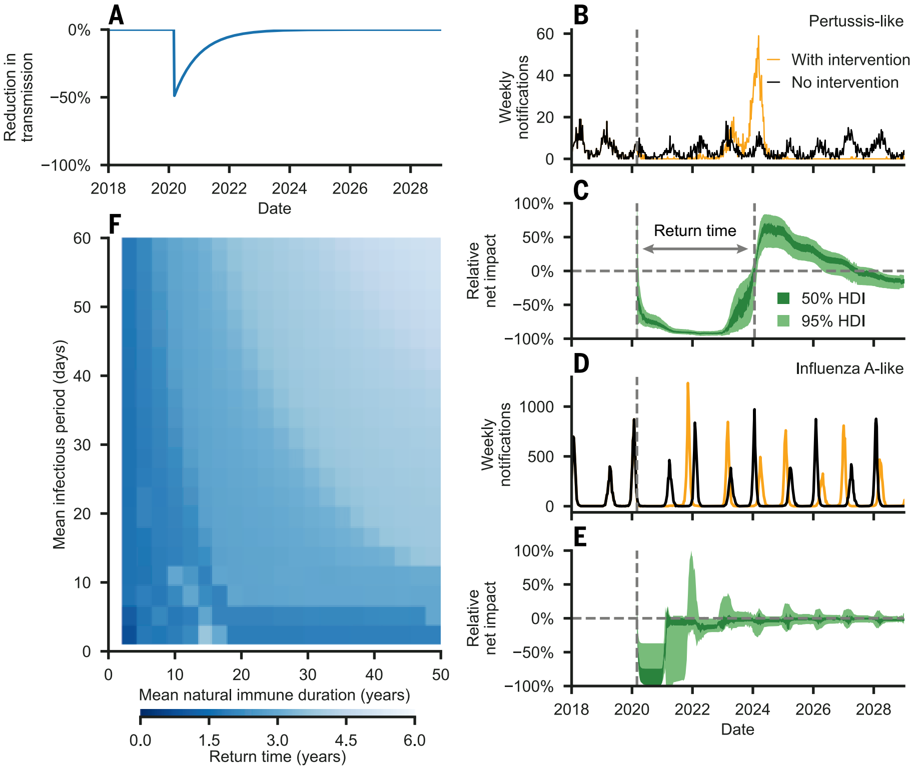

Fig. 5. Scenario analysis. (**A** to **E**) Simulated results using a stochastic SEIRV model (see materials and methods) subject to an initial 50% reduction in transmission rates (A). Results shown using plausible parameterizations for two ATIs, pertussis (B and C) and influenza A (D and E). (**F**) Dependence of the return time on the natural immune duration and infectious period for a pathogen with $R_0 = 4$. The return time was defined as the duration between the start of control measures and the mean relative net impact crossing –10% (C).

our nonmechanistic model. For instance, mumps and hepatitis A experienced pronounced outbreaks in several states during the prepandemic period (2014–2020), which led to rejection under statistical inclusion criteria (see materials and methods).

Our counterfactual analysis shows that notifications of some of the infectious diseases being investigated, in particular STIs, were largely unaffected by the pandemic (Fig. 4). From this observation, we infer that there was no generalized collapse in disease surveillance during the acute phase of the pandemic, and decreases in notifications of other diseases likely reflect actual reductions in transmission. Nevertheless, we cannot rule out the possibility of disproportionate disruption to the surveillance of specific diseases or in specific states.

The limited effect on notifications of the three STIs during 2020 and 2021 is puzzling, given the severe lockdown measures imposed and their effect on SARS-CoV-2 and ATI transmission. Our analysis of a gonorrhea-like transmission model suggests that even a moderate (initially 25%) short-lived reduction in transmission rates should have had a greater discernible net impact than observed for most state-disease pairs in the STI cluster (fig. S17). The longer serial interval of STIs relative to ATIs alone cannot explain the limited drop in notifications during 2020 (figs. S17 to S20). Another unexplained observation in these data (2014–2024) is that increasing trends in notifications that predated the pandemic have been absent since 2020, a phenomenon repeated across states and STIs in the study. Our results point to a persistent change in STI transmission dynamics that appears to us unexplained.

It is not surprising that ATIs were most affected by the pandemic, given the types of recommended control measures (e.g., mask wearing, reductions in mass gatherings, school and workplace closures) that were implemented to stop the spread of an aerosol-transmitted virus such as SARS-CoV-2. However, the delay in the rebound of these infectious diseases is noteworthy. For instance, in the US, despite public health interventions, contact rates were still sufficient for the rapid spread of the alpha, delta, and omicron variants in 2021 and influenza A in winter 2022 (*46*). By contrast, over the same period, the incidence of influenza B, invasive *H. influenzae*, mumps, pertussis, and varicella all remained below expected levels. Epidemiological modeling indicated a number of possible mechanisms (Fig. 5 and fig. S19). Specifically, the suppressed infectious diseases have longer serial intervals (resulting in slower epidemiological growth rates), lower transmissibility, and longer durations of immunity (and therefore slower susceptible recruitment). Regardless of parameterization, our modeling suggests that the effect of the pandemic is unlikely to extend beyond about 6 years. Our results point to a need for more systematic study of the underlying mechanisms. Indeed, the disruptive effects of the pandemic on the circulation of other infectious diseases provides a valuable opportunity to better understand the epidemiology of these pathogens.

Of the ATIs, it is not clear why influenza A and B notifications were disproportionately affected (Fig. 4B). Perhaps this is a result of disrupted international travel, which is known to play an important role in the circulation and seeding of novel influenza antigenic variants (*47*, *48*); however, curiously, influenza A was less affected by this perturbation than influenza B, despite the higher frequency of variant introductions before the pandemic (*48*). Alternatively, viral interference after SARS-CoV-2 infection and vaccination may have affected sympatric viruses (*49*). Apart from SARS CoV-2, influenza viruses are the only viruses in our study that infect the respiratory tract; therefore, it is possible that they experienced the greatest interference from the emergence of SARS-CoV-2.

Our quantification of the pandemic's impact has focused on the USA, where SARS-CoV-2 has circulated continuously since early 2020. However, the pandemic left a qualitatively similar footprint on notifications data for influenza in Australia (fig. S21) and pertussis in New Zealand (fig. S22), countries that adopted a zero-COVID strategy and largely suppressed SARS-CoV-2 circulation until late 2021. Timing of interventions relative to epidemic phase was found to affect the return time, with simulations where transmission reductions coincided with the start of the epidemic season demonstrating longer disruption (fig. S20).

Our findings are consistent with available studies of other populations [US military personnel (*50*)] and disease systems [*Salmonella* in Germany (*51*)]. An intriguing study of seasonal endemic respiratory viruses in Washington state, including a number of viruses not part of the NNDSS, found that the non-enveloped viruses in the study (human rhinoviruses, enteroviruses, and adenoviruses) were the first to rebound after the lifting of lockdown measures (*52*). The authors speculate that virological factors, such as environmental stability and ability to penetrate face masks, may have facilitated their rapid spread. Alternatively, our results suggest that short serial intervals and short-lasting immunity ($\lesssim$ 2 years) are sufficient to explain their rapid rebound.

In 2025, notifications of the ATIs largely rebounded to prepandemic levels as expected (*11*, *13*). It was unclear whether the rebound in these diseases would exceed the incidence prevented by pandemic control measures, owing to the immunity gap created by reduced pathogen circulation and missed routine vaccinations. Our results show that cumulative notifications of most ATIs in most states since 2020 remained at a net deficit compared with counterfactual projections at the start of 2024. Given that we do not find evidence for a substantial collapse in disease reporting during 2020, we expect this deficit to reflect an overall reduction in the burden of disease. Although governmental-response measures to control the pandemic undoubtedly had adverse psychological, economic, and societal consequences (*53*), considered solely through the lens of infectious disease notifications, lockdown measures were beneficial for human health and did not lead to a collateral excess of sympatric disease. Extrapolating from disease notifications to the total number of infections in the population, and the implications for population immunity, can only be done on a disease-by-disease basis and remains a pressing need for further study such as through serological surveillance (*54*) and pathogen transmission modeling (*45*).

REFERENCES AND NOTES

1. N. Zhu *et al.*, *N. Engl. J. Med.* **382**, 727–733 (2020).
2. T. Hale *et al.*, *Nat. Hum. Behav.* **5**, 529–538 (2021).
3. L. Rodgers *et al.*, *Clin. Infect. Dis.* **73** (Suppl 1), S110–S117 (2021).
4. K. Hirae, T. Hoshina, H. Koga, *Int. J. Infect. Dis.* **128**, 265–271 (2023).
5. J. Hatoun, E. T. Correa, S. M. A. Donahue, L. Vernacchio, *Pediatrics* **146**, e2020006460 (2020).
6. A. Ullrich *et al.*, *Lancet Reg. Health Eur.* **6**, 100103 (2021).
7. J. A. McBride, J. Eickhoff, E. R. Wald, *Pediatr. Infect. Dis. J.* **39**, e449–e452 (2020).
8. M. J. Geng *et al.*, *Nat. Commun.* **12**, 6923 (2021).
9. S. Matczak *et al.*, *Euro Surveill.* **27**, 2100933 (2022).
10. E. Tessier *et al.*, *BMC Public Health* **22**, 405 (2022).
11. R. E. Baker *et al.*, *Proc. Natl. Acad. Sci. U.S.A.* **117**, 30547–30553 (2020).
12. M. W. Fong, N. H. L. Leung, B. J. Cowling, P. Wu, *Emerg. Infect. Dis.* **27**, 1525–1527 (2021).
13. K. Messacar *et al.*, *Lancet* **400**, 1663–1665 (2022).
14. A. G. Feldman, S. T. O'Leary, L. Danziger-Isakov, *Clin. Infect. Dis.* **73**, 1920–1923 (2021).
15. D. N. Durrheim *et al.*, *Nat. Med.* **27**, 360–361 (2021).
16. A. Handel, I. M. Longini Jr., R. Antia, *Proc. Biol. Sci.* **274**, 833–837 (2007).
17. T. D. Hollingsworth, D. Klinkenberg, H. Heesterbeek, R. M. Anderson, *PLOS Comput. Biol.* **7**, e1001076 (2011).
18. E. Rios-Guzman *et al.*, *Nat. Commun.* **15**, 3374 (2024).
19. C. Rodrigues *et al.*, *Euro Surveill.* **29**, 2400459 (2024).
20. K. Causey *et al.*, *Lancet* **398**, 522–534 (2021).
21. R. Moynihan *et al.*, *BMJ Open* **11**, e045343 (2021).
22. C. Arsenault *et al.*, *Nat. Med.* **28**, 1314–1324 (2022).
23. P. Rohani, C. J. Green, N. B. Mantilla-Beniers, B. T. Grenfell, *Nature* **422**, 885–888 (2003).
24. D. A. Vasco, H. J. Wearing, P. Rohani, *J. Theor. Biol.* **245**, 9–25 (2007).
25. J. A. Hay *et al.*, *Science* **373**, eabh0635 (2021).
26. R. E. Baker *et al.*, *Nat. Rev. Microbiol.* **20**, 193–205 (2022).
27. C. M. Zipfel, V. Colizza, S. Bansal, *Vaccine* **39**, 3645–3648 (2021).
28. S. S. Lee, C. Viboud, E. Petersen, *Int. J. Infect. Dis.* **122**, 1002–1004 (2022).
29. Z. Zheng, V. E. Pitzer, E. D. Shapiro, L. J. Bont, D. M. Weinberger, *JAMA Netw. Open* **4**, e2141779–e2141779 (2021).
30. D. A. Kalkowska *et al.*, *Vaccine* **41** (Suppl 1), A12–A18 (2023).
31. C. F. McQuaid *et al.*, *Eur. Respir. J.* **56**, 2001718 (2020).
32. L. Cilloni *et al.*, *EClinicalMedicine* **28**, 100603 (2020).
33. M. Briga, E. Goult, T. S. Brett, P. Rohani, M. Domenech de Cellès, *Nat. Commun.* **15**, 921 (2024).
34. H. He *et al.*, *Vaccine* **40**, 6956–6962 (2022).
35. S. W. Park *et al.*, *Epidemics* **46**, 100736 (2024).
36. US Centers for Disease Control and Prevention (CDC), NNDSS Data Tables [Internet]. 2023. Available from: https://data.cdc.gov/browse?q=NNDSS
37. Centers for Disease Control & Prevention, Weekly U.S. Influenza Surveillance Report 2024; https://www.cdc.gov/fluview/index.html [cited 11 February 2024].
38. M. A. Foster *et al.*, *MMWR Morb. Mortal. Wkly. Rep.* **68**, 413–415 (2019).
39. X. Ma *et al.*, *J. Am. Vet. Med. Assoc.* **260**, 1157–1165 (2022).
40. K. H. Brodersen, F. Gallusser, J. Koehler, N. Remy, S. L. Scott, *Ann. Appl. Stat.* **9**, 247 (2015).
41. D. M. Weinberger *et al.*, *JAMA Intern. Med.* **180**, 1336–1344 (2020).
42. D. J. Earn, P. Rohani, B. M. Bolker, B. T. Grenfell, *Science* **287**, 667–670 (2000).
43. D. A. Salmon, M. Z. Dudley, J. M. Glanz, S. B. Omer, *Vaccine* **33** (suppl. 4), D66–D71 (2015).
44. A. Sasaki, S. Lion, M. Boots, *Nat. Ecol. Evol.* **6**, 51–62 (2022).
45. D. V. Gokhale, T. S. Brett, B. He, A. A. King, P. Rohani, *Proc. Natl. Acad. Sci. U.S.A.* **120**, e2207595120 (2023).
46. T. S. Brett, P. Rohani, *PNAS Nexus* **1**, pgac159 (2022).
47. T. Bedford *et al.*, *Nature* **523**, 217–220 (2015).
48. Z. Chen *et al.*, *Science* **386**, eadq3003 (2024).
49. J. Piret, G. Boivin, *Emerg. Infect. Dis.* **28**, 273–281 (2022).
50. B. Manuelpillai, B. Lopman, C. R. Doran, C. Porter, *J. Infect. Dis.* **231**, e1075–e1079 (2025).
51. K. Nelson, B. Lopman, *Science* **377**, 33–34 (2022).
52. A. C. Perofsky *et al.*, *Nat. Commun.* **15**, 4164 (2024).
53. H. G. Nijhuis, L. J. G. van der Maesen, *Int J Soc Qual.* **11**, v–xx (2021).
54. C. J. E. Metcalf *et al.*, *Lancet* **388**, 728–730 (2016).
55. T. Hastie, R. Tibshirani, J. H. Friedman, *The Elements of Statistical Learning: Data Mining, Inference, and Prediction* (Springer, 2009), vol. 2.
56. P. J. Rousseeuw, *J. Comput. Appl. Math.* **20**, 53–65 (1987).
57. T. Brett, Data for: Collateral effects of COVID-19 pandemic control on the US, Zenodo (2025); https://doi.org/10.5281/zenodo.16772531.

ACKNOWLEDGMENTS

We thank B. Grenfell and the Rohani lab for comments on this work. **Funding:** National Institutes of Health (R21AI171509 (P.R., T.B.). National Institute of Allergy and Infectious Diseases, National Institutes of Health, Department of Health and Human Services, under contract no. 75N93021C00018 (NIAID Centers of Excellence for Influenza Research and Response, CEIRR) (P.R.). **Author contributions:** Conceptualization: T.B., P.R. Methodology: T.B., P.R. Investigation: T.B. Visualization: T.B. Funding acquisition: P.R. Project administration: P.R. Supervision: P.R. Writing – original draft: T.B. Writing – review & editing: T.B., P.R. **Competing interests:** The authors declare that they have no competing interests. **Data and materials availability:** All data and code to reproduce results have been deposited in Zenodo (*57*) (https://doi.org/10.5281/zenodo.16772531).

SUPPLEMENTARY MATERIALS

science.org/doi/10.1126/science.adw4964
Materials and Methods; Figs. S1 to S22; Tables S1 and S2; References (*58*–*71*);
MDAR Reproducibility Checklist

Submitted 5 February 2025; accepted 8 August 2025

10.1126/science.adw4964

CATALYSIS

Trace-level halogen blocks CO_2 emission in Fischer-Tropsch synthesis for olefins production

Yi Cai[1,2]†, Maolin Wang[3]†, Shu Zhao[4]†, Xi Liu[5]†, Junzhong Xie[3]†, Xing-Wu Liu[1,3,6]*, Yao Xu[3], Jie Zhang[3], Lingzhen Zeng[3], Fei Qian[1,2], Zirui Gao[3], Zeyan Cen[3], Xingchen Liu[1], Hong Wang[6], Bingjun Xu[3], Graham J. Hutchings[7], Yong Yang[1,6], Yong-Wang Li[6], Xiao-Dong Wen[1,2]*, Ding Ma[3]*

Sustainable production of fuels and olefins from syngas (carbon monoxide and hydrogen) through the Fischer-Tropsch synthesis process requires catalysts that deliver high selectivity, industrial productivity, and minimal carbon dioxide (CO_2) emissions. Current industrial iron catalysts form substantial CO_2 by-product that limits carbon efficiency. We report that introducing trace amounts [parts per million (ppm) level] of halogen-containing compounds into the feed gas can suppress CO_2 formation using iron-based catalysts and boost olefin selectivity over paraffin and olefin productivity. Cofeeding 20 ppm bromomethane over an iron carbide catalyst decreased CO_2 selectivity to <1% and increased olefin selectivity to ~85% among all carbon-containing products. Surface-bound halogens modulated the catalyst surface structure and selectively inhibited pathways responsible for CO_2 generation and olefin hydrogenation. This strategy provides a simple, scalable, and broadly applicable route for carbon-efficient syngas conversion.

Developing efficient catalytic systems for direct α-olefin production from syngas (CO and H_2) through Fischer-Tropsch synthesis (FTS) is essential to address the growing global demand for olefins and is of importance for regions with limited petroleum resources (*1*–*3*). A key challenge is the design of low-cost, non–noble-metal catalysts that operate under moderate conditions that also minimize CO_2 emissions to ensure sustainable carbon utilization (*4*–*8*). Among current approaches, iron-based Fischer-Tropsch to olefins (FTO) catalysts (*9*–*11*) and oxide-zeolite (OX-ZEO) tandem systems (*2*, *12*, *13*) have emerged as leading candidates. However, iron-based catalysts often yield only moderate olefin selectivity, whereas OX-ZEO systems suffer from high CO_2 selectivity (32 to 45%) and limited olefin space-time yields (*12*). These limitations constrain overall carbon efficiency and hinder their large-scale industrial implementation. Thus, there is an urgent need for new catalytic systems that combine ultralow CO_2 selectivity, high α-olefin space-time yields, and robust long-term stability.

Iron-based catalysts are particularly attractive for FTS because of their low cost, natural abundance, tunable product distribution, and high space-time yields of the products. Currently, more than two-thirds of the global FTS capacity (15.70 million tons per year) relies on iron catalysts. However, one drawback is their intrinsic promotion of the water-gas shift (WGS) and Boudouard reactions, resulting in excessive CO_2 formation (typically showing a selectivity of 18 to 35%) that reduces carbon utilization efficiency (*14*, *15*). The formation of CO_2 not only contributes to greenhouse gas emissions but also depletes valuable carbon feedstocks.

Suppressing CO_2 formation in Fe-based FTS remains a major challenge. Previous strategies to inhibit the WGS reaction have focused on limiting water readsorption by shielding iron catalysts with hydrophobic silica coatings (*11*) or graphene layers (*8*), which effectively reduces CO_2 selectivity to <13%. More recently, modified pure-phase iron carbide catalysts have achieved CO_2 selectivity as low as ~10% (*10*, *16*), but only under conditions of low CO conversion and limited olefin productivity (~0.6 $g \cdot g_{cat}^{-1} \cdot hour^{-1}$) (*10*). Therefore, the development of catalytic systems that concurrently minimize CO_2 formation and maximize α-olefin productivity under practical conditions remains a critical and unmet challenge.

We demonstrate that the introduction of parts per million (ppm) concentrations of halomethanes into the syngas feed fundamentally transforms the catalytic behavior of Fe-based FTS systems. Specifically, cofeeding 20 ppm of bromomethane (CH_3Br) effectively suppressed CO_2 formation, reducing CO_2 selectivity to <1% and drastically enhancing the olefin/paraffin (o/p) ratio from 1.3 (on unpromoted χ-Fe_5C_2) to as high as 13. Under optimized conditions, this strategy achieved an olefin space-time yield of 1.08 $g \cdot g_{cat}^{-1} \cdot hour^{-1}$ with an unprecedented olefin selectivity of 85.2%, calculated relative to all carbon-containing products. This simple and easily implementable halomethane-promotion strategy is compatible with a broad range of Fe-based FTS catalysts, including commercial formulations. Mechanistic insights from transient kinetic analyses and density functional theory (DFT) calculations reveal that surface-bound halogens modulate the properties of the catalyst and selectively inhibit key side reactions—specifically, the Boudouard reaction and WGS reaction—thereby suppressing CO_2 generation. We introduce a simple yet robust and broadly applicable strategy to achieve sustainable and highly efficient olefin or liquid fuels production with exceptional carbon efficiency.

The impact of halogen on the Fe-based FTS process

A series of iron carbide catalysts (ε-Fe_2C, θ-Fe_3C, *h*-Fe_7C_3, and χ-Fe_5C_2) were synthesized following established protocols (*17*, *18*). The unpromoted χ-Fe_5C_2 catalyst, one of the most active phases for FTS, exhibited a CO_2 selectivity of 31.4% at a CO conversion of 93.3% (Fig. 1A) (*19*). The primary products were C_{2+} olefins and paraffins with an o/p ratio of 1.3 under typical FTS conditions ($H_2/CO = 2$, 300°C, 20 bar, 12,000 $ml \cdot g_{cat}^{-1} \cdot hour^{-1}$). The native iron carbide catalysts favored CO_2 formation and exhibited similar selectivity toward olefins and paraffins.

We then introduced 20 ppm of halomethanes (CH_3X, where X = F, Cl, Br, or I) into the syngas during FTS. CH_3F reduced CO_2 selectivity to 27.8%, accompanied by a slight increase in olefin content. A progressive trend was observed from CH_3F to CH_3Cl, CH_3Br, and CH_3I, with CO_2 selectivity continuously decreasing (Fig. 1A and table S1). Notably, cofeeding CH_3Br or CH_3I suppressed CO_2 formation, yielding near-zero CO_2 selectivity (~1%). Concurrently, olefin selectivity was substantially enhanced, with the o/p ratio rising to ~7 in the case of CH_3Cl. These results demonstrate that cofeeding trace amounts of halomethane effectively suppressed CO_2 production while promoting olefin selectivity in Fe-based FTS catalysts.

We next investigated the effect of CH_3Br concentration in the syngas on performance of FTS. Even a low cofeed concentration of 3 ppm CH_3Br markedly suppressed CO_2 formation, reducing its selectivity to 4.2%, decreasing CO conversion from 89.4% to 41.1%, and increasing the o/p ratio from 1.0 to 6.1 (Fig. 1B, figs. S1 and S2, and table S2). Chain propagation remained unaffected, and the olefin selectivity was much higher than that obtained with the unmodified χ-Fe_5C_2 catalyst (81% versus 23%; Fig. 1B, figs. S3 and S4, and table S2). The decrease in CO conversion mainly came from the inhibition of the CO_2 formation (fig. S2), which accounted for >70% of the reduction

---

[1]State Key Laboratory of Coal Conversion, Institute of Coal Chemistry, Chinese Academy of Sciences, Taiyuan, China. [2]University of Chinese Academy of Sciences, Beijing, China. [3]Beijing National Laboratory for Molecular Sciences, New Cornerstone Science Laboratory, College of Chemistry and Molecular Engineering, Peking University, Beijing, China. [4]College of Materials Science and Engineering, Beijing University of Technology, Beijing, China. [5]School of Chemistry and Chemical Engineering, Ningxia University, Yinchuan, China. [6]National Energy Center for Coal to Liquids, Huairou District, Beijing, China. [7]Max Planck Centre on the Fundamentals of Heterogeneous Catalysis (FUNCAT), Cardiff Catalysis Institute, School of Chemistry, Cardiff University, Cardiff, UK. ***Corresponding author. Email: liuxingwu@sxicc.ac.cn (X.-W.L.); wxd@sxicc.ac.cn (X.-D.W.); dma@pku.edu.cn (D.M.)** †These authors contributed equally to this work.

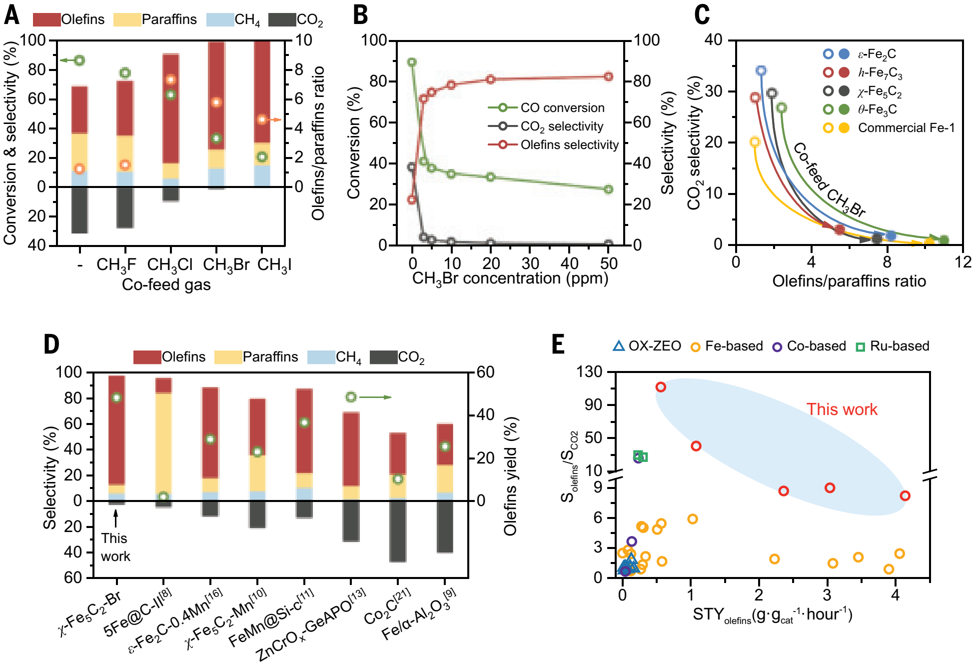

Fig. 1. Impact of halogen cofeeding on catalytic performance in FTS. (**A**) Effect of cofeeding halomethanes (CH_3F, CH_3Cl, CH_3Br, and CH_3I, 20 ppm) on CO conversion and product selectivity in FTS reaction over χ-Fe_5C_2 catalyst. Reaction conditions: 300°C, 20 bar, 12,000 $ml\cdot g_{cat}^{-1}\cdot hour^{-1}$, $H_2/CO = 2$. (**B**) Dependence of CO conversion and selectivity of CO_2 and olefin on the concentration of cofeeding CH_3Br (0 to 50 ppm). Reaction conditions: 300°C, 10 bar, 12,000 $ml\cdot g_{cat}^{-1}\cdot hour^{-1}$, $H_2/CO = 2$. (**C**) Influence of olefin/paraffin ratio and CO_2 selectivity for different iron carbide catalysts (ε-Fe_2C, *h*-Fe_7C_3, χ-Fe_5C_2, and θ-Fe_3C) and commercial Fe-1 under 20 ppm CH_3Br cofeeding. Reaction conditions: 300°C, 10 bar, $H_2/CO = 2$, CO conversion controlled at ~30% for all data points. (**D**) Comparison of catalytic selectivity and olefin yield of χ-Fe_5C_2 catalyst with CH_3Br cofeed against representative literature-reported catalysts. The χ-Fe_5C_2-Br catalyst demonstrates simultaneous ultralow CO_2 selectivity and higher olefin yield compared with state-of-the-art catalytic systems. (**E**) Plot of olefin-to-CO_2 selectivity ratio ($S_{olefins}/S_{CO2}$) against olefin space-time yield ($STY_{olefins}$) on χ-Fe_5C_2-Br (this work, red circles) and various catalytic systems from literature: OX-ZEO (*12*, *13*, *37*–*41*) (blue triangles), Fe-based (*8*–*11*, *16*, *20*, *27*, *32*, *42*–*45*) (yellow circles), Co-based (*21*, *46*, *47*) (purple circles), and Ru-based (*22*) (green squares). Note that the selectivity of olefins is based on all carbon-containing products. The shaded region highlights the exceptional catalytic performance of the χ-Fe_5C_2-Br catalyst.

in CO conversion, in the case of 3 ppm CH_3Br cofeeding (table S3). Although previous studies reported that cofeeding HCl or HBr can reduce CO_2 selectivity (*20*), they also observed a pronounced decline in FTS activity and limited CO_2 suppression (fig. S5). In contrast, CH_3Br cofeeding in this work enables near-zero CO_2 formation with minimal loss in FTS activity (fig. S5 and table S3). As the concentration of cofed CH_3Br increased, CO_2 selectivity progressively decreased—dropping to <1% at 50 ppm—whereas olefin selectivity showed a slight increase (Fig. 1B).

This halogen modulation strategy was further extended to other iron carbide phases, including ε-Fe_2C, θ-Fe_3C, and *h*-Fe_7C_3 (fig. S6) (*17*, *18*). In all cases, ppm concentrations of CH_3Br cofeeding suppressed CO_2 selectivity to <5% and enhanced o/p ratios by factors of three to four (Fig. 1C), underscoring the broad applicability and robustness of the approach. When we applied this strategy to a commercial iron catalyst ("Commercial Fe-1"), CO_2 selectivity could be suppressed to <1% (Fig. 1C).

To benchmark this halogen cofeeding method, we performed comparative analyses with state-of-the-art olefin synthesis catalysts, that is, Fe- and Co-based FTO catalysts and OX-ZEO systems (*8*–*11*, *13*, *16*, *21*) (Fig. 1D, figs. S7 to S11, and tables S4 to S8). Notably, the χ-Fe_5C_2 catalyst with Br cofeeding (denoted χ-Fe_5C_2-Br) exhibited superior olefin yield (~48% of total carbon-containing products) while maintaining ultralow CO_2 selectivity (<3%). In contrast, previously reported Fe- or Co-based and OX-ZEO catalysts typically exhibited CO_2 selectivity exceeding 10% or had a relatively low olefin yield (figs. S12 and S13).

Our strategy overcame the traditional trade-off between high olefin yield and low CO_2 selectivity, demonstrating unprecedented performance in the syngas-to-olefins reaction. A plot of the ratio of olefin-to-CO_2 selectivity ($S_{olefins}/S_{CO2}$) versus olefin space-time yield ($STY_{olefins}$) shows the overall catalytic performance (Fig. 1E). Although OX-ZEO catalysts offer good olefin selectivity among hydrocarbons, their low $STY_{olefins}$ and high CO_2 emissions constrain their practical utility (*13*). Similarly, Ru- and Co-based systems suffer from low $STY_{olefins}$ under conventional FTS conditions (*21*, *22*). In contrast, χ-Fe_5C_2-Br (Cl) catalysts delivered both high $STY_{olefins}$ and favorable olefin-to-CO_2 ratios. These results establish halogen cofeeding as an effective solution that enables high olefin space-time yield and high olefin yield with low CO_2 emissions in FTS. If C_{5+} olefins are used as liquid fuels, this strategy could also benefit conventional Fe-based FTS by blocking CO_2 emissions in standard FTS processes.

We also tracked the fate of CH_3Br in the product stream. Of the 20 ppm CH_3Br introduced, ~70% (14.2 ppm) was recovered as unreacted CH_3Br in the outlet gas, with <6 ppm detected in the aqueous phase. Only trace amounts of Br (<1 ppm) were found in the oil-phase products, indicating negligible incorporation into the hydrocarbon products (fig. S14 and tables S9 to S11). Notably, although only a small amount of Br remained on the surface of the iron catalyst (fig. S15 and table S12), it exerted a pronounced effect on the overall catalytic performance.

Structure of χ-Fe_5C_2 catalyst with CH_3Br cofeed

Cofeeding halomethanes induced a drastic shift in the reaction behavior of Fe-based FTS and largely suppressed CO_2 emissions (fig. S16). We hypothesized that halogen species play a critical role in modulating the structure of the working iron catalyst. To probe the structural consequences of halogen exposure, we characterized the χ-Fe_5C_2 catalyst after CH_3Br-cofeeding reaction (referred to as χ-Fe_5C_2-Br-spent). The catalysts with or without cofeeding halogen had similar morphologies and particle sizes (fig. S17). X-ray diffraction (XRD) analysis revealed that, in addition to the dominant χ-Fe_5C_2 phase, χ-Fe_5C_2-Br-spent exhibited new diffraction peaks associated with Fe_3O_4. In contrast, the control sample (χ-Fe_5C_2-spent, without CH_3Br) predominantly retained the carbide phase (Fig. 2A).

These results were corroborated by Mössbauer spectroscopy, electron microscopy, and extended x-ray absorption fine structure (EXAFS) fitting (figs. S18 to S24 and tables S13 to S16). X-ray photoelectron spectroscopy (XPS) further confirmed the presence of surface FeO_x, with detectable iron oxide species on both spent samples (Fig. 2B). The presence of FeO_x is commonly associated with the WGS reaction and therefore the CO_2 production in Fe-based FTS (*23*, *24*). Thus, the role of halogen was not to suppress the formation of iron oxides during the reaction.

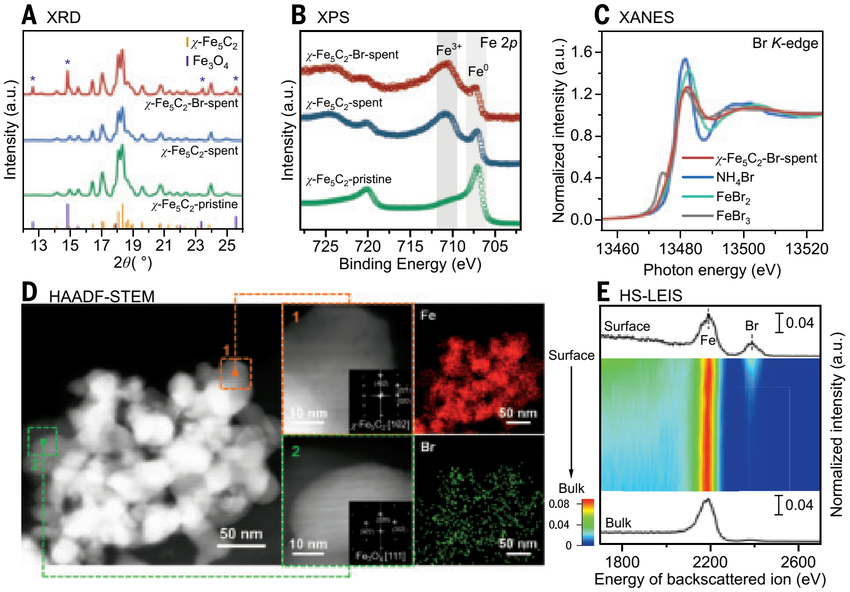

Fig. 2. Structure of χ-Fe_5C_2 and χ-Fe_5C_2-Br catalysts. Synchrotron XRD patterns (**A**) and Fe 2p XPS spectra (**B**) of pristine and spent χ-Fe_5C_2 and χ-Fe_5C_2-Br catalysts. a.u., arbitrary units. (**C**) Br K-edge XANES spectra of χ-Fe_5C_2-Br-spent catalyst compared with reference bromide compounds. (**D**) HAADF-STEM image and corresponding EDS mapping of Fe and Br distributions in χ-Fe_5C_2-Br-spent catalyst. (**E**) HS-LEIS depth profile of χ-Fe_5C_2-Br-spent catalyst. Reaction conditions: 100 mg catalyst, 300°C, 10 bar, 12,000 ml·g_{cat}^{-1}·$hour^{-1}$, $H_2/CO = 2$. χ-Fe_5C_2, syngas; χ-Fe_5C_2-Br, syngas with cofeeding 20 ppm CH_3Br. Catalysts were pretreated at 280°C and 1 bar for 6 hours, 12,000 ml·g_{cat}^{-1}·$hour^{-1}$, $H_2/CO = 2$ (χ-Fe_5C_2, syngas; χ-Fe_5C_2-Br, syngas with cofeeding 20 ppm CH_3Br).

Notably, elemental analysis, Br K-edge x-ray absorption near-edge structure (XANES), and Br 3d XPS revealed residual bromine species on χ-Fe_5C_2-Br-spent (Fig. 2C and fig. S25). The Br K-edge XANES spectra exhibited fingerprinting features similar to those of iron bromide, indicating strong Fe-Br interactions like that in iron bromide. High-angle annular dark-field scanning transmission electron microscopy (HAADF-STEM) imaging coupled with energy-dispersive x-ray spectroscopy (EDS) mapping showed homogeneous Br distribution across both Fe_3O_4 and χ-Fe_5C_2 domains (Fig. 2D and figs. S26 and S27), demonstrating homogeneous colocalization of Br and Fe species.

It remained uncertain whether Br was incorporated into the bulk lattice or was distributed on the surface. XRD showed no evidence of a new bromine-containing iron phase, suggesting that a surface-bound Br species was more likely (Fig. 2A and fig. S6). To confirm this hypothesis, we performed variable-energy XPS, which revealed substantial Br surface enrichment on the χ-Fe_5C_2-Br-spent catalyst (fig. S28). High-sensitivity low-energy ion scattering spectroscopy (HS-LEIS) is a surface-sensitive technique (*25*). From the HS-LEIS depth profile of the catalyst, we observed that Br was primarily enriched on the surface of the catalyst (Fig. 2E). Collectively, these findings strongly suggest that surface-bound Br modulates the chemical environment of active sites of Fe catalysts (both the iron carbide and oxide domains), suppressing CO_2 formation and enhancing olefin selectivity.

Inhibition mechanism of Br on CO_2 and paraffin formation

The reaction networks of the FTS process depicted in Fig. 3A were used to understand the mechanistic origin of this inhibition effect. Aside from the main reactions leading to the production of olefin and paraffin, there are two major side reactions that produce CO_2: WGS (highlighted in red) over iron oxide and the Boudouard reaction ($2CO \rightarrow C + CO_2$, highlighted in blue) over iron carbide (*14*, *26*). Although the primary products of Fe-based FTS were olefins, undesirable hydrogenation of olefins could lead to the production of less valuable paraffins ($C_nH_{2n} + H_2 \rightarrow C_nH_{2n+2}$, highlighted in purple) and a low o/p ratio (*27*).

On χ-Fe_5C_2 catalysts, both the Boudouard reaction and WGS routes contributed appreciably across typical reaction temperatures, with the WGS reaction becoming more pronounced at high conversions (fig. S29) (*15*, *24*, *26*, *28*). The drastic suppression of CO_2 formation observed in halogen-modified FTS suggested a fundamental alteration of reaction pathways by the Br on the surface of iron catalysts (fig. S30). To elucidate the underlying mechanism, we investigated catalytic reactivity by using transient kinetic analyses and surface-sensitive characterizations as well as computational modeling of reaction energetics, focusing on these two dominant CO_2-producing reactions in Fe-based FTS.

Both iron oxides (e.g., Fe_3O_4 and FeO_x clusters) and iron carbides may contribute to the observed WGS activity (*23*, *26*, *29*–*31*). In this study, Fe_3O_4 was selected as the model WGS catalyst under our conditions, while acknowledging that iron carbides can also play a role depending on temperature and surface state. We found that CH_3Br cofeeding could suppress WGS activity by more than two orders of magnitude (Fig. 3B and fig. S31). Given the established WGS mechanism wherein H_2O dissociates to generate surface hydroxyl (OH*), which then reacts with CO to form CO_2 (figs. S32 and S33), we first checked the adsorption and activation behavior of H_2O on the catalysts. Temperature-programmed desorption of water (H_2O-TPD) experiments revealed that both Fe_3O_4 and Br-pretreated Fe_3O_4 (referred to as Fe_3O_4-Br) showed similar H_2O adsorption abilities (desorbed at ~120°C). However, H_2 formation, an indicator for H_2O dissociation, was active on Fe_3O_4 but completely absent on Fe_3O_4-Br (Fig. 3C). In situ XPS further confirmed this suppression effect, showing minimal OH* production on Fe_3O_4-Br compared with Fe_3O_4 (Fig. 3D, figs. S34 and S35, and tables S17 and S18). Diffuse reflectance infrared Fourier transform spectroscopy (DRIFTS) and transient kinetic analysis (TKA) experiments corroborated this inhibition effect (figs. S33 and S36). These results established that Br disrupted the key step of H_2O dissociation in the WGS reaction, then effectively blocking CO_2 generation through this pathway.

These experimental findings were supported by DFT calculations on $Fe_3O_4(111)$. In the absence of Br, H_2O can readily dissociate ($H_2O \rightarrow OH^* + H^*$) with the activation barrier (E_{a2}) of 0.73 eV. However, increasing Br coverage from $\theta_{Br} = 1/5$ to 1/3 raised this barrier to $E_{a2} >$ 1.2 eV. At a higher coverage of $\theta_{Br} = 2/5$, H_2O dissociation was completely inhibited (fig. S37). These findings aligned with TPD and XPS results, suggesting that surface-bound Br passivates reactive Fe sites and disrupts WGS reaction.

We then considered the Boudouard reaction. We performed CO pulse experiments on χ-Fe_5C_2 and χ-Fe_5C_2-Br catalysts. Both catalysts exhibited similar CO adsorption properties (figs. S38 and S39). However, CO_2 formation was observed on χ-Fe_5C_2, which was nearly completely suppressed on the χ-Fe_5C_2-Br in CO pulse, indicating that the Boudouard reaction was largely inhibited (Fig. 3E). Moreover, Ar → $C^{18}O$ TKA experiments also showed no production of $C^{16}O^{18}O$ and $C^{18}O_2$ on χ-Fe_5C_2-Br but formation of $C^{16}O$ after introduction of $C^{18}O$, which may result from the recombination of dissociatively adsorbed CO (Fig. 3F). Notably, introduction of ^{13}CO to ^{18}O-precovered surface yielded $^{13}C^{18}O$ on χ-Fe_5C_2-Br (fig. S40), confirming that CO dissociation remained active. Temperature-programmed surface reaction (TPSR) experiments using a mixture of $C^{18}O$/He/Ar as feed further substantiated this selective blocking effect (fig. S41). These results suggest that

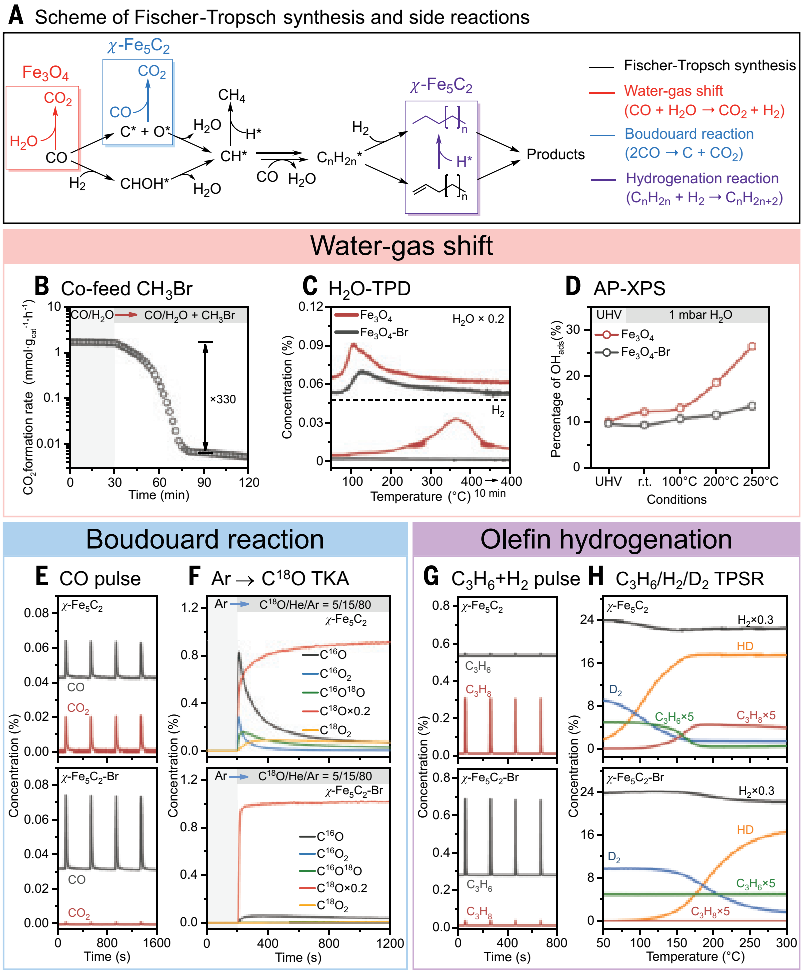

Fig. 3. Mechanism of Br in regulating catalytic behavior. (**A**) The reaction pathways in the FTS network. (**B**) Inhibition effect of CH_3Br cofeeding on CO_2 formation in water-gas shift reaction over Fe_3O_4 catalyst. Reaction conditions: 50 mg catalyst, 300°C, 1 bar, 10 ml/min $CO/H_2O/Ar = 2/2/96$ switched to $CO/H_2O/Ar = 2/2/96$ with cofeeding 300 ppm CH_3Br. (**C**) Temperature-programmed desorption of H_2O over Fe_3O_4 and Fe_3O_4-Br catalysts. Reaction conditions: 100 mg catalyst, 1 bar, pretreated in 20 ml/min $H_2O/Ar = 2.5/97.5$ at 50°C; then switched to 20 ml/min Ar, purging for 20 min, followed by temperature ramping from 50°C to 300°C at 10°C/min. (**D**) Near ambient pressure XPS results of Fe_3O_4 and Fe_3O_4-Br catalysts at different temperatures in 1 mbar H_2O. Conditions: Catalysts were pretreated at 400°C in Ar for 1 hour, cooled to room temperature, introduced to 1 mbar H_2O, and treated at different temperatures. UHV, ultrahigh vacuum. (**E**) CO pulse experiment over χ-Fe_5C_2 and χ-Fe_5C_2-Br catalysts. Reaction conditions: 100 mg catalyst, 300°C, 1 bar, 5 ml/min Ar, 250 μl sampling loop, pulse gas: $CO/He = 0.5/99.5$. (**F**) Transient kinetic analysis of Ar → $C^{18}O/He/Ar = 5/15/80$ over χ-Fe_5C_2 and χ-Fe_5C_2-Br catalysts. Reaction conditions: 50 mg catalyst, 300°C, 1 bar, 10 ml/min Ar switched to $C^{18}O/He/Ar = 5/15/80$. (**G**) Pulse experiment of C_3H_6 in H_2 for χ-Fe_5C_2 and χ-Fe_5C_2-Br catalysts. Reaction conditions: 50 mg catalyst, 300°C, 1 bar, 20 ml/min H_2, 250 μl sampling loop, pulse gas: $C_3H_6/Ar/He = 3/3/94$. (**H**) Temperature-programmed experiment of C_3H_6 hydrogenation for χ-Fe_5C_2 and χ-Fe_5C_2-Br catalysts with cofeeding D_2. Reaction conditions: 50 mg catalyst, 1 bar, 10 ml/min $C_3H_6/H_2/D_2/Ar = 1/82/10/7$, temperature ramping from 50°C to 300°C at 10°C/min.

Br selectively inhibits the CO*-O* recombination step while preserving CO dissociation activity, which is in good agreement with DFT calculations (fig. S42).

From the results presented above, we conclude that surface Br species suppressed both WGS and Boudouard reactions. Another question is how Br modulated the o/p ratio in the reaction. Although promoters such as alkali metals or Mn for Fe-based catalysts are typically required to achieve a high olefin selectivity (*16*, *27*, *32*, *33*), we added no alkali metal or Mn in the current high-olefin-selectivity χ-Fe_5C_2-Br catalysts. To understand the origin of the ability of χ-Fe_5C_2-Br to achieve a high o/p ratio, we used propene hydrogenation as a probe to study the olefin hydrogenation process. Propene pulse experiments in H_2 showed a drastic reduction in propene hydrogenation activity on χ-Fe_5C_2-Br compared with χ-Fe_5C_2 (Fig. 3G), which indicated that surface Br species suppressed the olefin hydrogenation reaction.

Weakened H_2 activation ability on the Br-modified surface could be one reason for high olefin selectivity, but this explanation appeared unlikely, because hydrocarbon formation was still observed. Another possibility is that the olefin hydrogenation step is suppressed. To further substantiate this point, we conducted TPSR experiments using a $C_3H_6/H_2/D_2/Ar = 1/82/10/7$ mixture feed. Hydrogen deuteride (HD) formation through H-D exchange was used as a probe to monitor H_2 activation. On χ-Fe_5C_2, both H-D exchange and C_3H_6 hydrogenation increased with temperature, reaching near-complete C_3H_6 conversion at around 180°C. In contrast, on χ-Fe_5C_2-Br, although activation of H_2 was slightly suppressed at low temperatures and became very active above 200°C, no detectable hydrogenation of C_3H_6 was observed even at temperatures up to 300°C (Fig. 3H). These results demonstrated that the high olefin selectivity came from inhibition of olefin hydrogenation ability by Br.

DFT simulations confirmed that Br altered hydrogenation energetics. On clean χ-Fe_5C_2(100), the two-step hydrogenation of C_3H_6 proceeds with low barriers (0.22 and 0.26 eV), facilitating paraffin formation (Fig. 4A). With $\theta_{Br} = 1/3$, the barrier of the first step ($C_3H_6^* + H^* \rightarrow C_3H_7^*$) increased to 0.66 eV, surpassing C_3H_6 desorption energy, making desorption more favorable than hydrogenation. Detailed electronic analyses (figs. S43 to S45) and optimized transition state geometries (figs. S46 and S47) revealed that surface-bound Br species not only electronically modified Fe active sites but also introduced substantial steric hindrance. This steric effect obstructed the H* approach and altered the Fe-C_3H_6 binding geometry. As a result, secondary hydrogenation was selectively suppressed under Br-modified conditions.

Finally, we examined the catalytic stability of the χ-Fe_5C_2 catalyst with 20 ppm CH_3Br cofeeding, a critical measurement for practical applications. As shown in Fig. 4B, the catalyst exhibited excellent stability for >450 hours. At a steady CO conversion of ~35%, the system maintained an exceptionally high C_{2+} olefin selectivity of >80%. Notably, the formation of undesired by-products such as methane and CO_2 remained minimal throughout the test, with CO_2 selectivity consistently <1.5%. Such sustained performance—combining high olefin selectivity and near-zero CO_2 emissions—has not been previously reported in the century-long development of Fe-based FTS. These findings underscore the transformative potential of halogen cofeeding for enabling low-emission, high-efficiency olefin production at scale.

Conclusions

We demonstrated a simple yet powerful strategy to enhance FTS-to-olefins performance by cofeeding ppm levels of CH_3Br into Fe-based catalytic systems. Surface-bound Br species electronically interacted with Fe active sites, selectively inhibiting H_2O dissociation, CO*-O* recombination, and olefin hydrogenation, while largely preserving CO and H_2 adsorption and activation. The strategy reported in this work enables a near-zero-CO_2 pathway for highly selective olefin (or liquid fuels) production in Fe-based FTS processes that achieve high

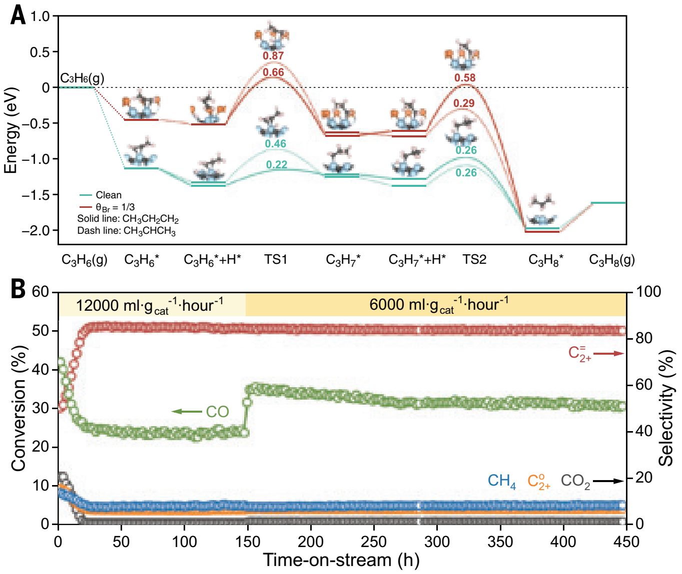

Fig. 4. Theoretical investigation of olefin hydrogenation inhibition mechanism and catalytic stability of χ-Fe_5C_2 catalyst with CH_3Br cofeed in the FTS process. (**A**) DFT-calculated reaction energy profiles for propene hydrogenation on clean and Br-covered ($\theta_{Br} = 1/3$) χ-Fe_5C_2(100) surfaces. Reaction intermediates and transition states illustrate two hydrogenation pathways, through $CH_3CH_2CH_2$ (solid line) and CH_3CHCH_3 (dotted line), highlighting increased hydrogenation barriers upon Br modification. (**B**) Catalytic stability and product selectivity of the χ-Fe_5C_2-Br catalyst. Reaction conditions: 100 mg catalyst, 300°C, 5 bar, $H_2/CO = 2$, cofeeding 20 ppm CH_3Br. The catalyst exhibited stable CO conversion and sustained high selectivity toward C_{2+} olefins with minimal CH_4 and CO_2 by-product formation over 450 hours at two different space velocities (12,000 and 6000 ml·g_{cat}^{-1}·$hour^{-1}$).

α-olefin selectivity and maintain industrially competitive activity, surpassing other reported low-CO_2 systems (table S8).

Although halogen-containing cofeed could pose challenges in scaled-up industrial reactors, similar strategies have been adopted in commercialized processes, such as chlorine cofeed silver-catalyzed ethylene epoxidation process (*34*, *35*). Coupled with CO_2-free gasification reaction (e.g., $CH_4 + 3CO_2 = 4CO + 2H_2O$) and green hydrogen from water electrolysis (*36*), the process developed in this work could offer a viable pathway toward carbon-neutral coal-to-liquid/olefins or gas-to-liquid/olefins processes.

REFERENCES AND NOTES

1. K. T. Rommens, M. Saeys, *Chem. Rev.* **123**, 5798–5858 (2023).
2. X. Pan, F. Jiao, D. Miao, X. Bao, *Chem. Rev.* **121**, 6588–6609 (2021).
3. J. Li *et al.*, *Nat. Catal.* **1**, 787–793 (2018).
4. H. Zhao *et al.*, *CCS Chem.* **3**, 2712–2724 (2021).
5. P. Wang *et al.*, *Sci. Adv.* **4**, eaau2947 (2018).
6. S. Lyu *et al.*, *Nat. Commun.* **11**, 6219 (2020).
7. D. Wang *et al.*, *ACS Catal.* **15**, 7028–7039 (2025).
8. X. Zhang *et al.*, *Proc. Natl. Acad. Sci. U.S.A.* **121**, e2407624121 (2024).
9. H. M. Torres Galvis *et al.*, *Science* **335**, 835–838 (2012).
10. P. Wang *et al.*, *Nature* **635**, 102–107 (2024).
11. Y. Xu *et al.*, *Science* **371**, 610–613 (2021).
12. F. Jiao *et al.*, *Science* **351**, 1065–1068 (2016).
13. F. Jiao *et al.*, *Science* **380**, 727–730 (2023).
14. E. de Smit *et al.*, *Angew. Chem. Int. Ed.* **50**, 1584–1588 (2011).
15. M. Ojeda *et al.*, *J. Catal.* **272**, 287–297 (2010).
16. F. Qian *et al.*, *Nat. Commun.* **15**, 5128 (2024).
17. X.-W. Liu *et al.*, *J. Phys. Chem. C* **121**, 21390–21396 (2017).
18. X. W. Liu *et al.*, *Sci. Rep.* **6**, 26184 (2016).
19. C. Yang, H. Zhao, Y. Hou, D. Ma, *J. Am. Chem. Soc.* **134**, 15814–15821 (2012).
20. W. Ma *et al.*, *ACS Catal.* **5**, 3124–3136 (2015).
21. L. Zhong *et al.*, *Nature* **538**, 84–87 (2016).
22. H. Yu *et al.*, *Nat. Commun.* **13**, 5987 (2022).
23. M. Claeys *et al.*, *ACS Catal.* **11**, 13866–13879 (2021).
24. E. de Smit *et al.*, *J. Am. Chem. Soc.* **132**, 14928–14941 (2010).
25. C. Zhan *et al.*, *J. Am. Chem. Soc.* **142**, 14134–14141 (2020).
26. C. J. Keturakis *et al.*, *ACS Catal.* **6**, 4786–4798 (2016).
27. P. Zhai *et al.*, *Angew. Chem. Int. Ed.* **55**, 9902–9907 (2016).
28. R. Gubo *et al.*, *ACS Catal.* **14**, 14721–14732 (2024).
29. M. Zhu, I. E. Wachs, *ACS Catal.* **6**, 722–732 (2015).
30. F. Polo-Garzon *et al.*, *J. Am. Chem. Soc.* **141**, 7990–7999 (2019).
31. H. Yan *et al.*, *Appl. Catal. B* **226**, 182–193 (2018).
32. Y. Liu, J.-F. Chen, J. Bao, Y. Zhang, *ACS Catal.* **5**, 3905–3909 (2015).
33. R. Wang *et al.*, *ACS Catal.* **14**, 11121–11130 (2024).
34. V. P. Santos *et al.*, *ACS Catal.* **14**, 10839–10852 (2024).
35. R. M. Lambert, R. L. Cropley, A. Husain, M. S. Tikhov, *Chem. Commun.* **2003**, 1184–1185 (2003).
36. L. C. Buelens, V. V. Galvita, H. Poelman, C. Detavernier, G. B. Marin, *Science* **354**, 449–452 (2016).
37. K. Cheng *et al.*, *Angew. Chem. Int. Ed.* **55**, 4725–4728 (2016).
38. F. Jiao *et al.*, *Angew. Chem. Int. Ed.* **57**, 4692–4696 (2018).
39. Y. Ni *et al.*, *ACS Catal.* **9**, 1026–1032 (2019).
40. Y. Zhu *et al.*, *ACS Catal.* **7**, 2800–2804 (2017).
41. J. Su *et al.*, *Nat. Commun.* **10**, 1297 (2019).
42. J. Lu *et al.*, *ACS Catal.* **4**, 613–621 (2014).
43. O. Zhuo *et al.*, *Chem. Sci.* **10**, 6083–6090 (2019).
44. Y. He, H. Shi, O. Johnson, B. Joseph, J. N. Kuhn, *ACS Catal.* **11**, 15177–15186 (2021).
45. J. Wang *et al.*, *ACS Appl. Mater. Interfaces* **10**, 43578–43587 (2018).
46. J. Xie *et al.*, *Nat. Commun.* **10**, 167 (2019).
47. T. Lin *et al.*, *Appl. Catal. B* **299**, 120683 (2021).

ACKNOWLEDGMENTS

This work is dedicated to the 100th anniversary of the FTS process. The authors acknowledge the staff of the BL02U2 beamlines at the Shanghai Synchrotron Radiation Facility (https://cstr.cn/31124.02.SSRF.BL02U2) for their technical support and assistance with XRD measurements. The authors acknowledge the BL02B01 and BL20U1 beamlines at the Shanghai Synchrotron Radiation Facility (https://cstr.cn/31124.02.SSRF.BL02B01, https://cstr.cn/31124.02.SSRF.BL20U1) for technical support and assistance with XPS and XAS measurements, respectively. The authors thank the BL01B1 beamline at SPring-8, Japan, for their valuable technical support and assistance with XAS data collection. The artificial intelligence (AI)–driven experiments, simulations, and model training were performed on the robotic AI-Scientist platform of the Chinese Academy of Sciences. We thank W. Zhou and J. Gao for helpful discussions. The authors gratefully acknowledge the resources and financial support provided by the Research and Design Center of Synfuels China Co., Ltd. D.M. acknowledges support from the New Cornerstone Science Foundation through the XPLORER PRIZE and New Cornerstone Investigator Program. **Funding:** National Science Fund for Distinguished Young Scholars of China 22225206 (X.-D.W.) and 22025804 (Y.Y.); National Key R&D Program of China 2022YFB4101200 (Y.Y.), 2023YFB4103100 (Y.X.), 2021YFA1501102 (D.M.), and 2021YFA1500300 (X.L.); National Natural Science Foundation of China 22172183 (X.-W.L.), 22572210 (X.-W.L.), 22232001 (D.M.), and 22272106 (X.L.); Beijing Natural Science Foundation L255001 (X.-W.L.); Ordos Key R&D Program YF20232316 (X.-W.L.) and YF20232317 (X.-D.W.). **Author contributions:** D.M., X.-D.W., and X.-W.L. conceived of and supervised the project. Y.C. and X.-W.L. conducted most of the catalytic reactions. M.W. performed the transient kinetic experiments. F.Q. performed Mössbauer spectroscopy. M.W., L.Z., Z.C., and Y.X. carried out and analyzed the x-ray–based characterizations (XRD, XAS, and XPS). Y.C., X.-W.L., and X.L. conducted the electron microscopy studies. S.Z., X.-W.L., and X.-D.W. performed the DFT calculations. Y.C., M.W., X.-W.L., S.Z., and D.M. wrote the original draft. B.X., G.J.H., H.W., J.X., J.Z., Y.-W.L., Y.Y., X.L., X.C.L., and Z.R.G. provided scientific guidance and critical discussion. All authors contributed to discussions and revisions of the manuscript. **Competing interests:** A Chinese patent covering the strategy of cofeeding halogen-containing gases, as reported in this paper, has been filed. Other than this, the authors declare that they have no competing interests. **Data and materials availability:** All data supporting the findings of this study are available within the paper and its supplementary materials.

SUPPLEMENTARY MATERIALS

science.org/doi/10.1126/science.aea1655
Materials and Methods; Figs. S1 to S47; Tables S1 to S18; References (*48*–*57*)

Submitted 28 June 2025; accepted 8 September 2025

10.1126/science.aea1655

COMPARATIVE COGNITION

Chimpanzees rationally revise their beliefs

Hanna Schleihauf[1,2]†, Emily M. Sanford[3]†, Bill D. Thompson[3], Snow Zhang[4], Joshua Rukundo[5], Josep Call[6,7], Esther Herrmann[8]‡, Jan M. Engelmann[3]*‡

The selective revision of beliefs in light of new evidence has been considered one of the hallmarks of human-level rationality. However, tests of this ability in other species are lacking. We examined whether and how chimpanzees (*Pan troglodytes*) update their initial belief about the location of a reward in response to conflicting evidence. Chimpanzees responded to counterevidence in ways predicted by a formal model of rational belief revision: They remained committed to their initial belief when the evidence supporting the alternative belief was weaker, but they revised their initial belief when the supporting evidence was stronger. Results suggest that this pattern of belief revision was guided by the explicit representation and weighing of evidence. Taken together, these findings indicate that chimpanzees metacognitively evaluate conflicting pieces of evidence within a reflective process.

Rationality is a hallmark of human thinking. Rational agents form beliefs about the world on the basis of evidence (*1*), but as new evidence emerges, they revise their beliefs by weighing the strength of their prior beliefs in relation to the strength of the new evidence (*2*). Selective belief revision is a particularly strong indicator of rationality (*3*).

From a Bayesian perspective, the rational response to counter-evidence is to revise a belief in hypothesis h_1 to a belief that supports an alternative hypothesis h_2 when the counterevidence causes the posterior probability of h_2 to exceed the posterior probability of h_1:

$$\frac{p(h_2 \mid e_{Old}, e_{New})}{p(h_1 \mid e_{Old}, e_{New})} = \frac{p(e_{Old}, e_{New} \mid h_2)\, p(h_2)}{p(e_{Old}, e_{New} \mid h_1)\, p(h_1)} > 1$$

When both hypotheses have equal probabilities a priori, this condition is met when the strength of the evidence (e_{Old}) supporting the initial hypothesis is exceeded by the strength of new evidence (e_{New}) supporting the alternative hypothesis [see supplementary materials (SM)]. A reasoner should maintain their initial belief when the evidence in support of their initial belief is stronger and revise their belief if the evidence in support of the alternative belief is stronger.

Humans' closest primate relatives adjust their beliefs in response to evidence. For example, great apes draw inferences based on auditory, visual, and tactile cues during problem solving (*4*–*12*). Chimpanzees infer food locations from left-behind traces (*13*, *14*), weight effects (*15*), or a food's absence from an alternative location (*16*, *17*). They flexibly distinguish between appearance and reality, discounting misleading cues such as apparent food size (*18*), and they actively seek additional information when faced with contradictory evidence (*19*). It is not known, however, whether chimpanzees demonstrate the metacognitive ability to rationally evaluate the strength of new evidence and compare it with the strength of their existing beliefs—and so revise their beliefs only when appropriate, as humans can.

We tested whether chimpanzees' patterns of belief change conform to the predictions of a Bayesian formulation of rational belief revision (Experiments 1 and 2). We then probed the cognitive mechanisms underlying chimpanzees' belief revision. We asked whether chimpanzees represent both possible hypotheses before choosing between them (Experiment 3), individuate evidence (differentiate new from redundant evidence; Experiment 4), and respond to second-order evidence (evidence about the validity of the first-order evidence; Experiment 5).

Chimpanzees' response to counterevidence

In Experiments 1 and 2 (preregistered), chimpanzees ($N = 15$) were presented with a piece of food, which was then hidden in one of two possible locations. Next, they were given evidence that the food was in one of the locations and made their first choice. Subjects were then given a different form of evidence that favored the other location and made a second choice (which confirmed or changed their first choice). In the "strong evidence first" condition, chimpanzees were provided with strong evidence for one of the locations before their first choice and then weak evidence for the alternative location before their second choice. In the "weak evidence first" condition, the order was reversed (Fig. 1). Our classifications for strong versus weak evidence were based on previous research (*13*, *16*). In Experiment 1, we classified visual evidence (seeing food) as strong evidence and auditory evidence (hearing food) as weak evidence (Fig. 1A). In Experiment 2, we classified auditory evidence as strong evidence and indirect visual evidence (seeing food traces) as weak evidence (Fig. 1B). Chimpanzees' first choices validated these classifications (Experiment 1: $\chi^2 = 8.37$, df = 1, $p = 0.004$; Experiment 2: $\chi^2 = 11.99$, df = 1, $p = 0.001$; Fig. 2A and SM).

We assessed whether chimpanzees' choices aligned with the predictions of rational belief revision. In Experiment 1, chimpanzees were significantly more likely to revise their beliefs in the "weak evidence first" condition than in the "strong evidence first" condition ($\chi^2 = 14.03$, df = 1, $p < 0.001$; Fig. 2B). We found no evidence that chimpanzees simply learned the appropriate behavior over time: Neither trial number ($\chi^2 = 0.85$, df = 1, $p = 0.398$) nor the interaction between trial number and condition ($\chi^2 = 3.56$, df = 1, $p = 0.151$) had a significant effect on performance. In Experiment 2, chimpanzees also revised their belief significantly more often in the "weak evidence first" condition than in the "strong evidence first" condition ($\chi^2 = 20.52$, df = 1, $p < 0.001$; Fig. 2B). Again, we found no evidence that chimpanzees simply learned the behavior across trials: Neither trial number ($\chi^2 = 0.93$, df = 1, $p = 0.336$) nor the interaction between trial number and condition ($\chi^2 = 1.60$, df = 1, $p = 0.206$) had a significant effect on the likelihood of belief revision.

The results also confirm that chimpanzees' choices were in line with the principle of commutativity, which holds that one's belief should depend on the sum total of all previously perceived evidence, independent of the order in which that evidence was acquired (*20*). After receiving both strong and weak evidence, chimpanzees chose the location supported by strong evidence at above chance levels in both conditions in Experiment 1 [proportion choosing strong evidence side: weak evidence first condition = 0.93, 95% confidence interval (CI) (0.88, 1.00); strong evidence first condition = 0.92, 95% CI (0.85, 1.00)] and Experiment 2 [weak evidence first condition = 0.96, 95% CI (0.93, 1.00); strong evidence first condition = 0.86, 95% CI (0.77, 1.00)]. Moreover, the likelihood of endorsing the strong evidence at the second choice did not differ depending on whether it was presented first (strong evidence first condition) or second (weak evidence first condition) in Experiment 1 ($\chi^2 = 1.64$, df = 1, $p = 0.286$) or Experiment 2 ($\chi^2 = 1.40$, df = 1, $p = 0.330$).

---

[1] Department for Developmental Psychology, Utrecht University, Utrecht, Netherlands. [2] German Primate Center, Leibniz Institute for Primate Research, Göttingen, Germany. [3] Department of Psychology, University of California, Berkeley, Berkeley, CA, USA. [4] Department of Philosophy, University of California, Berkeley, Berkeley, CA, USA. [5] Ngamba Island Chimpanzee Sanctuary/Chimpanzee Trust, Entebbe, Uganda. [6] School of Psychology and Neuroscience, University of St Andrews, St. Andrews, UK. [7] Global Research Centre for Diverse Intelligences, University of St Andrews, St. Andrews, UK. [8] School of Psychology, Sport and Health Sciences, University of Portsmouth, Portsmouth, UK. ***Corresponding author. Email: jan_engelmann@berkeley.edu** †These authors contributed equally to this work. ‡These authors contributed equally to this work.

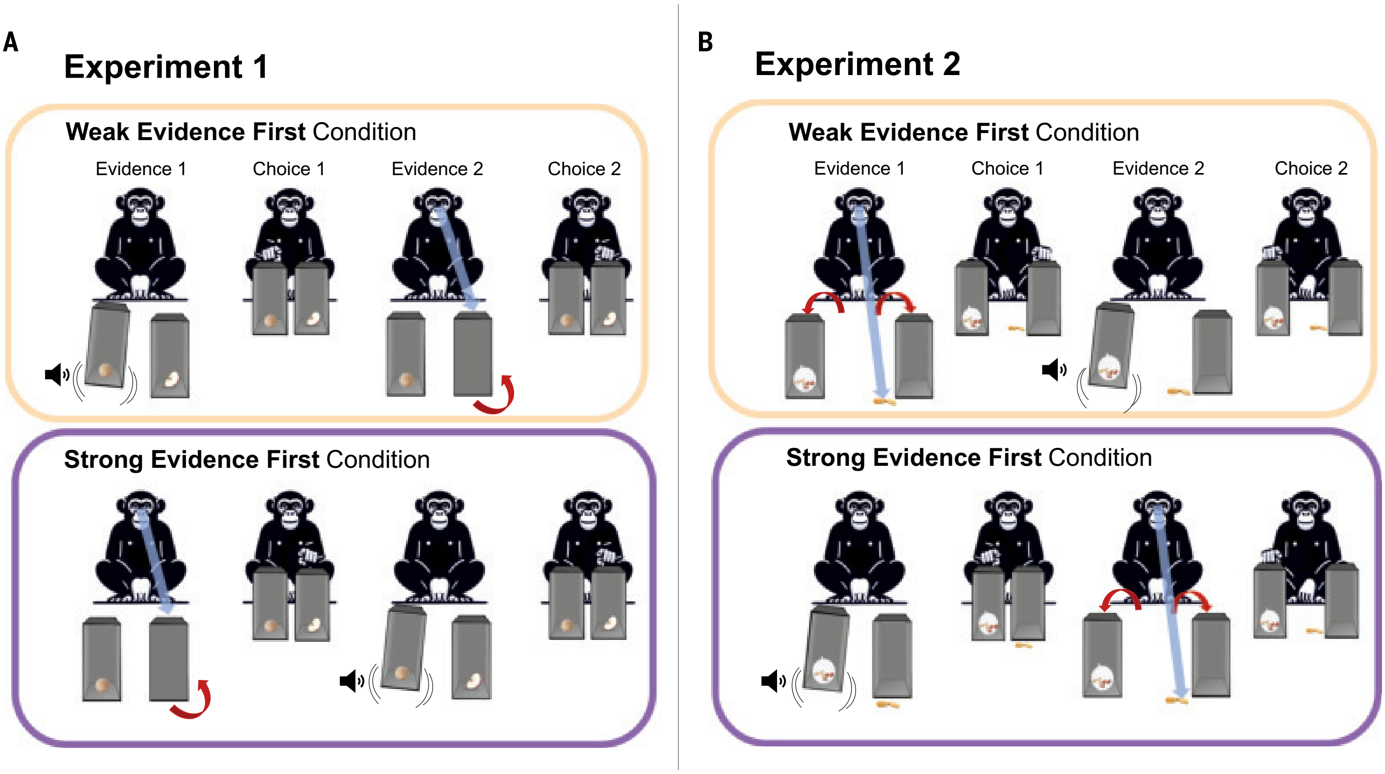

Fig. 1. Procedure of Experiments 1 and 2. (**A**) Experiment 1, Weak evidence first condition: Chimpanzees first received weak evidence (auditory evidence: shaking the box with a piece of wood in it) for one of the boxes and made a first choice. Then they received strong evidence (direct visual evidence: seeing into the box through a glass pane) for the other box and made a second choice. Strong evidence first condition: The same types of evidence were presented but in reverse order. (**B**) Experiment 2, Weak evidence first condition: Chimpanzees first received weak evidence (indirect visual evidence: seeing traces of the food behind the box) for one of the boxes and made a first choice. Then they received strong evidence (auditory evidence: shaking the box with a plastic capsule containing peanuts in it) for the other box and made a second choice. Strong evidence first condition: The same types of evidence were presented but in opposite order. Note: The red arrows indicate that the box was rotated (Experiment 1) or moved to the side (Experiment 2) to reveal visual evidence. In Experiments 1 and 2, in addition to the weak evidence first condition and the strong evidence first condition, chimpanzees also participated in filler trials, during which they received one piece of evidence, made a single choice, and received the contents of the box that they picked on their first choice (there was no second piece of evidence and no second choice). Filler trials were included such that subjects could not, on any given trial, predict whether their first or second choice would count (for details, see SM).

We also implemented a Bayesian modeling analysis in Stan (*21*) to assess whether chimpanzees' choice behavior is consistent with a formal model of belief revision (rational choice model; fig. S3 and SM). We found that the core conditions for rationality were met: Inferred evidence strength for strong evidence was both larger than—and in the opposite direction of—weak evidence (Fig. 2C and SM). Furthermore, this rationality did not merely emerge at the group level: Across both experiments, this pattern held for nearly every individual subject (Fig. 2, C and D, and SM).

To assess whether the rational choice model provided the best explanation for chimpanzees' choices, we compared it against four alternatives (fig. S3 and SM): belief perseveration (*22*–*24*), recency bias (*25*, *26*), cue saliency (*27*, *28*), and a null model. For both experiments, the rational choice model outperformed the recency bias, belief perseveration, and null models, while the cue saliency model performed equally well compared with the rational choice model (see SM).

The cognitive underpinnings of chimpanzees' belief revision

The findings of Experiments 1 and 2 suggest that chimpanzees compare evidence in favor of two alternative options and endorse the option supported by stronger evidence. It is possible, however, that receiving strong evidence—such as seeing the food directly in Experiment 1—simply replaced representations based on weak evidence, without any comparison across represented options (cue saliency model). In Experiment 3, we tested whether the saliency of the strongest cue overrides other representations. Subjects ($N = 23$) were presented with three hiding locations and received strong evidence (seeing food) for one of the locations, weak evidence (hearing food) for a second location, and no evidence for the third location (Fig. 3). Then, the box supported by strong evidence was removed. Lastly, chimpanzees made a choice. We tested whether chimpanzees would select the option supported by weak evidence more often than the option supported by no evidence, which would suggest that weaker representations are maintained even when the evidence supporting them is not the most salient. Alternatively, they could choose randomly between the two remaining options, suggesting that only the representation supported by the most salient evidence is maintained. Chimpanzees chose the weak evidence option at a rate significantly above chance ($\beta_0 = 1.41$, standard error = 0.19, $z = 7.61$, $p < 0.001$), and the Bayesian analysis confirmed that their weight on weak evidence was significantly greater than 0 (see SM). This suggests that chimpanzees indeed represented both options during Experiments 1 and 2 [see fig. S4 and SM for an additional experiment replicating this finding; see also (*29*–*32*)].

If chimpanzees in Experiments 1 and 2 explicitly represented the evidence in favor of both options and compared their relative strength, they should demonstrate two further capacities: differentiating between new and redundant evidence (Experiment 4) and sensitivity to second-order evidence—evidence about the validity of the previous evidence (Experiment 5).

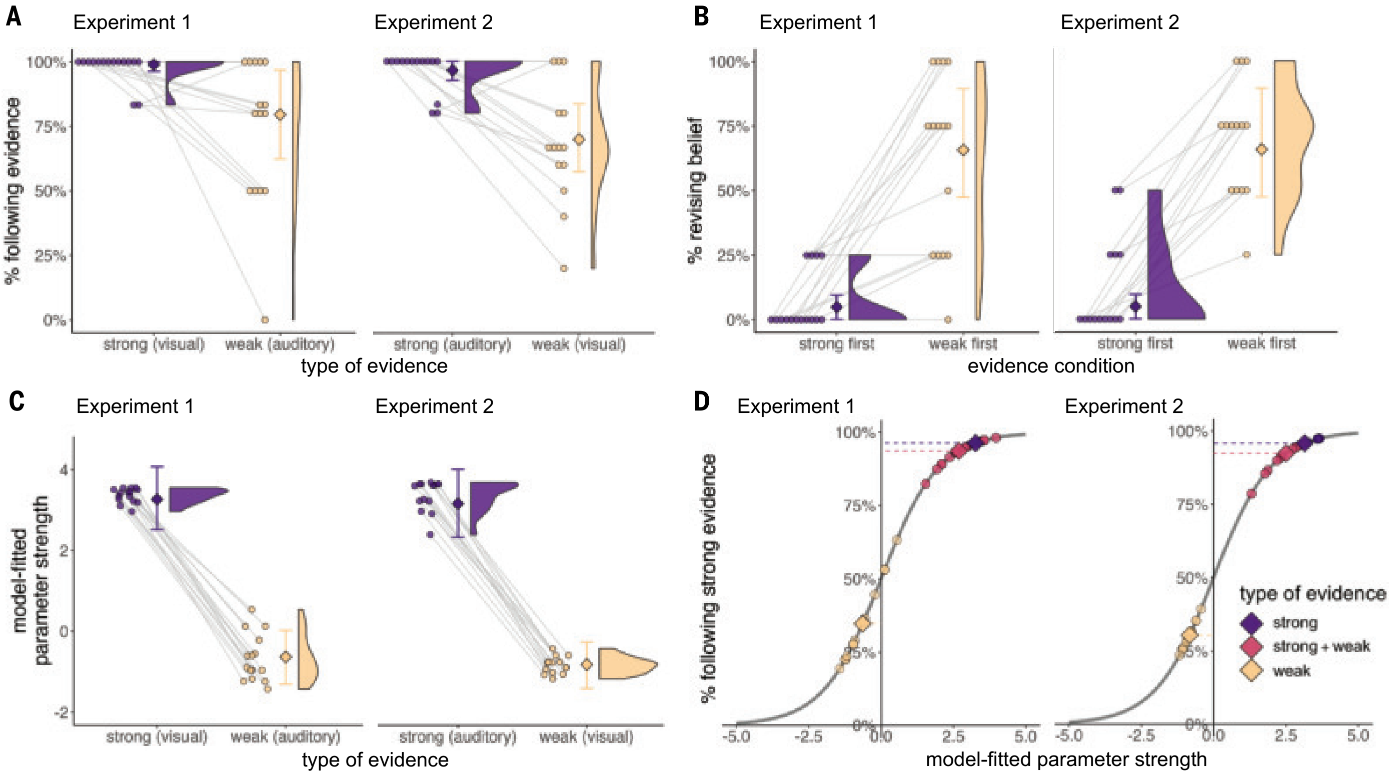

Fig. 2. Results of Experiments 1 and 2. (**A**) First choices by evidence type. Each point represents one chimpanzee's average response for that trial type. Error bars represent the bootstrapped 95% CIs of the generalized linear mixed model (GLMM) including all main effects. Diamonds represent the model predictions. Gray lines connect the behavior of one chimpanzee across both conditions within each experiment. (**B**) Belief revision by condition. Error bars represent the bootstrapped 95% CIs of the GLMM including all main effects. Diamonds represent the model predictions. Gray lines connect the behavior of one chimpanzee across both conditions within each experiment. (**C**) Rational choice model parameter estimates for individual subjects' e_{Strong} and e_{Weak} in Experiments 1 and 2. Error bars represent the model's 95% CIs on the group mean estimates (diamonds). (**D**) Predicted choice rates based on model-fitted evidence strengths across different evidence types (strong, weak, and strong + weak). Dots reflect individual subject parameters, and diamonds reflect group means. The dashed lines reflect the model's assumed relationship between evidence strength and choice rate.

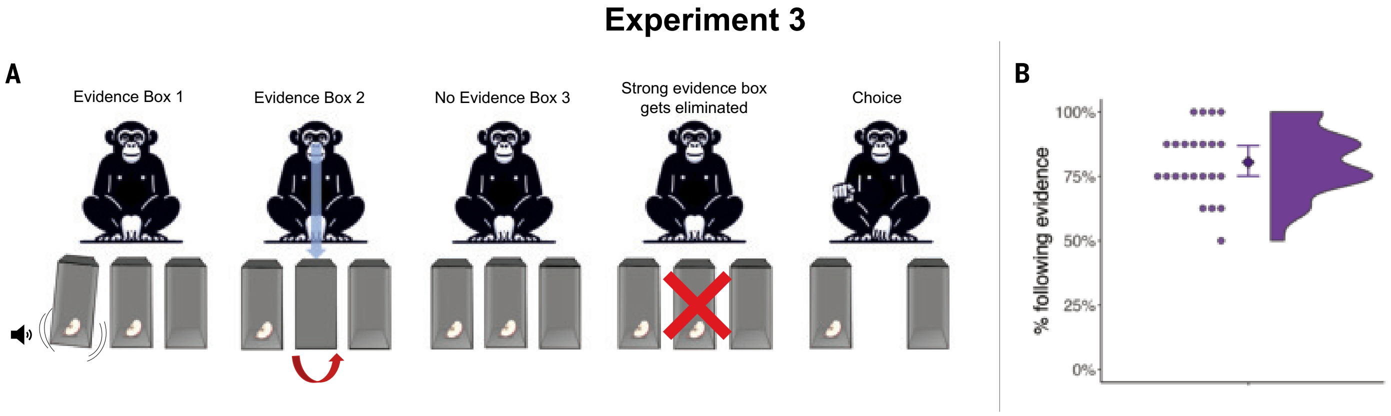

Fig. 3. Procedure and results of Experiment 3. (**A**) Chimpanzees received, in counterbalanced order, weak evidence for one box (auditory evidence: shaking the box with a piece of wood in it), strong evidence for a second box (direct visual evidence: seeing into the box through a glass pane), and no evidence for the third box (the box was touched for the same amount of time that each of the other two boxes was manipulated, but no evidence was provided). Then the experimenter removed the box supported by strong evidence before the chimpanzee was allowed to make a choice. (**B**) Chimpanzees were significantly more likely to select the box supported by weak evidence (rather than the box supported by no evidence) than would be expected by chance.

In Experiment 4, we asked whether chimpanzees ($N = 23$) would be swayed more by new evidence (evidence that comes from an independent, distinct source that provides additional information) compared with redundant evidence (evidence that comes from the same source as previous evidence and therefore provides no new information). In the "redundant evidence" condition, the weak evidence was auditory shaking evidence (which, when repeated, provides no new information), whereas in the "new evidence" condition, the weak evidence was auditory dropping evidence (which, when repeated, indicates that a second piece of food has been dropped into the box; Fig. 4 and SM).

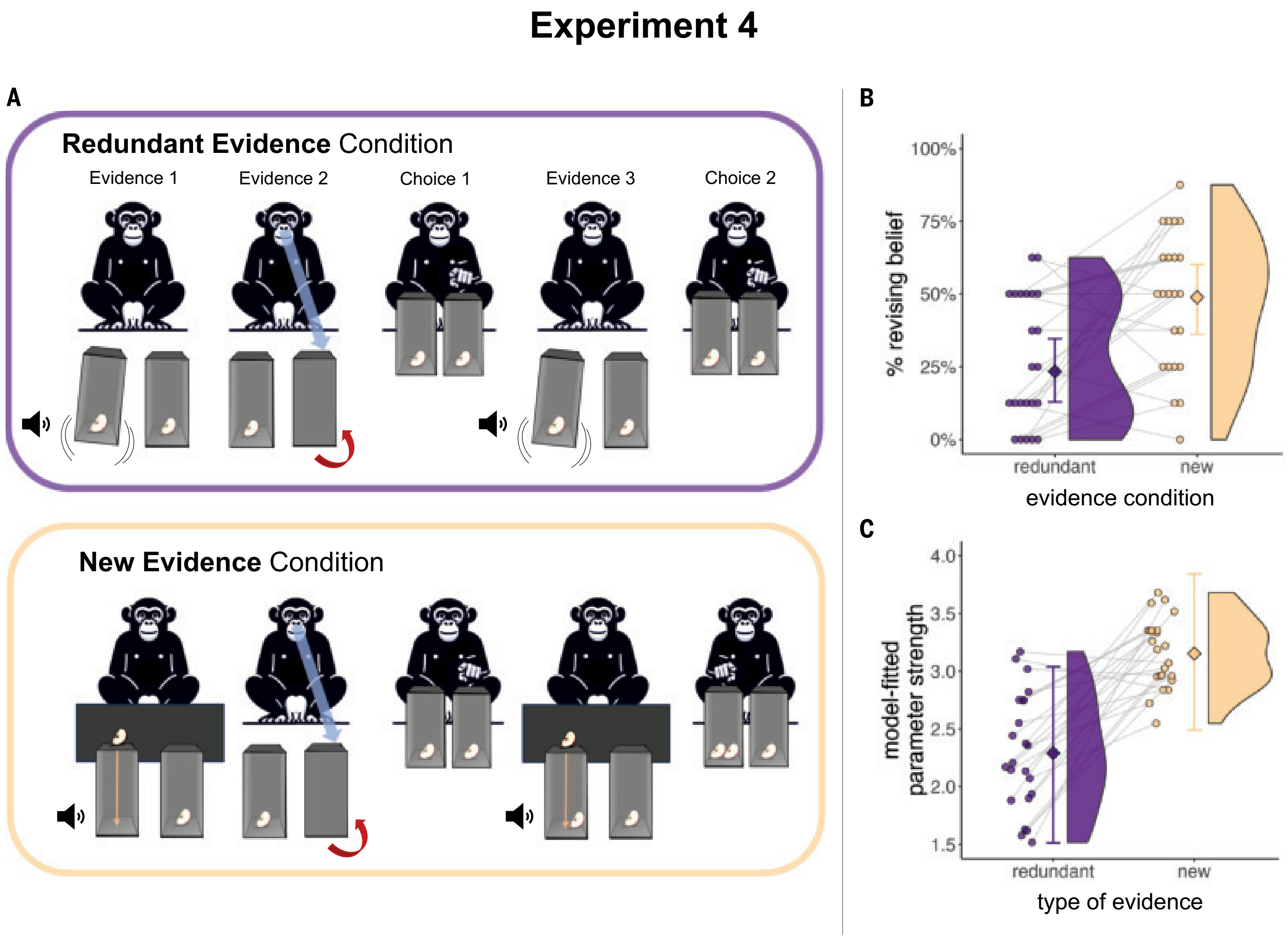

Fig. 4. Procedure and results of Experiment 4. Chimpanzees received weak evidence for one of the boxes, followed by strong evidence for the other box. They then made a first choice, after which they were presented with the same weak evidence again. The nature of the weak evidence varied according to condition. (**A**) In the redundant evidence condition, the weak evidence did not accumulate: The box was shaken a second time, providing no new information about its contents. In the new evidence condition, the weak evidence accumulated: The chimpanzees could infer on the basis of the second dropping noise that a second piece of apple had been dropped into the box. Notably, before presenting the second piece of evidence, the experimenter showed the chimpanzees a second piece of apple in both conditions. In the redundant evidence condition, the experimenter presented the apple and then placed it in their pocket. In the new evidence condition, the experimenter concealed the apple in their hands before dropping it into one of the boxes. (**B**) Chimpanzees were more likely to revise their beliefs when they heard a second piece of food drop into the box (new evidence condition) than when they heard the box shake for a second time (redundant evidence condition). (**C**) The rational choice model confirmed that for nearly every subject, the second piece of new evidence had a greater impact on their belief than the second piece of redundant evidence.

Across both conditions, chimpanzees were first presented with weak and strong (visual) evidence. Then, after they chose the option supported by the strong evidence, they were provided with a second instance of the weak evidence. Chimpanzees demonstrated a significantly higher tendency to revise their initial choice in the "new evidence" condition compared with the "redundant evidence" condition (χ^2 = 9.25, df = 1, p = 0.002; Fig. 4). Their tendency to revise beliefs decreased over trials ($\chi^2 = 5.06$, df = 1, $p = 0.024$), with a steeper decline in the "redundant evidence" condition ($\chi^2 = 5.59$, df = 1, $p = 0.018$; fig. S5 and SM). When presented on its own, the auditory dropping evidence presented in the "new evidence" condition was weaker than the auditory shaking evidence presented in the "redundant evidence" condition, showing that the strengths of these evidence types did not account for the difference in revision rate between conditions (see SM).

Furthermore, the rational choice model outperformed both the cue saliency and null models. A rational agent in this task would attribute a higher weight to the second instance of new evidence than the second instance of redundant evidence; the parameters for the rational choice model confirmed that this was the case (Fig. 5C and SM). These results confirm that chimpanzees can both remember the specific evidence used to form their beliefs and distinguish between new and redundant evidence when revising their beliefs.

In Experiment 5, we presented chimpanzees ($N = 22$) with second-order evidence (*33*, *34*): evidence that reduces the strength of the first-order evidence (so-called "undercutting defeaters"). This experiment consisted of two conditions: a "defeater" condition (in which first-order evidence was weakened) and a "non-defeater" condition (in which first-order evidence was not weakened). We ran both visual (Fig. 5) and auditory versions (fig. S6) of this task, using the strong evidence from Experiments 1 and 2, respectively. In the "visual defeater" condition, after chimpanzees had chosen the location supported by visual evidence (where they had seen the food), the experimenter pulled a glass

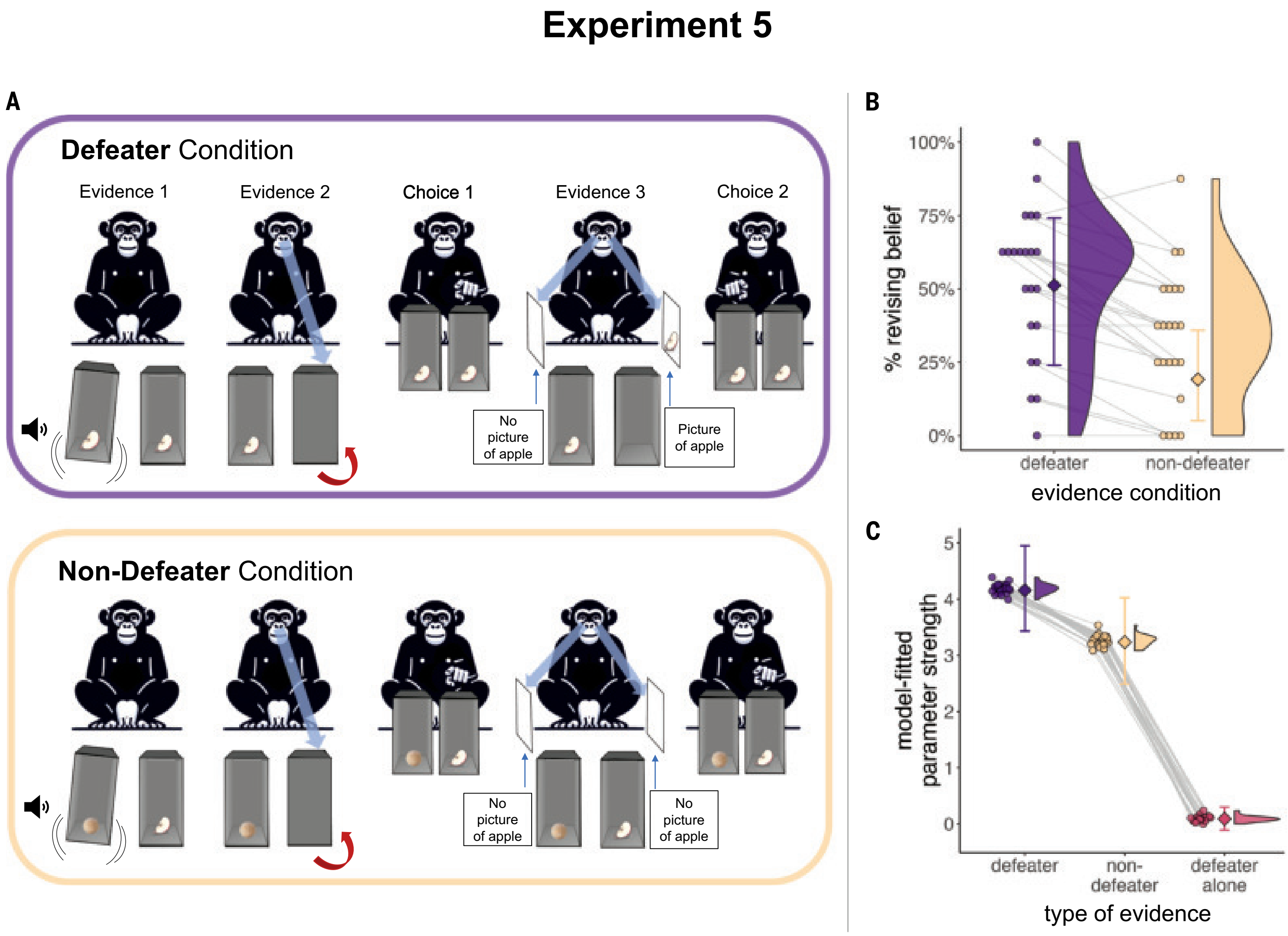

Fig. 5. Procedure and results of Experiment 5. (**A**) In the defeater condition, chimpanzees received weak evidence for one of the boxes, followed by strong evidence for the other box. They then made a first choice, after which they were presented with a defeater: second-order evidence that weakens the strength of the first-order evidence. The strong visual evidence was defeated when the experimenter revealed that the food they had previously seen inside the box was actually a picture on the box's window. In the non-defeater condition, the experimenter's actions were identical, but this time there was no picture on the window. (**B**) Chimpanzees were more likely to revise their belief in the defeater condition than in the non-defeater condition. The figure depicts the combined results of both the visual and auditory versions of the task (see SM for separate figures). (**C**) The rational choice model confirmed that the defeater affected the chimpanzees' beliefs more than the non-defeater, and that the defeater did not affect the chimpanzees' beliefs at all when it was presented alone (without first-order evidence). Note: For clarity, Fig. 5A only depicts the visual version of the task; for the auditory version, please refer to the SM and fig. S6.

window out of the box to reveal that it had a picture of an apple on it (figs. S6, S7, and SM). In the "visual non-defeater" condition, the experimenter also revealed the box's window, which was an empty pane of glass. In the "auditory defeater" condition, after chimpanzees had chosen the location supported by auditory evidence (where they had heard a sound inside the shaking box), the experimenter removed a stone from the box and showed it to the subject (fig. S7 and SM). In the "auditory non-defeater" condition, the experimenter removed a leaf from the box (which could not have caused the rattling sound). We asked whether chimpanzees would be more likely to switch to the box supported by weak evidence in the "defeater" condition, where the strong evidence had been weakened, compared with the "non-defeater" condition, where the strong evidence had not been weakened. The results confirmed this prediction: Chimpanzees were significantly more likely to switch in the "defeater" condition compared with the "non-defeater" condition ($\chi^2 = 16.27$, df = 1, $p < 0.001$). This effect held true in both the auditory (fig. S6d) and visual (fig. S6c) modalities; the interaction of task version and condition was not significant ($\chi^2 = 0.11$, df = 1, $p = 0.743$).

The rational choice model once again strongly outperformed both the cue saliency and null models on this task. Moreover, the best-fitting parameters for the rational choice model confirmed that subjects' beliefs were more affected by the defeater than the non-defeater. Notably, chimpanzees revised beliefs only when defeaters interacted with prior evidence, not when they were presented alone (Fig. 5C and SM).

Taken together, these findings suggest that chimpanzees appropriately respond to second-order evidence—evidence about evidence—which requires representing the evidential relation between evidence and belief.

Discussion

Chimpanzees' responses to counterevidence aligned with a Bayesian model of rational belief revision. They selectively maintained or revised their initial beliefs by evaluating the strength of the initial evidence relative to the strength of the counterevidence. In doing so, they demonstrated remarkable cognitive control and flexibility. Chimpanzees did not attribute a fixed value to each type of evidence; instead, they weighed the relative strength of evidence. For instance, auditory evidence was judged to be weaker than direct visual evidence in Experiment 1 and stronger than indirect visual evidence in Experiment 2. These responses were enabled by chimpanzees' capacity to represent (i) both possible hypotheses (Experiment 3) and (ii) the respective evidence in favor of them (Experiment 4). Chimpanzees also revised their beliefs in light of undercutting defeaters: second-order evidence that weakens the evidential connection between a piece of first-order evidence and a hypothesis (Experiment 5). Model comparisons demonstrate that these results are not explained in terms of nonrational processes such as belief perseveration, recency bias, or cue saliency. Instead, they suggest that chimpanzees engage in rational belief revision.

Selective belief revision is a metacognitively demanding and reflective cognitive process (*35*). Previous research has shown that chimpanzees appropriately respond to different types of direct and indirect evidence (*6*, *8*), but such evidence-based belief formation can occur in the absence of explicit reasoning about evidence and its bearing on different hypotheses. Indeed, it is often explained in terms of "unreflective evidence-responsiveness" (*33*). By contrast, the capacity to appropriately respond to counterevidence and, especially, to second-order evidence—evidence about the relevance of first-order evidence to one's belief—is thought to constitute a key standard of reflective engagement with evidence (*33*, *35*). It requires representing the three components of the so-called evidential relation: the evidence, the hypothesis, and their causal connection.

These results inform ongoing discussions about the metacognitive capacities of nonhuman animals. It has long been argued that linguistic representation is necessary for successful reflection on evidential relations (*36–39*). Yet recent empirical research on information search (*40*, *41*) and opt-out behaviors (*42–44*) has led theorists to attribute some metacognitive skills to primates (*45*). Despite this evidence, critics have maintained that behaviors such as searching for information and opting out are explainable in terms of cognition about the world and do not require metacognition—cognition about cognition (*46*).

Our findings present strong support for the view that chimpanzees have genuine metacognitive capacities. The particular form of metacognition demonstrated in the current experiments is "source monitoring": representing not only what one knows but also how one knows it (*47–50*). Evidence for this capacity comes from chimpanzees' responses to counterevidence, to new versus redundant evidence, and to second-order evidence. Reasoning about second-order evidence is, by definition, a form of metacognition. That chimpanzees represented second-order evidence as such is most strongly supported by the finding that the undercutting defeater in Experiment 5 affected chimpanzees' decisions only when it followed a piece of first-order evidence but not when presented on its own.

Accounts of major transitions in cognitive evolution identify key changes in the computational architecture of nervous systems that give rise to new cognitive capacities (*45*, *51*, *52*). The emergence of reflective processes—a system able to form representations of the cognitive processes themselves (*51*, *53*)—marks a key transition. The experiments presented here suggest that chimpanzees possess this capacity. Chimpanzees revise their beliefs selectively based on metacognitive awareness of the relation between evidence and hypothesis.

REFERENCES AND NOTES

1. J. Broome, *Rationality Through Reasoning* (Wiley Blackwell, 2013).
2. H. Kornblith, *Scientific Epistemology: An Introduction* (Oxford Univ. Press, 2021).
3. P. Gärdenfors, Ed., *Belief Revision* (Cambridge Univ. Press, ed. 1, 1992).
4. L. A. Heimbauer, R. L. Antworth, M. J. Owren, *Anim. Cogn.* **15**, 45–55 (2012).
5. O. Petit *et al.*, *Anim. Cogn.* **18**, 821–830 (2015).
6. R. Menzel, J. Fischer, Eds., *Animal Thinking: Contemporary Issues in Comparative Cognition*, Strüngmann Forum Reports (MIT Press, 2012).
7. V. Schmitt, J. Fischer, *J. Comp. Psychol.* **123**, 316–325 (2009).
8. C. J. Völter, J. Call, in *APA Handbook of Comparative Psychology: Perception, Learning, and Cognition*, J. Call, G. M. Burghardt, I. M. Pepperberg, C. T. Snowdon, T. Zentall, Eds. (American Psychological Association, 2017), pp. 643–671.
9. M. Tomasello, J. Call, *Primate Cognition* (Oxford Univ. Press, 1997).
10. B. L. Schwartz, M. J. Beran, Eds., *Primate Cognitive Studies* (Cambridge Univ. Press, 2022).
11. K. Andrews, *The Animal Mind: An Introduction to the Philosophy of Animal Cognition* (Routledge, ed. 2, 2020).
12. M. Bohn *et al.*, *Nat. Ecol. Evol.* **7**, 927–938 (2023).
13. C. J. Völter, J. Call, *J. Comp. Psychol.* **128**, 199–208 (2014).
14. Z. Civelek, C. J. Völter, A. M. Seed, *Proc. Biol. Sci.* **288**, 20211101 (2021).
15. D. Hanus, J. Call, *Curr. Biol.* **18**, R370–R372 (2008).
16. J. Call, *J. Comp. Psychol.* **118**, 232–241 (2004).
17. J. M. Engelmann *et al.*, *Child Dev.* **94**, 1102–1116 (2023).
18. K. Karg, M. Schmelz, J. Call, M. Tomasello, *J. Comp. Psychol.* **128**, 431–439 (2014).
19. C. O'Madagain *et al.*, *Proc. Biol. Sci.* **289**, 20212686 (2022).
20. G. Gardiner, *Episteme* **11**, 83–95 (2014).
21. B. Carpenter *et al.*, *J. Stat. Softw.* **76**, 1–32 (2017).
22. C. A. Anderson, *J. Exp. Soc. Psychol.* **19**, 93–108 (1983).
23. C. A. Anderson, K. L. Kellam, *Pers. Soc. Psychol. Bull.* **18**, 555–565 (1992).
24. S. Nestler, *Soc. Psychol.* **41**, 35–41 (2010).
25. F. Chiesi, C. Primi, Recency Effects in Primary-Age Children and College Students, *Int. Elect. J. Math. Ed.* **4**, 259–279 (2009).
26. D. Fudenberg, D. K. Levine, *Proc. Natl. Acad. Sci. U.S.A.* **111** (Suppl 3), 10826–10829 (2014).
27. J. N. Haney, J. L. Bruning, *Psychon. Sci.* **20**, 85–86 (1970).
28. A. M. Treisman, G. Gelade, *Cogn. Psychol.* **12**, 97–136 (1980).
29. M. J. Beran, *J. Comp. Psychol.* **115**, 181–191 (2001).
30. J. Call, *J. Comp. Psychol.* **114**, 136–147 (2000).
31. J. M. Engelmann *et al.*, *Curr. Biol.* **31**, R1377–R1378 (2021).
32. J. M. Engelmann *et al.*, *Biol. Lett.* **19**, 20230179 (2023).
33. G. Melis, S. Monsó, *Philos. Q.* **74**, 844–864 (2023).
34. H. Schleihauf, E. Herrmann, J. Fischer, J. M. Engelmann, *Child Dev.* **93**, 1072–1089 (2022).
35. D. Kuhn, *Educ. Psychol.* **57**, 73–86 (2022).
36. H. Mercier, D. Sperber, *Behav. Brain Sci.* **34**, 57–74 (2011).
37. C. M. Korsgaard, *Fellow Creatures: Our Obligations to the Other Animals*, *Uehiro Series in Practical Ethics* (Oxford Univ. Press, 2018).
38. R. Brandom, *Making It Explicit: Reasoning, Representing, and Discursive Commitment* (Harvard Univ. Press, ed. 4, 2001).
39. T. Burge, C. Peacocke, *Proc. Aristot. Soc.* **96**, 91–116 (1996).
40. J. Call, M. Carpenter, *Anim. Cogn.* **3**, 207–220 (2001).
41. A. G. Rosati, E. Felsche, M. F. Cole, R. Atencia, J. Rukundo, *Cognition* **251**, 105898 (2024).
42. J. D. Smith, J. J. Couchman, M. J. Beran, *J. Comp. Psychol.* **128**, 115–131 (2014).
43. R. R. Hampton, *Anim. Behav. Cogn.* **6**, 230–235 (2019).
44. R. R. Hampton, *Comp. Cogn. Behav. Rev.* **4**, 17–28 (2009).
45. M. Tomasello, *The Evolution of Agency: Behavioral Organization from Lizards to Humans* (MIT Press, 2022).
46. J. Perner, in *Foundations of Metacognition*, M. J. Beran, J. Brandl, J. Perner, J. Proust, Eds. (Oxford Univ. Press, 2012), pp. 94–116.
47. M. K. Johnson, S. Hashtroudi, D. S. Lindsay, *Psychol. Bull.* **114**, 3–28 (1993).
48. A. Gopnik, P. Graf, *Child Dev.* **59**, 1366–1371 (1988).
49. J. Nagel, *Episteme* **12**, 297–308 (2015).
50. L. Cosmides, J. Tooby, in *Metarepresentations*, D. Sperber, Ed. (Oxford Univ. Press, 2000), pp. 53–116.
51. A. B. Barron, M. Halina, C. Klein, *Proc. Biol. Sci.* **290**, 20230671 (2023).
52. P. Godfrey-Smith, *Complexity and the Function of Mind in Nature* (Cambridge Univ. Press, 1996).
53. P. Godfrey-Smith, in *The Philosophy of Daniel Dennett* (Oxford Univ. Press, 2018), pp. 224–253.
54. H. Schleihauf, E. Sanford, Chimpanzees rationally revise their beliefs, Dryad (2025); https://doi.org/10.5061/dryad.3bk3j9kz9.

ACKNOWLEDGMENTS

We thank T. Mukungu, I. Ampeire, P. Sekulya, A. Okello, B. Apamaku, D.y Basemera, H. Aligumisiriza, I. Ayebazibwe, and all the staff at Ngamba Island Chimpanzee Sanctuary. Thanks also go to M. Goddu, A.-C. Schneider, S. Thomaes, and M. Tomasello, who provided helpful feedback on the manuscript. **Funding:** J.M.E. and E.M.S. were supported by a grant from the Leakey Foundation, and H.S. was supported by an Audacity Grant from the Leibniz ScienceCampus Primate Cognition. **Author contributions:** Conceptualization: H.S., J.C., E.H., J.M.E., S.Z., E.M.S.; Investigation: H.S., J.M.E., E.H.; Methodology: H.S., E.M.S., B.D.T., J.C., E.H., J.M.E., S.Z.; Project administration: J.R., E.H., J.M.E.; Resources: J.R., H.S., J.M.E.; Visualization: H.S., E.M.S.; Writing – original draft: J.M.E., H.S., E.M.S.; Writing – review & editing: H.S., E.M.S., B.D.T., J.C., E.H., S.Z., J.M.E. **Competing interests:** The authors declare that they have no competing interests. **Data and materials availability:** All data and code used in the analyses are available on Dryad (*54*).

SUPPLEMENTARY MATERIALS

science.org/doi/10.1126/science.adq5229
Participant Information; Materials and Methods; Supplementary Text; Figs. S1 to S10; References (*55–66*); Tables S1 to S20; Movie S1 to S5; MDAR Reproducibility Checklist

Submitted 17 May 2024; resubmitted 22 November 2024; accepted 13 August 2025

10.1126/science.adq5229

EVOLUTION

Genomic architecture of egg mimicry and its consequences for speciation in parasitic cuckoos

Justin Merondun[1,2,3], Frode Fossøy[4], Swetlana Meshcheryagina[5], Phil Atkinson[6], Gennadiy Bachurin[7], Victor Bulyuk[8]†, Viktar Fenchuk[9], Mikhail Golovatin[5], Chris Hewson[6], Marcel Honza[10], Mikhail Markovets[8], Csaba Moskát[11], Gregory L. Owens[3], Petr Procházka[10], Yaroslav Red'kin[12,13], Jarkko Rutila[14], Michal Šulc[10], Kasper Thorup[15], Bård G. Stokke[16], Wei Liang[17], Jochen B. W. Wolf[1,2]*

Host-parasite arms races facilitate rapid evolution and can fuel speciation. *Cuculus* cuckoos are deceptive egg mimics that exhibit a broad diversity of counterfeit egg phenotypes, representing host-adapted subpopulations (gentes). Genome analysis of 298 common (*Cuculus canorus*) and 50 oriental cuckoos (*Cuculus optatus*) spanning 15 egg morphs revealed that eggshell background coloration is predominantly influenced by matrilineal genetic variation. Recurrent mitochondrial mutations and an ancient W chromosome–linked translocation of an autosomal assembly factor for respiratory complex I provide a tentative link between mitochondrial function and pigment synthesis through the heme pathway. Biparentally inherited loci contribute to phenotypic variation in both species, mainly for maculation. The evolutionary tug-of-war over a sex-limited, mimetic trait integrates autosomal components with the nonrecombining, matrilineal genome without catalyzing genome-wide divergence between gentes.

The common cuckoo (*Cuculus canorus*) is a textbook example of an obligate brood parasite that has fascinated naturalists since the birth of zoology (*1*, *2*). It exploits more than 100 host species (*3*, *4*) and displays large variation in mimetic egg phenotypes. It has been suggested that host-matched phenotypes evolved in subpopulations specialized in parasitizing a particular host species while maintaining evolutionary independence (host races or gentes) (*5*, *6*). Gens diversification is believed to be fueled by concurrent coevolutionary arms races between cuckoos and their passerine hosts, many of which are capable of rejecting parasitic eggs that are dissimilar from their own (*3*, *7*). Yet for the parasite, the expected evolutionary outcome strongly depends on the genetic architecture and inheritance of the traits involved (*8*, *9*).

Host switches can lead to reproductive isolation and promote speciation if the mimetic trait encompasses both sexes and is encoded on the autosomal genome and if mating is assortative by host (*10*, *11*). This is exemplified in indigobirds, whydahs, and bronze cuckoos, where host mimicry involves nestling traits expressed by both sexes (*12*, *13*). In combination with host-specific assortative mating mediated by imprinting [e.g., on host song (*14*)], coevolution has facilitated rapid diversification of parasitic lineages (*13*, *15*). Alternatively, female-limited parasitic traits, if encoded on the matrilineal component of the genome (mtDNA, W chromosome), can be stably inherited from mothers to daughters irrespective of assortative mating (*6*, *16*). Such a genetic architecture is less conducive to speciation (*8*) and has been suggested for honeyguides (*17*), cuckoo finches (*18*), and in small-scale genetic studies for common cuckoos (*3*, *19*–*22*).

Here, we revisit the two competing hypotheses governing diversification of host races in two brood parasitic *Cuculus* species: the common cuckoo (*C. canorus*; *canorus* hereafter) and the closely related oriental cuckoo (*C. optatus*; *optatus* hereafter) (*23*). We assess in both species whether host races, operationally defined by egg phenotype, are predicated on matrilineal variation (*3*, *19*–*22*) or whether biparental inheritance contributes to egg diversity (*24*, *25*).

Geographic structure of genetic variation

We characterized both matrilineal (mtDNA, W chromosome) and coinherited (autosomes, Z chromosome) genetic variation across the distributional range of 202 unrelated *canorus* and 50 *optatus* representing a total of 25 host species (21 *canorus*, 4 *optatus*) and 15 egg morphs (11 *canorus*, 4 *optatus*) (fig. S1 and table S1). Matrilineal phylogenies indicate seven primary haplogroups in *canorus* ($M_{CC}1$ to $M_{CC}7$) and four in *optatus* ($M_{CO}1$ to $M_{CO}4$) (Fig. 1A and fig. S2). An ancient split 1.4 million to 2.9 million years ago, exceeding *optatus* species boundaries [<1 million years (*23*)], separates east Asian *canorus* from European *canorus* (minimum and maximum 95% highest posterior density; figs. S3 to S5). An exception to this East-West geographic divide is the *canorus* lineage of blue egg–laying cuckoos in Finland ($M_{CC}1$) clustering with haplogroups $M_{CC}2$ and $M_{CC}3$ predominantly found in East Asia (*19*). Among the remaining four haplogroups ($M_{CC}4$ to $M_{CC}7$) of the *canorus* lineage, $M_{CC}4$ is closely related to *optatus* lineages $M_{CO}1$ and $M_{CO}2$. These haplogroups correspond exclusively to females of the rufous plumage morph, which, similar to egg phenotypic variation, appears to be subject to balancing selection (*23*) (Fig. 1A and figs. S2 and S3). In *canorus*, haplogroups are broadly spread across the species range, except for East Asian $M_{CC}3$ and the blue egg–associated $M_{CC}1$ of Finnish *canorus* (Fig. 1C). In *optatus*, $M_{CO}1$ is maintained across the distributional range, whereas the other haplogroups are geographically restricted (Fig. 1D and fig. S6).

Autosomal population structure in *canorus* comprises five major genetic clusters [$A_{CC}1$ to $A_{CC}5$, maximum fixation index (F_{ST}) = 0.085], each aligning with broad geographic areas across Eurasia (Fig. 1B and figs. S7 and S8). At finer resolution among 14 geographically defined groups (geographic clusters $G_{CC}1$ to $G_{CC}14$; fig. S9), significant isolation by distance is evident (Spearman's $\rho = 0.92$, $p = 2.4 \times 10^{-18}$). By contrast, matrilineal variation shows much weaker isolation by distance (W chromosome $\rho = 0.33$, $p = 0.04$) (Fig. 1, C and E, and fig. S10), counter to expectations from reduced effective population size but consistent with female-biased dispersal (*26*, *27*). These results highlight an association primarily between geographic location and biparental autosomal variation (Fig. 1E). Meanwhile, deeply divergent haplogroups are widely dispersed across the *canorus* range, offering an opportunity for host-specific selection to exploit segregating matrilineal variation (Fig. 1C and fig. S11). This pattern is reversed within *optatus*, where autosomal variation is less associated

---

[1]Department of Evolutionary Biology, LMU Munich, Planegg-Martinsried, Germany. [2]Department of Microevolution and Biodiversity, Max Planck Institute for Biological Intelligence, Seewiesen, Germany. [3]Department of Biology, University of Victoria, Victoria, BC, Canada. [4]Centre for Biodiversity Genetics, Norwegian Institute for Nature Research, Trondheim, Norway. [5]Institute of Plant and Animal Ecology, Ural Branch, Russian Academy of Sciences, Yekaterinburg, Russia. [6]British Trust for Ornithology, Thetford, UK. [7]Scientific and Practical Center of Biodiversity, Irbit, Russia. [8]Rybachy Biological Station, Zoological Institute, Russian Academy of Sciences, Rybachy, Russia. [9]The Frankfurt Zoological Society, Frankfurt, Germany. [10]Institute of Vertebrate Biology, Czech Academy of Sciences, Brno, Czech Republic. [11]Hungarian Natural History Museum, Budapest, Hungary. [12]Zoological Museum, Moscow State University, Moscow, Russia. [13]Institute of Biological Problems of the Cryolithozone, Siberian Branch, Russian Academy of Sciences, Yakutsk, Russia. [14]Department of Environmental and Biological Sciences, University of Eastern Finland, Joensuu, Finland. [15]Center for Macroecology, Evolution and Climate, Globe Institute, University of Copenhagen, Copenhagen, Denmark. [16]Department of Terrestrial Ecology, Norwegian Institute for Nature Research, Trondheim, Norway. [17]Ministry of Education Key Laboratory for Ecology of Tropical Islands, Hainan Normal University, Haikou, People's Republic of China. ***Corresponding author. Email: j.wolf@bio.lmu.de** †Deceased

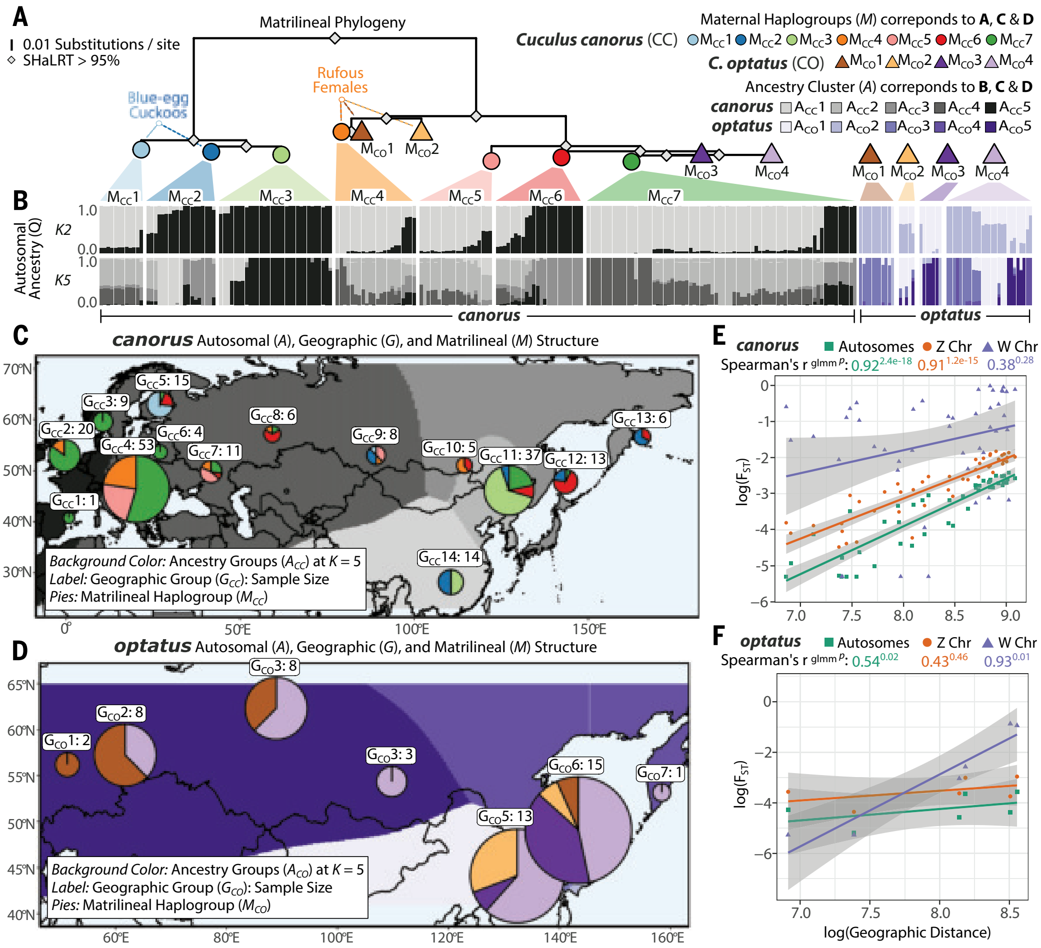

Fig. 1. Genetic structure across the geographic range of *C. canorus* and *C. optatus*. (**A**) Matrilineal phylogeny of the W chromosome ($N = 51{,}605$ SNPs) with truncated branches identifying seven *canorus* (CC) maternal haplogroups ($M_{CC}1$ to $M_{CC}7$) and four *optatus* (CO) haplogroups ($M_{CO}1$ to $M_{CO}4$). Diamonds indicate nodes with Shimodaira-Hasegawa approximate likelihood ratio test (SHaLRT) support >95%. (**B**) Ancestry analysis ($n = 202$ *canorus*, 50 *optatus*) inferred from unlinked autosomal SNPs ($N = 1{,}546{,}013$ *canorus*, 920,854 *optatus*), arranged by maternal haplogroup. (**C**) Spatial structuring of *canorus*. Background color (grayscale; fig. S6) indicates the spatial distribution of autosomal ancestry ($A_{CC}1$ to $A_{CC}5$) inferred using ADMIXTURE at (K) = 5. Pie charts indicate maternal haplogroups, with size corresponding to sample size. Samples are clustered into 14 geographic groups ($G_{CC}1$ to $G_{CC}14$) by k-means on latitude and longitude; group labels and sizes are shown above the pie charts. Please see supplementary materials for alternative symbology (figs. S8 and S11). (**D**) Spatial structuring of *opatus*. (**E**) Correlations between geographic distance (km) and genetic distance in *canorus*, summarized from autosomal (F_{ST}) or matrilineal (Φ_{ST}) variation across pairwise comparisons between geographic groups. Spearman's rank correlation (r_S) and generalized linear mixed model (glmm) Bonferroni-adjusted p (shown in superscript) for each genomic compartment are indicated above, with shading indicating 95% confidence intervals. (**F**) Correlations for *optatus*.

with geographic distance (Spearman's $\rho = 0.54$, $p = 1.0$) than matrilineal variation (W chromosome $\rho = 0.93$, $p = 0.03$) (Fig. 1, D and F, and fig. S10).

Genomic correlates of egg diversity

Next, limiting the dataset to females with known maternal egg phenotype (E_{CC}: $n = 60$ *canorus*; E_{CO}: $n = 27$ *optatus*), we assessed whether *canorus* and *optatus* egg diversification follows strict matrilineal inheritance (*5*, *19*, *21*, *28*) (M_{CC}, M_{CO}) or is better explained by autosomal contributions (*24*, *25*) (A_{CC}, A_{CO}) or geographic location reflecting local host availability (G_{CC}, G_{CO}) (Fig. 2, A and B, and fig. S12). We replicated the following analyses with an expanded dataset that included males ($n = 86$ *canorus*, 50 *optatus*), which yielded qualitatively identical patterns despite restricting the matrilineal component to mitochondria (figs. S13 and S14).

Within *optatus*, where egg phenotype variation is limited to differences in maculation on shared eggshell coloration and egg size (*29*), geographic location is the primary predictor (distance-based redundancy analysis pseudo-adjusted $R^2 = 0.78$), with weaker associations for matrilineal structure ($R^2 = 0.04$) and autosomal variation ($R^2 = 0.02$) (Fig. 2C). This finding is supported by classical machine learning, as adding a matrilineal component to geographic and autosomal predictors did not improve model predictions (Fig. 2F and fig. S13). By contrast, variation in *canorus* egg morphs, differing in both eggshell coloration and maculation, are most strongly associated with matrilineal variation (distance-based redundancy analysis pseudo-adjusted $R^2 = 0.26$), followed by geographic location ($R^2 = 0.16$) and autosomal ancestry ($R^2 = 0.02$) (Fig. 2, A and C, and fig. S14). Matrilineal inheritance is further supported by kinship analyses of 107 related *canorus* individuals: Phenotype concordance is complete among maternal relatives (100% across all kinship levels), whereas paternal relatives, particularly diagnostic cousins, show significantly less concordance (75.8%; $n = 50/66$ matches; Fisher's exact test $p = 0.01$) (Fig. 2D and fig. S15). Machine learning results reinforce the primacy of matrilineal inheritance, as adding haplogroup information substantially improves classification of *canorus* egg morphs (Fig. 2E). The effect persisted, though diminished,

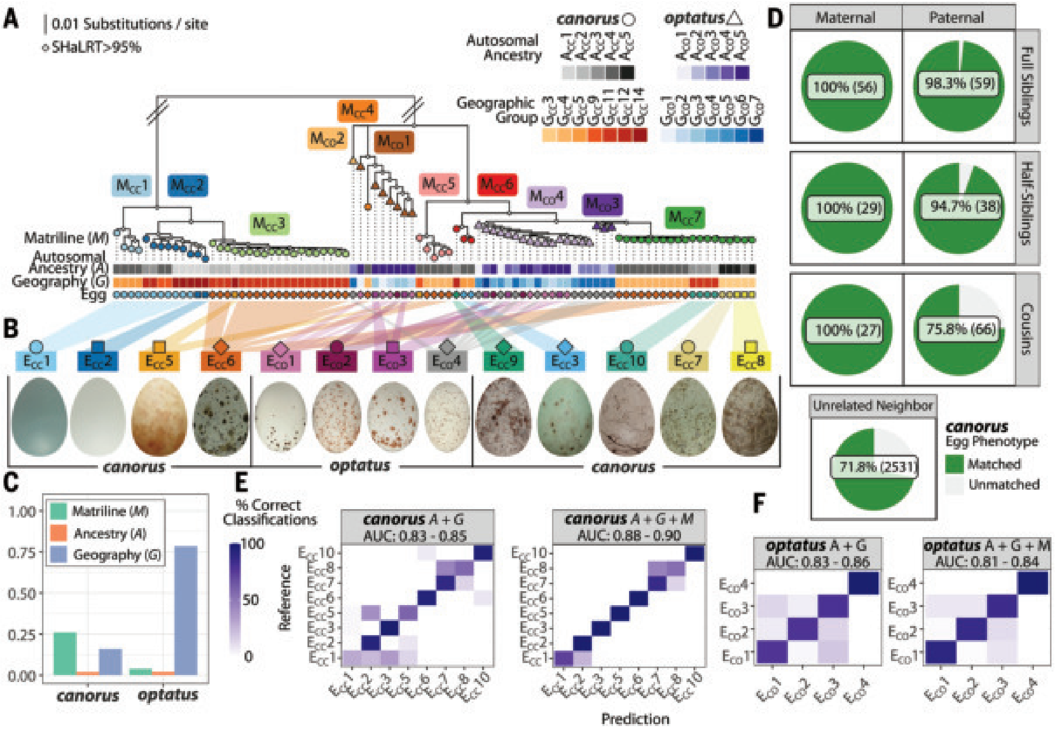

Fig. 2. Matrilineal variation is associated with egg diversification in *C. canorus*. (**A**) Matrilineal W chromosome phylogeny ($n = 60$ *canorus*, 27 *optatus*), with corresponding autosomal groups (*A*), geographic groups (*G*), and egg morphs indicated below each tip, each representing an unrelated female with known egg morph. Diamonds indicate node support exceeding 95% (SHaLRT). (**B**) Phenotypic variation within *canorus* (E_{CC}) and *optatus* (E_{CO}) egg morphs. (**C**) Variation explained (pseudo-R^2) by continuous pairwise distance matrices of matrilineal, geographic, or autosomal variation estimated with a distance-based redundancy analysis (compare figs. S13 and S14 for replicated analyses with mtDNA variation). (**D**) Egg phenotype matching among varying degrees of related *canorus*. (**E**) Egg morph predicted with machine learning using either autosomal ancestry cluster (*A*) and geographic group (*G*) alone (left) or with the addition of haplogroup (*M*) (right). Confusion matrix of predictive modeling shows the proportion of correct classifications across 100 bootstrapped replicates. The area under the curve (AUC) 95% confidence interval across replicates is indicated below each label. (**F**) Confusion matrix for *optatus*.

when divergent $M_{CC}1$, $M_{CC}2$, and $M_{CC}3$ haplogroups, including the immaculate blue egg ($E_{CC}1$) morph (*19*), were excluded (fig. S14G). However, subtle differences among most brownish egg morphs ($E_{CC}6$, $E_{CC}7$, $E_{CC}8$), which are largely associated with common *Acrocephalus* hosts, remain poorly resolved by any model (Fig. 2, B and E, and figs. S1 and S13). Stochastic character mapping of egg state on maternal and biparental phylogenies provided additional detail. By leveraging mitoautosomal discordance, it corroborated strong matrilineal association for both blue egg types $E_{CC}1$ and $E_{CC}3$ (figs. S16 to S18). Although $E_{CC}1$ has previously been linked to a deeply divergent mitochondrial lineage associated with blue eggs [see (*19*)], greater parsimony of egg-state transitions on the mitochondrial tree for $E_{CC}3$ suggests matrilineal association for a second, distinct blue-green egg phenotype (associated with brambling hosts; Fig. 2E and figs. S16 and S17).

Overall, these findings provide evidence for a matrilineal contribution of egg diversification in *canorus*, likely associated with changes in eggshell coloration evolving from a brownish, $E_{CC}6$-like ancestor (figs. S16 and S17), a widespread morph that allows exploitation of broadly distributed *Acrocephalus* hosts across the species range (*28*, *30–32*). Male mate choice appears largely opportunistic and shaped by local host availability (*3*, *5*, *25*, *28*, *33*, *34*), preventing stable genome-wide autosomal transmission through the patriline (*8*, *10*) (Fig. 2, C and E). Egg patterning, which distinguishes many of the nonancient haplogroup morphs within *canorus* and accounts for basically all variation in *optatus* samples, also covaries with geographic structure, enabling adaptation to locally abundant and stable hosts through biparentally inherited genetic variation.

Genetic basis of egg phenotype

Next, we sought to identify candidate genes associated with egg phenotype. Under the assumption that genomic regions with elevated genetic differentiation may flag genetic variation related to egg morph (*35*), we performed an all-versus-one F_{ST} scan with resampling [bootstrapped F_{ST} (bF_{ST}) in 10-kb windows, 100- base pairs for mtDNA]. Consistent with the genome-wide analysis described earlier in the text, matrilineal elements (W chromosome, mtDNA) are enriched for the blue $E_{CC}1$ morph, with W-linked enrichment relative to other egg morphs being more than twofold the permuted expectation (observed/permuted = 2.1, $p < 0.01$) (Fig. 3A and table S2). Conversely, significantly more autosomal outliers than expected were observed for $E_{CC}10$ (enrichment = 1.9; $p < 0.01$). By contrast, *optatus* egg morphs show significant enrichment only on autosomes and the Z chromosome (Fig. 3A).

Genes in close proximity to the main outlier regions include credible functional candidates that influence the two main components of egg phenotype variation: eggshell coloration and maculation. Eggshell color variation, which is more similar between closely related females (*36*), results from the mixing of two heme-derived pigments: protoporphyrin IX (reddish-brown) and biliverdin (blue-green) (*37*). Maculation forms as the egg passes through the uterus and is shaped by the distribution of pigment glands, timing of pigment release, and mode of egg rotation (*37*, *38*).

Of the biparentally inherited genes associated with differences in maculation, several relate to female reproductive function (table S3). In *canorus*, the top differentiated peak for $E_{CC}10$ lies close to *RLN3*, which is involved in pituitary and oviduct signaling in birds (*39*). In

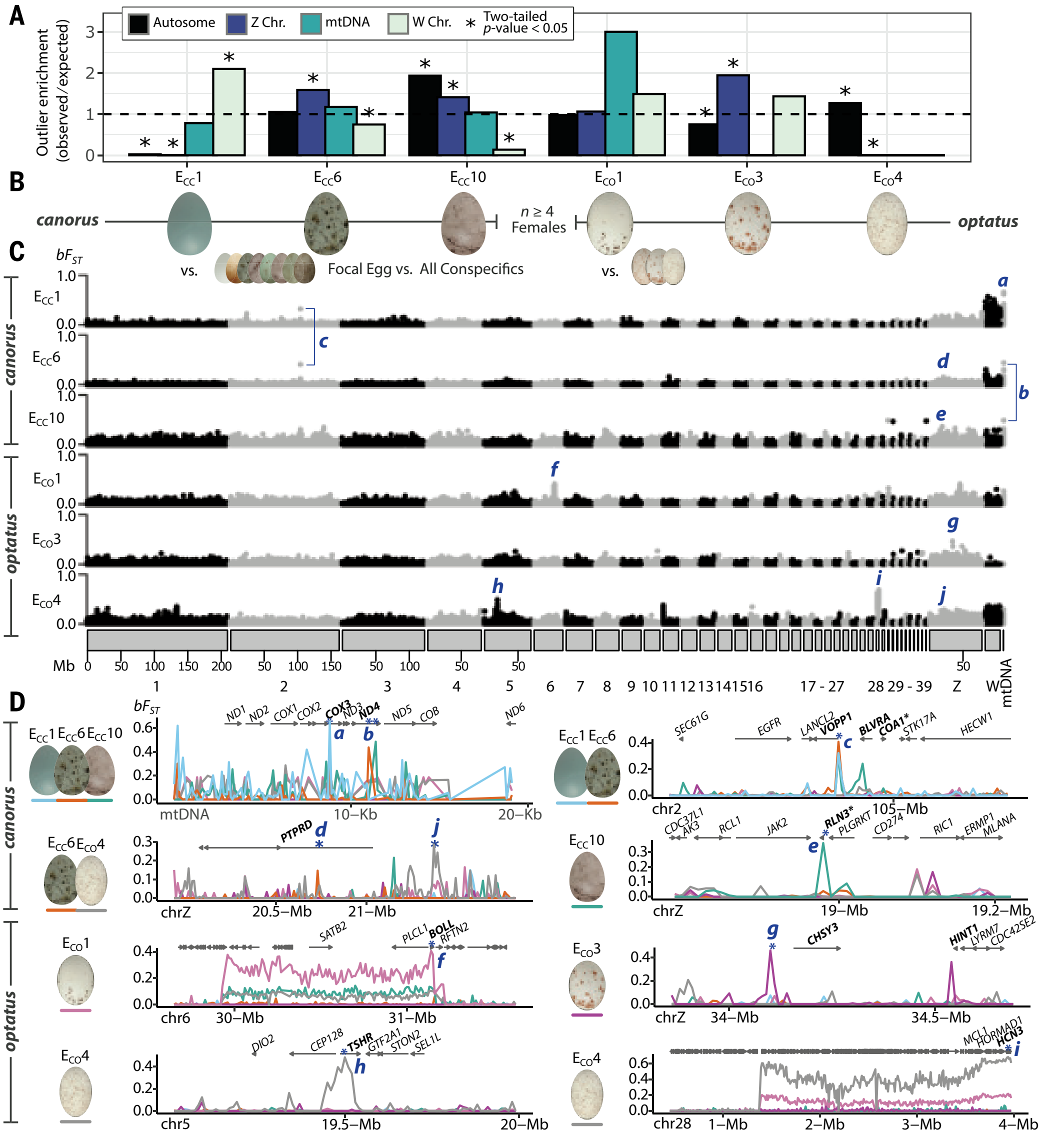

Fig. 3. Genetic basis of egg phenotype. (**A**) Permutation enrichment of bF_{ST} outliers per egg across chromosome class conducted separately for species. For joint analysis across species, see fig. S26 (Note: bF_{ST} is used throughout figure.) (**B**) Pairwise one-versus-all bF_{ST} comparisons, separated by species (*canorus* and *optatus*). (**C**) Genome-wide bF_{ST} in 10-kb windows, with the highest outlier windows indicated with blue letters. (**D**) bF_{ST} peak regions and nearby candidate genes (bold face), with the highest F_{ST} peak indicated with an asterisk. Line colors correspond to different egg morphs, with the primary candidate morph to the left of each plot. Black asterisks indicate unnamed genes with homology inferred from National Center for Biotechnology Information (NCBI) annotations (e.g., LOC104063035 = "relaxin-3"; LOC104065962 = "*COA1*-like"). The blue letters indicate the same outlier windows as in (C).

optatus, key outliers are linked to *BOLL* and *CHSY3* [involved in germ cell development (*40*, *41*)], *HINT1* [linked to embryogenesis and sex hormones (*42*)], and *TSHR* and *HCN3* [involved in hormone signaling and eggshell traits (*43*, *44*)] (table S3). Two regions show recombination suppression, potentially preserving trait combinations (fig. S19). *PTPRD*, linked to eggshell color in domestic chickens (*45*), is differentiated in both E$_{CC}$6 (*canorus*) and E$_{CO}$4 (*optatus*) within ~500 kb of the same locus (Fig. 3D). Secondary peaks across egg morphs also implicate genes in female reproductive development (fig. S20).

In *canorus*, biparentally inherited genes linked to eggshell coloration are either directly involved in the heme biosynthetic pathway or in mitochondrial homeostasis, which regulates this process through metabolic signaling and shared biosynthetic resources (*46*–*48*). Together with studies implicating oxidative stress in female avian reproduction (*49*, *50*), this suggests a tentative, mechanistic link of mitochondrial function and eggshell coloration, which is also observed in chickens (*51*). Consistent with this hypothesis, candidate regions for E$_{CC}$1 and E$_{CC}$6 lie within 170 kb of *BLVRA*, a key gene in heme catabolism that reduces oxidative stress by converting biliverdin to bilirubin (*52*), as well as *VOPP1* and *COA1*, which are both likewise linked to mitochondrial function (*53*, *54*) (Fig. 3, C and D). Analyses replicated using a relaxed threshold requiring three female nestlings for focal contrasts corroborated the association of *BLVRA* and *RLN3* and, for E$_{CC}$8, additionally implicated an autosomal gene involved in mitochondrial fission and associated with egg laying in chickens (*55*) (fig. S21 and table S3).

Isolating the matrilineal mutations for eggshell coloration is challenging owing to the large number of substitutions that have accumulated along long branches and the complete linkage of mitochondrial and W chromosome haplotypes. To identify candidate mutations, we

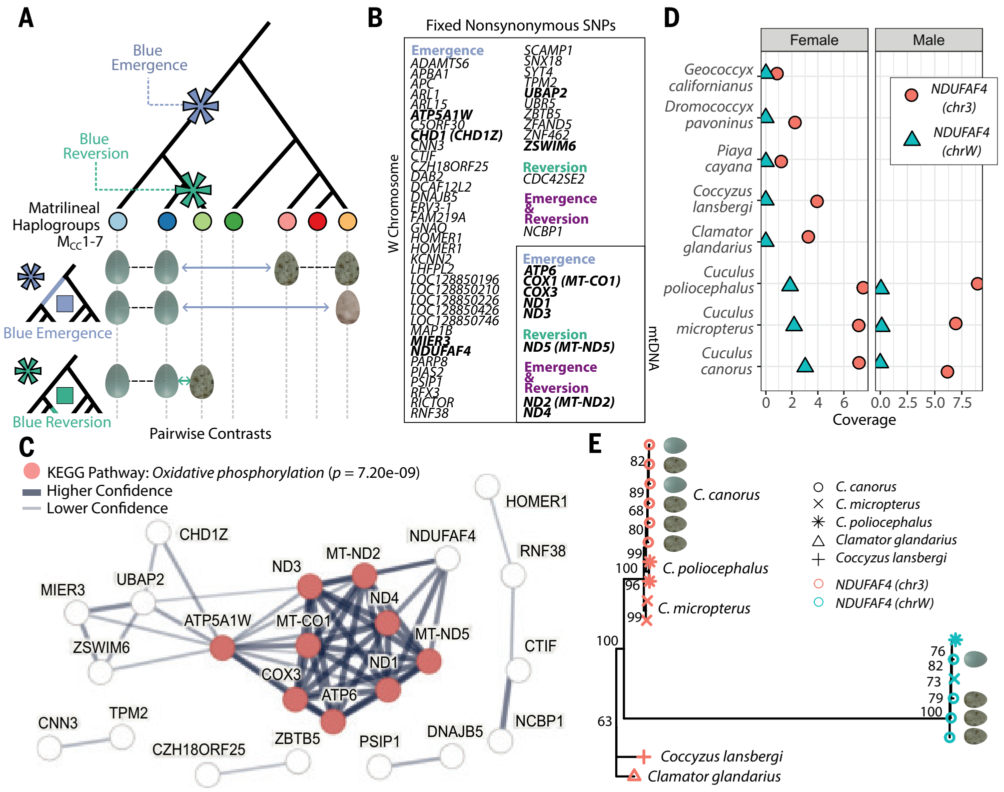

Fig. 4. *C. canorus* blue egg background predominantly maps to oxidative phosphorylation genes. (**A**) Schematic (top) depicting the evolutionary emergence and subsequent diversification of *canorus* egg morphs, with pivotal phenotypic shifts indicated by asterisks. Fixed differences in pairwise comparisons of haplogroups associated with same versus different egg types flag candidate mutations that contribute to phenotypic divergence. Investigated scenarios include the origin of the immaculate blue egg phenotype (blue emergence) and its subsequent reversal (blue reversion). Illustrative schematics (bottom) denote specific branches and mutations within the phylogeny where these evolutionary events are hypothesized to occur, along with the pairwise egg contrasts used to identify them. (**B**) Candidate genes containing a fixed nonsynonymous SNP for each contrast across the W chromosome and mtDNA. Genes in bold are shown in the Kyoto Encyclopedia of Genes and Genomes (KEGG) pathway in (C). (**C**) Gene network associations among candidate genes. Note that all nonmitochondrial genes are found on the W chromosome (table S6). (**D**) Resequencing coverage of the autosomal and W chromosome paralog of *NDUFAF4* across Cuculiformes. (**E**) Maximum-likelihood phylogenetic tree of the *NDUFAF4* paralogs, with bootstrap support indicated at each node.

screened for fixed differences between pairs of matrilines associated with an egg type ("matriline association mapping," e.g., $M_{CC}1$:$E_{CC}1$ versus $M_{CC}7$:$E_{CC}6$) (Fig. 4A). We focused on the immaculate blue egg morph ($E_{CC}1$), which occurs across two maternal haplogroups ($M_{CC}1$ and $M_{CC}2$), persists thousands of kilometers apart, and yet remains at high frequencies in the respective populations, putatively owing to highly discriminatory hosts (Fig. 1C) (*3*, *56*). Based on our matrilineal phylogenetic reconstruction, mutations along a long, ancient branch conferred the immaculate blue egg (blue emergence), followed by a reversion within this lineage to other eggshell colors in East Asia (blue reversion) (Fig. 4A). The remaining nonblue haplogroups (e.g., $M_{CC}4$ to $M_{CC}7$) diversified into other egg morphs but never to immaculate blue, based on present sampling and knowledge (Figs. 1A and 2A).

Consistent with the broad-stroke outlier analyses (Fig. 3), fixed single-nucleotide polymorphisms (SNPs) are predominantly observed in the matrilineal genome across both evolutionary scenarios. This is particularly pronounced for the origin of the blue egg (blue emergence), where 55% (n = 123/225) of mtDNA and 75% (n = 33,597/44,739) of W chromosomal SNPs are fixed, which is in stark contrast to none on the autosomes or Z chromosome (table S4). This pattern is reiterated for the reverted $E_{CC}6$ egg contrast (blue reversion) with 12% (n = 9/73) fixed SNPs in mtDNA, 5% (n = 413/8,490) in the W chromosome, and none on the autosomes or Z chromosome. Mitochondrial genes *ND2* and *ND4* harbor nonsynonymous SNPs linked to both emergence and reversion of blue eggshell coloration (Fig. 4B), a pattern corroborated with de novo mitochondrial assemblies that further implicates *COX1* and *ND5* (figs. S22 and S23). Together with biparentally inherited genes associated with mitochondrial homeostasis (Fig. 3D), these fixed nonsynonymous mutations could be implicated in mitochondrial regulation for eggshell coloration.

Although a mitochondrial shift in egg phenotype mediated by the heme pathway is mechanistically plausible, several W-linked genes containing a fixed nonsynonymous SNP also interact with the statistically enriched oxidative phosphorylation pathway ($p = 7.20 \times 10^{-9}$) (Fig. 4C and table S5). Among them, an *NDUFAF4*-like gene, a homolog of *NDUFAF4* acting in the respiratory complex I assembly, represents a candidate for further functional investigation (LOC128850245 in RefSeq Assembly GCF_017976375.1; table S6). It has a copy on the W chromosome (28 kb; mean female coverage = 6.4×, male coverage = 0.13×) in addition to an ancestral autosomal copy on chromosome 3 (4.0 kb; female coverage = 11×, male = 11×), which exhibits no autosomal differentiation among *canorus* egg morphs (Fig. 4D and fig. S24). Phylogenetic analysis across the Cuculiformes order suggests that the W paralog was acquired at the onset of the brood parasitic genus *Cuculus* (Fig. 4E and table S6). The W-linked copy contains the same number of exons and has full open reading frames (fig. S25) yet is substantially diverged from its autosomal paralog since insertion in the *Cuculus* ancestor (Fig. 4E). Although mitonuclear cross-talk has broad biological implications (*57*), our results suggest the possibility that polygenic autosomal–mitochondrial–W chromosome interactions contribute to egg background color diversification. Other avian species have co-opted autosomal genes to produce immaculate blue eggs, including SNPs upstream of efflux transporter *ABCG2* in ducks (*58*), an endogenous retroviral insertion upstream of anion transporter *SLCO1B3* in chickens (*59*), and a recessive gene in quail (*60*), illustrating the multiple mutational pathways that underlie egg diversification in birds.

Conclusions

In *canorus*, phenotypic variation in egg traits, especially eggshell coloration, appears primarily mediated by matrilineally inherited genes, as suggested nearly a century ago (*6*). This remains surprising, as exclusive matrilineal inheritance poses great challenges: Reduced effective population size limits the efficacy of selection, and beneficial mutations compete among matrilines rather than recombining into advantageous trait combinations. Thus, barring new mutations, we would not expect, for example, a female with rufous plumage (associated with haplogroup $M_{CC}4$) to lay immaculate blue eggs (associated with $M_{CC}1$ and $M_{CC}2$), supporting earlier speculations by Kunz that plumage coloration is linked to host choice and egg coloration (*61*). Additionally, the limited mutational target on mtDNA and the W chromosome may require recruitment of autosomal genes, as suggested here for the translocation of *NDUFAF4*. Despite these constraints, female-biased gene flow involving multiple matrilines maintained by balancing selection (*23*) appears to provide sufficient adaptive variation for exploiting multiple host species.

Biparental genetic contributions and local geographic structure also seem to contribute to phenotypic diversity. In *canorus*, co-option of nuclear genes with mitochondrial-related functions suggests that interactions between matrilineal and autosomal variation may contribute to eggshell coloration. By contrast, in *optatus*, variation is limited to maculation with exclusive contribution of autosomal genes. Such polygenic adaptation—which is also observed in egg phenotype variation of the village weaver (*Ploceus cucullatus*), a host species of Diederik cuckoo that exhibits extensive intra- and interclutch diversity as a defense against parasitism (*62*)—may develop in *canorus* over prolonged coexistence with abundant, accessible host species, such as *Acrocephalus* warblers (*28*, *30*–*32*). Although selective pressures differ for hosts and parasites, the involvement of many unlinked autosomal loci in both systems may reflect convergent selection on egg phenotype diversity.

Host race diversification in the common cuckoo seems largely predicated on matrilineal variation, limiting the potential for speciation. Though biparentally inherited loci contribute to regional egg diversity, mostly for maculation in *optatus*, they fail to establish strong, genome-wide barriers to gene flow that would place gentes on independent evolutionary trajectories.

REFERENCES AND NOTES

1. Aristotle, *Historia Animalium*, W. T. D'Arcy, Transl. (Clarendon Press, 1910).
2. E. Jenner, *Philos. Trans. R. Soc. London* **78**, 219–237 (1788).
3. A. Moksnes, E. Røskaft, *J. Zool.* **236**, 625–648 (1995).
4. R. B. Payne, *The Cuckoos*, vol. 15, Bird Families of the World Series (Oxford Univ. Press, 2005).
5. M. de L. Brooke, N. B. Davies, *Nature* **335**, 630–632 (1988).
6. R. C. Punnett, *Nature* **132**, 892–893 (1933).
7. M. C. Stoddard, M. Stevens, *Evolution* **65**, 2004–2013 (2011).
8. G. Dillenseger, *J. Avian Biol.* **2024**, 03252 (2024).
9. B. Sinervo, E. Svensson, *Heredity* **89**, 329–338 (2002).
10. O. Krüger, M. Kolss, *J. Evol. Biol.* **26**, 2447–2457 (2013).
11. O. Krüger, M. D. Sorenson, N. B. Davies, *Proc. Biol. Sci.* **276**, 3871–3879 (2009).
12. N. E. Langmore *et al.*, *Proc. Biol. Sci.* **278**, 2455–2463 (2011).
13. M. D. Sorenson, K. M. Sefc, R. B. Payne, *Nature* **424**, 928–931 (2003).
14. R. B. Payne, L. L. Payne, J. L. Woods, M. D. Sorenson, *Anim. Behav.* **59**, 69–81 (2000).
15. N. E. Langmore *et al.*, *Science* **384**, 1030–1036 (2024).
16. R. C. Jensen, *Nature* **209**, 827 (1966).
17. C. N. Spottiswoode, K. F. Stryjewski, S. Quader, J. F. R. Colebrook-Robjent, M. D. Sorenson, *Proc. Natl. Acad. Sci. U.S.A.* **108**, 17738–17742 (2011).
18. C. N. Spottiswoode *et al.*, *Proc. Natl. Acad. Sci. U.S.A.* **119**, e2121752119 (2022).
19. F. Fossøy *et al.*, *Nat. Commun.* **7**, 10272 (2016).
20. H. L. Gibbs, M. de L. Brooke, N. B. Davies, *Proc. Biol. Sci.* **263**, 89–96 (1996).
21. H. L. Gibbs *et al.*, *Nature* **407**, 183–186 (2000).
22. K. Marchetti, H. Nakamura, H. L. Gibbs, *Science* **282**, 471–472 (1998).
23. J. Merondun *et al.*, *Sci. Adv.* **10**, eadl5255 (2024).
24. F. Fossøy *et al.*, *Proc. Biol. Sci.* **278**, 1639–1645 (2011).
25. J.-W. Lee, H.-K. Moon, H.-J. Noh, M.-S. Kim, J.-C. Yoo, *Behav. Ecol.* **32**, 248–256 (2021).
26. P. J. Greenwood, *Anim. Behav.* **28**, 1140–1162 (1980).
27. R. J. Petit, L. Excoffier, *Trends Ecol. Evol.* **24**, 386–393 (2009).
28. N. Wang *et al.*, *Integr. Zool.* **20**, 144–159 (2025).
29. S. G. Meshcheryagina, A. Mashanova, G. N. Bachurin, I. S. Mitiay, M. G. Golovatin, *J. Zool.* **306**, 147–155 (2018).
30. O. Kleven *et al.*, *J. Avian Biol.* **35**, 394–398 (2004).
31. N. B. Davies, M. de L. Brooke, *Anim. Behav.* **36**, 262–284 (1988).
32. C.-C. Yang *et al.*, *Zool. Res.* **35**, 67–71 (2014).
33. J. Koleček, P. Procházka, V. Brlík, M. Honza, *Naturwissenschaften* **107**, 12 (2020).
34. C. Yang, W. Liang, A. P. Møller, *Behav. Ecol. Sociobiol.* **72**, 126 (2018).
35. R. C. Lewontin, J. Krakauer, *Genetics* **74**, 175–195 (1973).
36. M. Šulc *et al.*, *Zool. J. Linn. Soc.* **195**, 33–44 (2022).
37. G. Y. Kennedy, H. G. Vevers, *Comp. Biochem. Physiol. B* **55**, 117–123 (1976).
38. M. C. Stoddard, *Curr. Biol.* **32**, R1126–R1132 (2022).
39. C. Lv *et al.*, *Front. Physiol.* **13**, 1010851 (2022).
40. R. Rosario, A. J. Childs, R. A. Anderson, *Stem Cell Res.* **21**, 193–201 (2017).
41. C. Lian *et al.*, *In Vitro Cell. Dev. Biol. Anim.* **51**, 690–696 (2015).
42. Y.-P. Lin *et al.*, *Theriogenology* **74**, 1161–1178.e1, 8 (2010).
43. A. Fallahshahroudi *et al.*, *Genetics* **217**, 1–9 (2021).
44. W. Li *et al.*, *Poult. Sci.* **103**, 103715 (2024).
45. R. Liao *et al.*, *Anim. Genet.* **47**, 588–596 (2016).
46. Y. Y. Yien, M. Perfetto, *Front. Cell Dev. Biol.* **10**, 895521 (2022).
47. S. Sano, S. Inoue, Y. Tanabe, C. Sumiya, S. Koike, *Science* **129**, 275–276 (1959).
48. T. Shetty, K. Sishtla, B. Park, M. J. Repass, T. W. Corson, *iScience* **23**, 101391 (2020).
49. M. Bulla, M. Šálek, A. G. Gosler, *Auk* **129**, 26–35 (2012).
50. C. Alonso-Alvarez *et al.*, *Ecol. Lett.* **7**, 363–368 (2004).
51. M.-Y. Lu, W.-W. Wang, G.-H. Qi, L. Xu, J. Wang, *Poult. Sci.* **100**, 100811 (2021).
52. S. Y. Kim, H. T. Kang, H. R. Choi, S. C. Park, *Exp. Mol. Med.* **43**, 15–23 (2011).
53. A. S. Baras, A. Solomon, R. Davidson, C. A. Moskaluk, *Lab. Invest.* **91**, 1170–1180 (2011).
54. S. S. Shinde, S. Sharma, L. Teekas, A. Sharma, N. Vijay, *Sci. Rep.* **11**, 24437 (2021).
55. J. Hu *et al.*, *Theriogenology* **232**, 87–95 (2025).
56. C. Yang *et al.*, *PLOS ONE* **5**, e10816 (2010).
57. J. N. Wolff, E. D. Ladoukakis, J. A. Enríquez, D. K. Dowling, *Philos. Trans. R. Soc. London Ser. B* **369**, 20130443 (2014).
58. L. Chen *et al.*, *PLOS Genet.* **16**, e1009119 (2020).
59. Z. Wang *et al.*, *PLOS Genet.* **9**, e1003183 (2013).
60. S. Ito, M. Tsudzuki, M. Komori, M. Mizutani, *J. Hered.* **84**, 145–147 (1993).
61. G. H. Kunz, *Naumannia Arch. Für Ornithol. Vorzugsweise Eur.* **1**, 51–53 (1850).
62. E. C. Collias, *Auk* **110**, 683–692 (1993).
63. J. Merondun, merondun/cuculus_host: Revisions: August 2025 v2, version v1.3. Zenodo (2025); https://doi.org/10.5281/zenodo.16816856.

ACKNOWLEDGMENTS

We thank all the field biologists who assisted with field work and blood collection, including G. Rudolfsen, I. Hafstad, A. Antonov (the late), J. R. Vikan, L. Wang, C. Yang, B. Zhou, G. Zhong, K. Schulze-Hagen, J. Berstad, and M. Požgayová, as well as N. Schäffer for additional support. **Funding:** Computing was performed on the BioHPC hosted at Leibniz Rechenzentrum Munich funded by German Research Foundation grant INST 86/2050-1 FUGG (J.B.W.W.). This work was funded by LMU Munich (J.B.W.W.); German Research Foundation grant WO 1426/2-1 (J.B.W.W.); The Research Council of Norway grant 151641/177709/218144 (F.F. and B.G.S.); Russian Federation grant 122021000096-7 (M.G.); National Natural Science Foundation of China grants 32270526 and 32470513 (W.L.); and National Key R&D Program of China grant 2023YFF1304600 (W.L.). **Ethical approval:** All applicable international, national, and/or institutional guidelines for the care and use of animals were followed. Permission for blood sampling of wild common cuckoos was granted in the Czech Republic by the Hodonín Municipality Office (MUHOCJ 14306/2016/OŽP) with experimental design approved by the Czech Ministry of the Environment (3030/ENV/17–169/630/17). Collection of blood samples complied with the legal regulations of Bulgaria. Blood sampling and experimental procedures in China were in accordance with the Animal Research Ethics Committee of Hainan Provincial Education Centre for Ecology and Environment, Hainan Normal University (no. HNECEE-2012-002 and HNECEE-2012-003). In the UK, loose feathers from common cuckoos were collected as a by-product of tagging work carried out under license from the Special Marks Technical Panel of the British Trust for Ornithology Ringing Scheme, operating on behalf of the UK government's Home Office. Appropriate licenses were obtained for sampling in Finland (ESAVI/12343/2020). Permission for sampling of blood from wild common and oriental cuckoos in Russia in compliance with the Federal Law of Russian Federation no. 498-Ф3, as ensured by the Research Bioethics Committee of the Institute of Plant and Animal Ecology, Russian Academy of Sciences. Necessary compliance with the Nagoya protocol was ensured for each country from which genetic resources were obtained. **Author contributions:** Contributions are listed in alphabetical order. Conceptualization: J.B.W.W., F.F.; Methodology: J.B.W.W., J.M., G.L.O.; Investigation: J.B.W.W., J.M.; Formal analysis: J.M.; Visualization: J.M.; Funding acquisition: J.B.W.W.; Project administration: J.B.W.W., G.L.O.; Resources: B.G.S., C.H., C.M., G.B., J.R., K.T., M.G., M.H., M.M., M.Š., P.A., P.P., S.M., V.B., V.F., W.L., Y.R.; Supervision: J.B.W.W.; Writing – original draft: J.M.; Writing – review & editing: J.B.W.W., J.M. **Competing interests:** The authors declare that they have no competing interests. **Data and materials availability:** All associated sequence data are uploaded to the NCBI Sequence Read Archive (SRA) with biosample and run accessions indicated in table S1 under Bioproject PRJNA614488. All bioinformatic code in markdown .html and .md formats necessary to reproduce the findings presented here are available on GitHub (https://github.com/EvoBioWolf/CUCKOO_gentes) and are perpetually archived via Zenodo (*63*). **License information:** Copyright © 2025 the authors, some rights reserved; exclusive licensee American Association for the Advancement of Science. No claim to original US government works. https://www.science.org/about/science-licenses-journal-article-reuse. This research was funded in whole or in part by the German Research Foundation (INST 86/2050-1 FUGG and WO 1426/2-1); as required, the author will make the Author Accepted Manuscript (AAM) version available under a CC BY public copyright license.

SUPPLEMENTARY MATERIALS

science.org/doi/10.1126/science.adt9355
Materials and Methods; Tables S1 to S7; Figs. S1 to S32; References (*64*–*126*);
MDAR Reproducibility Checklist

Submitted 18 October 2024; resubmitted 9 May 2025; accepted 2 September 2025

10.1126/science.adt9355

Adjusting to retirement

Tod F. Stuessy

After more than 40 years in academia, I felt optimistic about the path ahead when I retired in 2012. I intended to continue working, focusing on research and writing now that I no longer had administrative and teaching responsibilities. But as I downsized my office and changed my email signature to Emeritus Professor, I was unprepared for the reality of retirement. I found it difficult to adjust to no longer holding decision-making roles. Colleagues were less likely to seek my opinions than before, which ate at my sense of self-worth and left me feeling that my ideas were no longer valued. Regaining my equilibrium and appreciating the positive aspects of retirement took months.

I had leadership roles throughout my career. After spending 27 years at a U.S. university, I pivoted to working as the deputy director of a natural history museum for 2 years followed by 15 years as a faculty member at a European university. In these positions, I had a range of decision-making responsibilities—departmental chair, botanical garden director, journal editor, secretary-general for an international scientific organization.

As I reached 68, I was ready to let those roles go. After so many cycles of dealing with administrative hurdles and other challenges, I had lost some of my drive. It seemed appropriate for more junior faculty to step into those shoes. But I hadn't fully processed what that might mean for me.

I was excited to have workdays free of the meetings and classes that broke up my days as a professor. I expected to have more time to finish manuscripts, start collaborative projects, and dive into book writing. That turned out to be true. But it was hard to ignore that meetings were being scheduled to which I was not invited. I was no longer an essential cog in the system.

As time wore on, I also had a nagging sense of being left behind scientifically, standing beside the track after the train had left the station. I continued to attend national and international conferences, but fewer than before. I didn't always hear about new developments, and I drifted away from old friends from other universities.

On my own campus, where I had a small office, the lack of daily chats in the laboratory with students and colleagues and discussions in the classroom left me feeling isolated. Retirement is a haven for the solitary worker, and working alone has never been a problem for me. But I did find that when bad news struck—such as learning that a paper had been rejected—I had no class later that day where a successful lecture could recharge my self-confidence.

Slowly, though, I began to ease into my new rhythm. Structure helped. I gave myself deadlines for completing manuscripts, and I set a schedule to get to the office by 10 a.m. each morning, which stimulated me to get out of bed and keep going. I also learned to see my isolation as a privilege rather than a penalty. In addition to being able to complete shorter manuscripts, I could focus on larger projects, such as review papers and books, which have proved very satisfying. Although retirement means I have lost influence with university decision-making, having the time to step back and take a broad, synthetic view of my field more than makes up for it.

For me, success in retirement has involved mapping out a realistic plan that is both enjoyable and academically fulfilling. When I do attend a conference, I go with reduced expectations—not to capture all the newest advances, but to learn about broad new trends and catch up with as many old friends as possible. The good news is that I am no longer being constantly evaluated by others—I am only being evaluated by myself. I have learned to keep pushing forward, at a more relaxed pace, and working with, rather than fighting against, these new challenges. □

Tod F. Stuessy is an emeritus professor at Ohio State University and the University of Vienna. Do you have an interesting career story to share? Send it to SciCareerEditor@aaas.org.

ILLUSTRATION: ROBERT NEUBECKER